Kiel University
Christian-Albrechts-Universität zu Kiel

Eddy covariance air-sea gas flux measurements

Regional sources and gas transfer limitation

DISSERTATION

zur Erlangung des

Doktorgrades

der Mathematisch-Naturwissenschaftliche Fakultät

der Christian-Albrechts-Universität zu Kiel

Erste Gutachterin: Prof. Dr. Christa A. Marandino

Zweiter Gutachter: Prof. Dr. Arne Körtzinger

eingereicht von

Alexander Zavarsky

mündliche Prüfung am 13. April 2018

Erklärung zur Verfassung der Arbeit

Alexander Zavarsky
Metzstraße 8, 24116 Kiel

Hiermit erkläre ich, dass ich diese Doktorarbeit, abgesehen durch die Beratung meiner Betreuerin, selbstständig verfasst, sowie alle wörtlichen und inhaltlichen Zitate als solche gekennzeichnet habe. Die Arbeit wurde unter Einhaltung der Regeln guter wissenschaftlicher Praxis der Deutschen Forschungsgemeinschaft verfasst. Sie hat weder ganz, noch in Teilen, einer anderen Stelle im Rahmen eines Prüfungsverfahrens vorgelegen, ist nicht veröffentlicht und auch nicht zur Veröffentlichung eingereicht.

Kiel, 15. August 2018

Alexander Zavarsky

Danksagung

Ich bedanke mich ganz herzlich bei Prof. Dr. Christa Marandino für die Möglichkeit in Ihrer Forschungsgruppe dieses spannende Thema zu bearbeiten. Ich habe dafür den Großteil Ihres Forschungsbudgets und Ihrer Geduld verbraucht. Ich hoffe ich kann die Erwartungen erfüllen.
Des weiteren möchte ich mich bei meinem Zweitgutachter Prof. Dr. Arne Körtzinger und dem Komitee der Disputation bedanken. Speziellen Dank geht an die Mitarbeiterinnen und Mitarbeiter der Meereschemie am GEOMAR. Sie habe meine Spleens, meine beiläufigen Gesangsdarbietungen und Zwischensprints ertragen. Ich möchte mich auch bei Anna Canning und Dennis Booge aus dem gemeinsamen Oval Office bedanken. Danke für das zweite Zuhause und das Korrekturlesen dieser Arbeit. Danke an die Kapitäne und Crews meiner Forschungsfahrten. Es war nicht immer leicht einen Ösi an Board zu haben, aber am Ende haben wird das Ding schon geschaukelt bekommen.
Ich bedanke mich bei meinen Eltern, meinem Bruder, meiner Familie und meine Freunden in Österreich, Deutschland, Norwegen, USA oder wo immer sie sich auch gerade befinden. Ein spezieller Dank geht an Kiel Rugby bei der FT Adler Kiel. Danke, dass ich diesen Sport auf dem Platz und neben dem Platz mit euch ausüben konnte. Danke auch an Mike ‚Ermittlerkönig' Visel, Corinna‚Zora' Müller und das Unrat für die schönen Tatortabende. Danke auch an Mauro vom Punto Italia Store, Mareike and the Cake, Freistil, Hansa II und das Castello für die Espressi. Ich bedanke mich bei dem Team der Kantine des Landtages welche mich all die Jahre zu Mittag durchgefüttert hat. Ich vergebe euch die Willkür bei der Vergabe der Mengenzuschläge.
Die Arbeit wurde in der Helmholtz Young Investigator Gruppe (TRASE-EC (VH-NG-819)) von Prof. Dr. Christa Marandino durchgeführt. Diese Arbeitsgruppe ist am GEOMAR Helmholtz-Zentrum für Meeresforschung in die Abteilung chemische Ozeanographie integriert.

Komm zeig es mir mit deiner Skala,
sei meines Outputs Interpret,
ich bin süchtig nach Kriterien,
denn ich zähle nur als Quantität.

Gregor Fröhlich und die Krisenstimmung

Abstract

Eddy covariance is a technique to measure air-sea gas exchange directly. A direct flux measurement has the advantage that, without parameterizations or major simplifications of processes, it can provide local information about the air-sea flux of trace gases. A local data set enables us to study sources, sinks and pathways of the exchanged substance, as well as to describe the environmental conditions which influence the magnitude of this flux. During the SO234-2/235 cruise in the western tropical Indian Ocean, the direct flux of dimethyl sulfide (DMS) and CO_2 was measured. Additionally, the flux of isoprene and sea-spray was estimated using the bulk flux formulation.

The major sources of aerosols in the marine boundary layer are DMS, isoprene and sea spray, which represent the predecessors of sulfur aerosols, secondary aerosols and primary organic/inorganic aerosols respectively. Aerosols have a direct impact on the radiative balance of the Earth through scattering of light. Acting as cloud condensation nuclei they promote cloud formation and as a consequence change the Earth's albedo. This is a secondary impact on the radiative balance. During the south-west monsoon, the western topical Indian Ocean is dominated by marine air masses. The steady strong winds enhance the air-sea flux of DMS, isoprene and sea spray. In Section 3, I focus on the efflux of these aerosol predecessors together with satellite derived aerosol numbers in the atmosphere. The oceanic emissions are tracked using the FLEXPART forward trajectory model, which provides the locations and the times for the satellite remote sensing. The averaged satellite aerosol numbers along the 12 h downwind trajectory were correlated with the magnitude of the oceanic sources, which was found to be a significant positive correlation. The results point to a local influence of air-sea fluxes on the aerosol number, which could give rise to local feedbacks.

Air-sea gas flux is commonly parameterized by the gas transfer velocity k. This parameterization is usually related to wind speed and monotonically increasing. Published eddy covariance measurements have shown that the k vs wind speed relation could decrease at medium to high wind speed. Bubbles, created by breaking waves, contribute significantly to air-sea gas exchange, especially for insoluble gases like CO_2. Due to the different solubility of DMS and CO_2, the difference between their gas transfer velocities is an estimate for the magnitude of bubble mediated gas transfer. My investigation in Section 4 uses gas transfer velocities derived from DMS and CO_2 eddy covariance measurements

to describe gas transfer limitations which is caused by a wind-wave interaction. This process is parameterized using the transformed Reynolds number Re_{tr}. Below a threshold of $|Re_{tr}| < 6.7 \cdot 10^5$, flow separation develops at the wave's lee side and causes a decoupling between the flow above the wave and the ocean surface. The gas exchange is then highly likely to be suppressed. Subsequently, it is shown that previously published gas transfer limitations also coincide with an increased occurrence of Re_{tr} below the threshold. Additionally, three parameterizations of whitecap fractions are used to calculate the influence of bubble mediated gas transfer on the total gas transfer. It is found that the functional form of the bubble mediated gas transfer in relation to wind speed is similar, differing by an offset, to a previous published one.

In Section 5 I calculate the impact of gas transfer limitation on gas transfer parameterizations and global climatologies of DMS and CO_2. Using two data sets with limited gas transfer velocities an algorithm, which corrects for the effect of gas transfer limitation, is presented. The data sets of two highly cited gas transfer parameterizations (Nightingale 2000 and Wanninkhoff 2014) are investigated with respect to gas transfer limitation. Based on these algorithms the Nightingale 2000 parameterization is found to be heavily gas transfer limited and its gas transfer velocity will increase on average by 22% if the correction is applied. The Wanninkhoff 2014 parameterization increases by 9.85% after correction. Subsequently, a 2014 global wave-model data set is analyzed for situations in which gas transfer limitation might occur. 18.6% of all data points are gas transfer limited. This reflects the 2014 global average. The correction is then applied to the global air-sea flux climatologies of DMS and CO_2 for the year 2014. Consideration of the gas transfer limitation decreases the DMS efflux by 11% and decreases the oceanic uptake of CO_2 by 6-7%. Gas transfer limitation has to be considered in global budget calculations of gases which have a significant air-sea gas exchange.

I show eddy covariance measurements are a powerful tool to investigate air-sea interaction processes, sources, sinks and pathways. The application of this approach is very versatile and works in very small and large scales . During this dissertation, three important topics are addressed: [1] The aerosol budget in the marine boundary layer: I propose a local influence of air-sea fluxes. [2] Gas transfer limitation: I developed a wind-wave model that explains this suppression of gas transfer. [3] The effect of gas transfer limitation on global budgets: Using a new algorithm, I apply gas transfer limitation to global DMS and CO_2 air-sea fluxes.

Kurzfassung

Die Eddy-Kovarianz-Methode ist eine Technik zur direkten Messung des Gasaustauschs zwischen Atmosphäre und Ozean. Eine direkte Gasflussmessung hat den Vorteil, dass sie ohne Parametrisierung oder wesentliche Vereinfachungen der Prozesse punktgenaue Informationen über den Austausch von Spurengasen liefern kann. Dieser genaue Datensatz ermöglicht es, Quellen, Senken und Trajektorien des ausgetauschten Gases zu untersuchen und die Umweltparameter zu beschreiben, welche zu diesem Gasaustausch führen. Während der SO234-2/235 Fahrt im westlichen tropischen Indischen Ozean wurden der direkte Fluss von Dimethylsulfid (DMS) und CO_2 gemessen. Zusätzlich wurde der Fluss von Isopren und das Auftreten von Gischt mit Hilfe einer Parametrisierung berechnet.

DMS, Isopren und Gischt sind in der Atmosphäre Ausgangsstoffe für Schwefelaerosole, sekundäre organischen Aerosole und primäre organische/anorganische Aerosole. Diese Gruppen sind die Hauptquellen für Aerosole in der atmosphärischen Grenzschicht über dem Ozean. Aerosole haben durch Reflexion einen direkten Einfluss auf das Strahlungshaushalt der Erde. Darüber hinaus agieren sie als Kondensationskeime für Wolken und fördern deren Bildung, welche das Albedo der Erde beeinflusst. Dies ist der sekundäre Einfluss auf den Strahlungshaushalt. Während des Sommermonsun wird der westliche tropische Indische Ozean von maritimen Luftmassen dominiert. Die stetigen starken Winde verstärken den Gasaustausch von DMS und Isopren und die Bildung von Gischt in der Atmosphäre. In Kapitel 3 untersuche ich den Einfluss dieser Aerosolquellen auf satellitengestützten Aerosolkonzentrationen in der Atmosphäre. Die Emissionen werden mit Hilfe des FLEXPART-Transportmodells, welches die Standorte und Zeiten für die Satellitenfernerkundung liefert, in Windrichtung verfolgt. Die gemittelten Aerosolkonzentrationen entlang der 12 stündigen Trajektorie wurden dann mit der Größe der Quelle korreliert. Die Korrelationen sind positiv und signifikant. Die Ergebnisse deuten auf einen lokalen Einfluss des Gasaustauschs auf die lokale Aerosolkonzentration hin, was zu lokalen Effekten und Rückkopplungen führen kann.

Der Gasaustausch zwischen Atmosphäre und Ozean kann durch die Gasaustauschgeschwindigkeit k beschrieben und modelliert werden. Diese Geschwindigkeit k ist normalerweise von der Windgeschwindigkeit anhängig und bezogen auf diese monoton ansteigend. Messungen mit der Eddy-Kovarianz-Methode haben gezeigt, dass die Relation zwischen k und Windgeschwindigkeit bei mittlerer bis hoher Windgeschwindigkeit jedoch abnehmen kann.

Ich verwendet in Kapitel 4 Gasaustauschgeschwindigkeiten, welche aus DMS und CO_2 Eddy-Kovarianz-Messungen berechnet wurden, um einen Prozess zu beschreiben, der eine Begrenzung des Gastransfers bewirkt. Dieser Prozess ist eine Wind-Wellen-Interaktion und wird, nach unserem Modell, mit Hilfe der transformierten Reynoldszahl Re_{tr} beschrieben. Unterhalb eines Wertes von $|Re_{tr}| < 6.7 \cdot 10^5$ entsteht ein Strömungsabriss an der Leeseite der Welle zwischen der Luftströmung über der Welle und der Meeresoberfläche. Der Gasaustausch wird dadurch unterdrückt. Schon veröffentlichte Beispiele dieser Limitierung des Gasaustausches können ebenfalls mit diesem Re_{tr} Modell beschrieben werden. Wegen der unterschiedlichen Löslichkeit von DMS und CO_2 in Meerwasser kann der Unterschied im Gasaustauschs dieser beiden Stoffe verwendet werden um den Einfluss von Gasblasen auf den Gasaustausch zu untersuchen. Drei Parametrisierungen des Blasenanteils im Meerwasser werden verwendet, um den Einfluss von diesen, durch brechende Wellen entstehenden, Blasen auf den Gasaustausch zu untersuchen. Die Funktion dieses Einflusses ist der Form nach ähnlich einer Funktion, welche schon publiziert wurde, jedoch unterscheidet sich diese Beiden um einen konstanten Betrag.

In Kapitel 5 berechne ich die Auswirkungen der Limitierung des Gasaustausches auf den Gasaustausch von globalen DMS und CO_2 Klimatologien. Durch die Analyse von zwei Datensätzen, mit limitierten Gasaustausch, wird ein Algorithmus entwickelt, welcher die Auswirkung der Limitierung quantifiziert. Zwei häufig verwendete Parametrisierungen des Gasaustauschs (Nightingale 2000 und Wanninkhoff 2014) werden auf das Auftreten von Limitierung in Ihren Datensätzen untersucht. Basierend auf diesen Berechnungen ist die Nightingale 2000 Parametrisierung einer sehr starken Limitierung ausgesetzt. Die Geschwindigkeit der Gasübertragung erhöht sich bei Anwendung der Korrektur für die Limitierung um 22%. Die Wanninkhoff 2014 Parametrisierung erhöht sich nach Korrektur um 9.85%. Anschließend wird ein globaler Datensatz eine Ozeanwellenmodells aus dem Jahr 2014 auf die Begrenzung des Gastransfers analysiert. 18.6% aller Datenpunkte zeigen eine Limitierung der Gasaustauschgeschwindigkeit. Dieser Wert ist der weltweite Durchschnitt im Jahr 2014. Der Korrekturalgorithmus für das Jahr 2014 wird dann auf die globalen Klimatologien von DMS und CO_2 angewendet. Durch die Begrenzung des Gastransfers sinkt der globale DMS-Ausstoß um 11%. Die Aufnahme von CO_2 durch den Ozean sinkt um 6-7%. Daraus folgt dass die Begrenzung des Gasaustausch durch Wind-Wellen Wechselwirkung in globalen Klimatologien berücksichtigt werden muss.

Eddy-Kovarianz Messungen sind ein wirksames Werkzeug um den Gasaustausch zwischen Atmosphäre und Ozean, Quellen, Senken sowie Transportwege zu beschreiben. Diese Arbeit zeigt die vielseitige Anwendbarkeit der Messmethode, von kleinen zu großen Skalen. Drei wichtige Themen wurden angesprochen: [1] Aerosolkonzentration in atmosphärischen Grenzschicht über dem Ozean: Ich stelle eine direkte Verbindung zwischen ozeanischen Quellen von Spurengasen und Aerosolkonzentrationen fest. [2] Limitierung der Gasaustauschgeschwindigkeit: Ich beschreibe eine Wind-Wellen Wechselwirkung welche eine Limitierung des Gasaustausches zur folgen haben kann. [3] Der Effekt der

Limitierung des Gasaustausches auf den globalen Haushalt von DMS und CO_2: Mit einem entwickeltem Algorithmus berechne ich Auswirkung auf den globalen Gasaustausch von DMS und CO_2.

Manuscript overview

Alex Zavarsky, Dennis Booge, Alina Fiehn, Kirstin Krüger, Elliot Atlas, and Christa Marandino. The influence of air-sea fluxes on atmospheric aerosols during the summer monsoon over the tropical indian ocean. *Geophysical Research Letters*, dec 2017. doi: 10.1002/2017gl076410

Contribution: I designed the study together with CM. I measured the eddy covariance flux of DMS and analyzed the correlations using the forward trajectories, calculated by AF, and the satellite data. EA and DB measured the air and water concentration of DMS and isoprene. I wrote the main part of the manuscript.

A. Zavarsky, L. Goodwijjn-Murphy, T. Steinhoff, and C.A. Marandino. Gas transfer of dms and co2 in the indian ocean. *JGR, Under Review*, 2018

Contribution: I designed the study together with CM. I measured the eddy covariance flux of DMS and CO_2 together with TS. The hypothesis of a wind-wave interaction leading to gas transfer limitation was developed by me. LGM investigated the bubble mediated gas transfer. I wrote the main part of the manuscript.

A. Zavarsky and C.A. Marandino. Influence of reynolds number dependent wind-wave interaction on air-sea gas exchange and the global budget of dms and co_2. *ACP, Under Review*, 2018

Contribution: I designed the study. I calculated the influence of gas transfer limitation on global DMS and CO_2 climatologies and on common gas transfer parameterizations. I wrote the main part of the manuscript.

Contents

CHAPTER 1

Introduction

1.1 Air-sea interaction

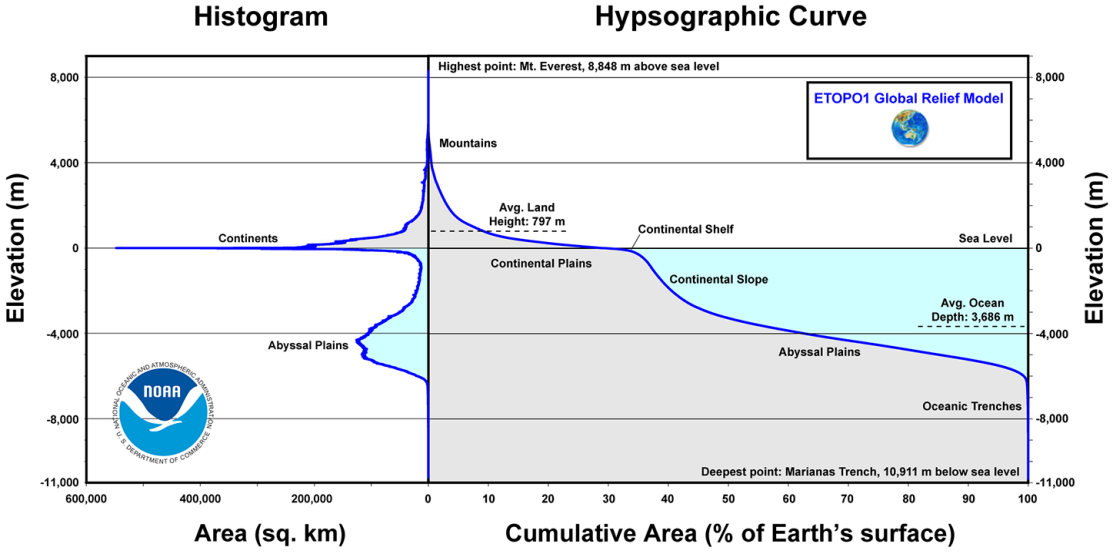

Figure 1.1: Histogram and hypsographic curve of the Earth's surface [National Centres for Environmental Information, 2018].

Just like skin of a human body, the ocean surface could be regarded as the biggest 'organ' of our planet. 71% of the earth's surface is covered by oceans. It is the interface between the atmosphere and the ocean body with its water masses. The dimensions of this body of water are enormous (Figure 1.1). The average depth of the ocean is 3700 m. In relation to the average land elevation of 800 m the ocean is in volume outnumbering all mountains and elevated plains of the Earth combined. From the Earth's surface to 4000 m

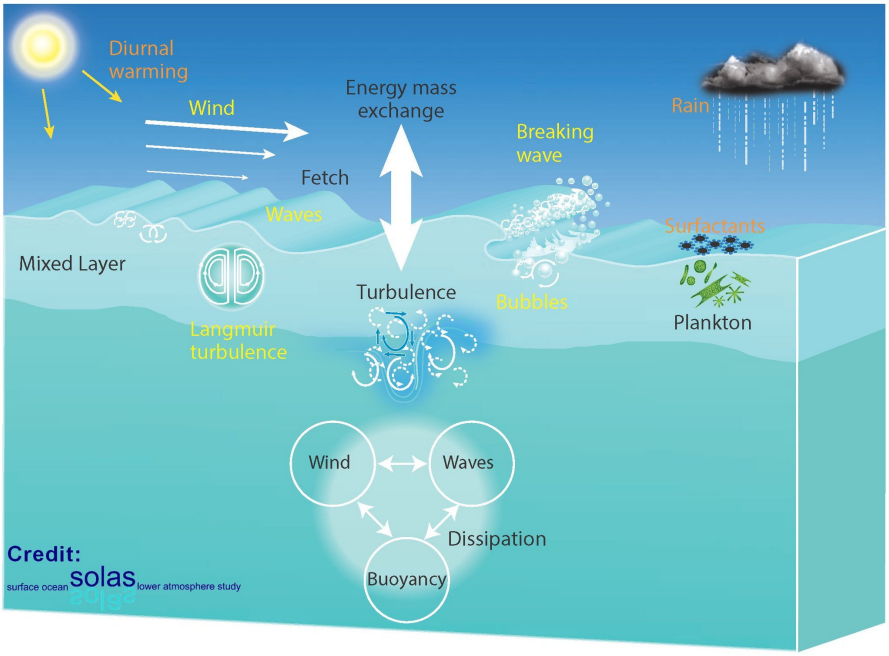

Figure 1.2: Graphical description of dominant air-sea interaction processes Brévière and the SOLAS Scientific Steering Committee [2016].

depth the ratio of continental rock (lithosphere) to water (hydrosphere) is 1:1. This means the oceans are an important storage volume for energy (temperature), momentum (waves, currents) and matter (water vapor, unfortunately waste and gases). Through the movement of water masses (currents, upwelling system) the stored quantities can be transported horizontally as well as vertically. The exchange of these stored quantities with the rest of the world is conducted through the ocean surface and is therefore regarded as an air-sea interaction (Figure 1.2). Even kids diving into the ocean or swimmers leaving traces of sunscreen on the sea surface can be seen as an interaction through the air-sea interface.

My work focuses on the exchange of gases between the ocean and the atmosphere. Flux is the transport of a quantity (in this case gas molecules) from one location to the other. Air-sea gas exchange is described as flux and has the units of mass per area per time. The respective mass is exchanged between the atmosphere and the ocean surface through a certain area in a certain time period. There is no stringent sign convention for the direction of the flux. In this manuscript a negative flux describes a transport from the atmosphere to the ocean (oceanic sink). A positive flux is a transport from the ocean to the atmosphere (oceanic source). The air-sea flux is not uniform in time and in space and generally variable over the ocean surface.

A globally relevant air-sea flux is the uptake of atmospheric carbon dioxide (CO_2) by the ocean (Figure 1.3). The amount of CO_2 exchanged (air-sea flux) is determined by air-sea interactions. About 30% of the anthropogenically emitted CO_2 is taken up by the ocean,

where it causes ocean acidification (decrease of seawater pH) with all its consequences for the flora and fauna. A change in the air-sea flux will impact atmospheric CO_2 levels and the chemical properties of ocean water. Therefore, it is important to study and understand the processes governing this flux.
A rather local influencing air-sea flux is the emission of dimethyl sulfide (DMS) from the ocean to the atmosphere. DMS is a major sulfur source to the atmosphere and an important aerosol predecessor in the marine boundary layer (MBL). There DMS largely contributes to the formation of cloud condensation nuclei (CCN). A larger DMS flux increases the CCN number in the MBL. CCN are important for the formation of cloud droplets and clouds. Regional variations of the DMS flux locally influence aerosol numbers and cloud formation. An understanding of local air-sea interaction processes is therefore essential.

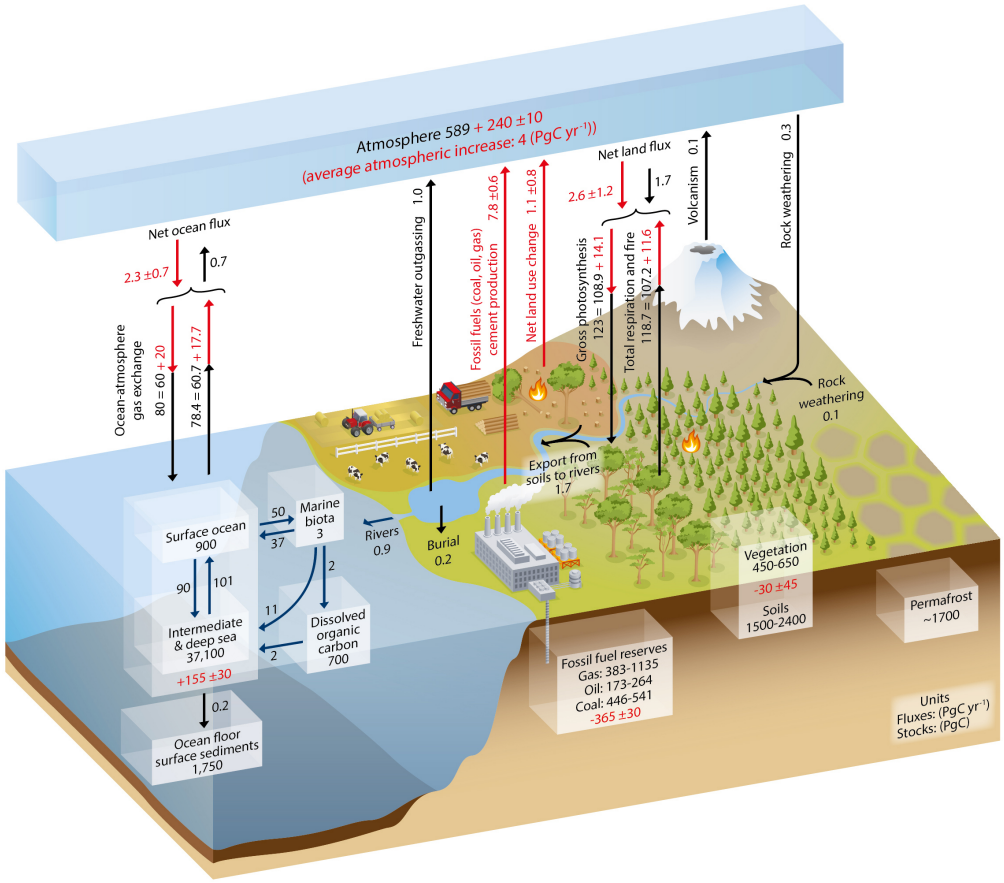

Figure 1.3: Global carbon cycle [on Climate Change, 2014].

1.2 Air-sea gas exchange

A common model of gas transfer is the bulk formulation. Like an electric circuit it uses a potential difference and a resistor to describe flux. Air-sea interaction is powered by a difference between the water and the atmosphere above. For example, these differences are velocity (momentum flux) or temperature (sensible heat flux). For gases the concentration difference ΔC acts as the potential and driving force of gas flux (Equation 1.1). The concentration difference between two phases (liquid and gas) can be compared using Henry's law constant H. Using Equation 1.1 the concentration difference ΔC, which is the displacement from equilibrium, can be calculated.

$$\Delta C = c_{air} - \frac{c_{water}}{H} \tag{1.1}$$

In contrast to an electric circuit, here the resistor is usually described with its inverse value, the conductance (gas transfer velocity). The gas transfer velocity k is the conductance in gas exchange and has the units of velocity, typically [cm h^{-1}]. k includes all processes that facilitate or impede gas transfer. Together with ΔC the bulk formulation describes gas flux F as follows:

$$F = k \cdot \Delta C = k \cdot \left(c_{air} - \frac{c_{water}}{H} \right) \tag{1.2}$$

As this is a simple mathematical description of a model, both parts k and ΔC are connected with uncertainties which can be summarized by these questions:

- Is ΔC a good representation of the driving potential of gas exchange?
- Can k be parameterized? How?

ΔC

The displacement from equilibrium between the air side and water side creates a potential which powers the gas exchange. Ideally, the air and water concentrations would be measured directly at the air-sea interface. However, bulk concentrations are usually measured from ship's 5 m seawater intake c_{water} and air sampling masts c_{air}, which are usually 20 m above sea level. These are spatially displaced to the air-sea interface and could significantly differ from the conditions responsible for gas exchange. Any change of concentration, due to chemical or biological production or destruction, between the measurement and the sea surface, is unaccounted for. On the waterside the sea surface microlayer (SML) is the uppermost surface of the ocean. It is between 1-1000 µm thick and accumulates organic compounds, gels and microorganisms [Engel et al., 2017]. The SML is biologically and chemically active and can alter the concentration through production or destruction of dissolved gases and therefore influence the air-sea gas transfer. So far, the SML is ignored in the measurement of c_{water}. Regarding CO_2, Turk et al. [2010] has found a dilution effect of rain on the pCO_2 which effects the surface down to 2 m by a reduction of pCO_2 up to 30 µ atm. c_{water} concentration measurements are

usually made at greater depths (approx. 5 m). This would mean that measured c_{water} is different to the concentration that causes the equilibrium displacement which powers the gas transfer.
On a temporal scale, improvements in technology, especially in the area of optical measurements, could increase the sampling frequency of the bulk measurements. Concentration measurements using gas chromatography have a sampling interval of minutes to hours. Optical gas concentration measurements, for example, decrease the frequency to seconds. In case of slow changing and homogeneous environments an hourly time scale can be sufficient, but within frontal systems to correlate the bulk with other data sets, a fast sampling is necessary [Gülzow et al., 2011].

Gas transfer velocity parameterization

The gas transfer velocity k is the coefficient which describes all processes facilitating and hindering gas transfer. Using direct flux measurements and by rearranging Equation 1.2 to

$$k = \frac{F}{\Delta C} \tag{1.3}$$

k can be directly calculated from measured quantities. If direct gas flux measurements are not available, the air-sea flux can be calculated using Equation 1.2 together with a k parameterization.
Usually, k is related to wind speed u_{10} (Figure 1.4). This is logical as wind speed is the main driver of turbulence at the interface. Furthermore, wind speed is a standard meteorological and easily measured quantity. Other parameterizations use friction velocity u^* [Landwehr et al., 2017, Brumer et al., 2017] or turbulent dissipation ϵ [Esters et al., 2016]. Additionally, special processes, such as, bubble mediated gas transfer influence the magnitude and the functional form of k. All these parameterizations are monotonically increasing functions. Wanninkhof et al. [2009] concludes that a 3rd order polynomial is sufficient to describe any wind speed dependent parameterization. However, the functional form is still in dispute. So far, the goal of identifying a universally usable, across all environments and gases, and accepted parameterization has not been reached. As a consequence, for a given ΔC value, different k parameterizations (Figure 1.4) lead to different results for air-sea gas exchange. For example, the uncertainty in model calculations of DMS flux due to different parameterizations is 30% [Lennartz et al., 2015].
The two layer model (Figure 1.5, [Liss and Slater, 1974]) is a simple description of k and the processes at the air-sea interface. It separately describes air and water processes and allows the addition of other processes, such as bubble mediated gas transfer [Merlivat and Memery, 1983, Woolf, 1997]. k is separated into an air-side gas transfer velocity k_{air} and into a water-side gas transfer velocity k_{water} (Equation 1.4).

$$\frac{1}{k} = \frac{1}{k_{air}} + \frac{1}{k_{water}} \tag{1.4}$$

Both, k_{air} and k_{water} describe, on their respective side of the interface, the transport through the diffusive layer (Figure 1.5). The thickness of the diffusive layer is itself

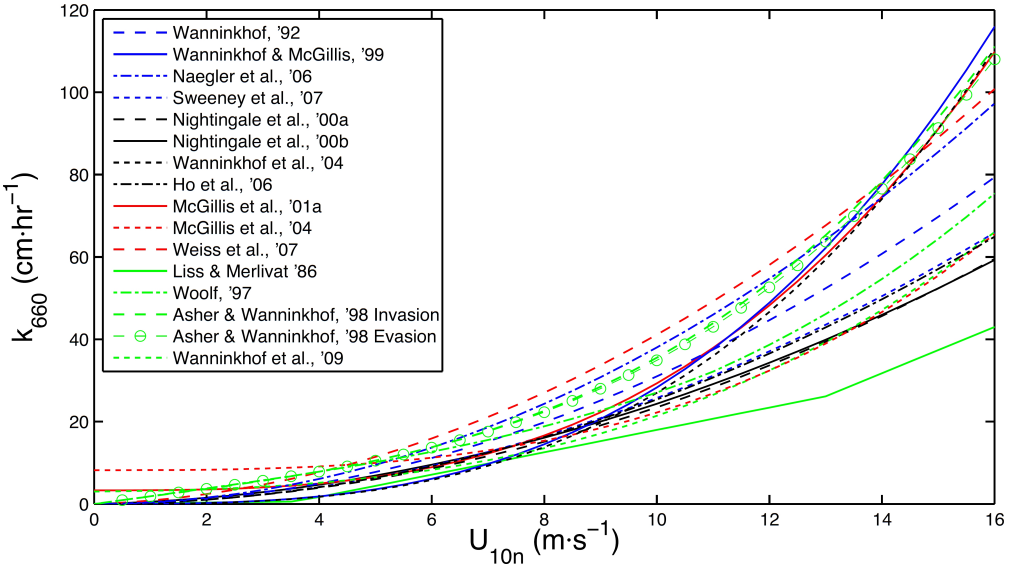

Figure 1.4: Wind speed based k parameterizations compiled by Prytherch [2011].

dependent on environmental conditions, such as wind speed and friction velocity.
To make gas transfer velocities of different gases comparable, Schmidt number Sc scaling was introduced. The Schmidt number is the ratio of diffusivity D and kinematic viscosity ν (Equation 1.5).

$$Sc = \frac{D}{\nu} \tag{1.5}$$

The ability of different gases to cross the molecular diffusion layer is dependent on Sc, therefore measurements of k have to be related to a set Sc. This is usually Sc=660, which is the Schmidt number for CO_2 in saltwater at 20^{o}C (Equation 1.6).

$$\frac{k_{660}}{k_{Sc}} = \left(\frac{660}{Sc}\right)^n \tag{1.6}$$

The exponent n depends on the surface conditions. For smooth surfaces n= $-\frac{2}{3}$, for rough wavy surfaces n= $-\frac{1}{2}$ [Komori et al., 2011]. In this thesis all calculations are made with n= $-\frac{1}{2}$.
k_b is the portion of gas transfer mediated through the injection of bubbles and added to the interfacial gas transfer velocity k_o (Equation 1.7), which is the bubble free transfer through the diffusive water layer. Bubble mediated gas transfer is dependent on the solubility of the gas. A rather soluble gas (DMS) is less influenced by k_b than an insoluble gas (CO_2, SF_6).

$$k_{water} = k_o + k_b \tag{1.7}$$

Sc scaling should not be applied to k_b. The calculation and parameterization of k_b is still uncertain. Usually k_b is parameterized using the whitecap fraction WC [Woolf, 1997]. WC describes the amount of sea surface covered with breaking waves. The global average

WC is 1% [Woolf, 1997]. The choice of the bubble model, as well as the choice of the WC parameterization, influences k_b. One possible way to quantify bubble mediated gas transfer requires direct flux measurements of two gases with different solubility. Preferably one (e.g. DMS) should be rather soluble, which makes it less influenced by bubbles, and the other one rather insoluble (e.g. CO_2) with a large k_b contribution. The difference of k between these two gases can then be attributed to the bubble mediated gas transfer. For DMS and CO_2, this has been published only two times by Miller et al. [2009], Bell et al. [2017] and it is discussed in Section 4.
Eddy covariance measurements [Bell et al., 2013, 2015, Yang et al., 2016] have shown a decrease of the k vs u_{10} relationship at medium to high wind speed. This is commonly referred to as 'rollover' (Figure 1.6). At first, it was regarded as a measurement error specifically related to the eddy covariance technique. As a consequence, the first occurrence was not published [Yang et al., 2011], but is now available at Blomquist et al. [2017] (Figure 1.6). So far only hypotheses, including wind-wave interactions [Toba et al., 2006, Bell et al., 2013, 2015], have been presented to explain the rollover.
The establishment of a common gas transfer parameterization has not been successful.

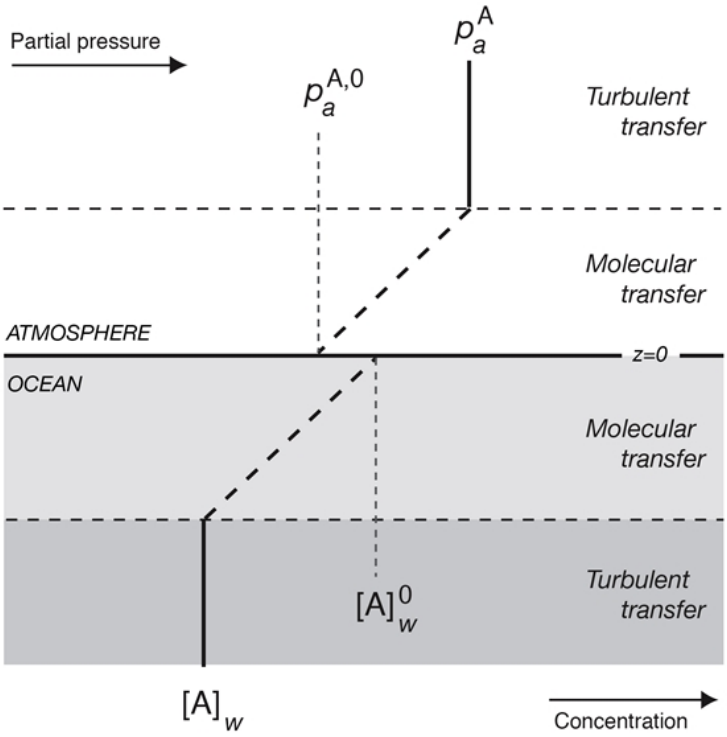

Figure 1.5: The two layer model of gas transfer. From both sides (air and water) the measured quantity has to overcome a layer which is dominated by molecular transport. Gas flux depends on Sc, ΔC and the thickness of this layer.

Even long investigated processes such as bubble mediated gas transfer are still poorly

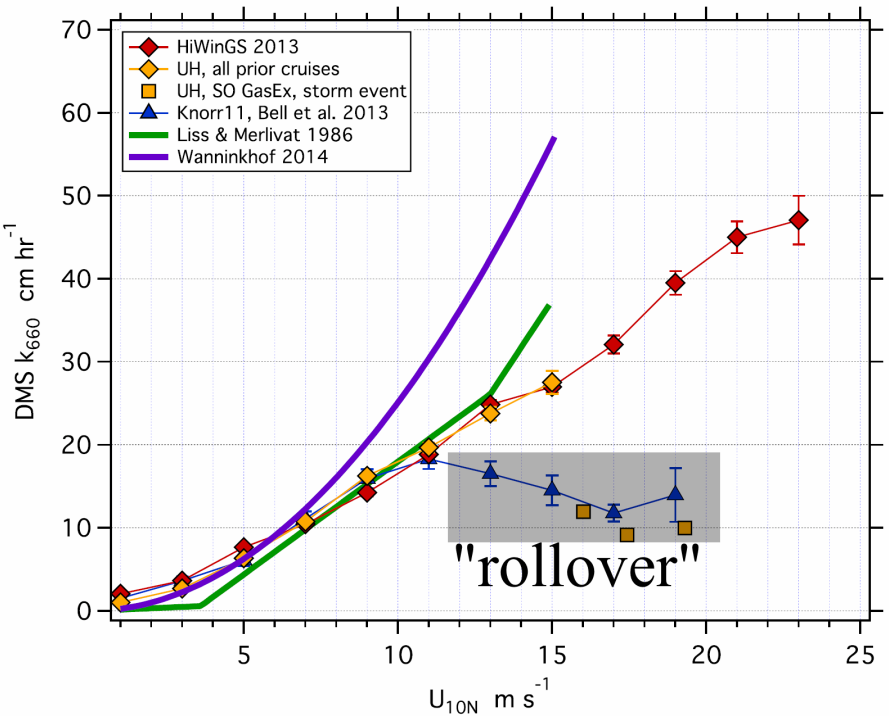

Figure 1.6: Gas transfer velocity measurements with (Knor11, SO GasEx storm event) and without rollover (all other lines). The data points subject to gas transfer limitation are inside the shaded box. Modified from Blomquist et al. [2017].

name	length scale	temporal scale	publication
Dual tracer	kilometers	days	[Wanninkhoff et al., 1985]
^{14}C radiocarbon	global	years	[Wanninkhof, 1992]
Controlled heat flux	meters	seconds	[Jähne et al., 1989]
Eddy covariance	kilometers	minutes	[Jones and Smith, 1977]
Microstructure (water)	centimeters	milliseconds	[Osborn, 1978]

Table 1.1: Flux measurement techniques, their scales and their first publication.

understood and poorly parameterized. New concepts like the surface micro layer get into focus. Wind-wave interactions have been long investigated but only recently gas transfer limitation was measured, which brings this interaction also into focus. The overall variety of processes causes large scatter within a measurement campaign, as well as differences among measurements of different campaigns. It is important to understand why they differ and which parameterization to use under which condition. The variety of parameterizations (Figure 1.4) cause disagreement in the bulk calculation of gas transfer.

1.3 Flux measurements

Using flux measurements one can estimate the actual energy, momentum or mass that is transferred between the ocean and the atmosphere. This data can be used in budget calculations, modeling or regional impact studies. Nonetheless, measured flux data has to be handled with care as different techniques act on different scales. Various processes more or less, depending on the scale, influence the measurement and therefore alter the conclusion. A change in the measurement technique might obscure one influence but disclose other interactions. Every measurement also provides information about the exchange process. One can describe influences which promote or prevent air-sea exchange. Generalizing these processes and influences lead to a basic description and parameterization of air sea exchange which can be provided to others for their calculations. I use the eddy covariance direct flux method which measures the turbulent wind, heat, water vapor or concentration fluctuations. Other methods such as dual tracer, ^{14}C radiocarbon and controlled heat flux (Table 1.1) measure the flux using concentration and budget calculations. Depending on the question asked, an investigator has to choose between time and length scales and as a consequence between measurement techniques (Table 1.1). This is challenging but enables researchers to focus on small scale as well as large scale processes. The horizontal scale can range from the circumference of the Earth to the wavelength of microbreaking waves. On the vertical scale, researchers deal with the MBL height on the order of 1 km, as well as the thickness of the SML, which is in the order of 1 µm [Wurl et al., 2017]. The temporal scale spans from paleo-oceanography times (millions of years ago) over the averaging period of eddy covariance measurements (15 min) to the turbulent motion scale (milliseconds).

1.3.1 Eddy Covariance

Air-flow is almost certainly turbulent in the MBL. Turbulent flux, which is caused by turbulent swirls called eddies, is under this condition much larger than molecular diffusion and therefore of primary interest. If the turbulent field and as a result the turbulent flux can be precisely recorded at a certain height above the sea surface the flux through this horizontal level can be calculated. Eddy covariance is able to measure the turbulent flux of momentum, mass or energy, by high temporal resolution measurements of turbulence. The flux through this horizontal level in the atmosphere, approx. 10-20 m above sea level, is the same as the air-sea flux through the water surface. Horizontal advection below this level is neglected.
Turbulent flux measurements capture the correlation between the fluctuation of vertical wind speed w' and the fluctuation of the respective transported property x'. The fluctuations can be calculated using the measured value x and the average $\overline{x}$ using Equation 1.8.

$$x' = x - \overline{x} \tag{1.8}$$

For momentum transfer the transport property is the fluctuation of the two dimensional wind velocities u' and v', for energy (sensible heat or latent heat) flux it is the air

temperature T or the absolute humidity e and for mass it is the concentration or mixing ratio c.
Equations 1.9-1.12 describe the turbulent flux of these properties.

$$F_{momentum} = \rho \cdot \sqrt{(\overline{u'w'}^2 + \overline{v'w'}^2)} \tag{1.9}$$

$$F_{sensible} = \rho \cdot c_p \cdot \overline{w'T'} \tag{1.10}$$

$$F_{latent} = \rho \cdot c_l \cdot \overline{w'e'} \tag{1.11}$$

$$F_{mass} = \rho \cdot \overline{w'c'} \tag{1.12}$$

Measurements of these turbulent fluxes have to satisfy the following conditions: [1] $\rho' = 0$, no turbulent density fluctuations. [2] $\overline{w} = 0$, no mean vertical flow of air and vertical advection; vertical flux only consists of turbulent flux. [3] Neutral stability of the boundary layer. At unstable conditions $\overline{w} \neq 0$ and at stable conditions turbulence is suppressed. [4] Taylor's hypothesis of frozen turbulence is valid. This hypothesis includes the requirement that the eddy velocity is much smaller than the mean wind speed. As a consequence, advection is only done by the mean wind speed and not by turbulent eddies. Over the open ocean these conditions are generally fulfilled. No. 2 and No. 3 are stability dependent and therefore generally influenced by water temperature, air temperature and wind speed. Especially at low wind speed u<3 m s^{-1} stable or unstable conditions can lead to inconclusive results. At low to high wind speed u>3 m s^{-1} the stability is usually neutral.

The sample rate of the eddy covariance measurement has to capture all relevant turbulent scales in the atmosphere. Figure 1.7 shows the power spectrum of the horizontal wind speed from the turbulent scales to variations of the large wind (mesoscale), storm (synoptic scale) and circulation systems (global scale). The spectral gap from 0.5-5 cycles h^{-1} separates the large scale variations (lower frequencies) from the turbulent scales (higher frequencies). This enables eddy covariance measurements to measure within a rather confined range, which spans from 0.02 s (50 Hz) to the averaging time of eddy covariance of 30 min (0.0005 Hz). Figure 1.8 shows the power spectrum of the turbulent scales. Kaimal et al. [1972] described undistorted turbulence over a wheat field in Kansas. As the shape and power spectrum of turbulence is ubiquitous, their measurements in Kansas are the main reference when comparing undisturbed turbulence spectra and their frequency distribution from all over the world.
Nowadays, the turbulent wind measurements can be made at sampling frequencies of up tp 50 Hz, which is sufficient to capture the total turbulence spectrum. However, the actual sampling rate is confined by the measurement frequency of temperature, humidity or the gas concentration. Improvements in the concentration measurement of gases will strongly improve the eddy covariance technique.

1.4 Local Budgets

Direct flux measurements are an important tool to investigate the influence of air-sea gas exchange on the local environment and local budgets. Especially, eddy covariance (Table

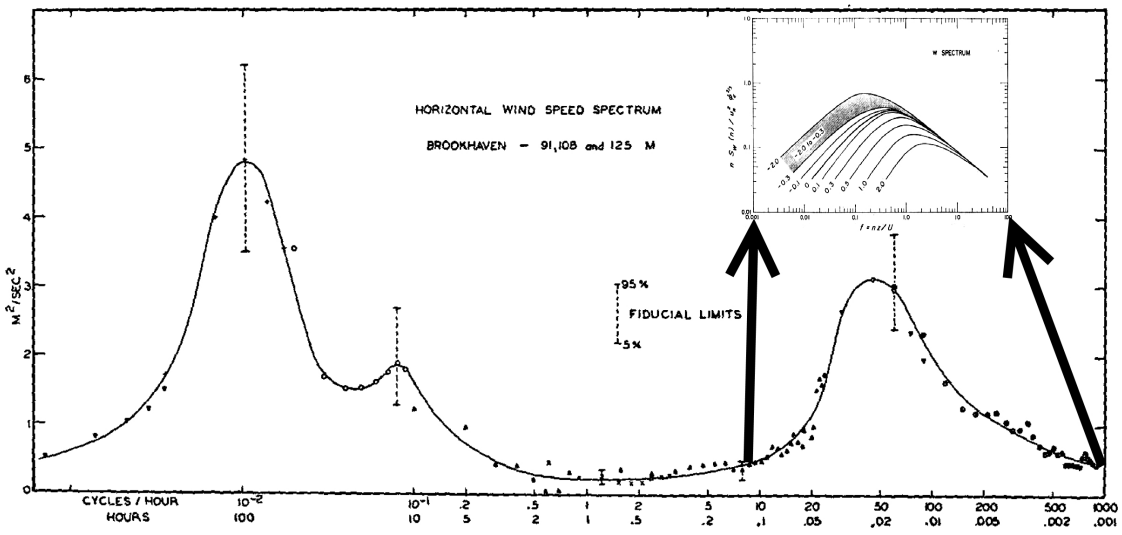

Figure 1.7: Horizontal wind power spectrum, modified from der Hoven [1957]. The x-axis is the frequency, the y-axis the corresponding power. The VanHoven spectrum covers all significant timescales of atmospheric measurements. The turbulent scale, between the two arrows, on the right hand side, was investigated in much more detail by Kaimal et al. [1972] [small top right panel (Figure 1.8)]. The spectral gap is found between 0.5-5 cycles h^{-1}. The two large peaks on the left hand side correspond to the diurnal wind pattern and the large scale wind, storm and circulations systems.

1.1) is suitable as the spatial resolution and temporal resolution are sufficiently small for local correlations and budgets. The spatial resolution is similar to that of most satellites. The temporal resolution is short and advantageous for interdisciplinary studies.
Gases with very short lifetimes in the atmosphere, such as isoprene (lifetime of hours), are ideally investigated with direct flux methods. The oceanic source of isoprene (1 Tg C yr^{-1}) is small compared to the terrestrial source (410-600 Tg C yr^{-1}) [Booge, 2018]. As the lifetime is so short the large terrestrial source has small influence on the atmospheric budget in the MBL. The atmospheric concentration of isoprene in the MBL is two times higher than predicted by models [Booge, 2018], which use the bulk formula to calculate air-sea fluxes. Eddy covariance flux measurement can help understanding finding this missing source. Direct flux measurements could reveal environmental conditions when the flux is much larger than predicted by the bulk formula and therefore correct the local budget. Isoprene is also a predecessor for secondary organic aerosols. These aerosols can directly impact, through light scattering and reflection, the Earth's radiative budget. Through the influence on CCN numbers (Figure 1.9) isoprene also influences cloud formation and, as a secondary effect, the Earth's radiative budget. DMS (lifetime of days) is a major sulfur source to the MBL and also an aerosol predecessor (Figure 1.9). In 1987 **C**harlson, **L**ovelock, **A**ndreae and **W**arren (CLAW) [Charlson et al., 1987] proposed a feedback loop depending on the emission of DMS from the ocean to the atmosphere. The emission positively correlates to aerosol numbers and cloud formation, which, through

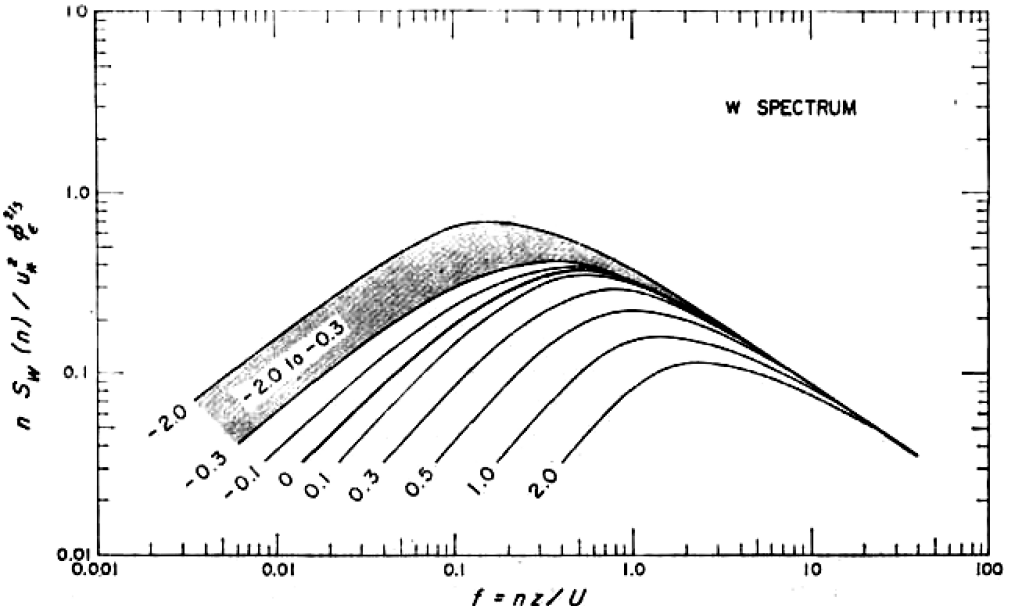

Figure 1.8: The power spectrum from Kaimal et al. [1972] shows the frequency distribution of the vertical wind fluctuations w' in the turbulent range. The x-axis is the normalized frequency, the y-axis the corresponding frequency weighted power.

the change in the radiative budget, influence the surface temperature and therefore productivity and DMS production. The feedback loop is closed. Ever since, it has been debated if the feedback-loop, or evidences of, it can be found. Recent studies [Quinn and Bates, 2011, Quinn et al., 2017] claim that no regional connections between DMS emission and aerosol number exist. Aerosol precursor substances, such as DMS or isoprene, are transported out of the MBL into the free troposphere and then re-entrained into the MBL. The re-entraining rate instead of the gas emission rate would then influence the aerosol number. There might be no final answer to the existence of the feedback loop. Quinn et al. [2017] claims that for all regions besides the Southern Ocean the oxidation product of DMS, $SO_4{}^{-2}$, is the largest contributor to cloud condensation nuclei in the marine boundary layer. According to Quinn et al. [2017], the exact transformation path is still unclear.
So far, the physical air-sea interaction processes have been the main focus of direct flux measurements. But their potential is also based in connecting local sources to products and sinks. Especially for short lived gases such as isoprene, eddy covariance measurements could really close a knowledge gap.

1.5 Global Budgets

Global budget calculations of atmospheric trace gases depend on the exchange between the atmosphere and the ocean which covers 71% of the earth's surface.

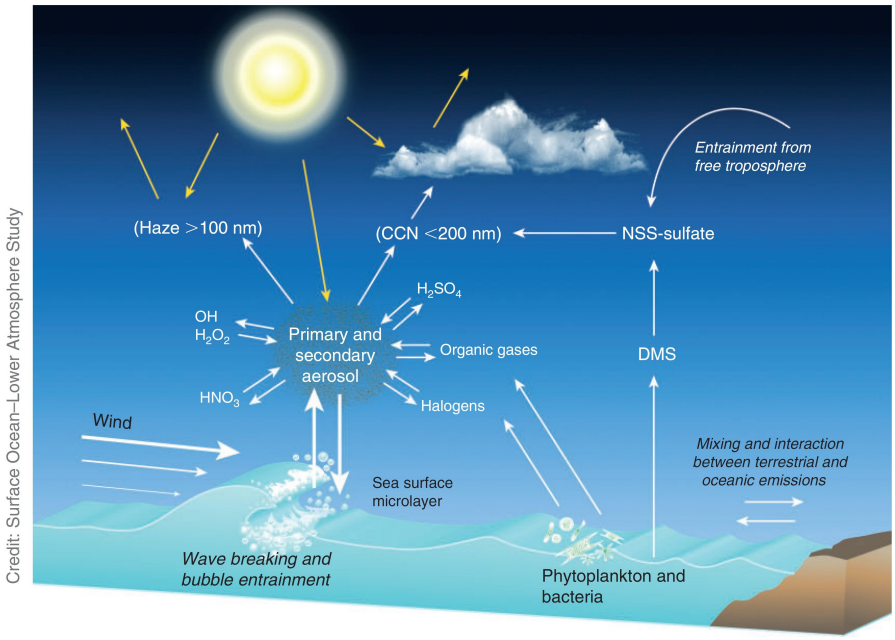

Figure 1.9: Aerosol formation in the marine boundary layer without anthropogenic influence [Brévière and the SOLAS Scientific Steering Committee, 2016].

For carbon, through the uptake of atmospheric CO_2 and river runoff, the ocean acts as a sink. (Figure 1.3). About 30% of anthropogenic CO_2 emissions are taken up by the ocean via air-sea gas transfer (Figure 1.10). Le Quéré et al. [2015] estimates a carbon uptake by the ocean of 2.9±0.5 Gt C for the year 2014, Takahashi et al. [2009] estimates 1.6±0.9 Pg C for the year 2000. In the ocean the carbon uptake causes increasing acidification with all its consequences on the chemistry, flora and fauna of the ocean. However, the estimation of the ocean CO_2 sink is based, to a certain extent, on k parameterizations for the gas exchange (Figure 1.4). This is especially important for short term changes. These k parameterizations are not universally accepted and the air-sea flux depends on their choice. Amongst emissions from land-use-change and the terrestrial CO_2 sink, CO_2 gas exchange has the largest uncertainties in the carbon budget (Figure 1.10). A significant improvement of understanding air-sea gas exchange triggers a reassessment of budgets calculations, as well as new constraints on the other highly uncertain carbon fluxes.
DMS is the largest sulfur source to the marine environment. Although DMS only accounts for 2% of the global tropospheric sulfur [Sheng et al., 2015], it is important for the atmospheric chemistry in the MBL and a major aerosol predecessor [Quinn et al., 2017]. Lennartz et al. [2015] estimates a yearly flux from the ocean to the atmosphere of 45 Tg DMS, Lana et al. [2011] 54.5 Tg DMS. The emission is strongly dependent on the chosen air-sea parameterization 33.38-48.7 Tg DMS yr^{-1}[Lennartz et al., 2015]. A change in k parameterization or the implementation of a new gas limitation transfer process

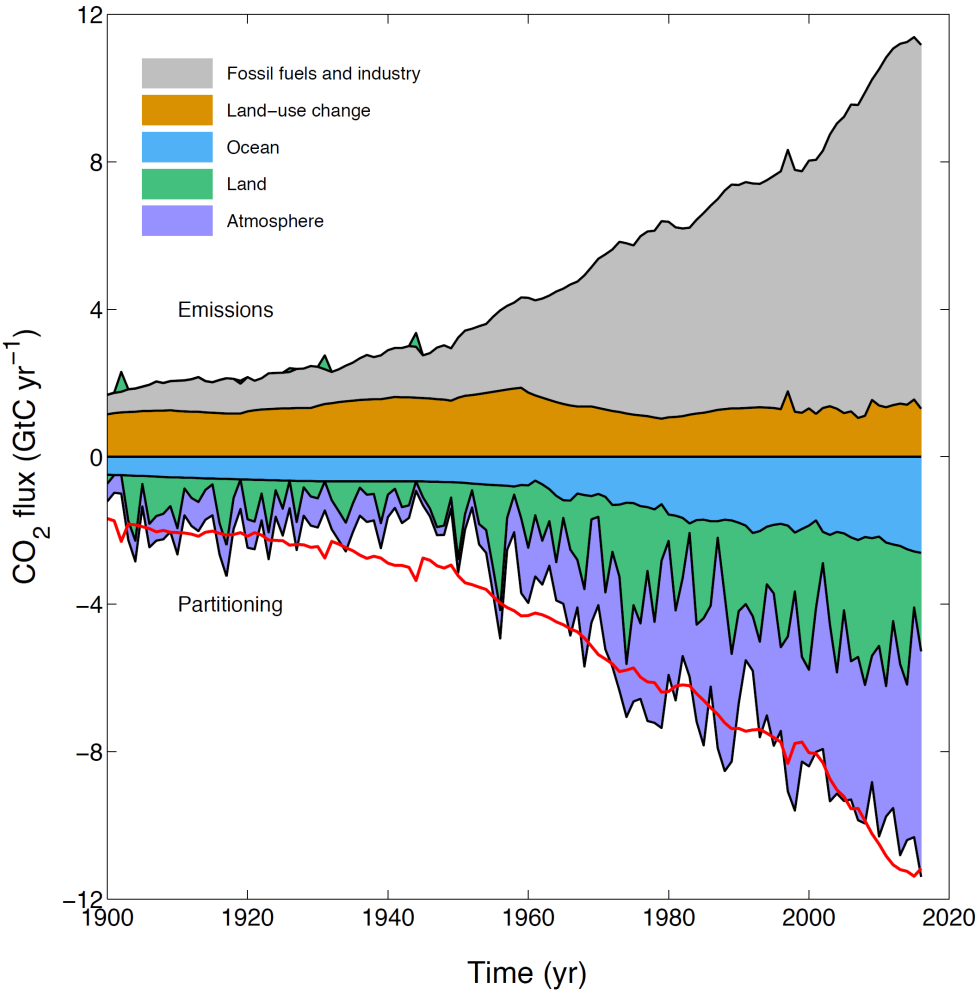

Figure 1.10: Global carbon sources and sinks until 2017 [Le Quéré et al., 2017]. The carbon sources are fossil fuel and industry (uncertainty 5%) and land use change (uncertainty 54%). The oceanic uptake (30% uncertainty) and the land carbon sink (50% uncertainty) share the largest uncertainties in relation to the atmospheric concentration (3% uncertainty)[Le Quéré et al., 2017]. The difference between the red line and the sum of ocean, land and atmosphere, reflects the imbalance in the budget of sources and sinks.

would influence the global sulfur budget calculations and the models for the chemical properties on the MBL.

1.6 Research questions

This thesis aims to look beyond the simple publication of emission numbers from DMS and CO_2 eddy covariance measurements. The measurements are more useful in connection with other in-situ measured parameters or remote sensing products.

Eddy covariance provides the opportunity to get an emission estimate on a spatial and temporal scale such that remote sensing products and trajectory analysis can be used to follow the emission and its evolution.
Can local emissions be correlated with local satellite aerosol numbers?

Eddy covariance data can provide understanding of mesoscale wind-wave interactions. These wind-wave interactions limit gas transfer and have only been detected by eddy covariance measurements.
Can gas transfer limitation be explained at medium to high wind speed? Can a parameterization using the wave and wind field describe the environments at which these gas transfer limitations occur?

A correction model of the gas transfer limitation is tested using previously published eddy covariance measurements. Using a global wave model and the correction algorithm, the consequence of gas transfer limitation on the global air-sea exchange of DMS and CO_2 is investigated.
How often does gas transfer limitation occur globally? Does it influence the global flux of DMS or CO_2? Are previously published gas transfer parameterizations influenced by gas transfer limitation?

References

T. G. Bell, W. De Bruyn, S. D. Miller, B. Ward, K. H. Christensen, and E. S. Saltzman. Air-sea dimethylsulfide (dms) gas transfer in the north atlantic: evidence for limited interfacial gas exchange at high wind speed. *Atmos. Chem. Phys.*, 13(21):11073–11087, nov 2013. ISSN 1680-7324. doi: 10.5194/acp-13-11073-2013. URL http://www.atmos-chem-phys.net/13/11073/2013/.

T. G. Bell, W. De Bruyn, C. A. Marandino, S. D. Miller, C. S. Law, M. J. Smith, and E. S. Saltzman. Dimethylsulfide gas transfer coefficients from algal blooms in the southern ocean. *Atmos. Chem. Phys.*, 15(4):1783–1794, feb 2015. ISSN 1680-7324. doi: 10.5194/acp-15-1783-2015. URL http://www.atmos-chem-phys.net/15/1783/2015/.

T. G. Bell, S. Landwehr, S. D. Miller, W. J. de Bruyn, A. H. Callaghan, B. Scanlon, B. Ward, M. Yang, and E. S. Saltzman. Estimation of bubble-mediated air–sea gas exchange from concurrent dms and co2 transfer velocities at intermediate–high wind speeds. *Atmospheric Chemistry and Physics*, 17(14):9019–9033, 2017. doi: 10.5194/acp-17-9019-2017. URL https://www.atmos-chem-phys.net/17/9019/2017/.

B. W. Blomquist, S. E. Brumer, C. W. Fairall, B. J. Huebert, C. J. Zappa, I. M. Brooks, M. Yang, L. Bariteau, J. Prytherch, J. E. Hare, H. Czerski, A. Matei, and R. W. Pascal. Wind speed and sea state dependencies of air-sea gas transfer: Results from the high wind speed gas exchange study (hiwings). *Journal of Geophysical Research: Oceans*, pages n/a–n/a, oct 2017. ISSN 2169-9291. doi: 10.1002/2017JC013181. URL http://dx.doi.org/10.1002/2017JC013181.

Dennis Booge. *MARINE ISOPRENE - FORMATION, EMISSIONS AND THEIR IMPACT ON THE ATMOSPHERIC CHEMISTRY*. PhD thesis, CAU Kiel - GEOMAR Helmholtz Centre for Ocean Research, 2018.

Sophia E. Brumer, Christopher J. Zappa, Ian M. Brooks, Hitoshi Tamura, Scott M. Brown, Byron W. Blomquist, Christopher W. Fairall, and Alejandro Cifuentes-Lorenzen. Whitecap coverage dependence on wind and wave statistics as observed during so gasex and hiwings. *Journal of Physical Oceanography*, 47(9):2211–2235, 2017. doi: 10.1175/JPO-D-17-0005.1. URL https://doi.org/10.1175/JPO-D-17-0005.1.

E. Brévière and the SOLAS Scientific Steering Committee, editors. *SOLAS 2015-2025: Science Plan and Organisation*. SOLAS International Project Office, GEOMAR Helmholtz Centre for Ocean Research Kiel, 2016.

Robert J. Charlson, James E. Lovelock, Meinrat O. Andreae, and Stephen G. Warren. Oceanic phytoplankton, atmospheric sulphur, cloud albedo and climate. *Nature*, 326 (6114):655–661, apr 1987. doi: 10.1038/326655a0. URL http://dx.doi.org/10.1038/326655a0.

Isaac Van der Hoven. Power spectrum of horizontal wind speed in the frequency range from 0.0007 to 900 cycles per hour. *Journal of Meteorology*, 14(2):160–164, 1957. doi: 10.1175/1520-0469(1957)014<0160:PSOHWS>2.0.CO;2. URL https://doi.org/10.1175/1520-0469(1957)014<0160:PSOHWS>2.0.CO;2.

Anja Engel, Hermann W. Bange, Michael Cunliffe, Susannah M. Burrows, Gernot Friedrichs, Luisa Galgani, Hartmut Herrmann, Norbert Hertkorn, Martin Johnson, Peter S. Liss, Patricia K. Quinn, Markus Schartau, Alexander Soloviev, Christian Stolle, Robert C. Upstill-Goddard, Manuela van Pinxteren, and Birthe Zäncker. The ocean's vital skin: Toward an integrated understanding of the sea surface microlayer. *Frontiers in Marine Science*, 4, may 2017. doi: 10.3389/fmars.2017.00165.

L Esters, S Landwehr, G Sutherland, T G Bell, E S Saltzman, K H Christensen, S D Miller, and B Ward. The relationship between ocean surface turbulence and air-sea gas transfer velocity: An in-situ evaluation. *IOP Conference Series: Earth and Environmental Science*, 35(1):012005, 2016. URL http://stacks.iop.org/1755-1315/35/i=1/a=012005.

Wanda Gülzow, Gregor Rehder, Bernd Schneider, Jens Schneider v. Deimling, and Bernd Sadkowiak. A new method for continuous measurement of methane and carbon dioxide in surface waters using off-axis integrated cavity output spectroscopy (icos): An example from the baltic sea. *Limnology and Oceanography: Methods*, 9(5):176–184, 2011. ISSN 1541-5856. doi: 10.4319/lom.2011.9.176. URL http://dx.doi.org/10.4319/lom.2011.9.176.

B. Jähne, P. Libner, R. Fischer, T. Billen, and E. J. Plate. Investigating the transfer processes across the free aqueous viscous boundary layer by the controlled flux method. *Tellus B: Chemical and Physical Meteorology*, 41(2):177–195, 1989. doi: 10.3402/tellusb.v41i2.15068. URL https://doi.org/10.3402/tellusb.v41i2.15068.

E. P. Jones and S. D. Smith. A first measurement of sea-air co2 flux by eddy correlation. *Journal of Geophysical Research*, 82(37):5990–5992, 1977. ISSN 2156-2202. doi: 10.1029/JC082i037p05990. URL http://dx.doi.org/10.1029/JC082i037p05990.

J. C. Kaimal, J. C. Wyngaard, Y. Izumi, and O. R. Coté. Spectral characteristics of surface-layer turbulence. *Quarterly Journal of the Royal Meteorological Society*, 98 (417):563–589, 1972. ISSN 1477-870X. doi: 10.1002/qj.49709841707. URL http://dx.doi.org/10.1002/qj.49709841707.

Satoru Komori, Wade McGillis, and Ryoichi Kurose. *Gas Transfer at Water Surfaces, 2010*. Kyoto University, 2011. URL http://hdl.handle.net/2433/156156.

A. Lana, T. G. Bell, R. Simo, S. M. Vallina, J. Ballabrera-Poy, A. J. Kettle, J. Dachs, L. Bopp, E. S. Saltzman, J. Stefels, J. E. Johnson, and P. S. Liss. An updated climatology of surface dimethlysulfide concentrations and emission fluxes in the global ocean. *Global Biogeochemical Cycles*, 25(1):n/a–n/a, jan 2011. ISSN 1944-9224. doi: 10.1029/2010GB003850. URL http://dx.doi.org/10.1029/2010GB003850.

S. Landwehr, S. D. Miller, M. J. Smith, T. G. Bell, E. S. Saltzman, and B. Ward. Using eddy covariance to measure the dependence of air-sea co_2 exchange rate on friction velocity. *Atmospheric Chemistry and Physics Discussions*, 2017:1–46, 2017. doi: 10.5194/acp-2017-861. URL https://www.atmos-chem-phys-discuss.net/acp-2017-861/.

C. Le Quéré, R. Moriarty, R. M. Andrew, J. G. Canadell, S. Sitch, J. I. Korsbakken, P. Friedlingstein, G. P. Peters, R. J. Andres, T. A. Boden, R. A. Houghton, J. I. House, R. F. Keeling, P. Tans, A. Arneth, D. C. E. Bakker, L. Barbero, L. Bopp, J. Chang, F. Chevallier, L. P. Chini, P. Ciais, M. Fader, R. A. Feely, T. Gkritzalis, I. Harris, J. Hauck, T. Ilyina, A. K. Jain, E. Kato, V. Kitidis, K. Klein Goldewijk, C. Koven, P. Landschützer, S. K. Lauvset, N. Lefèvre, A. Lenton, I. D. Lima, N. Metzl, F. Millero, D. R. Munro, A. Murata, J. E. M. S. Nabel, S. Nakaoka, Y. Nojiri, K. O'Brien, A. Olsen, T. Ono, F. F. Pérez, B. Pfeil, D. Pierrot, B. Poulter, G. Rehder, C. Rödenbeck, S. Saito, U. Schuster, J. Schwinger, R. Séférian, T. Steinhoff, B. D. Stocker, A. J. Sutton, T. Takahashi, B. Tilbrook, I. T. van der Laan-Luijkx, G. R. van der Werf, S. van Heuven, D. Vandemark, N. Viovy, A. Wiltshire, S. Zaehle, and N. Zeng. Global carbon budget 2015. *Earth System Science Data*, 7(2):349–396, 2015. doi: 10.5194/essd-7-349-2015. URL https://www.earth-syst-sci-data.net/7/349/2015/.

C. Le Quéré, R. M. Andrew, P. Friedlingstein, S. Sitch, J. Pongratz, A. C. Manning, J. I. Korsbakken, G. P. Peters, J. G. Canadell, R. B. Jackson, T. A. Boden, P. P. Tans, O. D. Andrews, V. K. Arora, D. C. E. Bakker, L. Barbero, M. Becker, R. A. Betts, L. Bopp, F. Chevallier, L. P. Chini, P. Ciais, C. E. Cosca, J. Cross, K. Currie, T. Gasser, I. Harris, J. Hauck, V. Haverd, R. A. Houghton, C. W. Hunt, G. Hurtt, T. Ilyina, A. K. Jain, E. Kato, M. Kautz, R. F. Keeling, K. Klein Goldewijk, A. Körtzinger, P. Landschützer, N. Lefèvre, A. Lenton, S. Lienert, I. Lima, D. Lombardozzi, N. Metzl, F. Millero, P. M. S. Monteiro, D. R. Munro, J. E. M. S. Nabel, S.-I. Nakaoka, Y. Nojiri, X. A. Padín, A. Peregon, B. Pfeil, D. Pierrot, B. Poulter, G. Rehder, J. Reimer, C. Rödenbeck, J. Schwinger, R. Séférian, I. Skjelvan, B. D. Stocker, H. Tian, B. Tilbrook, I. T. van der Laan-Luijkx, G. R. van der Werf, S. van Heuven, N. Viovy, N. Vuichard, A. P. Walker, A. J. Watson, A. J. Wiltshire, S. Zaehle, and D. Zhu. Global carbon budget 2017. *Earth System Science Data Discussions*, 2017:1–79, 2017. doi: 10.5194/essd-2017-123. URL https://www.earth-syst-sci-data-discuss.net/essd-2017-123/.

S. T. Lennartz, G. Krysztofiak, C. A. Marandino, B.-M. Sinnhuber, S. Tegtmeier, F. Ziska, R. Hossaini, K. Krüger, S. A. Montzka, E. Atlas, D. E. Oram, T. Keber, H. Bönisch, and B. Quack. Modelling marine emissions and atmospheric distributions of halocarbons and dimethyl sulfide: the influence of prescribed water concentration vs. prescribed emissions. *Atmospheric Chemistry and Physics*, 15(20):11753–11772, 2015. doi: 10.5194/acp-15-11753-2015. URL https://www.atmos-chem-phys.net/15/11753/2015/.

P. S. Liss and P. G. Slater. Flux of gases across the air-sea interface. *Nature*, 247:181, January 1974. URL http://dx.doi.org/10.1038/247181a0.

Liliane Merlivat and Laurent Memery. Gas exchange across an air-water interface: Experimental results and modeling of bubble contribution to transfer. *Journal of Geophysical Research: Oceans*, 88(C1):707–724, 1983. ISSN 2156-2202. doi: 10.1029/JC088iC01p00707. URL http://dx.doi.org/10.1029/JC088iC01p00707.

Scott Miller, Christa Marandino, Warren de Bruyn, and Eric S. Saltzman. Air-sea gas exchange of co2 and dms in the north atlantic by eddy covariance. *Geophysical Research Letters*, 36(15):n/a–n/a, aug 2009. ISSN 1944-8007. doi: 10.1029/2009GL038907. URL http://dx.doi.org/10.1029/2009GL038907.

NOAA National Centres for Environmental Information. Hypsographic curve of earth's surface from etopo1. *Webpage*, 2018. URL https://www.ngdc.noaa.gov/mgg/global/etopo1_surface_histogram.html.

Intergovernmental Panel on Climate Change. *Climate Change 2013 - The Physical Science Basis: Working Group I Contribution to the Fifth Assessment Report of the Intergovernmental Panel on Climate Change*. Cambridge University Press, 2014. ISBN 978-1-107-66182-0. URL https://www.amazon.com/Climate-Change-2013-Contribution-Intergovernmental/dp/110766182X?SubscriptionId=0JYN1NVW651KCA56C102&tag=techkie-20&linkCode=xm2&camp=2025&creative=165953&creativeASIN=110766182X.

T. R. Osborn. Measurements of energy dissipation adjacent to an island. *Journal of Geophysical Research: Oceans*, 83(C6):2939–2957, 1978. ISSN 2156-2202. doi: 10.1029/JC083iC06p02939. URL http://dx.doi.org/10.1029/JC083iC06p02939.

John Prytherch. *MEASUREMENT AND PARAMETERISATION OF THE AIR-SEA CO2 FLUX IN HIGH WINDS*. PhD thesis, UNIVERSITY OF SOUTHAMPTON, FACULTY OF NATURAL AND ENVIRONMENTAL SCIENCES, SCHOOL OF OCEAN & EARTH SCIENCE, 2011.

P. K. Quinn and T. S. Bates. The case against climate regulation via oceanic phytoplankton sulphur emissions. *Nature*, 480(7375):51–56, nov 2011. ISSN 0028-0836. doi: 10.1038/nature10580. URL http://dx.doi.org/10.1038/nature10580.

P. K. Quinn, D. J. Coffman, J. E. Johnson, L. M. Upchurch, and T. S. Bates. Small fraction of marine cloud condensation nuclei made up of sea spray aerosol. *Nature Geosci*, 10(9):674–679, September 2017. ISSN 1752-0894. URL http://dx.doi.org/10.1038/ngeo3003.

Jian-Xiong Sheng, Debra K. Weisenstein, Bei-Ping Luo, Eugene Rozanov, Andrea Stenke, Julien Anet, Heinz Bingemer, and Thomas Peter. Global atmospheric sulfur budget under volcanically quiescent conditions: Aerosol-chemistry-climate model predictions and validation. *Journal of Geophysical Research: Atmospheres*, 120(1):256–276, 2015. ISSN 2169-8996. doi: 10.1002/2014JD021985. URL http://dx.doi.org/10.1002/2014JD021985. 2014JD021985.

Taro Takahashi, Stewart C. Sutherland, Rik Wanninkhof, Colm Sweeney, Richard A. Feely, David W. Chipman, Burke Hales, Gernot Friederich, Francisco Chavez, Christopher Sabine, Andrew Watson, Dorothee C.E. Bakker, Ute Schuster, Nicolas Metzl, Hisayuki Yoshikawa-Inoue, Masao Ishii, Takashi Midorikawa, Yukihiro Nojiri, Arne Körtzinger, Tobias Steinhoff, Mario Hoppema, Jon Olafsson, Thorarinn S. Arnarson, Bronte Tilbrook, Truls Johannessen, Are Olsen, Richard Bellerby, C.S. Wong, Bruno Delille, N.R. Bates, and Hein J.W. de Baar. Climatological mean and decadal change in surface ocean pco2, and net sea–air co2 flux over the global oceans. *Deep Sea Research Part II: Topical Studies in Oceanography*, 56(8):554 – 577, 2009. ISSN 0967-0645. doi: http://dx.doi.org/10.1016/j.dsr2.2008.12.009. URL http://www.sciencedirect.com/science/article/pii/S0967064508004311. Surface Ocean CO2 Variability and Vulnerabilities.

Y. Toba, S. Komori, Y. Suzuki, and D. Zhao. Similarity and dissimilarity in air–sea momentum and CO2 transfers: the nondimensional transfer coefficients in light of the windsea reynolds number. In *Atmosphere-Ocean Interactions*, pages 53–82. WIT Press, feb 2006. doi: 10.2495/978-1-85312-929-2/03. URL https://doi.org/10.2495/978-1-85312-929-2/03.

Daniela Turk, Christopher J. Zappa, Christopher S. Meinen, James R. Christian, David T. Ho, Andrew G. Dickson, and Wade R. McGillis. Rain impacts on co2 exchange in the western equatorial pacific ocean. *Geophysical Research Letters*, 37(23):n/a–n/a, dec 2010. ISSN 1944-8007. doi: 10.1029/2010GL045520. URL http://dx.doi.org/10.1029/2010GL045520.

Rik Wanninkhof. Relationship between wind speed and gas exchange over the ocean. *Journal of Geophysical Research: Oceans*, 97(C5):7373–7382, 1992. ISSN 2156-2202. doi: 10.1029/92JC00188. URL http://dx.doi.org/10.1029/92JC00188.

Rik Wanninkhof, William E Asher, David T Ho, Colm Sweeney, and Wade R McGillis. Advances in quantifying air-sea gas exchange and environmental forcing. *Annual Review of Marine Science*, 1(1):213–244, jan 2009. doi: 10.1146/annurev.marine.010908.163742.

Rik Wanninkhoff, James R. Ledwell, and Wallace S. Broecker. Gas exchange-wind speed relation measured with sulfur hexafluoride on a lake. *Science*, 227(4691):1224–1226, 1985. ISSN 0036-8075. doi: 10.1126/science.227.4691.1224. URL http://science.sciencemag.org/content/227/4691/1224.

David K. Woolf. Bubbles and their role in gas exchange. In Peter S. Liss and Robert A. Duce, editors, *The Sea Surface and Global Change:*, pages 173–206. Cambridge University Press, Cambridge, 003 1997. doi: 10.1017/CBO9780511525025.007. URL https://www.cambridge.org/core/books/the-sea-surface-and-global-change/bubbles-and-their-role-in-gas-exchange/4DC4463FADA1EE5B852CAF45435C3929.

Oliver Wurl, Werner Ekau, William M. Landing, and Christopher J. Zappa. Sea surface microlayer in a changing ocean – a perspective. *Elem Sci Anth*, 5(0):31, jun 2017. doi: 10.1525/elementa.228.

M Yang, BW Blomquist, CW Fairall, SD Archer, and BJ Huebert. Air-sea exchange of dimethylsulfide in the southern ocean: Measurements from so gasex compared to temperate and tropical regions. *Journal of Geophysical Research: Oceans*, 116(C4), aug 2011. ISSN 2156-2202. doi: 10.1029/2010jc006526.

M Yang, T G Bell, B W Blomquist, C W Fairall, I M Brooks, and P D Nightingale. Air-sea transfer of gas phase controlled compounds. *IOP Conference Series: Earth and Environmental Science*, 35(1):012011, 2016. URL `http://stacks.iop.org/1755-1315/35/i=1/a=012011`.

CHAPTER 2

Methods

Eddy covariance measures turbulent gas fluxes in the atmosphere. The challenge of the measurement is, as mentioned in Section 1.3.1, to capture the fluctuations from the mean and to resolve the turbulent fluctuations. The measurement of w' and c' is done by two different systems, whose signals must be synchronized and merged for the flux calculation. Additionally on ships or moving objects, a correction for pseudo winds has to be made [Edson et al., 1998, Miller et al., 2008]. Data for the motion correction is recorded by an inertial measurement unit (IMU).

2.1 Measurement setting

On ships the measurement system consists of two separate parts (Figure 2.1): [1] Air sampling mast. [2] Lab container. The air sampling mast is placed at the front of the ship and holds the instruments for wind and motion (IMU, GPS, compass) measurements as well as the air sampling inlets. The placing on a mast and in the front of the ship ensures minimized influence by flow distortion and sampling of unpolluted marine air. The air is constantly pumped through two 1/2"tubes to a lab container for analysis. The mast is connected via power and data cables to the lab container for power supply and analog/digital communication. Two tubes run from the lab container to the mast that supply the air inlet with the reference gas, which is used as a concentration reference. At the lab container the air samples are analyzed with the respective system (Figure 2.2) and all analog/digital data streams are recorded. The flows in the tubes are controlled by mass flow controllers (MFC).
For DMS a part of the main flow is branched off and pumped to the inlet of the mass spectrometer (MS). Valves are integrated to bypass the air stream drier and to enable blank measurements (zero air).

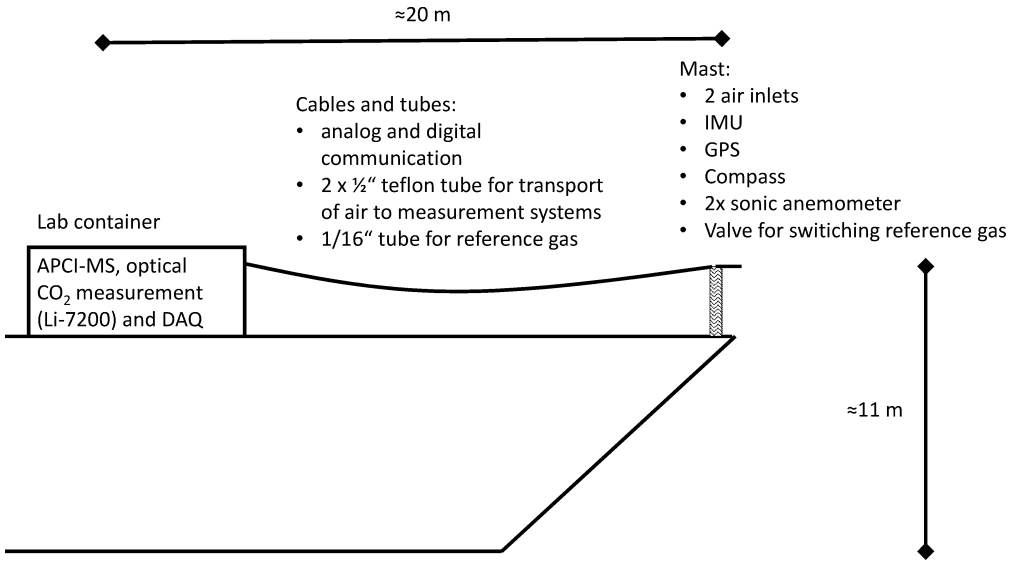

Figure 2.1: Configuration at the bow of the ship. The wind measurements are done with a sonic anemometer directly at the mast. Data acquisition and measurement of the gas concentrations are done in the lab container. These two locations are connected by power lines, electrical cables and tubes for air samples.

2.2 Wind measurement

A sonic anemometer is used to capture the turbulent 3-D wind field. It utilizes the run-time of three (one for every dimension) ultrasonic pulses to measure the wind speed in all dimension. During this work a Campbell CSAT3 was used. A 3D sonic anemometer of any other producer could be used as well [Mauder and Zeeman, 2017].
Special considerations have to be made on the placement of the sonic anemometer on the ship. Flow distortion is a problem as the ship usually represents a major obstacle for the wind [Popinet et al., 2004, OSullivan et al., 2013, 2015]. The sonic anemometer has to be placed free from obstacles such as antennas, masts or cranes distorting the flow. However, the ship itself creates a bow wash of air that can also distort airflow around the front of the ship. This is especially problematic for ships with large superstructures or container stacks, such as container vessels. Improvements have been made with the application of the planar fit method [Wilczak et al., 2001] to eddy covariance on moving platforms by Landwehr et al. [2015]. OSullivan et al. [2013] estimates that a correction of the magnitude of 6% for flow distortion is to be expected.

2.2.1 Motion correction

Wind, measured in the reference frame of a moving platforms, u_{obs} is influenced by the platform motion. For eddy covariance flux calculations the wind in the Earth's reference frame u_{true} is needed. The difference between u_{obs} and u_{true} are pseudo winds generated

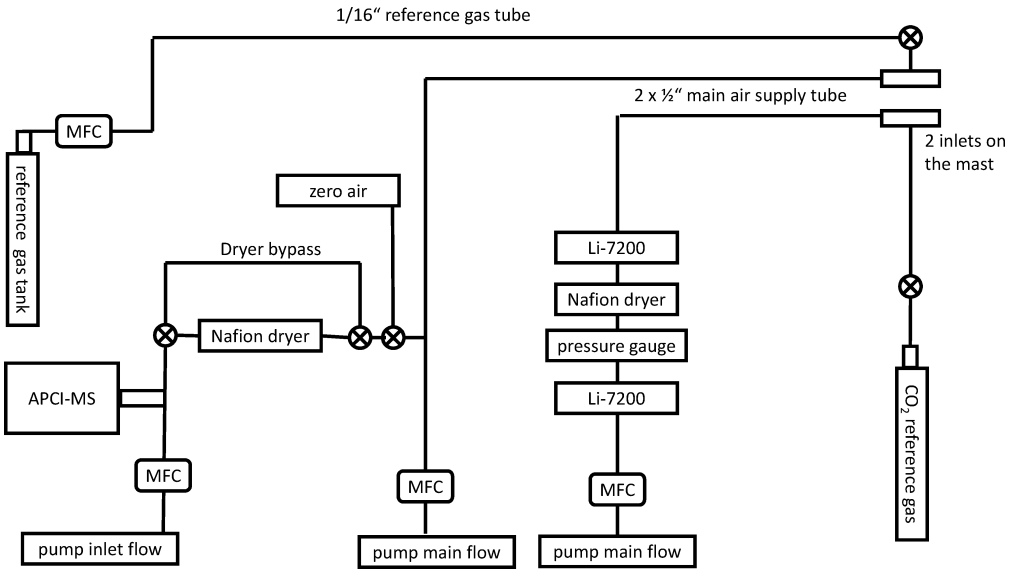

Figure 2.2: Schematic of the DMS and CO_2 measurement systems.

by the platform motion. Using two operations, one rotation and one translation (Equation 2.1 [Edson et al., 1998, Miller et al., 2008]), u_{obs} can be transformed into u_{true} of the Earth's reference system.

$$u_{true} = T\left(u_{obs} + \Omega_{obs} \times R\right) + v_{mot} \tag{2.1}$$

The platform motion, three angular rates and thee linear accelerations, is recorded by an IMU. v_{mot} is the velocity, integrated from the three linear accelerations, of the platform. Ω_{obs} are the angular rates of rotation of the platform. R is the vector from the location of the wind measurement to the location of the IMU. T is the rotation matrix that transforms the tilt of the platform into the horizontal and vertical reference frame of the Earth. The motion correction is applied point by point and produces wind speed in the Earth's reference frame. The power spectrum of a corrected (Earth's reference frame) and uncorrected wind (platform's reference frame) measurement is shown in Figure 2.3. Miller et al. [2010] found an influence of the ship's motion on the sensors of the Licor Li-7200 measurement cell. They linearly regressed the CO_2 signal against all six accelerations measured by the IMU and subtracted this linear function. The same procedure was applied here to this DMS and CO_2 data set.

Inertial measurement unit

An IMU records linear accelerations as well as rotational velocities along all three axes. Using the code based upon Edson et al. [1998], Miller et al. [2008] the rotation matrix T with respect to the Earth reference system (Euler angles), the velocity v_{mot} and Ω_{obs} can be calculated. This is necessary to subtract the pseudo wind from the measured wind. For the eddy covariance calculation, only the wind with respect to the Earth's reference

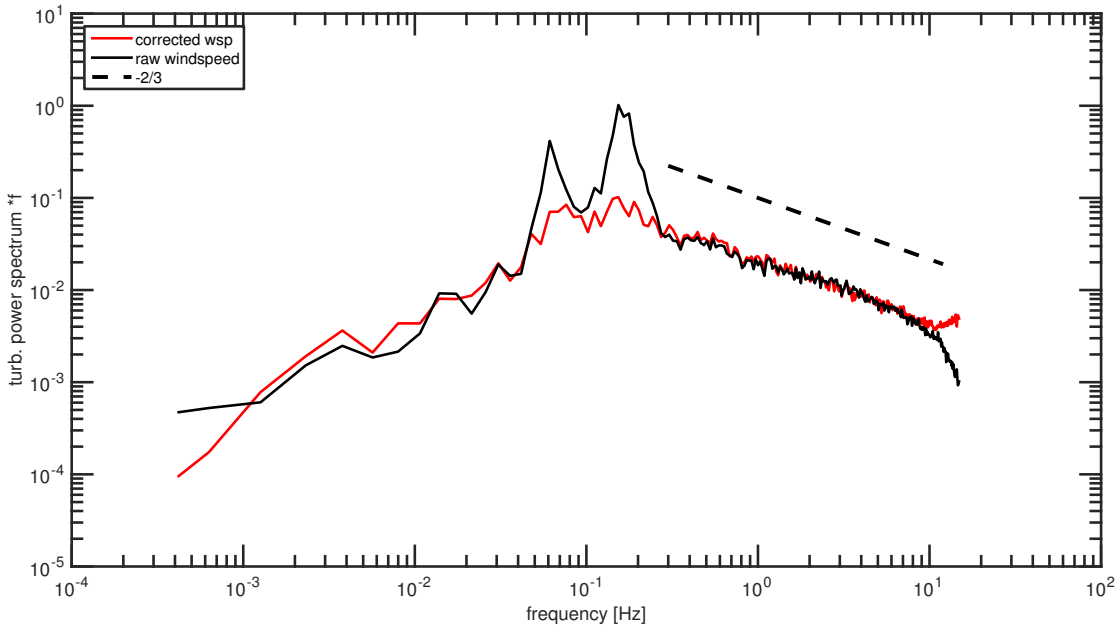

Figure 2.3: Frequency weighted power spectrum of w' the vertical wind fluctuations. The black solid line is an uncorrected power spectrum. The two peaks between 0.09-0.3 Hz represent influences by the motion of the ship. The red line is the corrected vertical wind power spectrum in the reference frame of the Earth. The dashed line shows the energy decay to the power of $-\frac{2}{3}$ in the inertial subrange.

system is considered. With the emerging market of drones, the range of available IMU increased dramatically. Nowadays, digital IMUs with pre-calculated Euler angles are available. Additionally they use an in-built GPS and magnetometer to refine the positions and especially heading. For eddy covariance, it is not necessary to invest in expensive tactical grade IMU, as consumer grade electronics are getting qualitatively better and adequate for this purpose. During this work the analog IMU Landmark10 from Gladiator Instruments was used.

2.3 Mass Spectrometry

An atmospheric pressure chemical ionization mass spectrometer (CIMS) provides a fast measurement rate and the accuracy to capture the fluctuation of trace gases in the atmosphere. The ionization at atmospheric pressure has the advantage that a large amount of the air sample, without dilution or pressure reduction, is ionized at ambient pressure at the inlet and then injected through a pinhole into the lens and low pressure system of the quadrupole MS. The first use of a CIMS for DMS flux measurement was by Bandy et al. [2002].

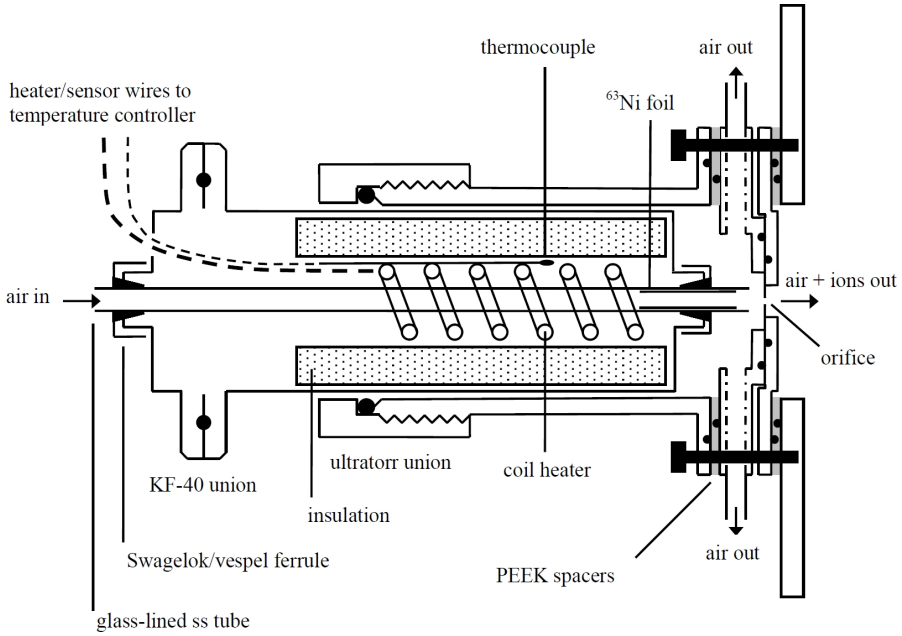

Figure 2.4: Schematic of the inlet from Saltzman et al. [2009]. An identical inlet was used during this work.

2.3.1 Ionization and Inlet

A mass spectrometer can only analyze molecules which are ionized and therefore separable using magnetic fields. The ionization is done in the inlet by electrons, from a radioactive source, stripping the electrons from the analyte molecules. The electron source is a radioactive ^{63}Ni foil (β^- decay) with the activity of 550 MBq and an electron energy of 66 keV. These electrons collide with the sampled air and ionize the nitrogen and oxygen. Equations 2.2-2.4 show the reaction scheme. Ionized oxygen then passes the positive charge (H^+) to water molecules (Equations 2.4-2.6).

$$e^- + N_2 \longrightarrow {N_2}^+ \xrightarrow[N_2]{O_2} {N_4}^+ \xrightarrow{O_2} {O_2}^+ \tag{2.2}$$

$$e^- + O_2 \longrightarrow {O_2}^+ \xrightarrow{O_2} {O_4}^+ \tag{2.3}$$

$${O_2}^+, {O_n}^+ + H_2O \longrightarrow {O_2}^+(H_2O) \tag{2.4}$$

$${O_2}^+(H_2O) + H_2O \longrightarrow {O_2}^+(H_2O_2)_2 \longrightarrow H_3O^+(OH) + O_2 \tag{2.5}$$

$$H_3O^+(OH) + H_2O \longrightarrow H_3O^+(H_2O) + OH \tag{2.6}$$

The hydronium ion-water cluster $H_3O^+(H_2O)$ can accumulate more water molecules (Equation 2.7).

$$H_3O^+(H_2O) + (H_2O)_n \longleftrightarrow H_3O^+(H_2O)_{n+1} \tag{2.7}$$

The final charge carrier are the water clusters with the hydronium ion. The total process of charge transfer from Equation 2.2 to Equation 2.7 happens in less then 1 ms.

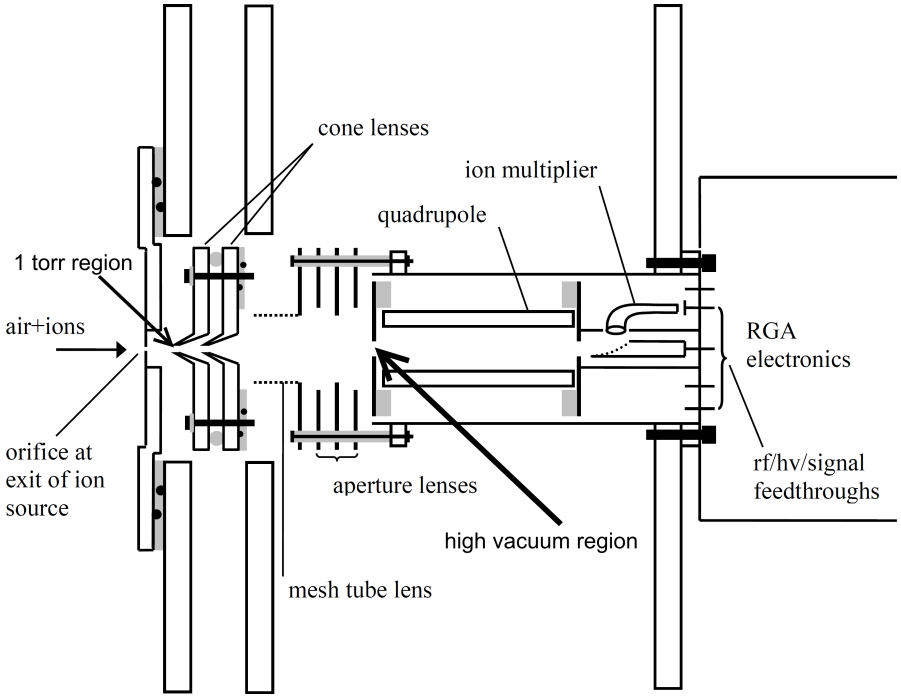

Figure 2.5: Schematic of the CIMS modified from Saltzman et al. [2009]. The inlet is attached to the left side and provides the air+ions flow. The cone lenses (1-torr region) are used to control the residence time and the water cluster size. The 1-torr region is connected via a pinhole cone lens with the high vacuum region. The high vacuum region contains the aperture lenses, for focusing. The ions are separated by the ratio of mass and charge $\frac{m}{q}$ with the quadrupole MS.

The water clusters $H_3O^+(H_2O)_n$ and their proton affinity have significant impact on the ionization capabilities. Only molecules with a larger proton affinity than water or water clusters can attract the charge and be ionized. Large water clusters have a higher proton affinity than smaller ones. The size of the water cluster is dependent on temperature, pressure, the amount of water vapor present and residence time in the clustering region. These parameters can be adjusted and significantly influence the sensitivity. If multiple molecules compete for the charge the one with the highest proton affinity will be excessively ionized. This is important when analyzing atmospheric samples which contain multiple trace gases. Ammonia NH_3 is an example for a trace gas that is preferentially ionized due to its proton affinity and significantly decreases the sensitivity for other trace gases.
The inlet (Figure 2.4) contains the electron source, which is responsible for the ionization, a heater and a orifice, which is the connection to the low pressure regions (Figure 2.5). The orifice has a diameter of 300 μm. Once the molecules are ionized, they are electrostatically steered into the 1 torr region containing the cone lenses. The pressure in the 1 torr region is 1-6 torr (1.33-7.98 mbar). Using these cone lenses the residence time

can be varied and as a consequence the size of the water clusters. The 1 torr region is connected to the high vacuum region via a pinhole-cone lens. The high vacuum region contains the aperture lenses, the quadrupoles and the electron multiplier. The pressure in the high vacuum region is 10^{-4}-10^{-5} mbar. The electron multiplier, operated in burst mode, amplifies the ion signal. The electric current is then converted by an amplification discriminator into a frequency which can be digitized by any I/O board and recorded. According to Sunner et al. [1988a,b], an inlet temperature of 480^{o}C yields the highest sensitivity for DMS. The high temperature reduces the number of larger water clusters, which have a higher proton affinity than DMS. As a consequence, more charges are available to DMS. As the temperature of maximum sensitivity was on the order of 280-300^{o}C for the other measured substances (acetone and isoprene), the temperature of the inlet was set to 400^{o}C. The optimum inlet flow (Figure 2.2) was empirical determined at each start-up and dependent on the pressure in the 1 torr region. A typical inlet flow is 2 L min^{-1}. The flow to the inlet was dried using a Nafion membrane, to reduce water vapor fluctuation and the overall humidity.

2.3.2 Calibration

The reaction scheme (Equations 2.2-2.6) heavily depends on the availability of water molecules. This also implies that the ionization yield is dependent on humidity. In lab conditions humidity may be controllable but measuring atmospheric samples needs a constant reference and calibration of the signal. In the field the air stream is dried using a Nafion membrane. This reduces excessive water vapor, which would favor large water clusters, and water vapor fluctuation, which would add a signal of latent heat flux to the DMS flux. To provide a long term calibration, a known mixing ratio of isotopically labeled reference gas is added. For DMS this is trideuterated DMS $D_3C-S-CH_3$ 3dDMS, which is stored at a known mixing ratio X_{iso} in an aluminum cylinder tank. The deuterated reference gas is then, at a constant flow F_{iso}, added to the air sample flow F_{total}. The known mixing ratio of 3dDMS together with the measured signal of 3dDMS S_{iso} can be used to constantly calibrate the measured DMS signal S_{DMS} (Equation 2.8).

$$X_{DMS} = \frac{S_{DMS}}{S_{iso}} \cdot \frac{F_{iso}}{F_{total}} \cdot X_{iso} \tag{2.8}$$

Three preparation steps have to be done before taking a reference gas bottle to the field: [1] Maintaining primary permeation tube standards in the lab and weighing regularly; [2] Preparing the secondary standards in pressurized gas tanks; [3] Calibrating the secondary standard with the primary standard.

The primary standard - permeation tube

Permeation tubes, kept at constant temperature and constantly purged with nitrogen N_2, are used as primary standards. These perm tubes cannot be taken to the field, as it is impossible to keep the conditions for a constant permeation rate stable outside of the laboratory. The permeation tubes are weighed usually once a week. The weight loss over

time results in a permeation rate $R_{perm,DMS}$=46.86 ng min^{-1}. The weight loss over time (two years) is shown in Figure 2.6. The linear fit to the weight measurements is used to determine the permeation rate. In Figure 2.6 a second fit, $R_{perm,DMS}$=48.52 ng min^{-1}, is shown which is applied to four month of measurements. A discussion of the difference between these two linear fits is presented in Section 2.6

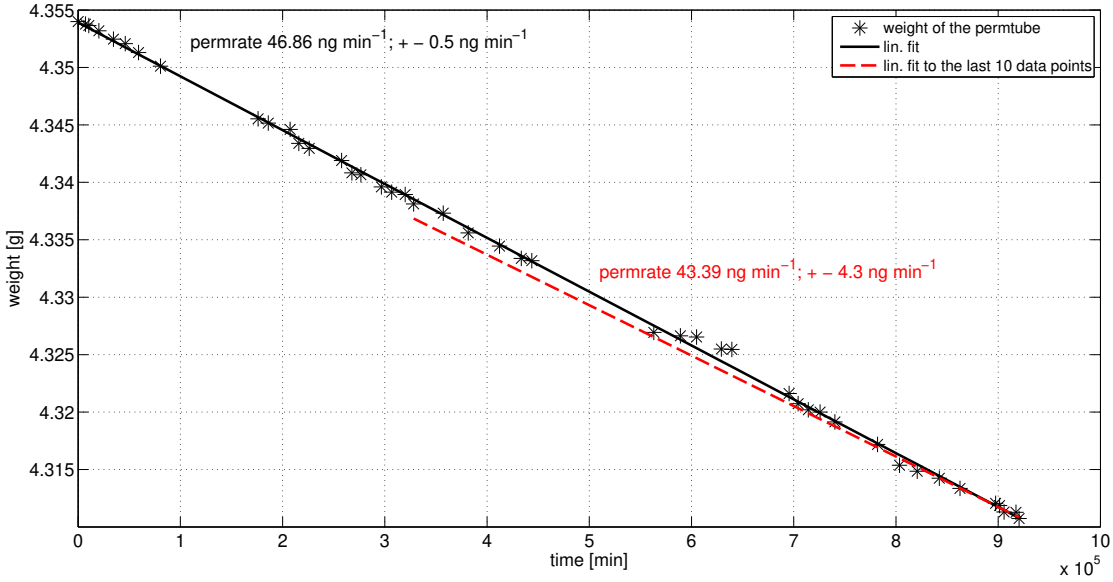

Figure 2.6: Weight measurements of a DMS permeation tube over time. The black solid line and the red dashed line are linear fits to two different time spans.

Bottling the reference gas tank

For bottling a self-designed bottling system was used (Figure 2.7). The reference gas tank is evacuated using the vacuum pump. Additional heating is applied to the reference tank, to remove substances with high vapor pressure. Then the pipes are flushed with N_2. The whole system is then evacuated again and the vacuum pump is shut off from the system. The deuterated substance is drawn into a syringe and then, under constant flow over the low pressure leg, injected through the membrane into the low pressure system. The flow is constantly directed to the reference gas cylinder and the cylinder is filled up to 1 bar. Then the three way valve is switched and the reference gas cylinder is filled up to the projected pressure via the high pressure leg. A typical calculation includes: Injection of 0.05 mL 3dDMS at 60 bar leads to a 20 ppm mixing ratio in the gas cylinder. With a F_{total} of 70 L min^{-1} and a F_{iso} of 2 mL min^{-1} the resulting mixing ratio at the inlet of the CIMS is 500 ppt, which is in the order of the DMS concentration in the atmosphere. The actual mixing ratio inside the bottle is then determined in the next step, when the reference gas tank is measured together with the primary standard.
This gas tank filling system was copied by the Plymouth Marine Laboratory and is also in use there.

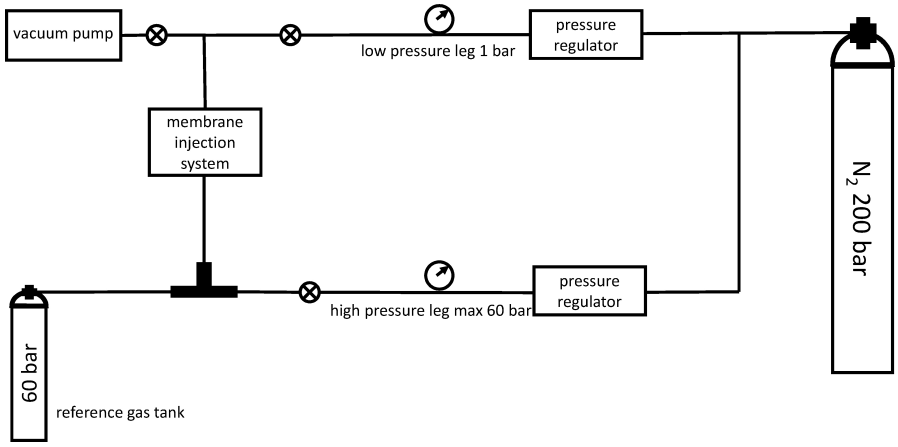

Figure 2.7: Schematic of the self-designed bottling system.

Calibration of the secondary standard - reference gas tank

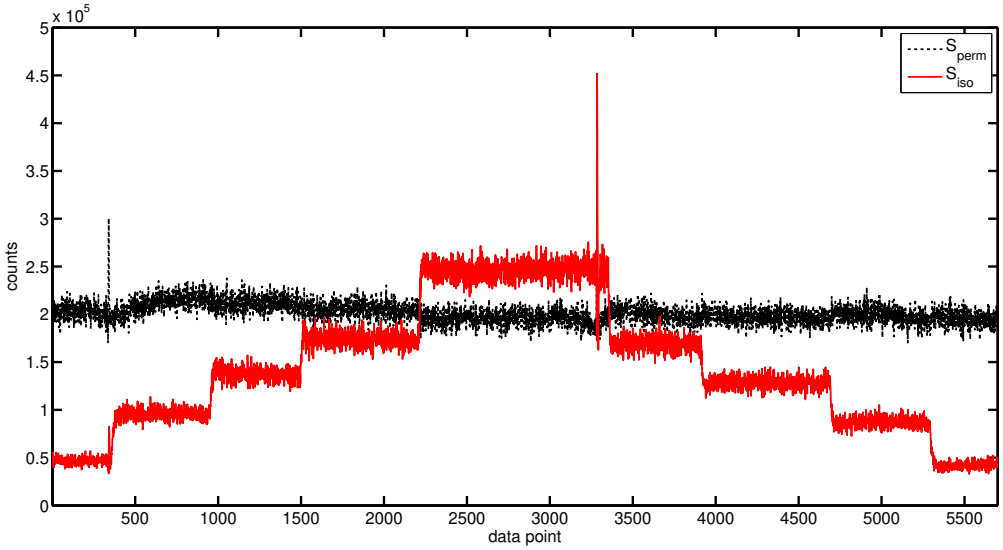

Figure 2.8: Calibration run with the signal from the cylinder gas tank (red) and the signal from the permeation tube (black). The flow rate of the tank (F_{iso}) is varied during the run.

The permeation tubes are used to calibrate the reference gas tanks containing the isotopically labeled reference gas. During the calibration of the cylinder gas tanks, the flow from the permeation tube F_{perm} is kept constant, the permeation rate R_{perm} is constant and known. The flow from the gas cylinder F_{iso} is increased stepwise (Figure 2.8). To determine X_{iso} the ratio of $\frac{S_{iso}}{S_{perm}}$ is plotted versus F_{iso}. The use of $\frac{S_{iso}}{S_{perm}}$ for the calculation has the advantage that any contamination of the isotopically labels 3dDMS

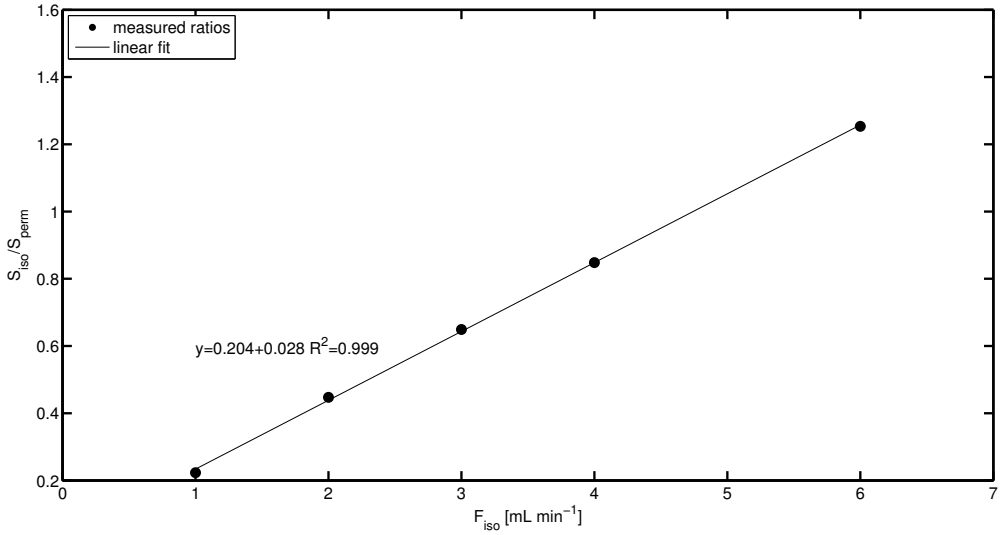

Figure 2.9: The ratio of $\frac{S_{iso}}{S_{perm}}$ plotted vs flow rate F_{iso}. A linear fit is applied to this data set.The function is shown in the figure. The slope is used to calculate X_{iso}.

with normal DMS is automatically accounted for. X_{iso} can be calculated with the slope m of the linear fit (Figure 2.9), the permeation rate (R_{perm}) and the number of moles of N_2 per mL (Equation 2.10).

$$m = \frac{S_{iso}}{S_{perm}} \tag{2.9}$$

$$X_{iso} = \frac{m \cdot R_{perm}}{n} \tag{2.10}$$

The measured, using the permeation tube reference, mixing ratio inside the reference gas tank was 3.49 ppm. This is less than a fifth of the projected 20 ppm. However, this still leads to a mixing ratio at the inlet of the CIMS of 100 ppt, which is in the range of the atmospheric concentration. The calculation made prior to the bottling is a best estimation. Therefore the calibration using the permeation tube is important. It is sufficient if the mixing ratio at the inlet of the CIMS reflects the range of concentrations expected to be encountered in the field. It is also possible to increase F_{iso} to achieve a higher mixing ratio of the deuterated calibration gas at the inlet.
The aluminum reference gas tanks are calibrated, using the perm tubes, before and after the research cruise. Table 2.1 shows the measured mixing ratio of deuterated DMS in the gas tanks before and after the cruise. Additionally, the tanks were measured by Dennis Booge with a gas chromatography (GC) MS. Ideally only one tank is used in the field. The others serve as a backup. Tank 2 was used during this work. The change in mixing ratio between before and after is less than 2%. The largest change occurred in Tank 4 with 31%, Tank 1 shows a change of 2%. A large discrepancy between the measured mixing ratios of the CIMS and the GC MS is evident. The reason might be that it is difficult to measure atmospheric values with the current GC MS system. This system is

Tank No.	CIMS before	CIMS after	GC before	GC after
Tank 1	$4.28{\cdot}10^{-6}$	$4.20{\cdot}10^{-6}$	$5.08{\cdot}10^{-6}$	$6.25{\cdot}10^{-6}$
Tank 2	$3.49{\cdot}10^{-6}$	$3.44{\cdot}10^{-6}$	$2.98{\cdot}10^{-6}$	$6.25{\cdot}10^{-6}$
Tank 3	$2.33{\cdot}10^{-6}$	N/A	$2.18{\cdot}10^{-6}$	N/A
Tank 4	$1.83{\cdot}10^{-6}$	$1.28{\cdot}10^{-6}$	$1.85{\cdot}10^{-6}$	N/A

Table 2.1: Calibration measurements of the deuterated DMS reference gas before and after the research cruise. The values are the mixing ratio of DMS in the respective reference gas tank.

designed to measure water concentrations and is usually tuned to use liquid standards. Additionally the air concentration values are crosschecked with air samples filled into stainless steel canisters during the cruise to be analyzed for more than fifty gases, including DMS, by the lab of Elliot Atlas at the University of Miami.

2.4 Optical gas measurement

CO_2 is measured using the absorption of infrared light by the gas molecules. The air sample enters the measurement cell and absorbs light in proportion to its concentration (Figure 2.10). The difference between the emitted infrared radiation and the radiation at the detector is directly linked to the amount of CO_2 molecules in the cell. During this work, two CO_2 measurement cells Li-7200 from Licor were used.
The challenge in optical CO_2 measurement is that the absorptance spectrum of CO_2 overlaps with that from H_2O. This means that water vapor fluctuation directly leak into the fluctuation measurement of CO_2 and create crosstalk between CO_2 and latent heat flux. To reduce and estimate the influence of latent heat flux on the CO_2 flux, two measurement cells are arranged in series (Figure 2.10, [Miller et al., 2010]). The first measurement cell records the air stream directly from the sampling inlet. Then the stream is dried using a Nafion and measured by the 2nd measurement cell. The CO_2 readings from the 2nd cell should not be influenced by water vapor fluctuations, due to the drier. One can compare the CO_2 and the H_2O readings from both cells. The H_2O readings should differ significantly, which is an indication that the air stream is dried. As a consequence, the 2nd measurement cell should record no proper turbulent spectrum of water vapor fluctuations (Figure 1.8). If this is the case the reading of the 2nd instrument can be used for the CO_2 flux calculation. The Licor instruments also have an inbuilt correction for the influence of water vapor on the CO_2 measurements. To my experience, the internal correction is sufficient, but needs to be verified by this two cell setup.
The pressure gauge in Figure 2.10 is used to correct for possible pressure fluctuation in the two measurement cells. These fluctuation could arise from variable pumping speed, dynamic pressure due to the ships motions or wind-wave interactions. If these pressure fluctuations correlate with w' a pseudo flux signal is recorded. Using a fast sampling pressure gauge (10 Hz) and a correction algorithm provided by Licor the pressure fluctuation were corrected.

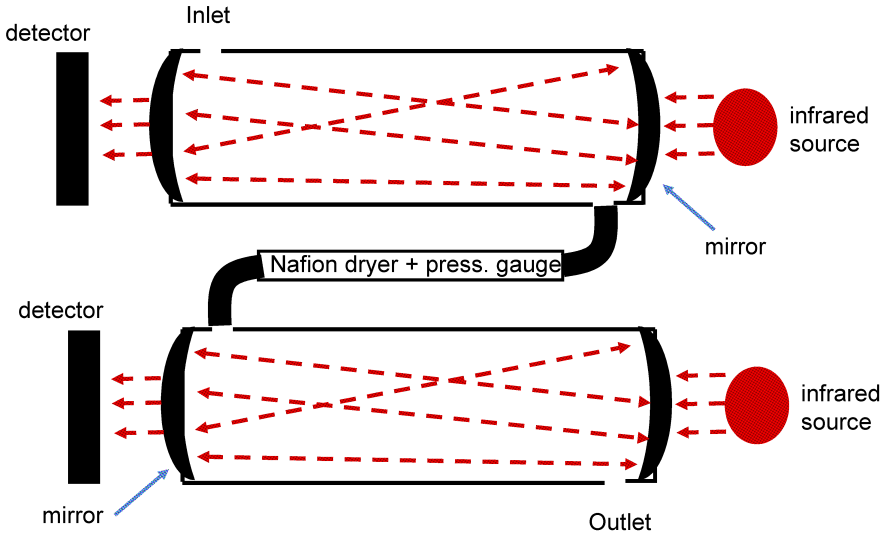

Figure 2.10: Measurement set-up of the two CO_2 measurement cells. The top cell is flushed with air directly form the air inlet at the sampling mast. The bottom cell analyzes the dried air stream.

2.4.1 Calibration

Ideally, three gases with different CO_2 mixing ratios are used for calibration. One of them should be CO_2 free and used for a zero-calibration, the other two should span the projected range of CO_2 mixing ratios. The calibration provides coefficients which are inserted in a polynomial equation provided by Licor. This polynomial calculates the CO_2 mixing ratio at a given temperature, pressure and detector voltage.
While the full calibration can be easily performed in the lab, it is possible to do only a zeroing in the field, if multiple CO_2 gases are not available. Zeroing can also be performed with ambient air and the use of soda lime.

2.5 Time synchronization, tube delay and frequency loss correction

The covariance c'w' of the concentration fluctuation c' and the vertical wind speed fluctuation w' determine the turbulent flux. It is necessary that these two measurements are synchronous. Also the motion measurement, using the IMU, has to be synchronous with the wind measurement to ensure a proper motion correction.
w' is measured directly at the mast and sent via an analog signal to the lab container and the data acquisition (DAQ) system. c' is measured after the air was pumped through the tube into the lab container. This pumping takes a certain time, the tube delay. This delay has to be considered in the correlation.
The pumping to the lab also results in a high frequency loss in the turbulent c' signal. The

tube acts as a low pass filter. This loss is described with a function linearly dependent on wind speed.

2.5.1 Time synchronization

The challenge is to synchronize the data recorded in different formats (analog/digital), with different software and different systems. Usually the internal clock of the DAQ is not precise enough and can shift for several seconds each day. A central time server, distributing a time signal with the network time protocol, is problematic due to the unknown synchronization events and possible time jumps during the measurements.
During this work, following time synchronization protocol was developed:[1] Reset of the clocks on all measurement devices with daily check of time delay between all clocks and GPS-UTC. [2] Distribution of an analog sawtooth signal as correlation signal.

Clock reset and delay check

At the start of the measurement campaign all clocks of all measurement devices are set preferably to UTC. UTC can be taken from a hand-held GPS device. The internal clocks of the measurement devices drift with respect to UTC (Figure 2.11) which is, from now on, not interfered with. Each following day the difference between the hand-held GPS, with its UTC time, and each measurement clock is noted. This can be done by just comparing the time on the hand-held GPS and the clock displayed on the monitor. After one week a good estimation of the clock drift is possible. At the end of the measurement campaign a linear fit is run through the delay data set and it is then possible to calculate the time difference to UTC for every measured point.

Sawtooth time signal

The comparison between the measurement clocks and the hand-held GPS provides a good time synchronization basis. However, with this method no internal memory or buffer delays are monitored. An easy way to capture internal delay processes is to distribute an analog signal (sawtooth) to all devices and to record it simultaneously together with the data from the wind and concentration measurements. The sawtooth signal should undergo the same memory or buffer processes as the other signals. This provides the information for time shift of the other relevant signals. The same sawtooth signals recorded by two measurement devices can be cross-correlated (Figure 2.12). The cross-correlation provides a value for the time shift between the devices. This can be corrected and as a consequence both devices are synchronized.

2.5.2 Tube delay

The first approximation for the tube delay is provided by the flow through the tube which is controlled by the MFC. Using the volume of the tube and the flow rate, the first approximation of the tube delay can be calculated. This is only a rough estimate. Additionally, tube delay tests are performed. Using the reference gas valves at the air

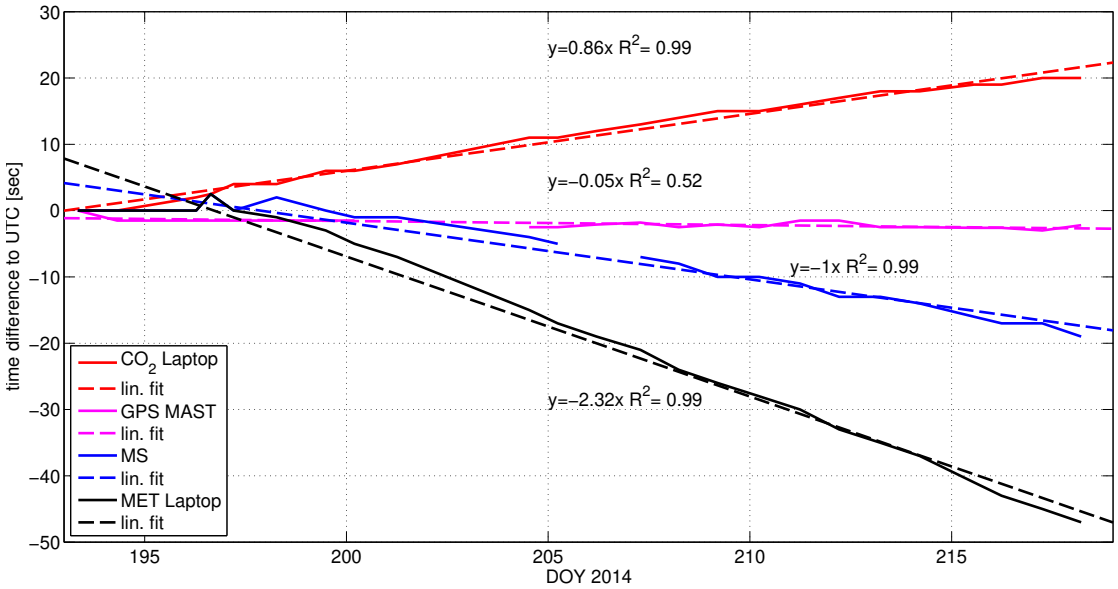

Figure 2.11: Clock drift of the various measurement systems with respect to UTC. A negative value indicates that the clock runs slower than the UTC reference. The dashed lines are linear fits to the clock drift. Using the linear function each clock of the measurement systems can be corrected to UTC.

inlet, the flow of reference gas is switched ON and OFF. The time from the ON/OFF switch until the signal increase/decreases in the measurement system is the tube delay. This is usually performed several times a day. Using this information a look up table of the tube delay over the whole cruise is generated and applied to the data set.
The assumption for eddy covariance is that, during existence of turbulent flux, a positive or negative correlation between c' and w' exists. The final tube delay correction is a cross-correlation of the c' and w' data sets. One data set is shifted by one data point at a time relative to the other data set. At each step the correlation is calculated. If there is a positive upward flux, a maximum should appear next to the zero shift (the zero shift includes all other previously mentioned corrections) (Figure 2.13). For a negative downward flux a minimum is expected. In my experience, a distinct minimum or maximum (Figure 2.13), in between a ± 0.7 s time delay, most of the time represented a good and usable w' power spectrum (Figure 2.3) and w'c' cospectrum (Figure 2.14). This cross-correlation can be also used as a quality check and is the last step of data synchronization.

2.5.3 High frequency correction

The air is pumped at 70 L min^{-1} through the tube. The high pumping speed is done for two reasons: [1] A short residence time in the tube and [2] the support of a turbulent flow regime in the tube. However, due to the confined space and the wall interaction, the tube

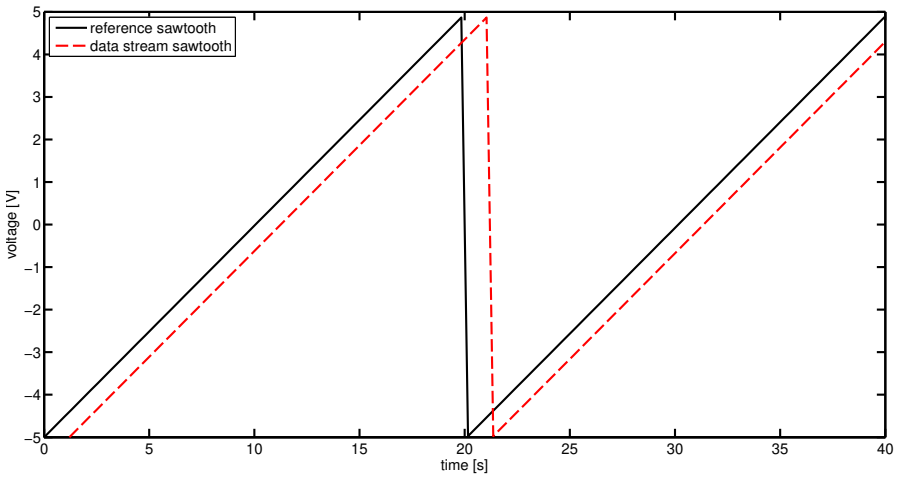

Figure 2.12: The black solid line is the reference sawtooth signal. The red dashed line is the sawtooth as recorded together with a data stream. The shift between these two signals is equal to the time shift of the data stream to the reference time.

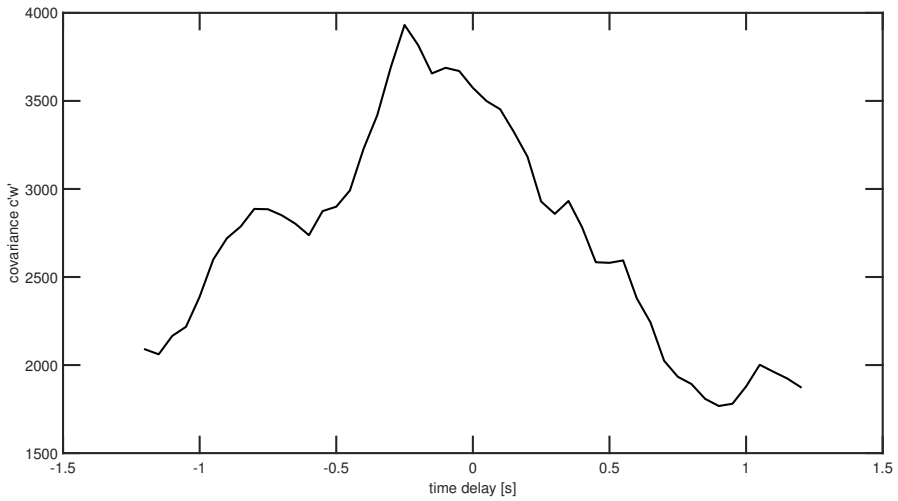

Figure 2.13: The delay offset vs the covariance c'w' between DMS and vertical wind speed. In this example the offset was set to -0.3 seconds. This means that the time lag between wind speed and concentration measurements was -0.3 seconds, after taking the volume/pumping speed calculation and the valve switch into account.

acts as a low pass filter for the atmospheric turbulence until it reaches the measurement system.
Using the ON/OFF switches of the tube delay test, it is possible to correct for the high frequency loss. The delay test generates a square wave signal of the reference gas concentration in the tube, which is also subject to the high frequency loss. The frequency loss can be modeled with a first-order low-pass butterworth filter. A butterworth filter

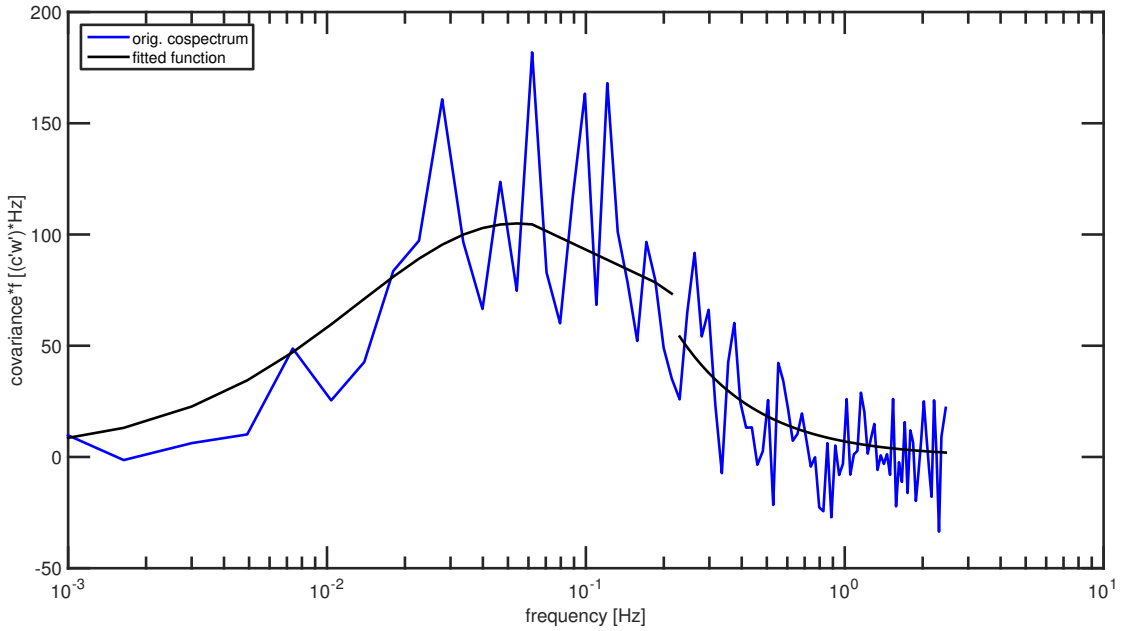

Figure 2.14: Cospectrum of DMS concentration fluctuations c' with motion corrected vertical wind correction w'. The solid black line is an idealized function form from Kaimal et al. [1972] fitted to the measured cospectrum.

applied to a modeled ideal square signal should provide a good approximation to the signal measured from the ON/OFF switches of the tube delay test. The parameters of the butterworth filter, which describe the frequency loss, are adapted such that the modeled signal (low pass butterworth filter applied to a square wave) fits the measured signal from the delay test (Figure 2.15).
This butterworth filter is then inversely applied to the spectrum of c'w'. The area under the spectrum c'w' is equal to the correlation c'w' and therefore the flux. This application increases the area at the high frequency end and corrects for this frequency loss. A linear fit is applied to the flux increase, due to the high frequency correction, vs wind speed. This linear function is then used for the correction of the whole data set. The applied correction functions are shown in Equations 2.11 and 2.12.

$$G_{DMS} = 1.032 + 0.0021 \cdot u_{10} \tag{2.11}$$

$$G_{CO_2} = 1.0128 + 0.0021 \cdot u_{10} \tag{2.12}$$

2.6 Error estimation

An error estimation for eddy covariance is difficult. Data with uncertainties from various measurements are collected and correlated. I will provide an error estimation based

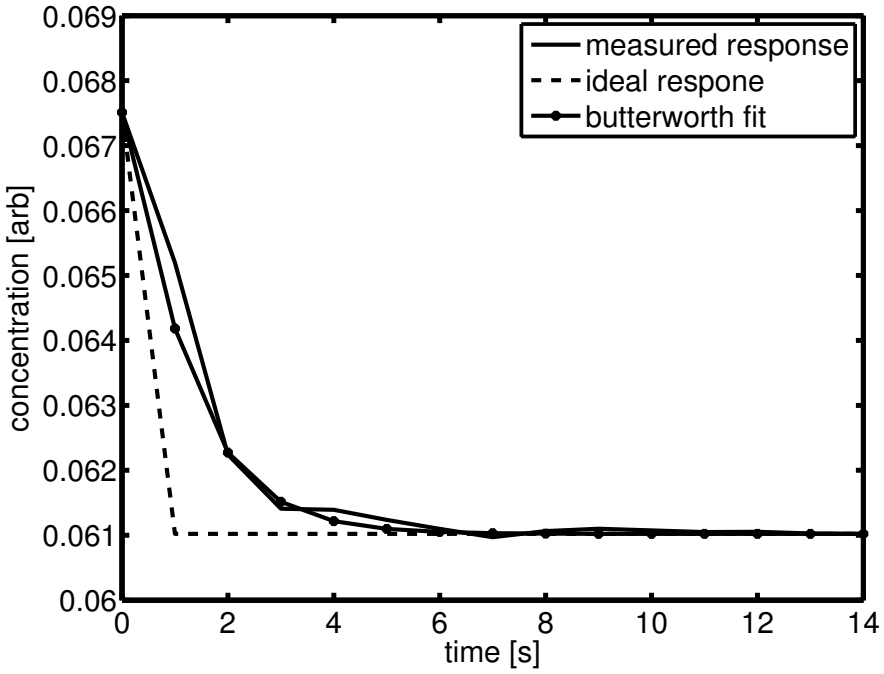

Figure 2.15: The concentration of the isotopically labeled reference gas during a valve switch. The parameters of a low-pass butterworth filter were tuned to fit an ideal valve switch to the measured progression. The high frequency loss in the tube was corrected using the low-pass filter parameters.

upon estimations of the individual measurement systems and compare them to literature values.

CIMS

During the reference gas tank calibration (Figure 2.8), the CIMS is checked for linearity (Figure 2.9) and hysteresis over a range of concentrations. The error of these two properties can be estimated less than 1% based on the calibration data and the R^2 of the linear fit in Figure 2.9. The uncertainty of the measurement of c' is estimated with counting statistics and the sensitivity of the instrument. On average the sensitivity was 1000 $\frac{counts}{ppt_{DMS}} \frac{1}{s}$. The amplitude of fluctuations c' for DMS is on the order of ppt. The relative standard deviation of counting std_c is given by Equation 2.13.

$$std_c = \frac{100}{\sqrt{counts}} \tag{2.13}$$

Given an air concentration of 500 ppt, 39000 counts are recorded during the integration time of 40 ms. The relative standard deviation is therefore std_c=0.5%. According to counting statistics the CIMS uncertainty is less then 1% on the average air mixing ratio. However, this means that the uncertainty is of the same order as the fluctuations,

which would question the ability in measuring these fluctuations. The correlation acts as averaging. The correlation is averaged for the time period of approximately 30 min. As a consequence the stochastic error is minimized.

Permeation tubes

The permeation tubes are used a primary standard. They are enclosed in a temperature stabilized box and constantly purged with nitrogen to ensure a constant permeation rate. To determine the permeation rate the tubes are weighed each week. Figure 2.6 shows two linear fits to these measurements. One fit (black solid line) is applied to the data set over a two years period. This represents the long term stability. The other fit (red dashed line) represents the short term permeation rate (4 months). The relative difference between these two rates is 3.5%. One must include, if using the short term permeation rate, the relative error of 6%. In this thesis the long time permeation rate was used. However, I estimate an error of 10% on the permeation tubes.

Reference tank drift

Table 2.1 shows the reference gas tank calibration before and after the cruise. The tanks are usually bottled and calibrated two months before the start of the research cruise, then used for one month at the research cruise and then shipped back to the lab, which takes again two months. Over the course of five months the mixing ratio of the deuterated reference gas is changing, which is shown in Table 2.1. The largest drift occurred at Tank 4 with 30% the lowest was for Tank 2, which was used, 2%. I estimate the relative error as 5%.

Sonic anemometer

According to the technical notes of Campbell Scientific the readings form the sonic anemometer (CSAT3) have an error of 6%.

Mass flow controller

Typical MFCs have an error of 1% in controlling the flow rate.

Licor CO_2

Licor states an error of 1% on the CO_2 measurement using an Li-7200.

2.6.1 DMS flux and k uncertainty

Just looking at the covariance c'w' the measurement error is due to the long averaging period (aprrox. 30 min) relatively low <1%. The errors of the MFCs, the reference gas tank drift, flow distortion (Section 2.2) and the permeation tubes are fully affecting the result. These are combined 23%. Making a conservative estimate the error for DMS

fluxes could be around 25%. This is a pure back of the envelope estimation, nevertheless also backed up by an estimation of Marandino et al. [2009], which also estimate a flux error of 25%. They also estimate the error of the concentration gradient measurement ΔC to 10%. As the ΔC measurements were performed in a similar way during this work, I also use this value as the error. Combined, an uncertainty for k of 25% is reasonable.

2.6.2 CO_2 flux and k uncertainty

The same considerations, as for DMS, hold for the uncertainty of CO_2. However, CO_2 uses certified primary standards as reference. This would largely decrease the uncertainties in relation to tank drift and the permeation tubes. The uncertainty for the CO_2 measurement is of the same magnitude as for DMS. I estimate the uncertainty for the flux of CO_2 as well as for the calculated gas transfer velocity is 15%.

References

Alan R. Bandy, Donald C. Thornton, Fang H. Tu, Byron W. Blomquist, Wolfgang Nadler, Glenn M. Mitchell, and Donald H. Lenschow. Determination of the vertical flux of dimethyl sulfide by eddy correlation and atmospheric pressure ionization mass spectrometry (apims). *Journal of Geophysical Research: Atmospheres*, 107(D24): ACH 3–1–ACH 3–9, 2002. ISSN 2156-2202. doi: 10.1029/2002JD002472. URL http://dx.doi.org/10.1029/2002JD002472. 4743.

J. B. Edson, A. A. Hinton, K. E. Prada, J. E. Hare, and C. W. Fairall. Direct covariance flux estimates from mobile platforms at sea. *Journal of Atmospheric and Oceanic Technology*, 15(2):547–562, apr 1998. doi: 10.1175/1520-0426(1998)015<0547:dcfefm>2.0.co;2. URL http://journals.ametsoc.org/doi/abs/10.1175/1520-0426%281998%29015%3C0547%3ADCFEFM%3E2.0.CO%3B2.

J. C. Kaimal, J. C. Wyngaard, Y. Izumi, and O. R. Coté. Spectral characteristics of surface-layer turbulence. *Quarterly Journal of the Royal Meteorological Society*, 98 (417):563–589, 1972. ISSN 1477-870X. doi: 10.1002/qj.49709841707. URL http://dx.doi.org/10.1002/qj.49709841707.

Sebastian Landwehr, Niall O'Sullivan, and Brian Ward. Direct flux measurements from mobile platforms at sea: Motion and airflow distortion corrections revisited. *Journal of Atmospheric and Oceanic Technology*, 32(6):1163–1178, jun 2015. doi: 10.1175/jtech-d-14-00137.1. URL http://journals.ametsoc.org/doi/abs/10.1175/JTECH-D-14-00137.1.

C. A. Marandino, W. J. De Bruyn, S. D. Miller, and E. S. Saltzman. Open ocean dms air/sea fluxes over the eastern south pacific ocean. *Atmos. Chem. Phys.*, 9 (2):345–356, jan 2009. ISSN 1680-7324. doi: 10.5194/acp-9-345-2009. URL http://www.atmos-chem-phys.net/9/345/2009/.

M. Mauder and M. J. Zeeman. Field intercomparison of prevailing sonic anemometers. *Atmospheric Measurement Techniques Discussions*, 2017:1–22, 2017. doi: 10.5194/amt-2017-284. URL https://www.atmos-meas-tech-discuss.net/amt-2017-284/.

Scott D. Miller, Tihomir S. Hristov, James B. Edson, and Carl A. Friehe. Platform motion effects on measurements of turbulence and air–sea exchange over the open ocean. *Journal of Atmospheric and Oceanic Technology*, 25(9):1683–1694, sep 2008. doi: 10.1175/2008jtecho547.1. URL http://journals.ametsoc.org/doi/abs/10.1175/2008JTECHO547.1.

Scott D. Miller, Christa Marandino, and Eric S. Saltzman. Ship-based measurement of air-sea co2 exchange by eddy covariance. *Journal of Geophysical Research: Atmospheres*, 115(D2):n/a–n/a, jan 2010. ISSN 2156-2202. doi: 10.1029/2009JD012193. URL http://dx.doi.org/10.1029/2009JD012193.

N. OSullivan, S. Landwehr, and B. Ward. Mapping flow distortion on oceanographic platforms using computational fluid dynamics. *Ocean Science*, 9(5):855–866, 2013. doi: 10.5194/os-9-855-2013. URL https://www.ocean-sci.net/9/855/2013/.

Niall OSullivan, Sebastian Landwehr, and Brian Ward. Air-flow distortion and wave interactions on research vessels: An experimental and numerical comparison. *Methods in Oceanography*, 12(Supplement C):1 – 17, 2015. ISSN 2211-1220. doi: https://doi.org/10.1016/j.mio.2015.03.001. URL http://www.sciencedirect.com/science/article/pii/S2211122015000213.

Stéphane Popinet, Murray Smith, and Craig Stevens. Experimental and numerical study of the turbulence characteristics of airflow around a research vessel. *Journal of Atmospheric and Oceanic Technology*, 21(10):1575–1589, 2004. doi: 10.1175/1520-0426(2004)021<1575:EANSOT>2.0.CO;2. URL https://doi.org/10.1175/1520-0426(2004)021<1575:EANSOT>2.0.CO;2.

E. S. Saltzman, W. J. De Bruyn, M. J. Lawler, C. A. Marandino, and C. A. McCormick. A chemical ionization mass spectrometer for continuous underway shipboard analysis of dimethylsulfide in near-surface seawater. *Ocean Sci.*, 5(4):537–546, nov 2009. ISSN 1812-0792. doi: 10.5194/os-5-537-2009. URL http://www.ocean-sci.net/5/537/2009/.

Jan. Sunner, Michael G. Ikonomou, and Paul. Kebarle. Sensitivity enhancements obtained at high temperatures in atmospheric pressure ionization mass spectrometry. *Analytical Chemistry*, 60(13):1308–1313, 1988a. doi: 10.1021/ac00164a013. URL http://dx.doi.org/10.1021/ac00164a013.

Jan. Sunner, Gordon. Nicol, and Paul. Kebarle. Factors determining relative sensitivity of analytes in positive mode atmospheric pressure ionization mass spectrometry. *Analytical Chemistry*, 60(13):1300–1307, 1988b. doi: 10.1021/ac00164a012. URL http://dx.doi.org/10.1021/ac00164a012.

James M. Wilczak, Steven P. Oncley, and Steven A. Stage. Sonic anemometer tilt correction algorithms. *Boundary-Layer Meteorology*, 99(1):127–150, Apr 2001. ISSN 1573-1472. doi: 10.1023/A:1018966204465. URL https://doi.org/10.1023/A:1018966204465.

CHAPTER 3

The influence of air-sea fluxes on atmospheric aerosols during the summer monsoon over the tropical Indian Ocean

3.1 Abstract

During the summer monsoon, the western tropical Indian Ocean is predicted to be a hotspot for dimethylsulfide emissions, the major marine sulfur source to the atmosphere and an important aerosol precursor. Other aerosol relevant fluxes, such as isoprene and sea spray, should also be enhanced, due to the steady strong winds during the monsoon. Marine air masses dominate the area during the summer monsoon, excluding the influence of continentally derived pollutants. During the SO234-2/235 cruise in the western tropical Indian Ocean from July-August, 2014, directly measured eddy covariance DMS fluxes confirm that the area is a large source of sulfur to the atmosphere (cruise average 9.1 µmol m^{-2} d^{-1}). The directly measured fluxes, as well as computed isoprene and sea spray fluxes, were combined with FLEXPART back- and forward trajectories to track the emissions in space and time. The fluxes show a significant positive correlation with aerosol data from the Terra and Suomi-NPP satellites, indicating a local influence of marine emissions on atmospheric aerosol numbers.

3.2 Introduction

The CLAW hypothesis [Charlson et al., 1987], still heavily debated in the scientific community [Quinn and Bates, 2011], describes a feedback process connecting oceanic

production to cloud formation, which influences Earth's albedo and as a consequence oceanic production. One of the main steps of the CLAW hypothesis is the formation of aerosols and cloud condensation nuclei (CCN) in the marine boundary layer (MBL). The original publication proposed dimethyl sulfide (DMS) to be the key source of CCN and driver of the feedback. DMS is produced by phytoplankton in the ocean and then released into the atmosphere, where it is one of the major sulfur sources [Quinn and Bates, 2011]. In the atmosphere it undergoes oxidation to either sulfur dioxide, sulfuric acid or methane sulfonic acid and subsequently forms CCN. In more recent years other CCN sources, for instance sea spray and other biogenic trace gases such as isoprene, have come into focus. Quinn and Bates [2011] argue that only 40-50% of the MBL-CCN can be attributed to sulfur emissions and, depending on the region, up to 65% can be attributed to sea salt aerosols. For the tropics the sea spray contributions decreases to 30% [Quinn et al., 2017]. The quantitative impact of isoprene is still unclear. Furthermore, Quinn and Bates [2011], Quinn et al. [2017] claim that most of the DMS derived CCN are actually formed in the free troposphere and then entrained into the boundary layer again. This would mean a regional decoupling of the DMS emissions and the formation of clouds, which is in opposition to the CLAW feedback. As pointed out by Vallina et al. [2006], Green and Hatton [2014] most studies lack the temporal and spatial coverage to give a significant answer to the importance of DMS in the CCN forming process in the MBL. In contrast to the arguments of Quinn and Bates [2011], Lana et al. [2012] performed a satellite based correlation-study, connecting DMS and sea spray fluxes (SSPF) with satellite derived CCN number concentrations. They found a rather uniform positive correlation for DMS-CCN (with some areas of weak correlation at the boundaries of the tropics). For sea spray-CCN the correlation depended on latitude: The tropics exhibited a positive correlation, the northern midlatitudes exhibited a negative correlation, the southern mid-latitudes exhibited a mixed correlation. These findings provide a basis for further investigation, but no studies have correlated air-sea fluxes with aerosol numbers on a regional level or multi-day timescales.

According to the Lana climatology [Lana et al., 2011], the western tropical Indian Ocean (WTIO) is a hotspot for DMS flux during the months July and August. The efflux is one of the highest worldwide (63.32 µmol m^{-2} d^{-1}). The WTIO is associated with marine influenced air masses during the boreal summer [Rhoads et al., 1997]. Biological productivity, especially in the upwelling areas of the WTIO (off north east Africa and the north Arabian Sea), is strongly correlated with the monsoon seasonal cycle [Yoder et al., 1993]. This production influences the DMS concentration in the surface water and, together with steady strong winds, enhances gas transfer.

Thus, the WTIO could be an important source of sulfur to the atmosphere and the SO234-2/235 cruise provides the opportunity to study the DMS-aerosol connection. We focus on linking source gases and aerosol numbers in order to evaluate the Lana et al. [2012] correlations. We use an improved approach, as our DMS fluxes were directly measured and coupled to the atmospheric transport model FLEXPART to study atmospheric sulfur transformations on a regional scale above the WTIO.

3.3 Methods

We performed direct eddy covariance DMS flux measurements aboard the RV Sonne sailing from Durban, SA to Port Louis, MU (SO234-2, 8 July - 20 July 2014) and from Port Louis, MU to Malé, MV (SO235, 23 July - 8 August 2014)(Figure 3.1). Additionally, we measured DMS and isoprene surface water and air concentrations. Basic meteorological observations were done by the ship's weather station. For the span of the cruise, back- and forward trajectories were calculated using the FLEXPART model [Stohl et al., 2005] with ERA-interim reanalysis (Figure 3.2). Aerosol satellite data from the Terra and Suomi-NPP satellites were acquired for the area and time covered by the cruise track and the trajectories.

3.3.1 Eddy covariance measurements

The eddy covariance flux F (Equation 3.1) is a product of the dry air density (ρ), the fluctuation of vertical wind speed (w') and the fluctuation of the mixing ratio (c').

$$F = \rho \cdot c'w' \tag{3.1}$$

We recorded DMS air mixing ratios at 5 Hz using an atmospheric pressure chemical ionization mass spectrometer (AP-CIMS) similar to that described by Saltzman et al. [2009]. The air was sampled from a mast at the bow of the ship (11 m a.s.l.) and pumped at 50-70 L min^{-1} (Flow$_{total}$) through a 1/2"diameter and 25 m long polytetrafluoroethylene tube to a laboratory container where the AP-CIMS was placed. The air stream was dried using a Nafion membrane (Perma Pure) prior to analysis. For calibration, we continuously added a deuterated DMS standard (DMS-d3, 2.28 ppm C$_{tank}$) to the inlet at the rate of 2 mL min^{-1} (Flow$_{std}$). Using the ratio of the deuterated DMS counts (Counts$_{66}$) to the natural DMS counts (Counts$_{63}$), the concentration of atmospheric DMS (DMS$_{air}$) was calculated:

$$DMS_{air} = \frac{Flow_{std}}{Flow_{total}} \cdot \frac{Counts_{63}}{Counts_{66}} \cdot C_{tank} \tag{3.2}$$

Two ultrasonic anemometers (CSAT3), mounted next to the air-sample inlet, measured the 3D turbulent wind field. We determined the delay, between the passage of the air parcel at the inlet and the measurement at the AP-CIMS, with a valve switch before each 1 h eddy covariance measurement run. A GPS and an inertial measurement unit (Landmark 10), positioned next to the sonic anemometers provided the data for the motion correction of the 3D wind, which we performed based on Edson et al. [1998], Miller et al. [2008], with an update by Landwehr et al. [2015]. We recorded a total of 130.15 h DMS air measurements. The data set was split into 477 running intervals (10 min step), each 29.6 min long. These intervals fulfilled the flow distortion relative wind direction criterion of $\pm 90^{\circ}$ degrees from the bow and the Landwehr requirement of steady wind direction.

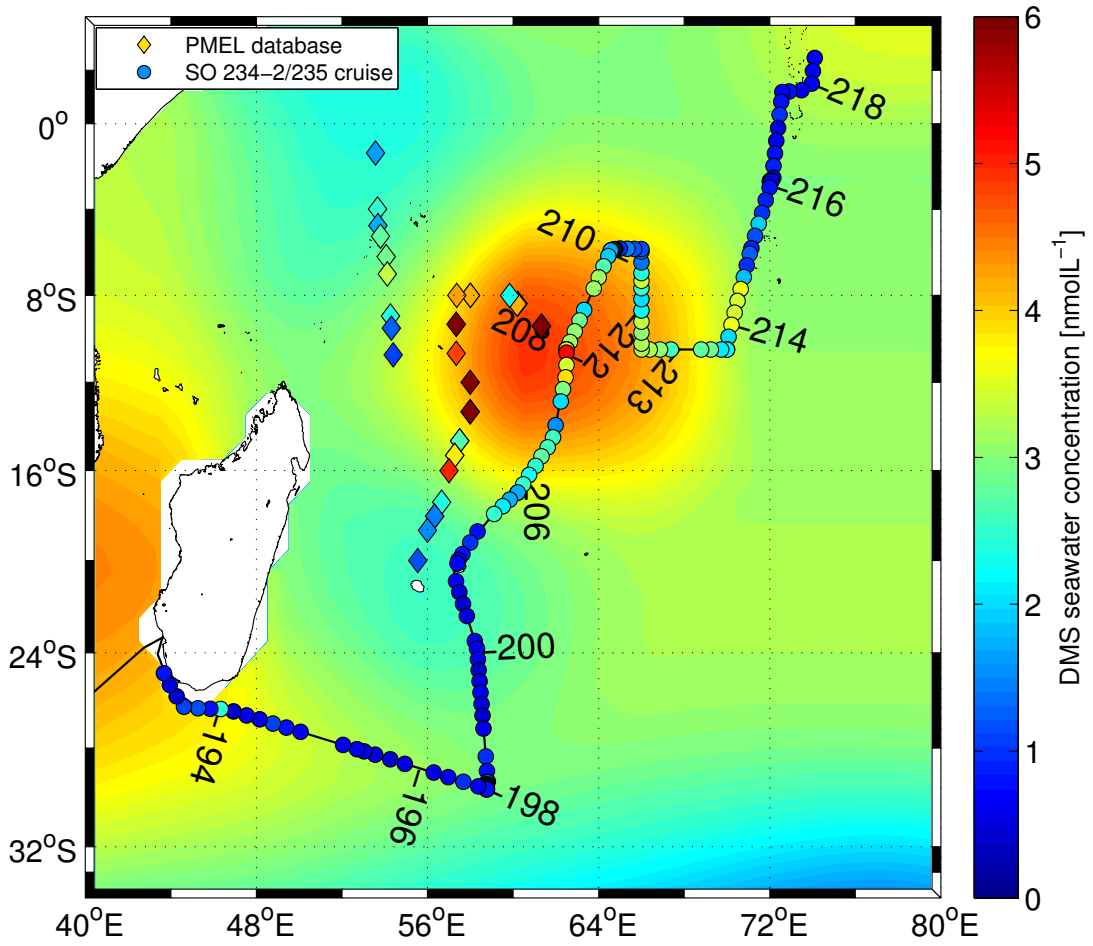

Figure 3.1: Cruise track (black solid line) of SO234-2/235. Circles are discrete sampled surface water DMS concentrations. Diamonds are all recorded DMS values within the PMEL database for July and August. July DMS surface concentrations from the Lana climatology are color coded in the background. The numbers indicate the Day of Year (DOY).

3.3.2 Bulk air and seawater measurements

Seawater DMS and isoprene concentrations were measured using a purge and trap system attached to a gas chromatograph/mass spectrometer (GC/MS; Agilent 7890A/Agilent 5975C). We sampled the water from a constant stream out of the ship's moon pool at 5 m depth and measured within 15 min of collection. The gases were purged from the water sample for 15 min and then dried using potassium carbonate. The dried gas was preconcentrated in a trap cooled with liquid nitrogen and injected into the GC. We obtained a total of 162 DMS and isoprene sea surface concentration values (3 h sampling

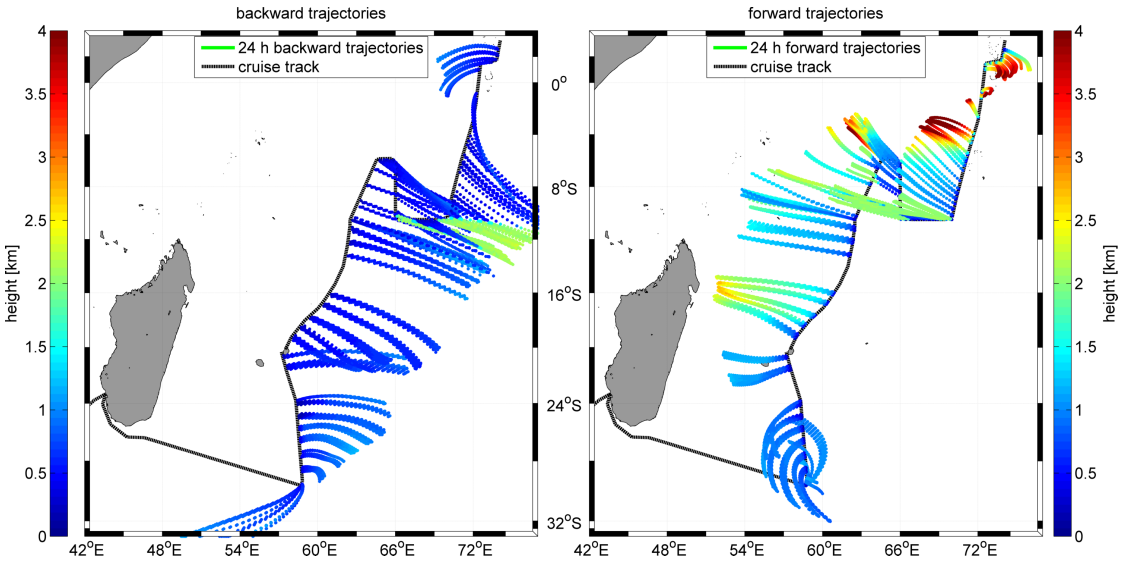

Figure 3.2: [Left] Backward trajectories; [Right] Forward trajectories (24 h) calculated using FLEXPART/ERA-Interim. The color shows the average height of the trajectory. In total 435 back- and forward trajectories are shown. For the correlation calculation forward (downwind) trajectories up to 12 h were used.

interval). At the same time and interval, we filled stainless steel canisters with air samples (25 m sampling height), which were analyzed for more than fifty gases, including DMS and isoprene, at the University of Miami.
We calculated isoprene fluxes using the bulk method (Equation 3.3), where c_a and c_w are the respective air and water concentrations, H is the dimensionless form of Henry's law constant and k the gas transfer velocity by Nightingale et al. [2000]. This parameterization was used, because direct flux CO_2 measurements show a k vs wind speed relationship following Nightingale et al. [2000]. CO_2 and isporene have approximately the same solubility.

$$Flux = k \cdot \left(c_w - \frac{c_a}{H} \right) \tag{3.3}$$

SSPF ($F_{seaspray}$, billion particles ejected per m^2 per day [Gpart m^{-2} d^{-1}]) was parameterized using Equation 3.4, which was proposed by O'Dowd et al. [2008]. The wind speed at 22 m (u_{22}) was calculated using the parameterization by Hsu et al. [1994].

$$F_{seaspray} = 1.854 \cdot 10^{-3} \cdot u_{22}^{2.706} \tag{3.4}$$

3.3.3 Back- and forward trajectories

For the trajectory calculations, we used the Lagrangian Particle Dispersion Model FLEXPART Version 9.2 [Stohl et al., 2005]. The model includes moist convection and turbulence parameterizations in the atmospheric boundary layer and free troposphere

[Stohl and Thomson, 1999, Forster et al., 2007]. We used FLEXPART with the European Centre for Medium-Range Weather Forecasts reanalysis product ERA-Interim [Dee et al., 2011] with a horizontal resolution of 1° x 1° and 60 vertical model levels as meteorological input fields with a 6 hourly temporal resolution. During the cruise we launched radiosondes to improve meteorological reanalysis (e.g. ERA-Interim) for the later use in the transport model [Fiehn et al., 2017]. FLEXPART was run with a synchronization interval of 900 *s* and with a quarter of this time step in the atmospheric boundary layer to resolve turbulent fluxes on short time scales. The model output was recorded hourly. An ensemble of 10,000 forward and 1,000 backward trajectories are started at the positions and times of the 435 direct DMS flux measurements and run for 10 days. From the hourly trajectory positions we calculated the mean trajectory as an average of all ensemble members. Trajectories reaching 12 h backwards and 12 h forwards were used in the correlation calculation 3.2. Longer time spans up to 10 days were used to assess the possible influence of terrestrial pollution (Figure 3.5).

3.3.4 Remote sensing

We obtained total column CCN and aerosol optical depth (AOD) data (Level 3, MODIS-Terra 6 collection [Hubanks et al., 2016]), provided on a global 1° x 1° grid, from the MODIS instrument on board the Terra satellite. Terra has a sun synchronous orbit and an overpass at 10:30 local time. Additionally, total column aerosol optical thickness (AOT) was obtained from the Visible Infrared Imaging Radiometer Suite instrument on board the Suomi-NPP satellite, which has a sun synchronous orbit and an overpass at 13:30 local time. The level-2 aerosol product has a resolution of 0.25° x 0.25°. AOD and AOT both describe the degree to which aerosols prevent the transmission of light by absorption or scattering of light. In total we obtained daily files from 27 June 2014 to 19 Aug 2014 for all products. The output describes the aerosol properties at the time of the overpass. Using two different satellites gives the opportunity to test the data with two independent systems. A cross-check was done between the Aqua, Terra and NPP-Suomi satellites, which shows consistent results (data shown in the supplement).
The satellite data was linearly interpolated to the specific location of each forward- and backward trajectory output. If, due to missing values, the first interpolation was not successful, following steps were carried out successively and stopped if one interpolation returned a valid result: [1] a nearest interpolation (space and time) [2] linear interpolation (space, at closest time step) [3] mean of nearest-neighbors (space, at closest time step). The majority of missing values were caused by clouds. An error estimation of the satellite data is presented in the supplement (Table 3.4, [Levy et al., 2013, Huang et al., 2016, Rosenfeld et al., 2016].

3.3.5 Correlation

To link the oceanic sources to the aerosol numbers, we analyze the trend of the aerosol properties in the downwind (forward trajectories) area. This approach has already been established for volcanoes [Mace and Abernathy, 2016, Eguchi et al., 2011, Yuan et al.,

2011] and focuses on the absolute aerosol number or cloud density. We have extended their method and, instead of a single point source (volcano), we correlate multiple point sources, all measured fluxes from the cruise track, with the satellite aerosol properties in the downwind area. We hypothesize that a higher efflux of aerosol precursor, such as DMS, isoprene, sea spray, should lead to a higher value of satellite sensed aerosol numbers. Therefore a positive correlation between aerosol predecessor and aerosol number should be observed. We calculated FLEXPART/ERA-Interim forward trajectories to pinpoint to pinpoint the downwind location of the directly measured fluxes. We used the locations from the time of the measurements until 12 h into the downwind area to obtain the satellite based aerosol values. We averaged these values for every forward trajectory and then correlated them to the fluxes from the cruise track. The averaging along each trajectory provides a more representative picture of the aerosol numbers in the downwind area.
We used Spearman's rank as correlation method, which describes a monotonically increasing relationship between two independent variables. The bootstrap method was used to prove the level of significance. A correlation coefficient of 0.2 is statistically significant with a probability of 0.995. 435 datapoints were correlated.

3.4 Results and Discussion

The cruise took place during the Asian summer monsoon season, with prevailing southeasterly winds south of the Equator and southwesterly winds north of the Equator. The SO234-2/235 cruise track spanned a range of oceanic areas, traversing the Agulhas current, the Antarctic circumpolar current (an area of high carbon dioxide drawdown), the Indian Ocean Gyre, the South Equatorial Current, the Equatorial Countercurrent, and the North Equatorial Current. Shallow areas (e.g. the Mascarene Plateau) and reef areas (e.g. Maldives) were also traversed. We encountered an average oceanic mixed layer depth of 60 m, sea surface temperatures from 19^{o}C to 25^{o}C, practical salinity from 34 to 36 and generally low nutrient levels (below 0.1 µmol L^{-1} for nitrate and below 0.2 µmol L^{-1} for phosphate). Some areas of enhanced nutrients were encountered between 10^o and 5^{o}S. Chlorophyll levels were between 0.05-0.59 µg L^{-1} with a mean of 0.23 µg L^{-1}. During the first leg (SO234-2), 30 min averaged wind speed below 10 m s^{-1} was measured. North of Mauritius the wind speed increased to a maximum of 16 m s^{-1} and then gradually declined towards the Maldives. Lower wind speed prevailed closer to the Equator, which is in agreement with the monsoon circulation. The average MBL height was 0.8 km, determined by radiosonde soundings applying a threshold of the critical Richardson number of Ric=0.25 [Fiehn et al., 2017]. The relative humidity varied between 50% and 90%, and air temperatures ranged between 14^{o}C and 30^{o}C [Fiehn et al., 2017]. Precipitation was variable over the cruise tracks. Generally, the air masses encountered were unpolluted and originated from over the ocean (Figure 3.2). This is supported by 10-day backward trajectories and profiles from ozone sonde soundings, where averaged cruise values reveal low tropospheric ozone values (22 ppb near the surface, 26 ppb at 1 km, and 51 ppb at 5 km) (Figures 3.5 and 3.6).

3.4.1 Seawater concentrations

Measured DMS surface seawater concentrations ranged from 0.4-5.19 nmol L^{-1} (Figure 3.3). During the first leg (SO234-2), the concentrations stayed below 1.4 nmol L^{-1}, with one exception of 2.4 nmol L^{-1} at the southern tip of Madagascar, where a shallow biological productive area (Banc d'Etoile) was crossed. DMS values started increasing up to the maximum value of 5.19 nmol L^{-1} north of Mauritius in the area between 18°S and 5°S. Further north, the values declined to sub 1 nmol L^{-1} levels. Two main features influenced the DMS values north of Mauritius: [1] The Mascarene Plateau (between 55/65°E;5/20°S) [Smythe-Wright et al., 2005], which is an extensive submarine plateau reaching a shallowness of up to 50 m. [2] As described by Schott et al. [2009], during both monsoon seasons a southward Ekman transport subducts underneath the equatorial roll. This leads to upwelling south of this roll in the area between 10°S and 6°S, which elevates biological productivity and, as a result, also the production of biogenically produced trace gases.
Isoprene water concentrations ranged from 0.36 pmol L^{-1} to a maximum of 64 pmol L^{-1} (Figure 3.3). During SO234-2, from Durban to Mauritius, average values around 10 pmol L^{-1} were observed. North of Mauritius the isoprene concentration steadily increased from sub 1 pmol L^{-1} just off Mauritius to around 30 pmol L^{-1} at the Maldives. The maximum values of isoprene were reached at 6.1°S and 64.45°E on day of year 2014 (DOY) 209.45 [Booge et al., 2016]. The DMS and isoprene seawater distributions were anticorrelated over most of the cruise tracks.

3.4.2 Fluxes

Directly measured DMS fluxes ranged from 0.3-32.77 µmol m^{-2} d^{-1} (Figure 3.3). During SO234-2 from Durban to Mauritius and after DOY 214 the fluxes were low, which can be attributed to low wind speed (below 10 m s^{-1}) and low water concentrations. After Mauritius at DOY 205 a high wind speed event (wind speed maximum of 16 m s^{-1}) was encountered. High wind speed in conjunction with high seawater concentrations were measured, leading to an increase of the flux. Wind speed steadily decreased as the cruise continued, but seawater concentrations varied, causing the fluxes to vary accordingly in magnitude from DOY 210 onwards. The lowest fluxes occurred on DOY 198 and the highest on DOY 207. Isoprene fluxes ranged from 0-0.187 µmol m^{-2}- d^{-1}. Generally the isoprene fluxes of SO235 were higher, which is associated for the most part with the higher wind speed and secondly with the slightly higher water concentrations. The computed SSPF closely resembles the measured wind speed (Figure 3.3).

3.4.3 Comparison to the Lana climatology and PMEL database

Generally the sea surface DMS concentrations throughout the cruise legs are lower than those published in the Lana climatology [Lana et al., 2012] and the PMEL database (Figure 3.1) [Kettle et al., 1999]. A description of the Lana climatology and the PMEL database can be found in the supplement. The WTIO is heavily under-sampled, especially

in the months July and August. The only data available, and therefore used, in the Lana climatology are 34 samples from two cruises [Mihalopoulos et al., 1992, Smythe-Wright et al., 2005] (Diamonds, Figure 3.1). The influence of the Mascarene Plateau on biological productivity might be the reason for the general elevated DMS concentrations from both the PMEL database and the Lana climatology (background Figure 3.1). As the database's seawater concentrations were measured further west than our cruise track, they were located more directly in the region impacted by the Mascarene Plateau and values up to 9 nmol L^{-1} were incorporated in the climatology. Our highest measure value was 5.19 nmol L^{-1}.
On a global scale the WTIO represents the DMS flux hotspot for July. Our maximum value of 32.77 µmol m^{-2} d^{-1} is of the same magnitude as the worldwide maximum value (31.8 µmol m^{-2} d^{-1}), excluding the Indian Ocean (IO). The maximum value of the IO from the Lana climatology is 63.2 µmol m^{-2} d^{-1} and is twice as much as measured during our cruise. Although larger than our measurements, this value is still plausible because it is located at 10°S 59°E and therefore more directly influenced by the Mascarene Plateau. This supports the importance of the IO as a source of DMS during this season. Fluxes computed from the Lana climatology corresponding to our cruise location and dates range between 2.22-34.78 µmol m^{-2} d^{-1} (this study 0.3-32.77 µmol m^{-2} d^{-1}). On average, Lana's predicted fluxes are 60% higher (Lana mean:14.9 µmol m^{-2} d^{-1}, this study mean: 9.1 µmol m^{-2} d^{-1}, Figure 3.3). The reason for these differences is twofold. [1] The Lana climatology uses higher DMS seawater concentrations than those we measured in situ. [2] The air-sea flux parameterization (Equation 3.3) used in the climatology [Nightingale et al., 2000] has a quadratic dependence of the gas transfer velocity k on wind speed. However, our directly measured fluxes and the associated gas transfer velocity appear to have a linear relationship to wind speed. As the wind speed experienced during the cruise and the wind speed used by the climatology were similar (Figure 3.3), the difference in a quadratic and a linear dependence resulted in an increase of the Lana DMS flux.

3.4.4 Correlations with aerosol properties

Figure 3.4 shows a time series of the fluxes at the cruise track. Overlaid are the averaged satellite data from the downwind area. The averaging was done from the time of the flux measurement until 12 h into the forward trajectory. The largest fluxes of DMS, in the top panel, are around DOY 207-208. Additionally, at DOY 212-214, a secondary maximum, followed by a short decrease and sudden increase, can be seen. Similar characteristics are visible in all three satellite products. For isoprene, the highest fluxes occurred at DOY 209-211. Similar to DMS fluxes, the isoprene fluxes at the end of the cruise increase, decrease, then sharply increase again. CCN and AOD seem to roughly follow this feature. This is reflected in the correlation coefficients: DMS-CCN 0.425; DMS-AOD 0.625; Isoprene-AOD 0.4; Isoprene-AOT 0.43.
SSPF has its main feature at DOY 205, when the wind speed was highest, and steadily decreases over the cruise track. The Terra CCN product distribution follows the SSPF source distribution, whereas the other aerosol satellite product distributions do not appear similar to the trend of the SSPF distribution. This is supported by the correlation

coefficients: SSPF-CCN 0.49; SSPF-AOD 0.16; SSPF-AOT -0.04
All three fluxes in Figure 3.4 have distinct features at different times, corresponding to different trends in the downwind aerosol product distributions. This allows us to qualitatively estimate the influence of each source on the satellite product. The aerosol product distribution more closely resembles the trace gas fluxes than the SSPF distributions. Nonetheless, there are also differences between the two trace gases, which are reflected in the aerosol product distributions. For example, the spatial distribution of the isoprene fluxes is anti-correlated with the DMS fluxes at DOY 212 and 214 and the maxima and minima are offset for the two trace gas fluxes. A second example is the isoprene flux trend from DOY 209-211, which is not well represented in the downwind satellite product distribution. The SSPF distribution, which starts high and then gradually decreases, does not seem to have great influence on the satellite aerosol product distribution, which does not mean that overall SSPF is not an aerosol precursor in this study region. This is supported by Quinn et al. [2017] who find a 30% contribution of SSPF to the CCN budget in in the tropics. As quality control, we correlated the fluxes with the backward (upwind) trajectories up to -12 h. These correlations are insignificant or negative. The full collection of correlations and the full comparison of flux data and satellite data are shown in the supplement (Figures 3.7-3.10, Tables 3.1 and 3.2).

3.5 Conclusion

In this study, we observed that the WTIO during the summer monsoon period is one of the world's largest DMS source regions to the atmosphere. We correlated our directly measured DMS, as well as calculated isoprene fluxes and SSPF, with satellite derived aerosol numbers over the IO during the summer monsoon. The maximum correlations including regional transport, computed using trajectories from the FLEXPART/ERA-Interim model, were statistically significant. These results illustrate the regional coupling between marine-derived precursors and aerosol products in the remote MBL. This is important, as regional coupling can give rise to local feedback processes. Although we acknowledge that correlation results do not always imply causation, the ensemble findings support the idea that marine-derived biogenic trace gases, as well as sea spray, influence the aerosol properties on a regional scale.

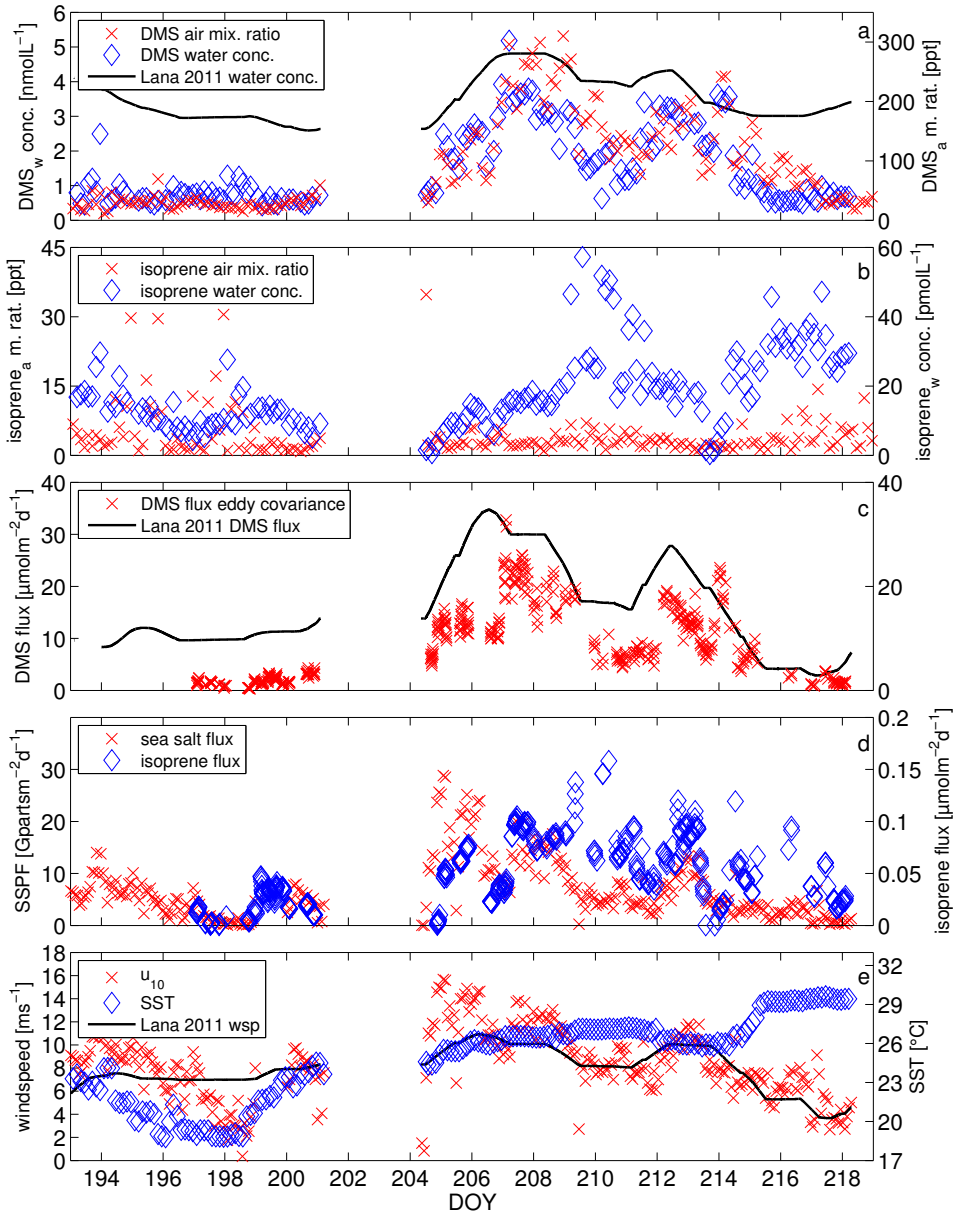

Figure 3.3: Time series along the cruise track (x-axis DOY 2014), [a] DMS surface seawater concentration (diamonds) and the air mixing ratio (crosses), [b] isoprene surface water concentrations (diamonds) and air mixing ratios (crosses), [c] the measured DMS flux (crosses) and Lana's climatological DMS flux (line), [d] isoprene flux and SSPF, [e] sea surface temperature (SST, diamonds) and u_{10} along the cruise track, measured (crosses) and used by the Lana climatology (line). The error estimates are: DMS_{air} 5%; DMS_{water} 10%; $Isoprene_{air}$ 5%; $Isoprene_{water}$ 10%; Eddy Covariance 25% [Edson et al., 1998, Marandino et al., 2007]

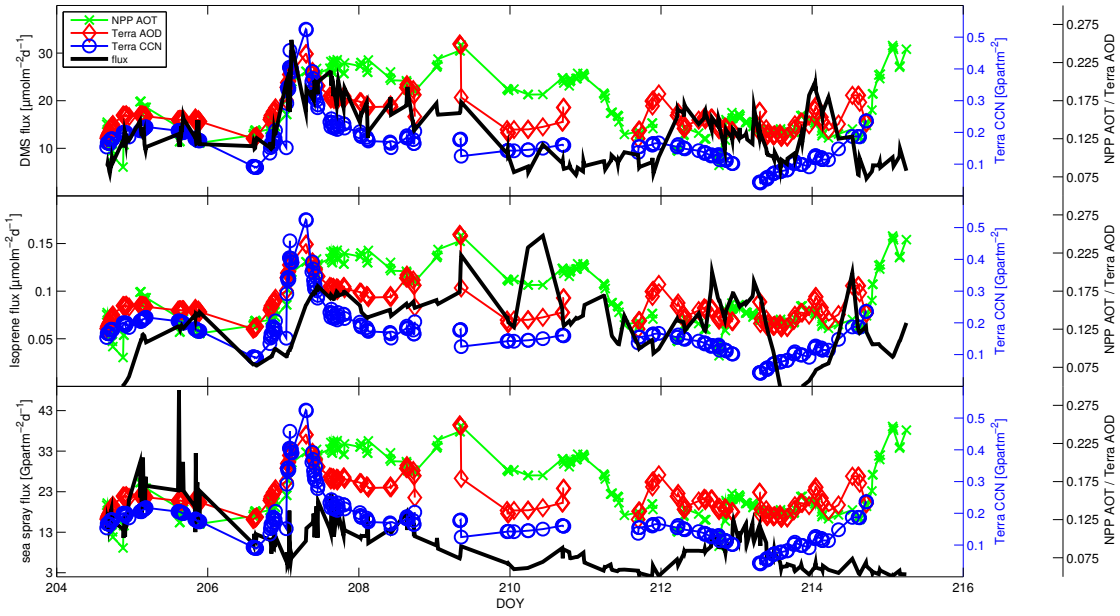

Figure 3.4: Time series of DMS flux [top panel], isoprene flux [middle panel] and SSPF [bottom panel] from DOY 204.66 to 215.25 shown together with the data from the Terra satellite (Terra-CCN, Terra-AOD) and the NPP satellite (NPP-AOT). The aerosol products shown are the average along the forward trajectory from the time of the flux measurement until 12 h. Uncertainty estimates are shown in the supplement.

Acknowledgements

The authors thank the crew of the RV Sonne (SO234-2/235). Steffen Fuhlbrügge prepared and carried out the ozone sondes preparations and launches and helped with the post-processing of the data. E. Atlas acknowledges support from the NASA UARP program and thanks Leslie Pope and Xiaorong Zhu for the canister preparation. The authors acknowledge NASA and NOAA for providing the satellite data. We thank the ECMWF for providing the ERA-Interim reanalysis data and the FLEXPART development team. This work was carried out under the Helmholtz Young Investigator Group of C. Marandino, TRASE-EC (VH-NG-819), from the Helmholtz Association. The cruise 234-2/235 and A. Fiehn were financed by the BMBF, 03G0235A. The authors declare no competing financial interests. The data is stored at the data portal of GEOMAR Kiel. Kirstin Krüger acknowledges financial support from the EU FP7 StratoClim project (603557).

3.6 Supplement

3.6.1 Eddy covariance high frequency correction and post processing

We screened the record for spikes, malfunctions, high and low frequency anomalies and proper time delay. 435 intervals were corrected for the high frequency loss in the tube. The high frequency correction was performed by fitting a rectangular signal using a low-pass filter to the signal of an actual isotope standard valve switch. The loss in high frequency power of the isotope standard valve switch is equal to the loss in the 1/2"teflon tube. The loss displayed a linear relationship with 10 m neutral wind speed (u_{10}). The gain factor (G_{hf}), which is corrects for the tube's high frequency loss, is seen in equation 3.5.

$$G_{hf} = 1.032 + 0.0021 \cdot u_{10} \tag{3.5}$$

3.6.2 PMEL Database and DMS climatology

The Pacific Marine Environmental Laboratory (PMEL) DMS database [Kettle et al., 1999]
http://saga.pmel.noaa.gov/dms/
collects global surface seawater DMS concentrations. Approximately 50 000 measured samples from all over the world can be accessed through this database. The Lana DMS climatology [Lana et al., 2011] is based upon the PMEL database and provides a monthly global 1° x 1° grid of DMS sea surface concentrations. Using monthly mean winds from the NCEP/NCAR (1978 - 2008) reanalysis project and the Nightingale et al. [2000] gas transfer velocity parametrization the DMS climatology also provides global monthly DMS air-sea fluxes.

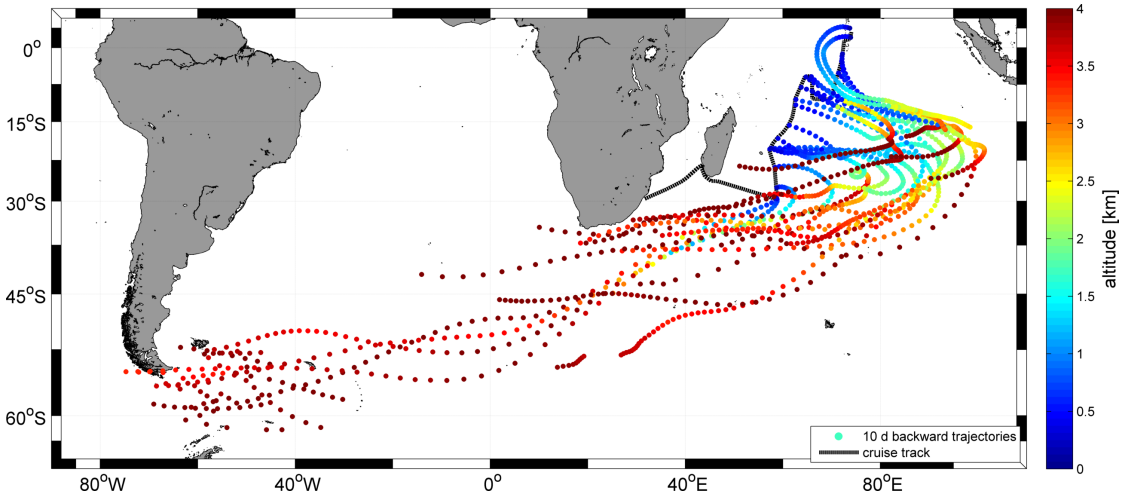

Figure 3.5: 10 day backtrajectories. The altitude of the trajectories is color coded.

3.6.3 Origin of air masses

Using the FLEXPART transport model [Stohl et al., 2005] with the ERA-interim [Dee et al., 2011] meteorological data, we calculated 10 day backward trajectories for the times of the eddy covariance measurements. The trajectories are shown in Figure 3.5. All trajectories originate from marine environments. The altitude of the trajectories is colored. We estimate from Figure 2 and Figure 3.5 that, prior to our measurement, the air parcel has been inside the marine boundary layer and in contact with the ocean for at least 24 h.
We also performed six ozone balloon soundings during the cruise. The locations, times and data of these soundings are shown in Figure 3.6. The average values are: near surface 22 ppb; 1 km 26 ppb; 5 km 51 ppb. The low ozone levels and backward trajectories provide evidence that the sampled air was unpolluted, with a marine origin.
We also performed six ozone balloon soundings during the cruise. The locations, times and data of these soundings are shown in Figure 3.6. The average values are: near surface 22 ppb; 1 km 26 ppb; 5 km 51 ppb. The low ozone levels and backward trajectories provide evidence that the sampled air was unpolluted, with a marine origin.

3.6.4 Correlations

We created a Lagrangian product using the satellite aerosol data at the time and location of the backward and forward trajectories (time span -12 h to +12 h) to analyze and correlate the data sets. The output of the FLEXPART model has an hourly resolution. For every hour we obtain aerosol satellite readings at the specific time and location. Figure 1 in the main manuscript shows the ensemble of back and forward trajectories for

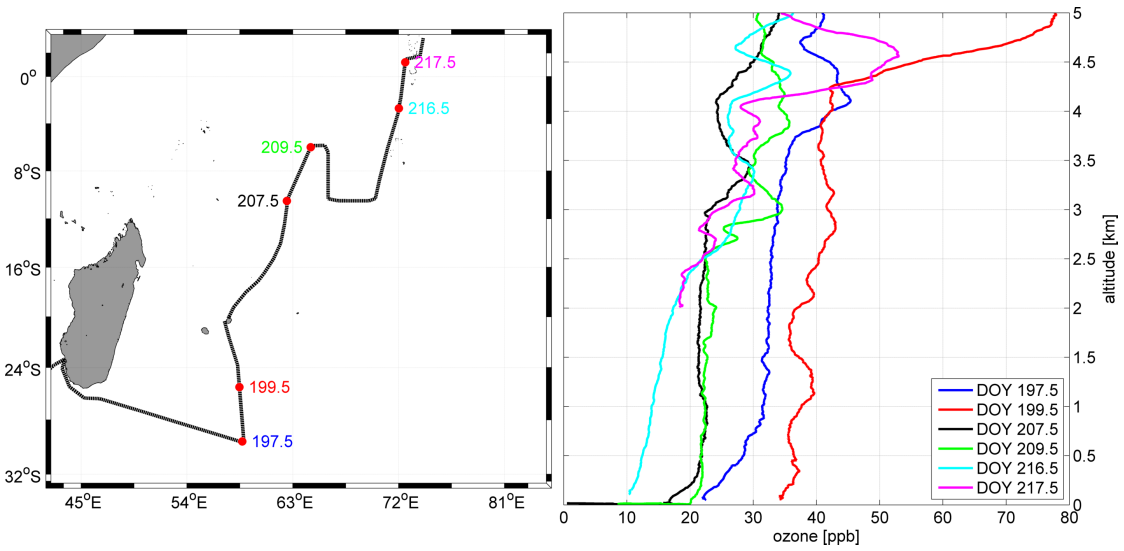

Figure 3.6: Dates and locations of the six balloon soundings (left). Ozone concentration from the surface until 5 km altitude for the six balloon ozone measurements (right).

a time span of -12 h to +12 h before and after the measurement of the air-sea flux. We started a forward and backward trajectory at the position of every flux measurement. We averaged the aerosol satellite data along these trajectories and correlate the 'downwind' (0 h to 12 h) and 'upwind' (-12 h to 0 h) data to the flux measured at the cruise. We hypothesize that the measured efflux has a direct influence on the aerosol properties of the air parcel and a significant correlation between these two values would be the consequence.

We created a Lagrangian product using the satellite aerosol data at the time and location of the backward and forward trajectories (time span -12 h to +12 h) to analyze and correlate the data sets. The output of the FLEXPART model has an hourly resolution. For every hour we obtain aerosol satellite readings at the specific time and location. Figure 1 in the main manuscript shows the ensemble of back and forward trajectories for a time span of -12 h to +12 h before and after the measurement of the air-sea flux. We started a forward and backward trajectory at the position of every flux measurement. We averaged the aerosol satellite data along these trajectories and correlate the 'downwind' (0 h to 12 h) and 'upwind' (-12 h to 0 h) data to the flux measured at the cruise. We hypothesize that the measured efflux has a direct influence on the aerosol properties of the air parcel and a significant correlation between these two values would be the consequence.

It is unreasonable to correlate an event (0 h, flux measured at cruise track) to air parcels and their aerosol properties that, in the future (-12 h until 0 h), will encounter this cruise track. However, the magnitudes of these correlations and data are used as a quality check and to assess the noise inflicted by the scan for satellite data in time and space. In an

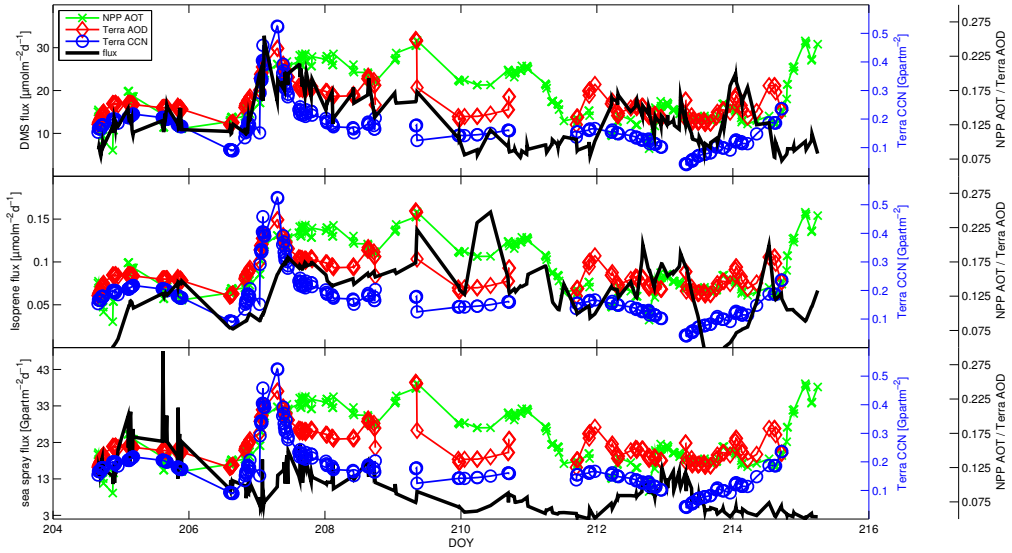

Figure 3.7: Averaged forward trajectories satellite data from Terra and Suomi-NPP satellite at the time of the measurement to 12 h. For the sake of completeness this is a copy of Figure 4 from the manuscript.

Table 3.1: Correlation of the forward trajectories

corr. product	corr. value Terra	corr. value Aqua	NPP
CCN-SSPF	0.49	0.49	N/A
CCN-DMS	0.425	0.5	N/A
CCN-ISOP	0.25	0.32	N/A
AOD/AOT-SSPF	0.16	-0.05	-0.04
AOD/AOT-DMS	0.65	0.49	0.25
AOD/AOT-ISOP	0.4	0.17	0.43

ideal world, all correlations from -12 h until 0 h should be close to zero, as causality is only established after the air parcel crossed (0 h until 12 h) the cruise track, when positive correlations should occur.
Figures 3.7 and 3.8 show the forward trajectory (downwind) averaged satellite data obtained from the Terra, Aqua and Suomi-NPP satellite. Data from the Aqua satellite supports the findings from the Terra and Suomi-NPP satellite. Correlation coefficients for all downwind satellite flux correlations are shown in Table 3.1. Figures 3.9 and 3.10 show the backward trajectory (upwind) averaged satellite date from the Terra, Aqua and Suomi-NPP satellite. Data from upwind show as expected insignificant or negative correlation to the measured fluxed. The correlation between the upwind satellite data and the measured flux is shown in Table 3.2.

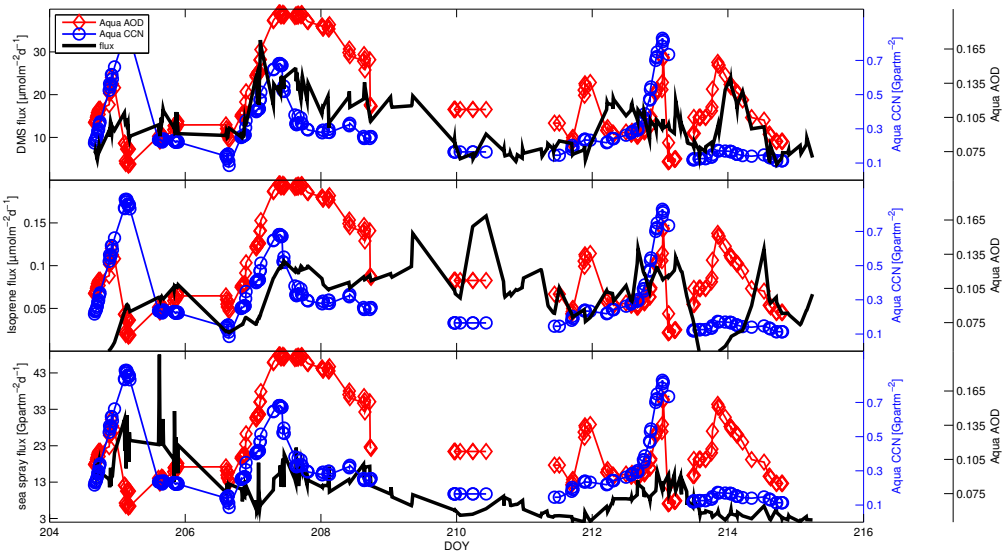

Figure 3.8: Averaged forward trajectories satellite data from Aqua at the time of the measurement to 12 h.

Table 3.2: Correlation of the backward trajectories

corr. product	corr. value Terra	corr. value Aqua	NPP
CCN-SSPF	-0.16	0.07	N/A
CCN-DMS	-0.5	-0.37	N/A
CCN-ISOP	-0.349	-0.05	N/A
AOD/AOT-SSPF	-0.26	-0.36	0.03
AOD/AOT-DMS	-0.42	-0.53	-0.49
AOD/AOT-ISOP	-0.26	-0.09	0.03

3.6.5 Spatial and time resolution

The hourly output of the FLEXPART model is justified by the spatial resolution of the satellites. With an average wind speed of 8.8 m s^{-1}, an air parcel takes 3 h 25 min to cross from one MODIS pixel to another. For the NPP resolution of 0.25° it would take 52 min. We can use data from every pixel the trajectory crosses. These hourly data is then used for averaging in the 'upwind' (-12 h to 0 h) and the 'downwind' (0 h to 12 h) area. Figure 3.11 shows a schematic model of the data retrieved by the satellite. The chimney represents the source. In the case of Mace and Abernathy [2016], Eguchi et al. [2011], Yuan et al. [2011] these chimneys are volcanos. In our case it is every flux measurement we performed. As a result we get a chain of chimneys along the cruise track. We track their 'exhaust plume' using the FLEXPART model and their aerosol products using the satellite data. The only constraint is that the chimney's exhaust is constant in the timescale of the satellite's sampling frequency.

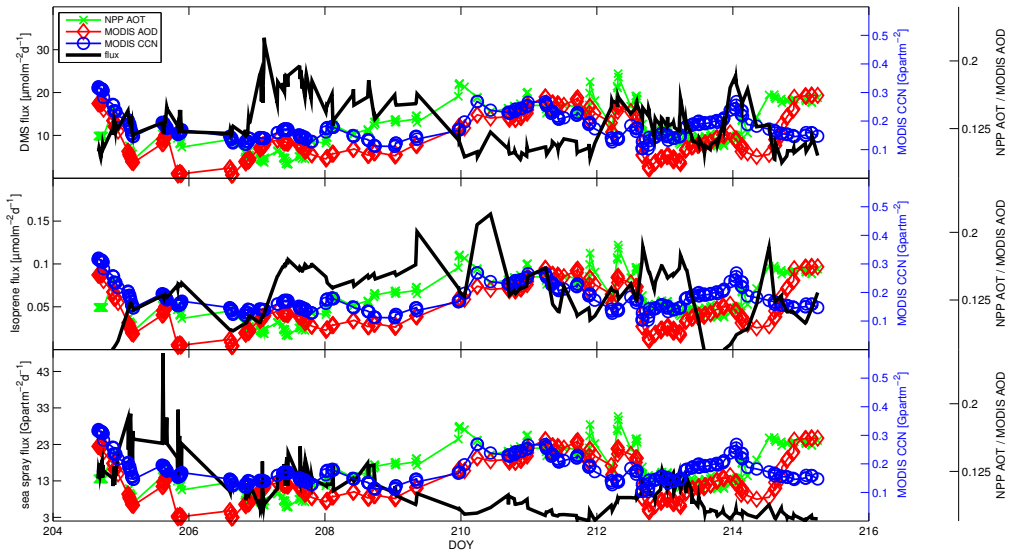

Figure 3.9: Averaged backward trajectories satellite data from Terra at the time of the measurement to 12 h.

We also performed spectral analysis on the DMS flux signal, DMS water concentration and wind speed along the cruise track, as shown in Figure 3.12. Changes in these signals are in timescales beyond 1 day. We also used a 1° by 1° sample quadrant at 15°S 16°E to asses the variability in the satellite readings as well as wind speed. The time series and the spectral analysis are shown in Figures 3.13 and 3.14. Additionally, we plotted an simulated daily changing signal for comparison. This saw tooth shaped signal represents a data signal which is changing on a daily basis. We compare the spectral power of a simulated daily changing signal to the spectral power of our data, to support the claim that most changes are on a temporal scale beyond 1 day. The spectral analysis in Figure 3.14 shows that most variation lies in timescales beyond 1 day. Yin and Min [2013] show that no significant diurnal variation is present for oceanic influenced AOD measurements sites. Therefore, it is reasonable to use a satellite product with daily resolution. This is also backed up by the expected spectral behavior of the boundary layer.

3.6.6 Satellite data

The description of all satellite products used is in Table 3.3. Table 3.4 shows the estimated error of the aerosol satellite products. Their references are listed in column three. Figure 3.15 shows uninterpolated satellite CCN data (Terra satellite) map over the cruise area from one day. In total we obtained 42 of these daily datasets. Figure 3.16 shows satellite data from the cruise track 48 hours before passing with ship and 48 hours after we passed with the ship. No significant feature can be found which persists over 96 hours. This is in agreement with our findings that using a satellite product, compiled of data from

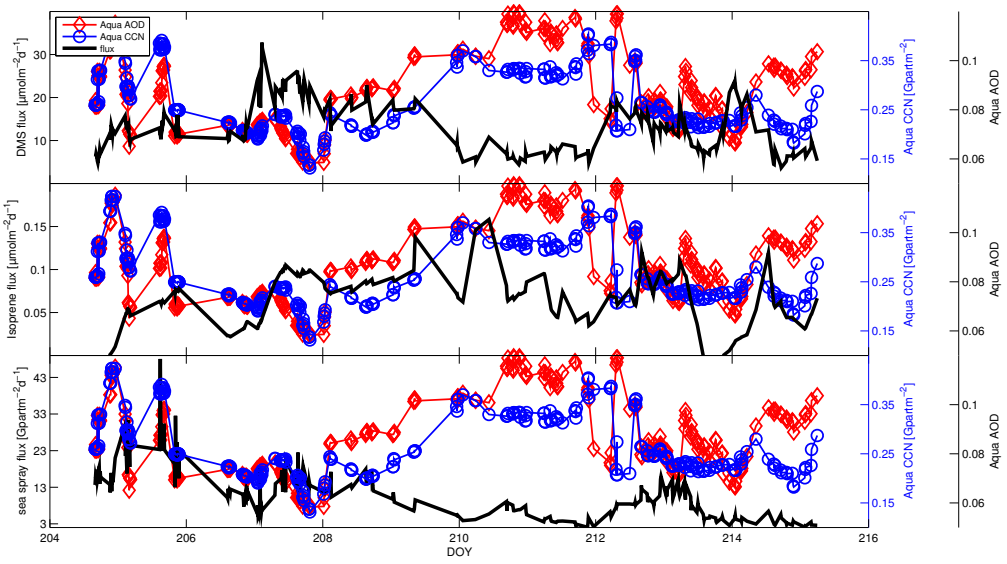

Figure 3.10: Averaged backward trajectories satellite data from Aqua at the time of the measurement to 12 h.

Table 3.3: Specific satellite, data set and variable used for the MODIS CCN, MODIS AOD and Suomi-NPP AOT product.

Product	Satellite	Selection	Variable
MODIS CCN	Terra	MYD08_D3	Aerosol_PSML003 _ Ocean_Mean
MODIS AOD	Terra	MYD08_D3	Aerosol _Optical_Depth _Land_Ocean_Mean
Suomi NPP AOT	Suomi NPP	N/A	npp _aot550 _edr

Table 3.4: Error estimates of the satellite products.

Product	Estimated error	reference
MODIS-CCN	30% at cloud base	Rosenfeld et al. [2016]
MODIS-AOD	±0.04+10%	Levy et al. [2013]
Suomi NPP-AOT	0.009+25%	Huang et al. [2016]

more two days, will not result in significant correlations.

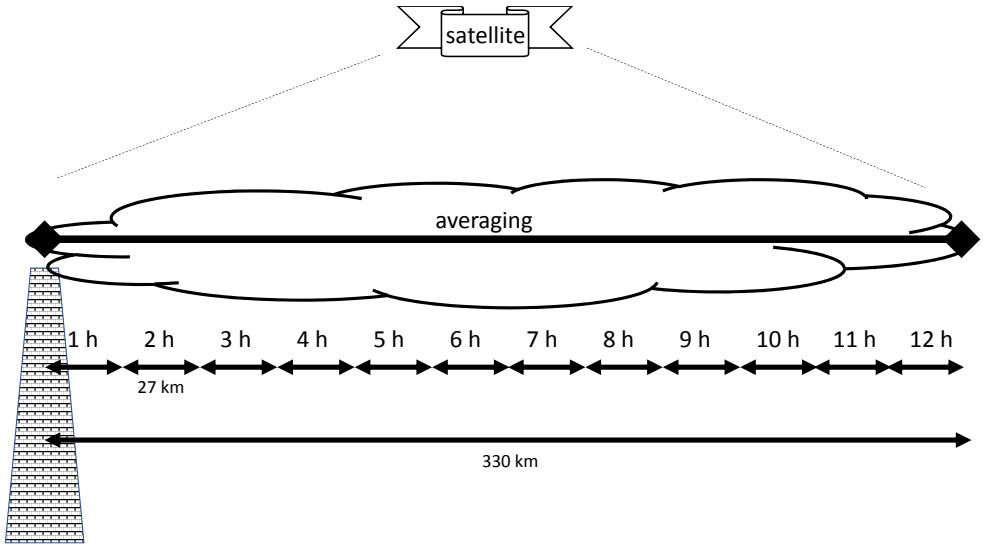

Figure 3.11: Schematic of the satellite retrieval using the spatial resolution of the SUOMI-NPP. At an average speed of 27 km h^{-1}, the satellite can track the evolution of the cloud in 1 hour steps. SUOMI-NPP has a 20 km spatial resolution. The only constraint is that the chimney has to have a steady output on a timescale longer than 1 day.

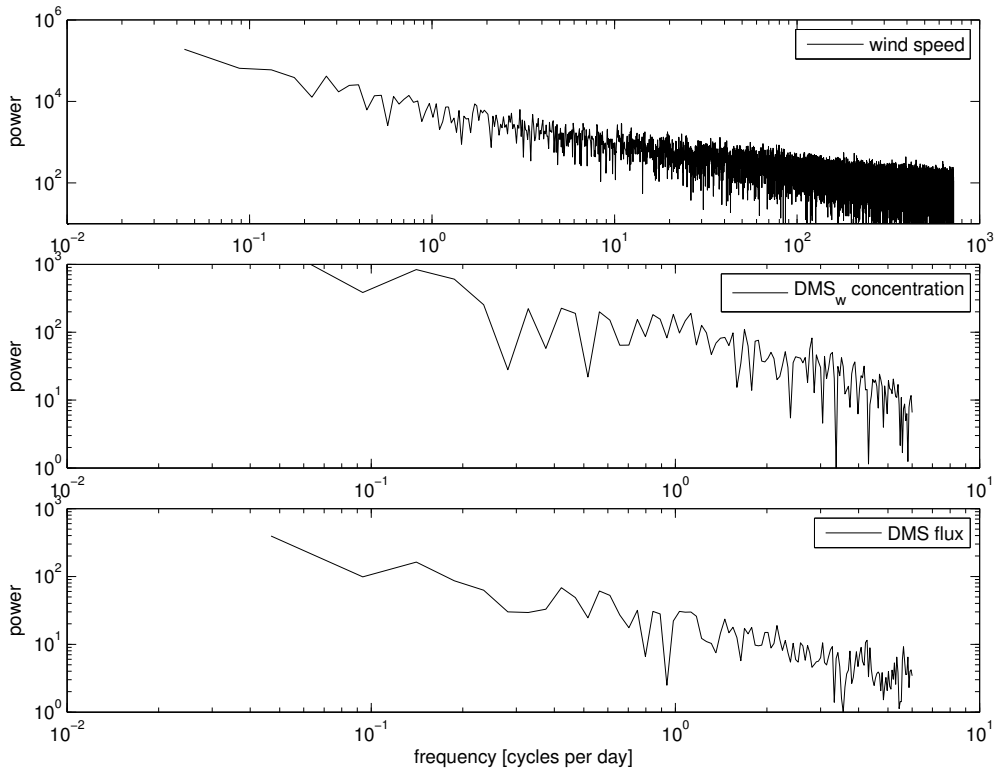

Figure 3.12: Frequency power spectrum of wind speed (top), DMS water concentration (middle) and DMS flux (bottom) along the cruise track.

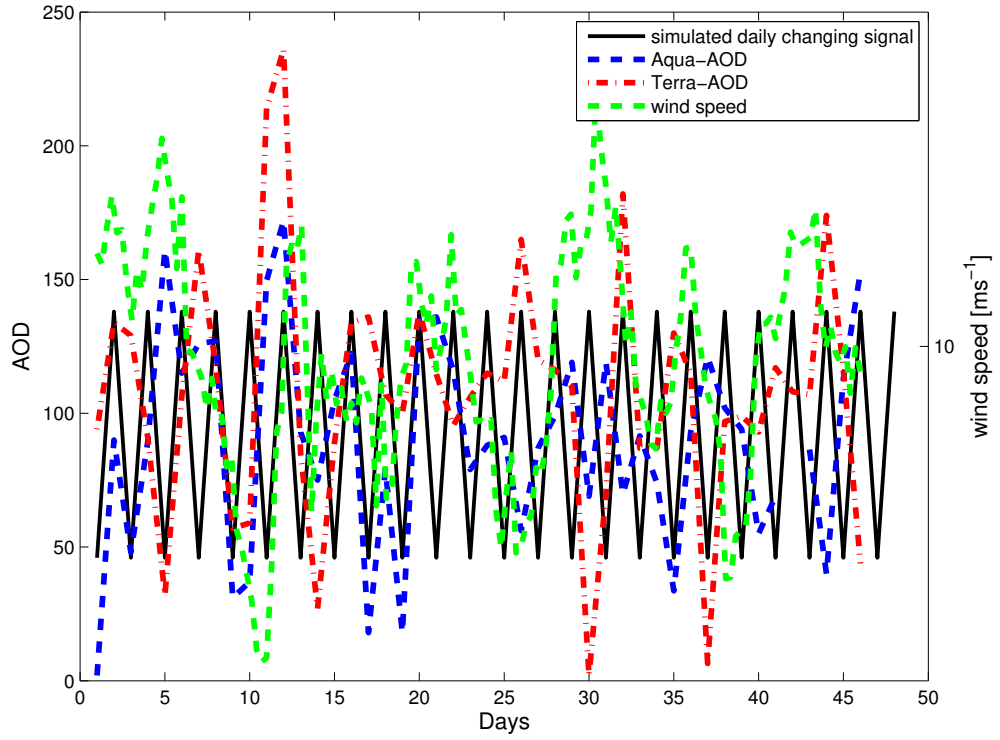

Figure 3.13: Time series of Aqua-AOD, Terra-AOD and wind speed at a 1° by 1° sample quadrant (15S/16E). Additionally a simulated daily changing signal is plotted for comparison.

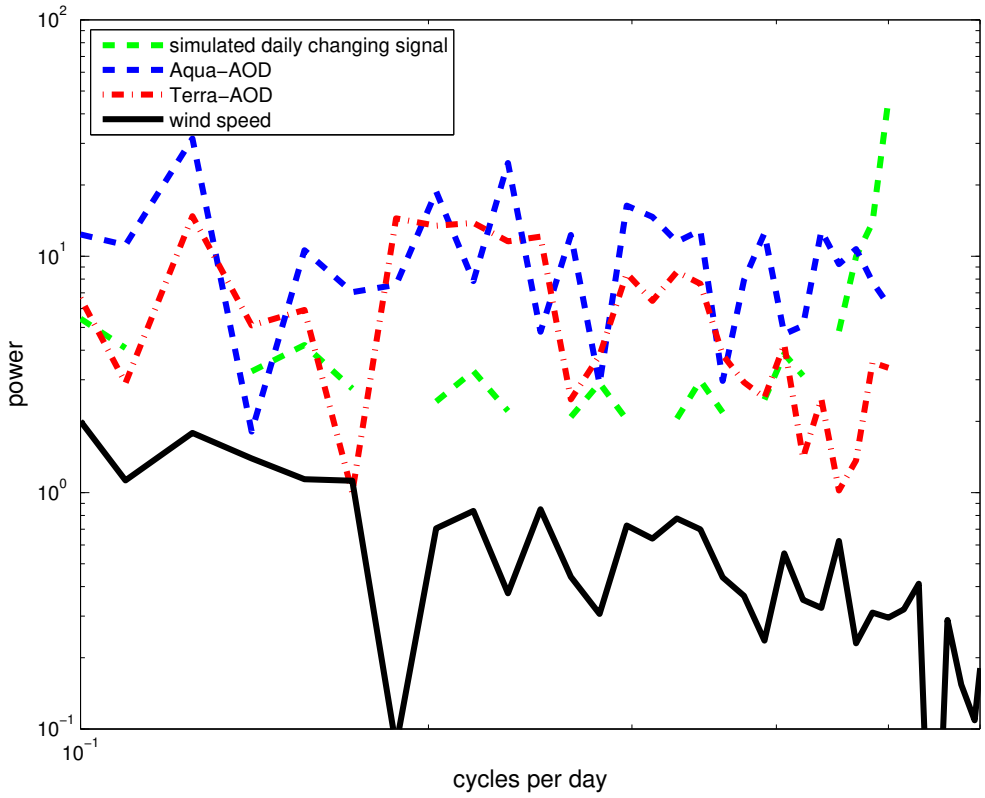

Figure 3.14: Frequency power spectrum of Aqua-AOD, Terra-AOD, wind speed and the simulated daily changing signal at the 1° by 1° sample quadrant (15S/16E).

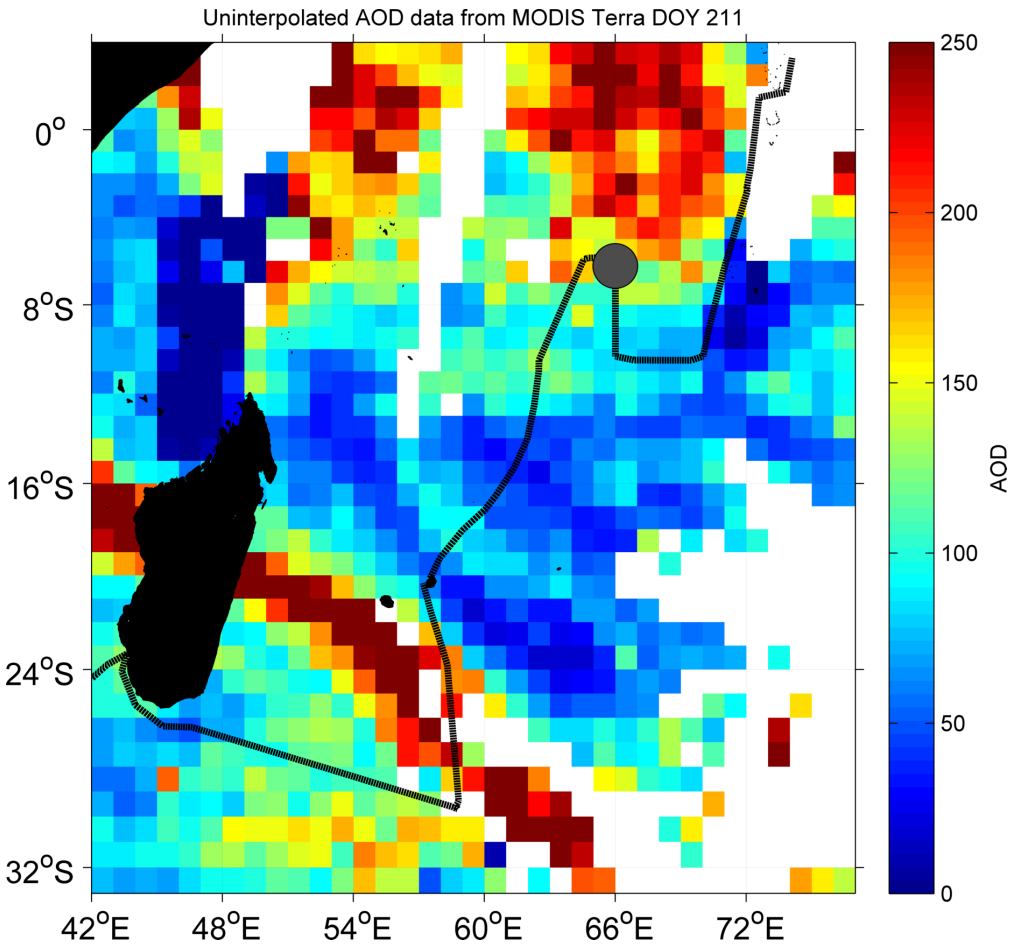

Figure 3.15: Uninterpolated AOD data from MODIS Terra from DOY 2011. The grey cirlce denotes the location of the ship at the time of this satellite passover.

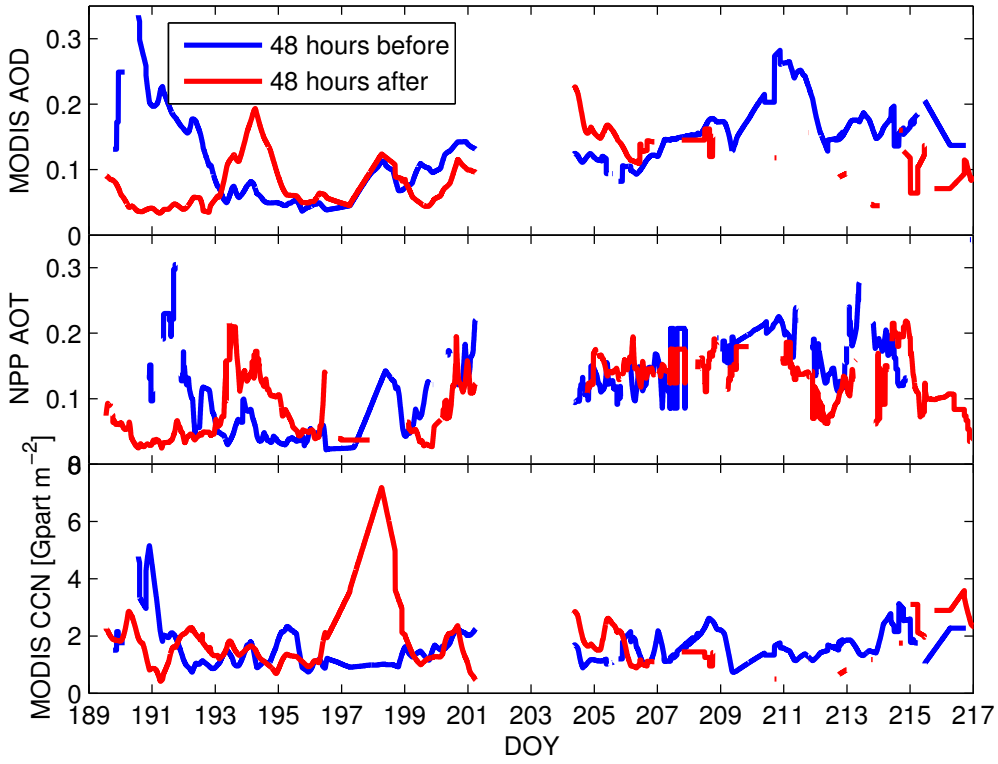

Figure 3.16: AOD, AOT and CCN satellite data from the cruise track 48 hours before the ship passed and 48 hours after the ship passed.

References

D. Booge, C. A. Marandino, C. Schlundt, P. I. Palmer, M. Schlundt, E. L. Atlas, A. Bracher, E. S. Saltzman, and D. W. R. Wallace. Can simple models predict large-scale surface ocean isoprene concentrations? *Atmospheric Chemistry and Physics*, 16(18):11807–11821, 2016. doi: 10.5194/acp-16-11807-2016. URL https://www.atmos-chem-phys.net/16/11807/2016/.

Robert J. Charlson, James E. Lovelock, Meinrat O. Andreae, and Stephen G. Warren. Oceanic phytoplankton, atmospheric sulphur, cloud albedo and climate. *Nature*, 326 (6114):655–661, apr 1987. doi: 10.1038/326655a0. URL http://dx.doi.org/10.1038/326655a0.

D. P. Dee, S. M. Uppala, A. J. Simmons, P. Berrisford, P. Poli, S. Kobayashi, U. Andrae, M. A. Balmaseda, G. Balsamo, P. Bauer, P. Bechtold, A. C. M. Beljaars, L. van de Berg, J. Bidlot, N. Bormann, C. Delsol, R. Dragani, M. Fuentes, A. J. Geer, L. Haimberger, S. B. Healy, H. Hersbach, E. V. Holm, L. Isaksen, P. Kållberg, M. Köhler, M. Matricardi, A. P. McNally, B. M. Monge-Sanz, J. J. Morcrette, B. K. Park, C. Peubey, P. de Rosnay, C. Tavolato, J. N. Thepaut, and F. Vitart. The era-interim reanalysis: configuration and performance of the data assimilation system. *Quarterly Journal of the Royal Meteorological Society*, 137(656):553–597, apr 2011. ISSN 1477-870X. doi: 10.1002/qj.828. URL http://dx.doi.org/10.1002/qj.828.

J. B. Edson, A. A. Hinton, K. E. Prada, J. E. Hare, and C. W. Fairall. Direct covariance flux estimates from mobile platforms at sea. *Journal of Atmospheric and Oceanic Technology*, 15(2):547–562, apr 1998. doi: 10.1175/1520-0426(1998)015<0547:dcfefm>2.0.co;2. URL http://journals.ametsoc.org/doi/abs/10.1175/1520-0426%281998%29015%3C0547%3ADCFEFM%3E2.0.CO%3B2.

Kenta Eguchi, Itsushi Uno, Keiya Yumimoto, Toshihiko Takemura, Takashi Y. Nakajima, Mitsuo Uematsu, and Zhaoyan Liu. Modulation of cloud droplets and radiation over the north pacific by sulfate aerosol erupted from mount kilauea. *SOLA*, 7:77–80, 2011. doi: 10.2151/sola.2011-020.

A. Fiehn, B. Quack, H. Hepach, S. Fuhlbrügge, S. Tegtmeier, M. Toohey, E. Atlas, and K. Krüger. Delivery of halogenated very short-lived substances from the west indian ocean to the stratosphere during asian summer monsoon. *Atmos. Chem. Phys. Discuss.*, 2017:1–40, jan 2017. ISSN 1680-7375. doi: 10.5194/acp-2017-8. URL http://www.atmos-chem-phys-discuss.net/acp-2017-8/.

Caroline Forster, Andreas Stohl, and Petra Seibert. Parameterization of convective transport in a lagrangian particle dispersion model and its evaluation. *Journal of Applied Meteorology and Climatology*, 46(4):403–422, apr 2007. doi: 10.1175/jam2470.1. URL http://journals.ametsoc.org/doi/abs/10.1175/JAM2470.1.

Tamara K Green and Angela D Hatton. *The Claw Hypothesis: A New Perspective on the Role of Biogenic Sulphur in the Regulation of Global Climate*, pages 315–336. Oceanography and Marine Biology - An Annual Review. CRC Press, aug 2014. ISBN 978-1-4822-2059-9. doi: 10.1201/b17143-7. URL http://dx.doi.org/10.1201/b17143-7.

S. A. Hsu, Eric A. Meindl, and David B. Gilhousen. Determining the power-law wind-profile exponent under near-neutral stability conditions at sea. *Journal of Applied Meteorology*, 33(6):757–765, jun 1994. doi: 10.1175/1520-0450(1994)033<0757:dtplwp>2.0.co;2. URL http://journals.ametsoc.org/doi/abs/10.1175/1520-0450%281994%29033%3C0757%3ADTPLWP%3E2.0.CO%3B2.

Jingfeng Huang, Shobha Kondragunta, Istvan Laszlo, Hongqing Liu, Lorraine A. Remer, Hai Zhang, Stephen Superczynski, Pubu Ciren, Brent N. Holben, and Maksym Petrenko. Validation and expected error estimation of suomi-npp viirs aerosol optical thickness and Ångström exponent with aeronet. *Journal of Geophysical Research: Atmospheres*, 121(12):7139–7160, 2016. ISSN 2169-8996. doi: 10.1002/2016JD024834. URL http://dx.doi.org/10.1002/2016JD024834. 2016JD024834.

Paula Hubanks, Steven Platnick, Michael King, and Bill Ridgway. Modis atmosphere l3 gridded product algorithm theoretical basis document for c6. Technical Report ATBD Reference Number: ATBD-MOD-30, NASA, 2016.

A. J. Kettle, M. O. Andreae, D. Amouroux, T. W. Andreae, T. S. Bates, H. Berresheim, H. Bingemer, R. Boniforti, M. A. J. Curran, G. R. DiTullio, G. Helas, G. B. Jones, M. D. Keller, R. P. Kiene, C. Leck, M. Levasseur, G. Malin, M. Maspero, P. Matrai, A. R. McTaggart, N. Mihalopoulos, B. C. Nguyen, A. Novo, J. P. Putaud, S. Rapsomanikis, G. Roberts, G. Schebeske, S. Sharma, R. Simo, R. Staubes, S. Turner, and G. Uher. A global database of sea surface dimethylsulfide (dms) measurements and a procedure to predict sea surface dms as a function of latitude, longitude, and month. *Global Biogeochemical Cycles*, 13(2):399–444, jun 1999. ISSN 1944-9224. doi: 10.1029/1999GB900004. URL http://dx.doi.org/10.1029/1999GB900004.

A. Lana, T. G. Bell, R. Simo, S. M. Vallina, J. Ballabrera-Poy, A. J. Kettle, J. Dachs, L. Bopp, E. S. Saltzman, J. Stefels, J. E. Johnson, and P. S. Liss. An updated climatology of surface dimethlysulfide concentrations and emission fluxes in the global ocean. *Global Biogeochemical Cycles*, 25(1):n/a–n/a, jan 2011. ISSN 1944-9224. doi: 10.1029/2010GB003850. URL http://dx.doi.org/10.1029/2010GB003850.

A. Lana, R. Simo, S. M. Vallina, and J. Dachs. Potential for a biogenic influence on cloud microphysics over the ocean: a correlation study with satellite-derived data. *Atmos. Chem. Phys.*, 12(17):7977–7993, sep 2012. ISSN 1680-7324. doi: 10.5194/acp-12-7977-2012. URL http://www.atmos-chem-phys.net/12/7977/2012/.

Sebastian Landwehr, Niall O'Sullivan, and Brian Ward. Direct flux measurements from mobile platforms at sea: Motion and airflow distortion corrections revisited.

Journal of Atmospheric and Oceanic Technology, 32(6):1163–1178, jun 2015. doi: 10.1175/jtech-d-14-00137.1. URL http://journals.ametsoc.org/doi/abs/10.1175/JTECH-D-14-00137.1.

R. C. Levy, S. Mattoo, L. A. Munchak, L. A. Remer, A. M. Sayer, F. Patadia, and N. C. Hsu. The collection 6 modis aerosol products over land and ocean. *Atmospheric Measurement Techniques*, 6(11):2989–3034, 2013. doi: 10.5194/amt-6-2989-2013. URL http://www.atmos-meas-tech.net/6/2989/2013/.

G. G. Mace and A. C. Abernathy. Observational evidence for aerosol invigoration in shallow cumulus downstream of mount kilauea. *Geophysical Research Letters*, 43 (6):2981–2988, 2016. ISSN 1944-8007. doi: 10.1002/2016GL067830. URL http://dx.doi.org/10.1002/2016GL067830. 2016GL067830.

C. A. Marandino, W. J. De Bruyn, S. D. Miller, and E. S. Saltzman. Eddy correlation measurements of the air/sea flux of dimethylsulfide over the north pacific ocean. *Journal of Geophysical Research: Atmospheres*, 112(D3):n/a–n/a, feb 2007. ISSN 2156-2202. doi: 10.1029/2006JD007293. URL http://dx.doi.org/10.1029/2006JD007293.

N. Mihalopoulos, B. C. Nguyen, J. P. Putaud, and S. Belviso. The oceanic source of carbonyl sulfide (cos). *Atmospheric Environment. Part A. General Topics*, 26(8): 1383–1394, jun 1992. ISSN 0960-1686. doi: 10.1016/0960-1686(92)90123-3. URL http://www.sciencedirect.com/science/article/pii/0960168692901233.

Scott D. Miller, Tihomir S. Hristov, James B. Edson, and Carl A. Friehe. Platform motion effects on measurements of turbulence and air–sea exchange over the open ocean. *Journal of Atmospheric and Oceanic Technology*, 25(9):1683–1694, sep 2008. doi: 10.1175/2008jtecho547.1. URL http://journals.ametsoc.org/doi/abs/10.1175/2008JTECHO547.1.

Philip D. Nightingale, Gill Malin, Cliff S. Law, Andrew J. Watson, Peter S. Liss, Malcolm I. Liddicoat, Jacqueline Boutin, and Robert C. Upstill-Goddard. In situ evaluation of air-sea gas exchange parameterizations using novel conservative and volatile tracers. *Global Biogeochemical Cycles*, 14(1):373–387, mar 2000. ISSN 1944-9224. doi: 10.1029/1999GB900091. URL http://dx.doi.org/10.1029/1999GB900091.

Colin D. O'Dowd, Baerbel Langmann, Saji Varghese, Claire Scannell, Darius Ceburnis, and Maria Cristina Facchini. A combined organic-inorganic sea-spray source function. *Geophysical Research Letters*, 35(1):n/a–n/a, jan 2008. ISSN 1944-8007. doi: 10.1029/2007GL030331. URL http://dx.doi.org/10.1029/2007GL030331.

P. K. Quinn and T. S. Bates. The case against climate regulation via oceanic phytoplankton sulphur emissions. *Nature*, 480(7375):51–56, nov 2011. ISSN 0028-0836. doi: 10.1038/nature10580. URL http://dx.doi.org/10.1038/nature10580.

P. K. Quinn, D. J. Coffman, J. E. Johnson, L. M. Upchurch, and T. S. Bates. Small fraction of marine cloud condensation nuclei made up of sea spray aerosol. *Nature*

Geosci, 10(9):674–679, September 2017. ISSN 1752-0894. URL http://dx.doi.org/10.1038/ngeo3003.

Kevin P. Rhoads, Paul Kelley, Russell R. Dickerson, Thomas P. Carsey, Michael Farmer, Dennis L. Savoie, and Joseph M. Prospero. Composition of the troposphere over the indian ocean during the monsoonal transition. *Journal of Geophysical Research: Atmospheres*, 102(D15):18981–18995, aug 1997. ISSN 2156-2202. doi: 10.1029/97JD01078. URL http://dx.doi.org/10.1029/97JD01078.

Daniel Rosenfeld, Youtong Zheng, Eyal Hashimshoni, Mira L. Pöhlker, Anne Jefferson, Christopher Pöhlker, Xing Yu, Yannian Zhu, Guihua Liu, Zhiguo Yue, Baruch Fischman, Zhanqing Li, David Giguzin, Tom Goren, Paulo Artaxo, Henrique M. J. Barbosa, Ulrich Pöschl, and Meinrat O. Andreae. Satellite retrieval of cloud condensation nuclei concentrations by using clouds as CCN chambers. *Proceedings of the National Academy of Sciences*, 113(21):5828–5834, mar 2016. doi: 10.1073/pnas.1514044113. URL http://www.pnas.org/content/113/21/5828.abstract.

E. S. Saltzman, W. J. De Bruyn, M. J. Lawler, C. A. Marandino, and C. A. McCormick. A chemical ionization mass spectrometer for continuous underway shipboard analysis of dimethylsulfide in near-surface seawater. *Ocean Sci.*, 5(4):537–546, nov 2009. ISSN 1812-0792. doi: 10.5194/os-5-537-2009. URL http://www.ocean-sci.net/5/537/2009/.

Friedrich A. Schott, Shang-Ping Xie, and Julian P. McCreary. Indian ocean circulation and climate variability. *Reviews of Geophysics*, 47(1):n/a–n/a, jan 2009. ISSN 1944-9208. doi: 10.1029/2007RG000245. URL http://dx.doi.org/10.1029/2007RG000245.

D. Smythe-Wright, S. M. Boswell, C. H. Lucas, A. L. New, and M. S. Varney. Halocarbon and dimethyl sulphide studies around the mascarene plateau. *Philosophical Transactions of the Royal Society A: Mathematical, Physical and Engineering Sciences*, 363(1826):169–185, jan 2005. doi: 10.1098/rsta.2004.1485.

A. Stohl, C. Forster, A. Frank, P. Seibert, and G. Wotawa. Technical note: The lagrangian particle dispersion model flexpart version 6.2. *Atmos. Chem. Phys.*, 5 (9):2461–2474, sep 2005. ISSN 1680-7324. doi: 10.5194/acp-5-2461-2005. URL http://www.atmos-chem-phys.net/5/2461/2005/.

Andreas Stohl and David J. Thomson. A density correction for lagrangian particle dispersion models. *Boundary-Layer Meteorology*, 90(1):155–167, 1999. ISSN 1573-1472. doi: 10.1023/a:1001741110696. URL http://dx.doi.org/10.1023/A:1001741110696.

S. M. Vallina, R. Simo, and S. Gasso. What controls ccn seasonality in the southern ocean? a statistical analysis based on satellite-derived chlorophyll and ccn and model-estimated oh radical and rainfall. *Global Biogeochemical Cycles*, 20(1):n/a–n/a, mar

2006. ISSN 1944-9224. doi: 10.1029/2005GB002597. URL http://dx.doi.org/10.1029/2005GB002597.

Bangsheng Yin and Qilong Min. Climatology of aerosol optical properties at acrf sites in the tropical warm pool region. *Journal of Geophysical Research: Atmospheres*, 118(6):2620–2628, 2013. ISSN 2169-8996. doi: 10.1002/jgrd.50234. URL http://dx.doi.org/10.1002/jgrd.50234.

James A. Yoder, Charles R. McClain, Gene C. Feldman, and Wayne E. Esaias. Annual cycles of phytoplankton chlorophyll concentrations in the global ocean: A satellite view. *Global Biogeochemical Cycles*, 7(1):181–193, mar 1993. ISSN 1944-9224. doi: 10.1029/93GB02358. URL http://dx.doi.org/10.1029/93GB02358.

T. Yuan, L. A. Remer, and H. Yu. Microphysical, macrophysical and radiative signatures of volcanic aerosols in trade wind cumulus observed by the a-train. *Atmospheric Chemistry and Physics*, 11(14):7119–7132, 2011. doi: 10.5194/acp-11-7119-2011. URL http://www.atmos-chem-phys.net/11/7119/2011/.

CHAPTER 4

Bubble mediated gas transfer and gas transfer limitation of DMS and CO_2

4.1 Abstract

Direct flux measurements using eddy covariance have shown a limitation of gas transfer at high wind speed. Processes, such as wave-wind interaction and sea spray generation, have been postulated to cause this limitation. Until now no process has been pinpointed to cause this gas transfer limitation. We measured dimethyl sulfide and carbon dioxide eddy covariance fluxes during the Asian summer monsoon in the western tropical Indian Ocean (July and August 2014). Both fluxes and their respective gas transfer velocities show signs of a gas transfer limitation above 10 m s^{-1}. Using wind-wave interactions we describe a flow separation process that could be responsible for a limitation of gas transfer. As a result we provide a Reynolds number based parameterization, which states the likelihood of a gas transfer limitation, for this cruise and previously published gas transfer data. Additionally, we compute the difference in the gas transfer velocities of DMS and CO_2 to estimate the bubble mediated gas transfer using a hybrid model and three bubble parameterizations.

4.2 Introduction

Gas flux F across the air-sea interface is commonly described as the product of the concentration difference ΔC across the interface and the gas transfer velocity k (Equation 4.1).

$$F = k \cdot \Delta C = k \cdot \left(\frac{C_{air}}{H} - C_{water} \right) \tag{4.1}$$

The concentration difference represents the gas displacement from equilibrium and acts as the driving force of gas exchange. The Henry's law constant H represents gas solubility, which depends on salinity and temperature, and allows the conversion between the gas and the liquid phase. Typically, ΔC is computed from the concentration measurements from 10 m in the atmosphere and 5 m depth in the ocean. It is an approximation to the concentration difference directly at the interface. The gas transfer velocity k can be seen as conductance of gas exchange. A main challenge for the gas exchange community is to find a model or parameterization for k that would be suitable for all gases across a wide range of solubilities and environmental conditions. There are three ways to describe k: [1] Mechanistically, which models the gas transfer based on fundamental boundary layer physics; [2] Empirically, which fits a parameter (wind-speed, friction velocity,...) dependent function through directly derived k values; [3] As a hybrid, which is a mechanistic model applied to and fed by directly derived k values. A mechanistic model is universal, but may not describe all important processes influencing gas transfer, as there may be unknown mechanisms at work. Empirical models capture all gas transfer processes, as they are based on measured field data, but most likely lack universality, as the measurement is performed at a specific time and place. In this study, we concentrate on the hybrid model description of k as this provides the best opportunity to combine in situ measured data and the physical laws governing them.
Direct flux measurements, such as eddy covariance, provide an in situ value for the air-sea gas transfer F_{direct}. F_{direct} can be used to estimate the total gas transfer velocity k_{total}, when the concentration difference is known, by rearranging Equation 4.1 to result in Equation 4.2.

$$k_{total} = \frac{F_{direct}}{\Delta C} \tag{4.2}$$

$$\frac{1}{k_{total}} = \frac{1}{k_{water}} + \frac{1}{k_{air}} \tag{4.3}$$

The resulting k_{total} is a combination of the water-side transfer velocity k_{water} and the air-side transfer velocity k_{air} (Equation 4.3). Either one can be, if significantly low, the limiting factor in gas transfer. Using multiple gases with different solubilites one can quantify the different contributions of k_{water} and k_{air} to the total gas transfer k_{total}. We use direct eddy covariance measurements of carbon dioxide (CO_2) and dimethylsulfide (DMS) to estimate both contributions to the gas transfer. For sparingly soluble gases like CO_2, the transfer is controlled by k_{water}. For more soluble gases like DMS, both terms must be included in the calculation. On a molecular level k_{water} is also dependent on the viscosity ν of the sea water and the diffusivity D of the gas through seawater, which is represented by the Schmidt number (Equation 4.4). To make gas transfer velocities of various gases comparable, Schmidt number (Sc) scaling was introduced, Equation 4.5.

$$Sc = \frac{\nu}{D} \tag{4.4}$$

$$\frac{k_{water,Sc}}{k_{water,660}} = \left(\frac{Sc}{660}\right)^n \tag{4.5}$$

The exponent n depends on the surface properties of the water and ranges from $-\frac{2}{3}$ for smooth surfaces to $-\frac{1}{2}$ for rough wavy surfaces [Komori et al., 2011]. For this study, we set $n = -\frac{1}{2}$ and the reference Schmidt number is Sc=660. Hereinafter, presented results of gas transfer velocities k correspond to the Schmidt number Sc=660 (otherwise indicated as Sc=xx), which is the Schmidt number of CO_2 in seawater at 20^oC and commonly used as reference point in gas transfer studies.
The most widely used parameterizations for k_{water} are dependent on wind speed e.g. Nightingale et al. [2000], Sweeney et al. [2007], Ho et al. [2006], Wanninkhof et al. [2009]. Generally, according to Wanninkhof et al. [2009], parameterizations are described by a 3rd degree polynomial, Equation 4.6, in u_{10} (10 m neutral wind speed) based on the dominant role of wind forcing and standard theories of turbulent transfer across the air-sea interface.

$$k_{water} = p_0 + p_1 \cdot u_{10} + p_2 \cdot u_{10}^2 + p_3 \cdot u_{10}^3 \tag{4.6}$$

In Equation 4.6, one or more coefficients (p_0, p_1, p_2, p_3) may be set to zero. However, eddy covariance measurements have pointed to discrepancies between empirically derived k values and those predicted using wind speed parameterizations. There are various hypotheses used to explain these discrepancies. One major example is the solubility dependence of gas transfer. Bubble mediated gas transfer, which is strongly solubility dependent and important at high wind speed, prevents a universal k vs wind speed relationship for all gases across a wide wind speed range. Many parameterizations do not perform well at high wind speed, when bubble-mediated exchange becomes more important through white cap formation, wave braking and bubble formation. Hybrid models have been developed to to tackle this discrepancy at high wind speed. Woolf [1997] presents a hybrid model in which the water gas transfer velocity k_{water} has two components: [1] k_o, the interfacial gas transfer which describes the molecular diffusion through the unbroken surface, and [2] k_b, the bubble mediated gas transfer, as described in Equation 4.7.

$$k_{water} = k_o + k_b \tag{4.7}$$

These hybrid models are based on actual measurements (empirical) of k_o and a model of bubble mediated gas transfer, for example Woolf [1997], Goddijn-Murphy et al. [2016]. Direct gas transfer k_o scaled to a common Sc, using Equation 4.5, should be similar for different gases and for the same gas under different physical conditions, but k_b is expected to depend on the solubility of the gas in seawater (k_b increases with decreasing solubility of the gas). Equation 4.5 is therefore not strictly applicable to insoluble gases, but is commonly applied in existing empirical parameterizations of k_{water}. k_o can be determined by measuring a more soluble gas, such as DMS, since DMS is not influenced greatly by bubble mediated transfer. CO_2, on the other hand, is influenced by the bubble mediated gas transfer k_b and, therefore, the difference between the CO_2 and DMS k_{water} values can be used to estimate the bubble mediated gas transfer velocity [Bell et al., 2017a].
In contrast to the gas transfer enhancing bubble effect, three studies [Bell et al., 2013, 2015, Yang et al., 2016] have indicated a limitation of gas transfer velocity at high wind speed, which has been referred to as 'rollover'. This is an exceptional phenomena, as

most models and theories do not include a process that could lead to such a decrease or flattening of k at high wind speed. Generally there are not many direct flux measurements at wind speed exceeding 12 m s^{-1}. Interestingly, this phenomena has only been published in relation to eddy covariance measurement systems and is not a general feature of high wind gas exchange. Wind-wave interaction has been hypothesized to be the main driver of the rollover phenomenon. Wind-wave interactions, however, have not been the main focus for parameterizing air-sea gas exchange. The challenges associated with this interaction is that the wave field is multi-spectral and is a superposition of wind sea, which is generated by local wind, and swell, which originates in the distance. Only recently, with the occurrence of the rollover phenomenon in eddy covariance data sets, the focus has shifted to towards wave influence. Bell et al. [2013, 2015] suggested that the limited gas transfer is caused by an influence of wind-wave dynamics on the gas-transfer. The wave crest shields the trough from the ambient wind and therefore decreases tangential stress [Reul et al., 1999, Veron et al., 2007, Reul et al., 2008]. Another hypothesis by Yang et al. [2016] suspects an influence of water drops as a result of wave breaking and high winds. Toba et al. [2006], Zhao and Xie [2010] proposed a Reynolds number, Equations 4.8 and 4.9, dependence of the air-sea gas exchange and parameterized the wave interaction, using wind speed u_{10}, friction velocity u_*, significant wave height H_s and the kinematic viscosity of air ν_a. However, Re_{Toba} is only valid for a pure wind-sea case and includes a mechanism of gas transfer limitation, but only explains a subset of cases leading to gas transfer limitation. Re_{Zhao} does not include a rollover mechanism. Furthermore they miss the influence of the sea state on the wind-wave interaction, which is usually expressed as a ratio of wind speed to wave speed and a directional dependance between wind and wave.

$$Re_{Toba} = \frac{u_* \cdot H_s}{\nu_a} \tag{4.8}$$

$$Re_{Zhao} = \frac{u_{10} \cdot H_s}{\nu_a} \tag{4.9}$$

$$Re_{Brumer} = \frac{u_*^2}{\nu_{water} \cdot \omega_p} \tag{4.10}$$

Brumer et al. [2017] use Equations 4.9 and 4.10 to find a more universal parameterization of the gas transfer velocity. Instead of the air kinematic viscosity they use the kinematic viscosity for seawater ν_{water}. They analyze the Knorr11 and SoGasEx cruises, which are discussed in this manuscript, but do not provide a parameterization for the limitation of gas transfer. Still, they include a direct wind-wave interaction using the ratio of friction velocity u_* over wave period ω_p, but this interaction does not have a directional dependance between wind and wave. Hence their approach is suitable to describe the general turbulence characteristics of gas transfer, but is not sufficient to describe gas transfer limitation.

In this study we want to estimate the interfacial gas transfer k_o using the DMS flux data. The difference between DMS and CO_2 flux data gives us an estimate of the bubble mediated gas transfer, which we test against our hybrid model [Goddijn-Murphy et al., 2016]. Both data sets show signs of rollover. We present a mechanism which could

lead to a limitation of gas transfer and a parameterization which describes the state where this mechanism is substantial. Therefore we propose the transformed Reynolds number Re_{tr} to describe the wind-wave interaction and establish a threshold where gas transfer is limited. It is the Reynolds number transformed into the wave's reference system. Through this transformation full vector characteristics of the wind speed as well as the wave's phase speed are taken into account. The state of the wave field is included through the transformation as the transformation depends on the velocity difference of wind and wave.

4.3 Methods and Materials

We performed direct CO_2/DMS flux measurements aboard the RV Sonne sailing from Durban, SA to Port Louis, MU (SO 234-2, 8 July - 20 July 2014) and from Port Louis, MU to Malé, MV (SO 235, 23 July - 8 August 2014). The cruise track is shown in Figure 4.1. Additionally, we recorded bulk air and seawater concentrations of CO_2 and DMS. Basic meteorological observations were done by the ship's automated weather station. We used the NOAA COARE 3.5 algorithm to describe the state of the boundary layer. The wind speed used throughout the text is measured by the ship's meteorological station and then recalculated by stability parameters of COARE to u_{10}, Figure 4.2.

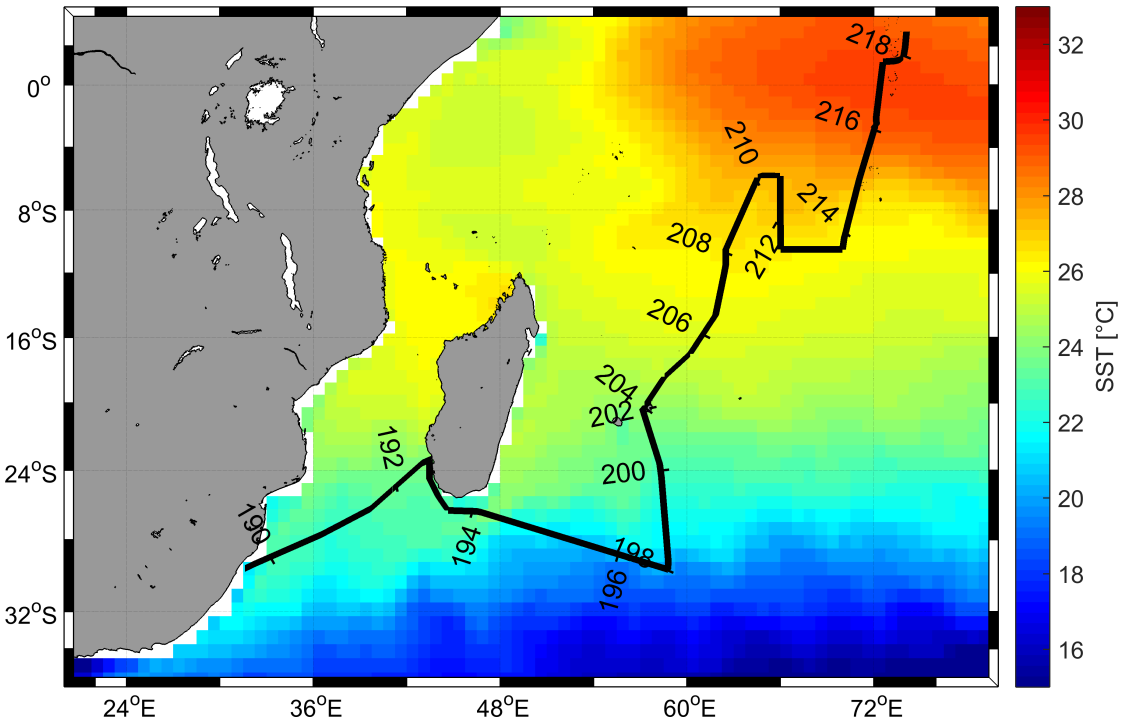

Figure 4.1: Cruise track with day of year (DOY) 2014 indicated. The mean SST, from ERA-interim, for the times of the cruise is color coded in the background.

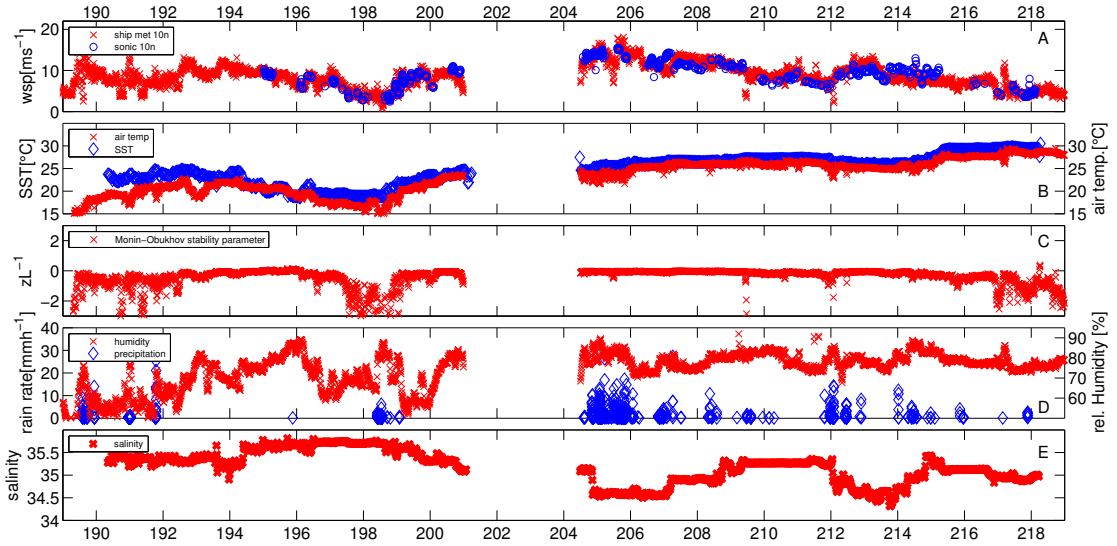

Figure 4.2: Boundary layer and sea surface properties during the cruise. [A] Wind speed measured by the sonic anemometer and wind speed measured by the ship's meteorological station. Both values were corrected using COARE to 10 m neutral wind speed. [B] Air temperature (red) and SST (blue). [C] Monin-Obhukov stability parameter. [D] Relative humidity (red) and rain rate (blue). [E] Salinity.

4.3.1 Eddy covariance

The eddy covariance method measures turbulent scalar fluxes. The flux F is the product of the dry air density ρ, the fluctuation of vertical wind speed w' and the fluctuation of the air concentration c' (Equation 4.11). High sampling rate and high precision measurements of vertical wind speed and air concentration are needed in order to capture turbulent deviations from the mean.

$$F = \rho \cdot c'w' \tag{4.11}$$

Our eddy covariance measurement system aboard the RV Sonne consisted of two parts: [1] The measurement mast at the bow of the ship, which incorporated the sample inlets, the wind measurements and acceleration measurements; [2] The concentration measurements in a lab container, 20 m behind the bow at the forecastle of the ship. We used two ultrasonic anemometers (Campbell CSAT3) which measured the 3-D turbulent wind field in duplicate. They were placed on the port and starboard forward stretching arms of the measurement mast 11 m above sea level. The DMS and CO_2 sampling tubes were connected to the respective DMS and CO_2 air-sample inlet at the port side sonic anemometer. The port side sonic anemometer was used for all data processing. The starboard sonic anemometer served as a backup. The sampling rate of the sonic anemometers was 30 Hz. For eddy covariance calculations, this sampling rate was then reduced by a running mean and nearest interpolation to the respective lower sampling rate of the DMS or CO_2 measurements.

We corrected the wind measurements for ship motion based on Edson et al. [1998], Miller et al. [2010]. We also included the planar fit and flow distortion update by Landwehr et al. [2015]. The required linear-accelerations, angular velocities, ship's course/heading and ship's speed were recorded by an inertial navigation unit (30 Hz, Landmark 10, Gladiator Technologies) and a GPS, 1 Hz sampling rate. Both devices were also mounted on the measurement mast. Additionally, we recorded atmospheric properties and navigational data using the ship's inbuilt sensors at 1 Hz sampling rate. Unless otherwise stated, all data presented were recorded by our eddy covariance measurement system.

DMS eddy covariance measurements

We recorded DMS air concentrations at 5 Hz in the lab container using an atmospheric pressure chemical ionization mass spectrometer (AP-CIMS) similar to those described by Marandino et al. [2007], Saltzman et al. [2009]. The air was sampled from the mast at the bow of the ship (11 m above sea level) and pumped at 50-70 Lmin^{-1} Flow$_{total}$ through a $\frac{1}{2}$"diameter, 25 m long polytetrafluoroethylene (PTFE) tube to the AP-CIMS. The air stream was dried using a Nafion membrane (Perma Pure) prior to analysis. For calibration, we continuously added a deuterated DMS standard (DMS-d3, 2.28 ppm C$_{tank}$) to the inlet at at rate of 2 mL min^{-1} Flow$_{std}$. Using the count ratio of the deuterated DMS Counts$_{66}$ to the natural DMS Counts$_{63}$, the mixing ratio of atmospheric DMS DMS$_{air}$ was calculated as follows:

$$DMS_{air} = \frac{Flow_{std}}{Flow_{total}} \cdot \frac{Counts_{63}}{Counts_{66}} \cdot C_{tank} \tag{4.12}$$

The DMS mixing ratios was recorded approximately every 2 hours for 1 hour. A full mass scan from 10-100 and a delay test was done before and after each measurement period. This delay test determined the time an air parcel takes from the air-sampling inlet to the mass spectrometer using multiple valve on/off switches of the deuterated standard. In total we recorded 130.15 hours of DMS measurements, which fulfilled the relative wind direction criterion of ±90° degrees from the bow and the Landwehr requirement [Landwehr et al., 2015] of steady wind direction.

CO_2 eddy covariance measurements

The CO_2 eddy covariance measurements were made on the same mast and in the same laboratory container as the DMS eddy covariance system. The air sample was collected next to the DMS air intake and pumped at 15 L min^{-1} through a 25 m, 1/2"DECABON tube to the lab container with the CO_2 measurement system. We used a nondispersive infrared measurement system (LI-7200 by Licor) in the setup of Miller et al. [2010] to measure the dry partial pressure of CO_2 in the atmosphere. The data was collected at 10 Hz with two in line LI-7200. We placed a Nafion membrane (Perma Pure) between the two LI-7200 to dry the air stream and to ensure no cross-talk from the water vapor fluctuations. The sample air pressure was measured between the two LI-7200 using a pressure transducer (Mensor CPT6100) and corrected to each Licor's cell pressure using

the internal differential pressure transducer. In this analysis only data from the 2nd (dried air stream) LI-7200 is presented.
We recorded in total 281.7 hours of CO_2 measurements, which fulfilled the relative wind direction criterion of $\pm 90°$ degrees from the bow and the Landwehr requirement (Landwehr et al. [2015]) of steady wind direction. During the cruise we did 18 delay tests to measure the time it takes for the air parcel from the inlet to the CO_2 measurement cavity.

Post processing

We split the DMS and CO_2 records into running intervals (step size 10 min), each 29.6 minutes and merged them with the simultaneously recorded wind and navigation data. As a result we obtained 477 DMS and 942 CO_2 data records and screened them for spikes, malfunctions, high and low frequency anomalies. The determination of the delay was done in two steps. First we set the delay to the value obtained from the delay tests. Then, to increase the delay precision, we cross correlated the recorded wind w' and the respective air concentration c' and set the delay to the maximum positive correlation (flux out of the ocean) or a maximum negative correlation (flux into the ocean). At the right delay time the cospectrum and the cross-correlation graph were screened for anomalies and a decision of pass or rejection was made. Subsequently 435 DMS and 266 CO_2 intervals were corrected for the high frequency loss in the tube. A description of the delay cross-correlation and the high frequency correction is provided in the supplemental materials.

4.3.2 Bulk air and seawater measurements

The DMS seawater concentration was measured using a purge and trap system attached to a GC-MS system (GC/MS; Agilent 7890A/Agilent 5975C) operating in single ion mode. We sampled every 3 h from a constant stream out of the ship's moonpool (5 m depth). The samples were measured within 15 min of collection by purging the gases from the water sample for 15 min, drying the gas stream using potassium carbonate and preconcentrating the gases in a trap cooled with liquid nitrogen. After preconcentration the trap was heated and the gases were injected into the GC. We analyzed in total 162 DMS seawater samples.
We used the average DMS mixing ratios from the eddy covariance system as bulk air DMS mixing ratios. These values were crosschecked with stainless steel air canister samples (25 m sampling height), taken every 3 h at the same time as the DMS seawater samples and analyzed for more than fifty gases, including DMS and isoprene, at the University of Miami.
Oceanic measurements of pCO_2 were carried out using the setup described in Arevalo-Martinez et al. [2013]. Water was drawn on board using a submersible pump installed in the ship's moonpool at approximately 6 m depth and was subsequently conducted at a rate of about 5 L min^{-1} through the Weiss type equilibrator. Sample air from the headspace of the equilibrator was continuously pumped through the instruments and then

back to the equilibration chamber forming a closed loop. The air stream was dried using a refrigerated air dryer and a Nafion dryer before being injected into the analyzer (LI-COR, USA; LI-6252) in order to diminish interferences due to the water vapor content of the sample. The LI-COR analyzer was calibrated regularly using three non-zero standards traceable to WMO scale. Atmospheric air measurements were accomplished by drawing air into the system from an air inlet located at the ships mast at about 30 m height. The intake temperature was measured by a calibrated Seabird thermosalinograph (SBE37), which was installed next to the seawater intake. Due to a broken temperature sensor we had to estimate the temperature in the equilibrator by using the temperature readings of an Aanderaa oxygen optode (model 4330) which was installed in a flow-through box next to the Weiss equilibrator. The optode's temperature was compared to the SBE37 and the difference was less than 0.05°C. The data reduction was done following Pierrot et al. [2009]. The resulting accuracy of the seawater pCO_2 measurements is estimated to be better than 5 µatm.

4.3.3 Hybrid Model

The hybrid model defines water side gas transfer k_{water} (Equation 4.7) as a sum of direct gas transfer through the unbroken water surface k_o and bubble-mediated gas transfer through the broken water surface k_b. In the hybrid model, the enhancement of air-sea exchange of poorly soluble gases is solely attributed to wave breaking and associated bubble-mediated gas transfer via the Woolf [1997] parameterization. Assuming that bubble mediated gas transfer is negligible for DMS, linear regressions between u_{10} and k have been used to estimate k_o [Goddijn-Murphy et al., 2012, 2013]. We calculated k_b using Woolf's model for bubbles with a free and mobile surface, i.e., 'clean' bubbles, and for Woolf's 'independent bubble model', where the bubbles exchange gases with surrounding water independently of each other. In a very dense plume, we may expect the gas content of the interstitial water to change during the lifetime of that plume, making gas transfer sensitive to the void fraction (ratio of air volume to total volume) of the bubble plume. However, Goddijn-Murphy et al. [2016] show with Woolf's dense plume model that for DMS and CO_2 realistic void fractions have no or very small effect on k_b. Woolf's bubble model calculates $k_{b,1\%}$ for a whitecap coverage W of 1%. To calculate the bubble term k_b for any whitecap coverage Equation 4.13 is used.

$$k_b = W \cdot k_{b,1\%} \tag{4.13}$$

An alternative approach to the hybrid model, using Equation 4.13, is an empirical model that relates W to turbulence effects on k_{water} and to bubble-mediated gas transfer [Asher et al., 1996, Asher and Wanninkhof, 1998, Asher et al., 2013]. We estimated W using three common wind speed to W parameterizations proposed by Monahan and Muircheartaigh [1980] (MM), Stramska and Petelski [2003] (SP) for developed seas and Callaghan et al. [2008] (MAP). Finally, combining W and $k_{b,1\%}$ (Equation 4.13) we modeled k_b for DMS and CO_2 using concurrent u_{10}, Sc, sea surface temperature (SST) and salinity data, and scaled k_b to Sc=660 (Equation 4.5). This is not strictly correct because Equation

4.5 applies to direct gas transfer, but Sc scaling enables us to compare k_{water} for DMS and CO_2 and to other known k_{water} parameterizations. Waterside direct gas transfer, normalized to Sc=660, k_o should be the same for DMS and CO_2 so that their k_{water} difference equals their k_b difference. Measurements of total gas transfer velocity of DMS were first corrected for air side gas transfer to estimate k_{water}. Because CO_2 is sparingly soluble, gas transfer is controlled by water side resistance and we did not need to apply the correction for air side gas transfer. We only used measurements of k_{water} between -10 and 80 cm hr^{-1}.

4.3.4 COARE

The NOAA COARE 3.5 algorithm [Edson et al., 2013] is an update from it's first version COARE 2.5 [Fairall et al., 1996a,b] and provides stability parameters and standard meteorological variables of the boundary layer from bulk measurements. We used the ship's meteorological data and COARE 3.5 to calculate relevant boundary layer parameters and u_{10}. Ship's data outages are filled with data from the eddy covariance measurement system.

4.3.5 Wave parameters

We obtained global wave parameters from the Wave Watch III (WWIII) model [Tolman, 1997, 1999, 2009]. It is a multi-spectral third generation wind-wave model run by the Marine Modeling and Analysis Branch (MMAB) of the Environmental Modeling Center (EMC) of the National Center for Environmental Prediction (NCEP). The data set used is the production hindcast with NCEP reanalysis wind and ice fields as input forcing. No wave data is assimilated. The model is run at the end of each month with the available data and provides a global analysis of the ocean's wave field. The temporal resolution is 3 hours and the spatial resolution is 0.5° x 0.5°. We retrieved wind speed forcing u_x u_y, peak wave period T_p, significant wave height H_s and wave direction w_d for the times of the cruise and then linearly interpolated them to the cruise track. Using Equation 4.14 [Hanley et al., 2010], we converted the peak wave period T_p to phase speed c_p, assuming deep water waves.

$$c_p = \frac{g \cdot T_p}{2\pi} \tag{4.14}$$

4.3.6 Reynolds number

The Reynolds number is the ratio of the velocity scale (wind speed u_{10}) multiplied by the length scale (significant wave height H_s) and the kinematic viscosity of air. The kinematic viscosity was calculated using the air density from the COARE model and the dynamic viscosity adapted by Sutherland's law [White, 1991] (Equation 4.15).

$$\mu\,(T) = \mu_0 \cdot \left(\frac{T}{T_0}\right)^{\frac{3}{2}} \tag{4.15}$$

$\mu_0 = 1.716 \cdot 10^{-5}$ N s m^{-2} at T_o=273 K [White, 1991].

4.4 Results

The cruise took place during July and August 2014 during the Asian summer monsoon season (or southwest monsoon). Large scale meteorological features include northeasterly winds south of the Equator and southwesterly winds north of the Equator. The cruise track, displayed in Figure 4.1, spanned a range of oceanic areas, from the Agulhas current, the Antarctic circumpolar current (ACC), the Indian Ocean Gyre, the South Equatorial Current, the Equatorial Countercurrent, and the North Equatorial Current. These areas also provided a range of CO_2 and DMS air-sea gradients. The average oceanic mixed layer depth was 60 m, SST ranged from 19^{o}C to 25^{o}C. The salinity over the cruise track ranged between 34 and 36 and we encountered generally low nutrient levels (below 0.1 µmol L^{-1} for nitrate and below 0.2 µmol L^{-1} for phosphate). Some areas of enhanced nutrient concentrations were observed between 10^o and 5^{o}S. Measured chlorophyll levels were also generally low, 0.05-0.59 µg L^{-1} with a mean of 0.23 µg L^{-1} .

4.4.1 Boundary Layer

Measured wind speed, averaged over 30 min (an eddy covariance interval), was lower than 10 m s^{-1} at the outset of the cruise. The wind speed increased to a maximum of 16 m s^{-1} after leaving Mauritius and gradually declined towards the Maldives. Lower wind speed prevailed closer to the Equator, which is in agreement with the monsoon circulation wind patterns. The SST was slightly higher than the air temperature over most of the cruise track with a mean difference of 1.59°C. The Monin-Obhukov stability parameter, calculated with the COARE algorithm, indicated a neutral stratification ($\frac{z}{l} \approx 0$) over most of the cruise track. From day of year (DOY) 196-200 and after DOY 217, the boundary layer was found to be unstable, which can be attributed to lower wind speed and the SST being higher than the air temperature during these times (Figure 4.2). The average marine boundary layer heights were approximately 0.8 km, relative humidity varied between 50% and 90%, and air temperatures ranged between 14^{o}C and 30^{o}C [Fiehn et al., 2017]. Precipitation was variable over the cruise tracks, which also influenced the boundary layer stability. The basic parameters are shown in Figure 4.2.

4.4.2 DMS

Panel B of Figure 4.3 shows the measured air mixing ratio and the measured water concentration of DMS. During the first leg from DOY 197 to 201 the DMS water concentration was generally low between 0.4-1.0 nmol L^{-1}. The air mixing ratio showed low values as well, from 5.8-69.6 ppt, with a mean of 25.0 ppt. The water concentration and air mixing ratio indicate a high supersaturation of DMS in seawater. Eddy covariance measurements began on DOY 197. The wind speed ranged between 2.9-9.9 m s^{-1} from DOY 197 to 201. The average wind speed was 7.6 m s^{-1}. This average wind speed combined with the low DMS water concentration resulted in generally low fluxes (0.29-4.32 µmol m^{-2} d^{-1}).
After leaving Mauritius (SO 235), we encountered higher DMS water concentrations

of 0.48-3.66 nmol L^{-1}. The air mixing ratio closely followed the water concentration, 19.2-310 ppt with an average of 128.35. We experienced the highest wind speed of 16.3 m s^{-1} at the beginning of the second leg, which then gradually declined towards the Maldives. Wind speed range was 3.7-16.3 m s^{-1}, with an average of 9.7 m s^{-1}. Elevated wind speed together with elevated DMS water concentrations resulted in the DMS flux values between 0.83-32.78 µmol $m^{-2}d^{-1}$. The maximum flux was observed at DOY 207.1 just north of Mauritius. The time series of wind speed, friction velocity, DMS water concentrations, DMS air mixing ratio and DMS flux are shown in Figure 4.3.

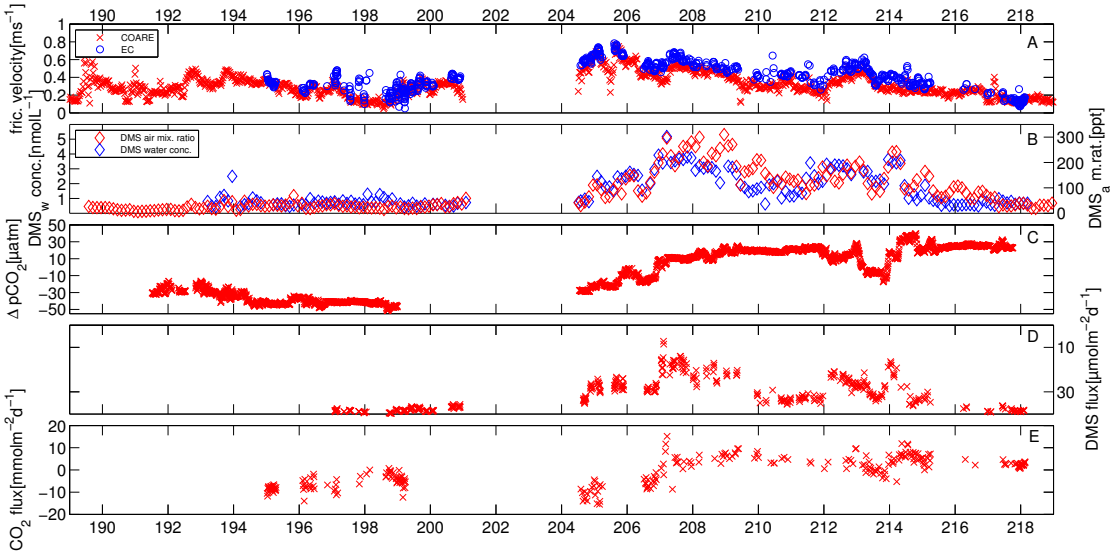

Figure 4.3: Fluxes and concentration gradients. [A] Friction velocity retrieved directly by the eddy covariance (EC) system (blue) and the COARE algorithm (red) using the ship's met station data. [B] DMS water concentration (blue) and air mixing ratio (red). [C] CO_2 partial pressure difference between atmosphere and surface water. [D] DMS flux [E] CO_2 flux.

4.4.3 CO_2

Figures 4.3 (panel C and E) and 4.4 show the pCO_2 difference (ΔpCO_2) between the ocean and the overlying atmosphere and the resulting fluxes. Negative values denote areas where CO_2 is undersaturated in the surface water with respect to the atmosphere and vice versa. Figure 4.4 compares the measured ΔpCO_2 with the climatological values from Takahashi et al. [2009]. Our data are generally in good agreement, but show some fine structured divergence of up to 10 µatm. During the first part of the data set (SO234-2) the observed values are all negative, starting from -20 µatm close to Madagascar and going down to -40 µatm at the southernmost part of the cruise track at around 30°S (between DOY 196 and 198). At this position a surface drifter was deployed for 48 hours. The ship stayed within 2 nautical miles of the drifter measuring surface water pCO_2 in

order to observe diurnal trends by staying in the same water mass. During the drift experiment no diurnal signal could be observed. This corroborates the findings of former studies [Sabine et al., 2000, Bates et al., 2006] that the observed strong undersaturation in the southern Indian Ocean is mostly due to surface water cooling. The minimum values at DOY 196 (beginning of drift experiment) and DOY 198 (end of drift experiment) are due to observed eddies in this area that have different surface properties than the surrounding water. The second part of the cruise track is characterized by higher pCO_2 values. The observed values follow the climatological values most of the time. Between DOY 212 and 214 (4^oS-12^oS), the observations differ significantly from the climatological mean by up to 20 µatm. This area is part of the Central Indian Ridge that comes closest to the Chagos-Laccadive Ridge on the east and the Mascarene Plateau on the west. Both features are close to the ocean surface and can influence the upper ocean [Tomczak and Godfrey, 2006]. The SST drops by 1^oC which indicates intrusion of deeper water masses to the surface. Upwelling of deeper (carbon rich) water masses should lead to an increase in pCO_2. We speculate that the observed decrease of 20 µatm might be due to biological activity in this oligotrophic area. Other evidence for enhanced biological activity was found for DMS (Section 4.4.2), halogens [Fiehn et al., 2017] and isoprene [Booge et al., 2017]. During the rest of the cruise track (DOY 215 and later), slight supersaturation of surface water CO_2 was observed, which is typical for tropical warm water regions.
The CO_2 flux is shown in Figure 4.3 (panel E). During SO234-2, the CO_2 flux was negative most of the time with a minimum of -14 mmol m^{-2} d^{-1} and an average of -6.1 mmol m^{-2} d^{-1}. Although, we measured the highest ΔpCO_2 values during that time, low wind speed led to reduced CO_2 flux. After leaving Mauritius (SO235), the direction of the flux changed twice. This section of the cruise experienced lower ΔpCO_2, but higher wind speeds than earlier. This resulted in average fluxes with magnitudes similar to SO 234-2. The average of all negative values (into the ocean) was -6.4 mmol m^{-2} d^{-1} with a maximum of -15.4 mmol m^{-2} d^{-1}. The positive values (out of the ocean) had an average of 4.6 mmol m^{-2} d^{-1} with a maximum of 15.1 mmol m^{-2} d^{-1}. The low average of the positive flux can be explained by the low wind speed at the end of the cruise.

4.4.4 Gas Transfer Velocity

Figures 4.5 and 4.6 show the gas transfer velocity k_{total} plotted versus wind speed. The water concentrations (DMS) and the air-sea concentration differences (CO_2) are color coded. We averaged the gas transfer velocities into 1 m s^{-1} wind speed bins. The binned data is plotted as a solid line including the standard deviation of each bin as the error bar.
For DMS (Figure 4.5), the binned values are above the plotted Nightingale et al. [2000](N00) parameterization until 10 m s^{-1} wind speed. They exhibit a linear dependence on wind speed until that point. After 10 m s^{-1} a change of slope is evident and most k values lie below N00. As a consequence we fitted linear curves to parts of the binned data set (Figure 4.7). The equations for the linear fits are shown in Table 4.1. The difference in slopes between k and wind speed up to 10 m s^{-1} and beyond 10 m s^{-1} is clear and significant. The slope for the lower wind speed range is approximately three

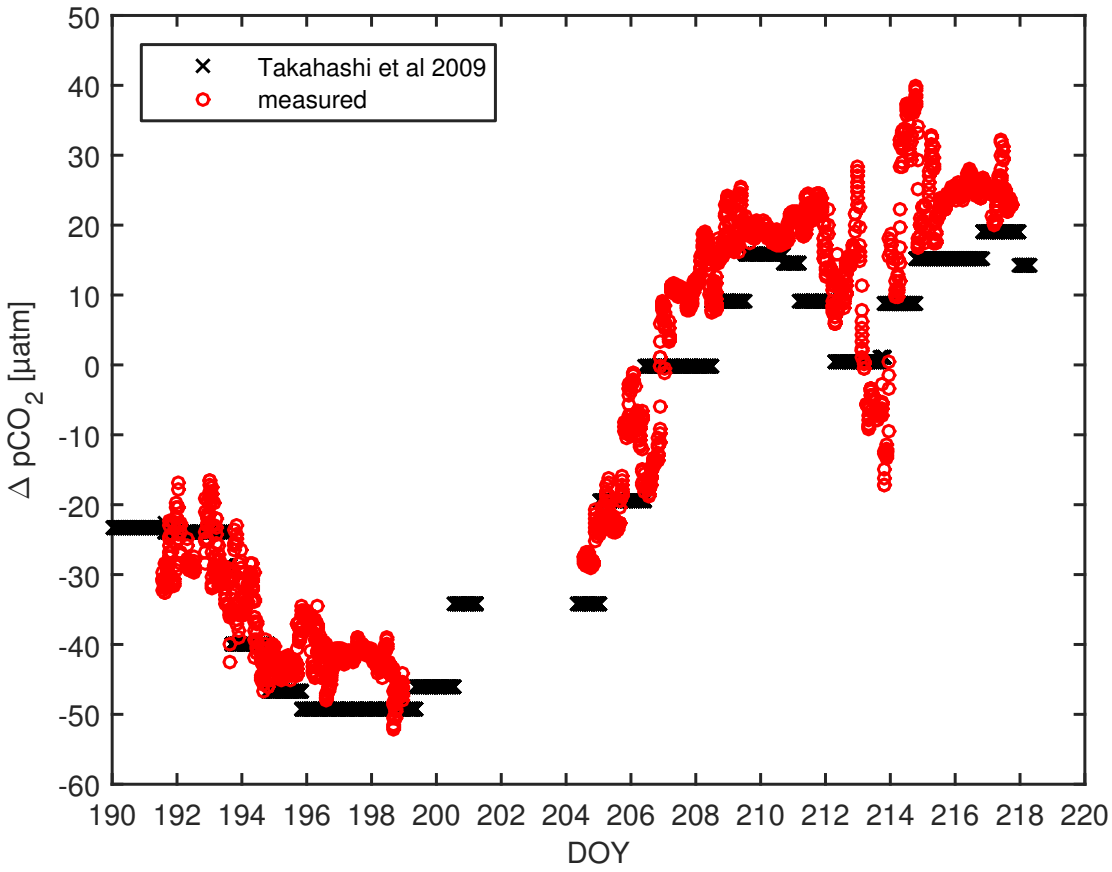

Figure 4.4: Measured air-sea CO_2 partial pressure difference between air and water (red). Negative values denote undersaturation of the ocean with respect to the atmosphere. Climatological partial pressure difference between air and water (black) by Takahashi et al. [2009]

times higher than for the higher wind speed range and the standard deviation of the three highest wind speed bins does not cross the k vs u relationship in the lower wind speed range. The observed change in slope is in agreement with the results from Bell et al. [2013, 2015] showing rollover of k beyond 10 m s^{-1}. The linear fit to all binned data shows average agreement with the whole data set, but can clearly not describe the trend of the two distinct lower (<10 m s^{-1}) and higher (>10 m s^{-1}) wind speed regimes. Interestingly the overall fit is similar to an updated parameterization by Marandino et al. [2009]. She compiled six DMS eddy covariance measurement campaigns and fit a linear k vs. u parameterization. Goddijn-Murphy et al. [2012] also suggests a linear relation between k and u using field data of eight cruises that provided DMS gas transfer velocity measurements. All DMS parameterizations are presented in Table 4.1. Generally it appears that the DMS k values exhibits a linear wind speed dependence and can be used as an estimate of the interfacial gas transfer k_o. However it is apparent that this

Table 4.1: Equations of the linear fits to the DMS k vs wind speed transfer velocity. Marandino et al. [2009] and the top three parameterizations are shown in Figure 4.7. Goddijn-Murphy et al. [2012] is added to this table as a comparison.

fit	k_{660}[cm h^{-1}]
linear fit to all	k_{total}=2·u_{10}+0.94
linear fit <10 m s^{-1}	k_{total}=3.1·u_{10}-5.37
linear fit >10 m s^{-1}	k_{total}=1.13·u_{10}+12
Marandino et al. [2009]	k_{total}=2·u_{10}+1
Goddijn-Murphy et al. [2012]	k_{total}=2.4·u_{10}-5
Goddijn-Murphy et al. [2012]	k_{water}=2.6·u_{10}-5.7

linear relationship breaks down during high wind speed events, causing the perceived rollover. This will be discussed in more detail below.

The gas transfer velocity of CO_2 in Figure 4.6 closely resembles the parameterization N00 until 12 ms^{-1}. Above 12 ms^{-1} the binned gas transfer velocities are below the N00 curve, but tend to return to the parameterization at the highest wind speed bin. We think that this change in k vs. u_{10} functional form points towards the rollover phenomenon, as it should affect the interfacial gas transfer of all gases equally. However, due to the likely enhancement of CO_2 air-sea exchange compared to DMS at high wind speed as a result of the bubble effect (see Section 4.4.6), the rollover is not as prominent for CO_2 as for DMS. Negative values of gas transfer velocity are present at small ΔpCO_2 values. Together with measurement uncertainty, the spatial distance of the flux footprint to the water intake and the averaging period of 30 min, this could cause negative gas transfer velocities.

Figure 4.8 shows binned DMS, fitted with a linear function, and binned CO_2, fitted with a quadratic function, over u_{10}. The two curves begin to separate above 11 m s^{-1}. A similar overlap and coherence of DMS and CO_2 has been previously reported by Miller et al. [2009]. The data of Bell et al. [2017a] show a separation much earlier at around 6 m s^{-1}. They attribute the difference to the bubble mediated gas transfer, which is solubility dependent.

4.4.5 Roll over and Reynolds number

The gas transfer velocities of DMS and CO_2 in Figures 4.5 and 4.6 show signs of limited gas transfer at a wind speed above 10 ms^{-1} and 12 ms^{-1}, respectively. For DMS, this is underlined by the slopes of the linear fits in Table 4.1. Similar findings have been reported previously by Bell et al. [2013, 2015], Yang et al. [2016].

In order to improve the characterization of wind-wave interaction and its influence on gas exchange, we introduce the vector characteristics and the directional dependencies in the calculation of the Reynolds number. The new parameter is the transferred Reynolds number Re_{tr} (Equation 4.16).

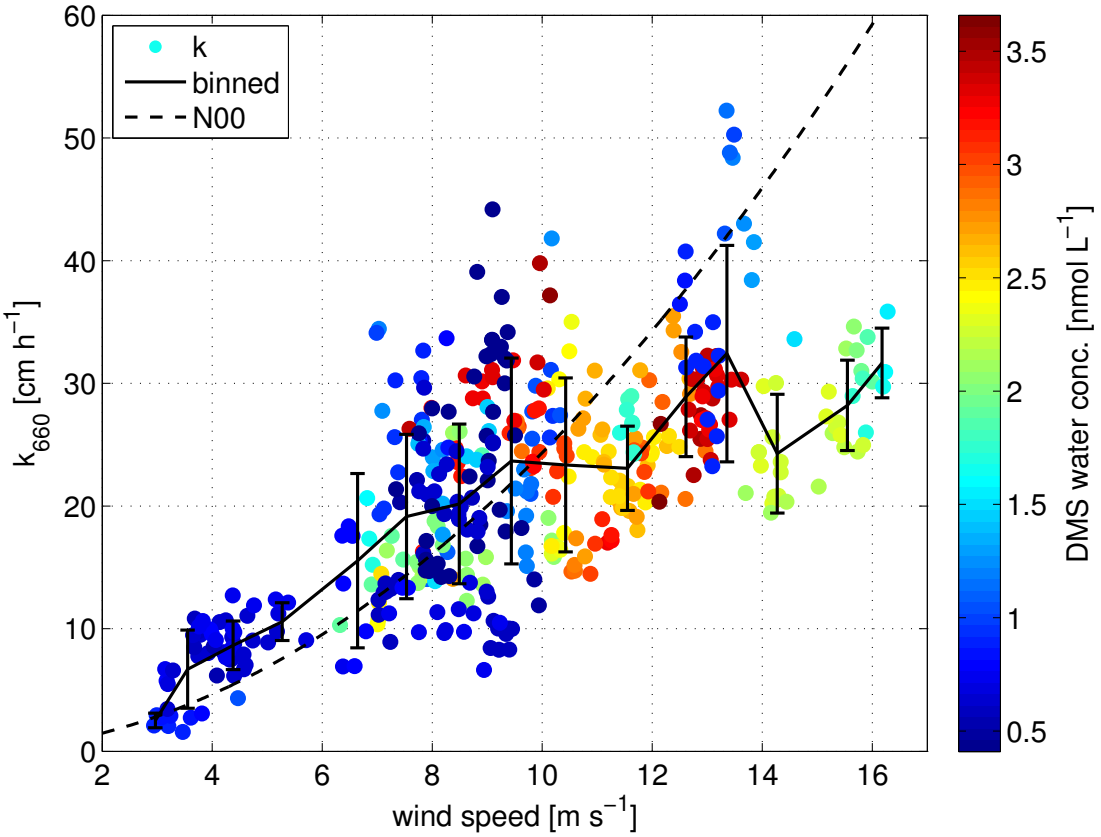

Figure 4.5: DMS gas transfer velocities versus wind speed. The DMS water concentration is color coded and the binned gas transfer velocity is plotted as a solid line. The dashed line is the Nightingale et al. [2000] parameterization as reference. Error bars denote the standard deviation of the gas transfer velocities within the bin.

It is possible to deduce properties of the rollover, given the circumstances of this phenomenon and the fact that, so far, the rollover has only been seen in data retrieved from eddy covariance measurements: The rollover is [1] a feature of high wind speed, but not universally present above a certain wind speed [2] a result of a mesoscale process [3] a completely new process and possibly linked to wind-wave interaction. We also point out that eddy covariance is so far the only technique that is measuring transfer velocities of relatively soluble gases. For these gases the interfacial gas exchange k_o is dominant. Measurements of k using the dual tracer technique, however, use insoluble gases, for which k_b become more important. If the mechanism causing the rollover influences k_o, it would be likely that eddy covariance measurements exhibit these characteristics. As stated in the introduction, Bell et al. [2013, 2015] suspect a possible screening of wind speed by high waves or swell, which would agree with all of the deduced properties. Indeed studies [Kawai, 1982, Veron et al., 2007] have discussed and shown a flow separation between the wind above the crest and the flow entering the trough. Veron et al. [2007] measured

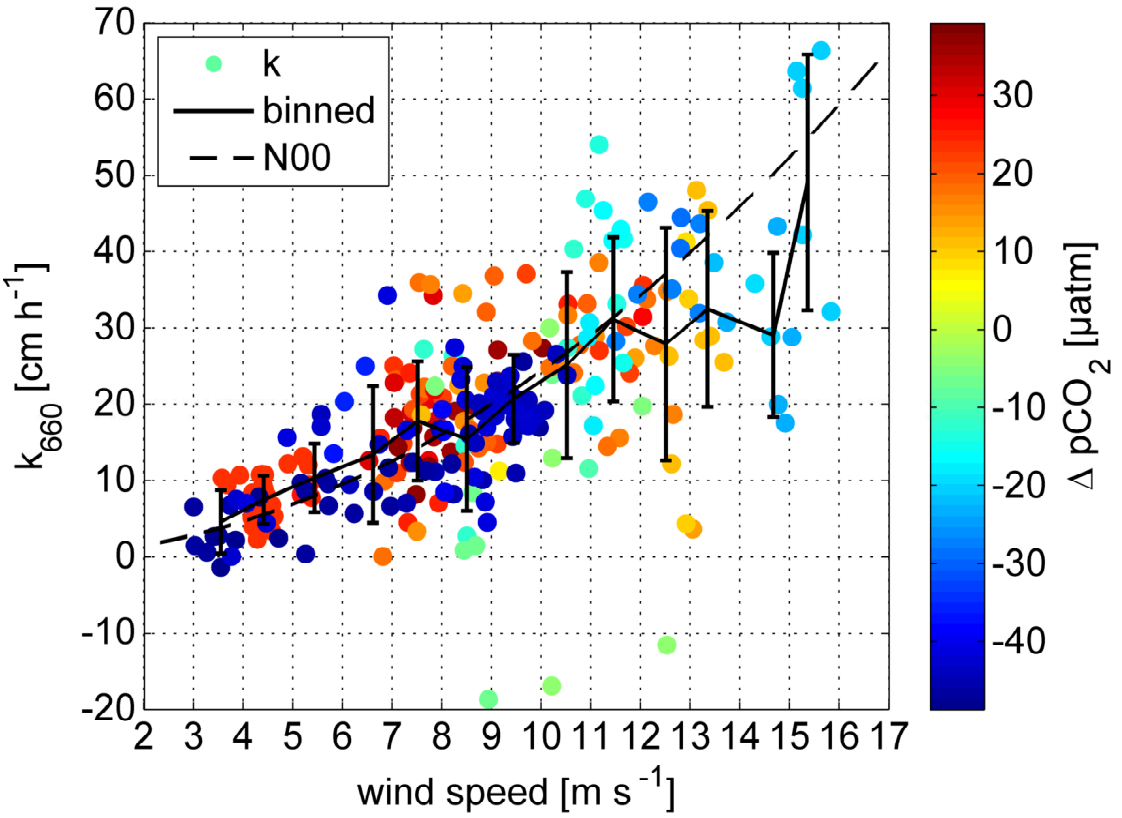

Figure 4.6: CO_2 gas transfer velocities versus wind speed. The CO_2 partial pressure difference is color coded and the binned gas transfer velocity is plotted as a solid line. The dashed line is the Nightingale et al. [2000] parameterization for reference. Error bars denote the standard deviation of the gas transfer velocities within the bin.

flow separation at even low wind speed and found a drop in wind speed and tangential stress in the flow separation regime. Furthermore, Yang and Shen [2017] provide a direct numerical simulation of wind-wave interaction at three different wave age cases. Through quadrant analysis they simulate the influence of waves and wave age on turbulence and, hence, on the scalar transport. Yet they provide neither a positive nor a negative overall correlation of wave age and scalar transport. They state two main weaknesses of their simulation: [1] The use of single frequency waves in their simulation. In the real world, open ocean waves and swell have a broad frequency spectrum; [2] Wind direction and wave direction are always perfectly aligned in their simulation, which is not true for the real world case.

$$Re_{tr} = \frac{u_{tr} \cdot H_s}{\nu} \cdot cos\,(\theta) \tag{4.16}$$

u_{tr} is the wind speed in the wave's reference system. The length scale is the significant wave height H_s. The angle θ describes the directional dependency and is the angle

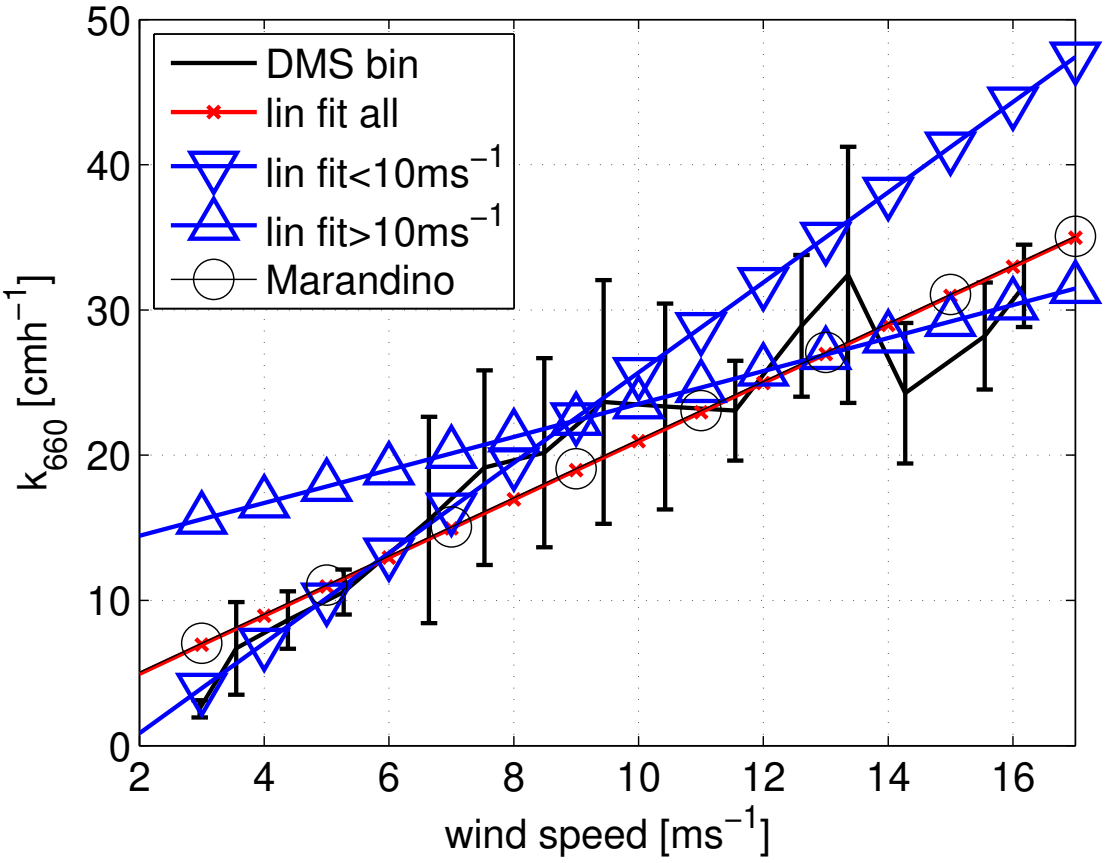

Figure 4.7: Binned (size 1 ms^{-1}) DMS gas transfer velocities and linear fits of the binned data below 10 m s^{-1} and above 10 ms^{-1}. An overall fit and the linear parameterization, updated from Marandino et al. [2009], is added.

between the wind direction and the wave direction in the wave's system. Until now parameterizations (e.g. for Reynolds number or wave age) used absolute quantities, but our parameterization has the advantage that both wind and wave velocities are treated as vectors at the transformation. We use a Galilean transformation to move the Reynolds number and the wind-wave interaction into the wave's reference frame and treat the interaction as flow around an object. The Navier-Stokes equation is invariant under this transformation. A detailed description of the transformation is available in the supplemental material.

We conceptualize air flow above waves to flow around a cylinder [Shapiro, 1961, Mathieu, 2000]. This standard model can be used as an analogy for our wind-wave interaction scheme. At low Reynolds numbers $Re_{tr} < 10^2$, a Stokes flow establishes with respect to the wave's phase speed. With increasing relative velocity and Reynolds number $10^2 < Re_{tr} < 10^4$, a laminar boundary layer flow is established with a separation point at the leeward face. At this separation point the flow is detached from the sea surface

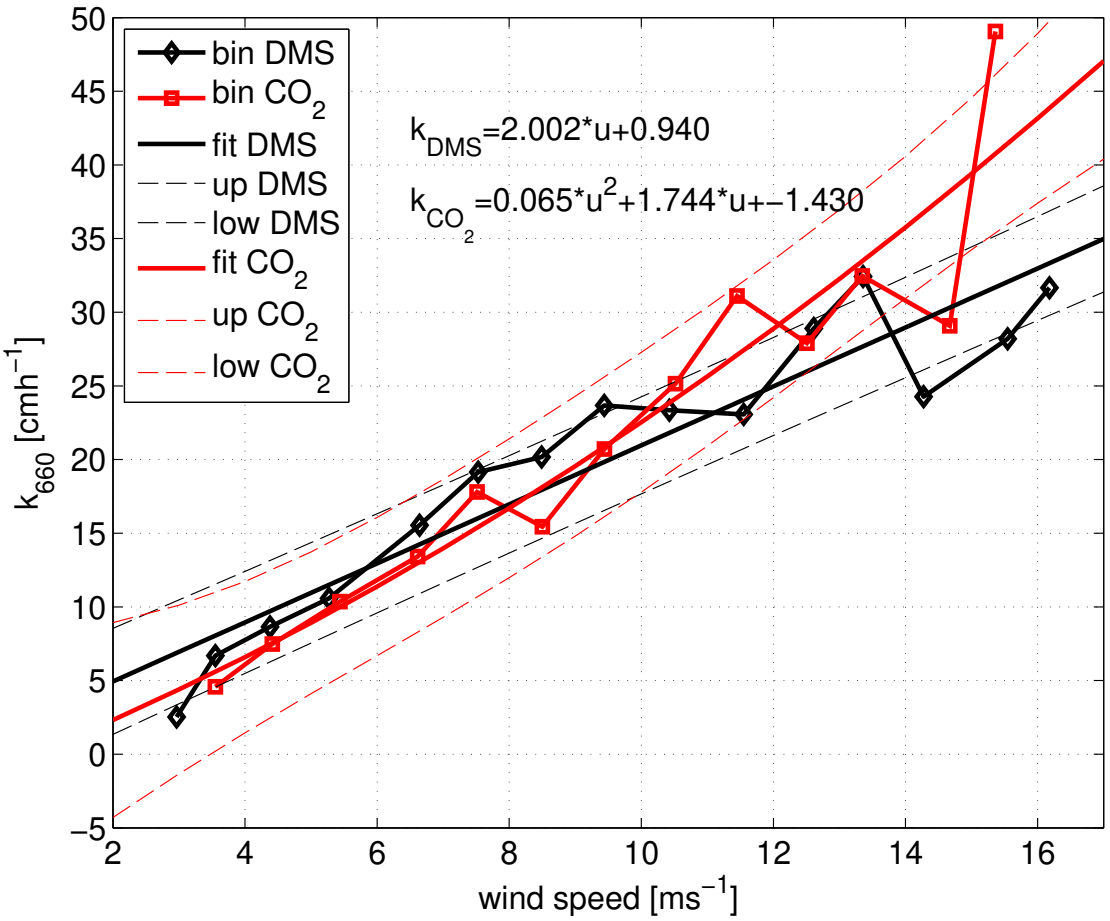

Figure 4.8: Binned gas transfer velocities of DMS and CO_2 (solid line with markers) vs wind speed. The DMS gas transfer velocity is fitted with a linear relationship (black solid line), the CO_2 transfer velocity is fitted with a quadratic relationship (red solid line). The dashed lines represent the area of 50% fit probability.

and forms a vortex and, subsequently, a van Karman vortex street behind the wave. At $Re_{tr} > 10^5$, the separation point moves further leewards and decreases the area of flow separation, until the boundary flow turns fully turbulent $Re_{tr} \approx 10^5$ and the flow separation is extinguished. We hypothesize that a detached flow regime above the wave limits gas transfer. At higher Reynolds numbers, when the turbulent boundary layer is again completely attached to the surface, the gas transfer follows the generally accepted wind speed gas transfer relationships. We include the horizontal angle of attack by introducing the angle θ, relative to the wave's direction into the equation. It is the angular difference between the wave direction and the wind direction in the wave's reference system. Wind flowing at $\theta = 90^o$, for example, does not experience a wave crest or trough, but a corrugated surface. The significant wave height, in this case, is

reduced to zero, because $cos\,(90^o) = 0$. For all angular values in between $0 < \theta < \pm 180^o$, the significant wave height turns into an effective wave height by the factor of $cos(\theta)$. Angles lower than 90^o specify a wind direction unidirectional to the wave direction, angles greater than 90^o specify a counter-direction between wind and wave direction. We do not expect a dependence of gas transfer on the sign of Re_{tr} and, in fact, do not see this dependence in the data. Therefore the absolute value of Re_{tr} is used.
The gas exchange limiting threshold value for Re_{tr} is empirically set to $6.7{\cdot}10^5$. It was determined from the gas transfer velocities of the SO234-2/235 cruises and lies in the predicted range, where the flow separation is destroyed by the increasing turbulent boundary layer flow. The separation of the gas transfer velocity for the SO234-2/235 cruises in a gas limiting $|Re_{tr}| < 6.7 \cdot 10^5$ and a non-limiting $|Re_{tr}| > 6.7 \cdot 10^5$ regime is shown in Figure 4.9 for DMS and Figure 4.10 for CO_2. It is apparent that the gas transfer velocities of the limited regime are significantly below the linear fit for DMS and the N00 parameterization for CO_2. We associate the return of the CO_2 gas transfer velocity above 15 m s^{-1} with the incipient bubble effect, which might compensate for the gas limitation effect. The four exceptionally high data points around 13 m s^{-1} in the limiting case for DMS (Figure 4.9, left panel) are associated with low DMS water concentrations, where scatter in the measurement is enhanced. The very low gas transfer velocities between 12 and 15 m s^{-1} are close to the gas transfer limiting threshold. It is also notable that for DMS and CO_2 an overlap, with respect to wind speed, of limited and non-limited gas transfer velocities is present (Figures 4.9 and 4.10). This means our parameterization Re_{tr} is not a function of wind speed only, but describes the wind-wave interaction.
Figure 4.11 (right panel) shows wind speed vs a global probability density for the year 2014 of Re_{tr}. The data has been retrieved from the WWIII model. The left panel shows the ratio of instances of gas limitation (below the threshold) and the total number of data points over wind speed. The ratio is described in Equation 4.17.

$$r = \frac{\sum \prec 6.7e5}{\sum \prec 6.7e5 + \sum \succ 6.7e5} \tag{4.17}$$

A white line is drawn along the threshold of $+6.7 \cdot 10^5$ and a dashed line along $-6.7 \cdot 10^5$. The area of limited gas transfer is between the dashed and solid white line, as there should be no directional dependency. Globally, in 2014, 19% of all data points are within the gas transfer limiting regime. Between the wind speed of 12 - 17 ms^{-1} close to 30% of all data points would be in a gas transfer limiting regime. This peak plateau supports the occurrence of limited gas transfer at a wind speed above 19 ms^{-1}.
We tested the new Re_{tr} parameterization against previously published data of DMS eddy covariance direct flux measurements (SoGasEx [Yang et al., 2011], Knorr11 [Bell et al., 2013], SOAP [Bell et al., 2015] and this data set). We should be able to calculate the transformed Reynolds number Re_{tr} for the wind-wave interactions during previous cruises and explain if they were in a gas transfer limiting or a non-limiting gas transfer regime. The Re_{tr} was calculated using wind speed, wind direction and the wave data from WWIII along the previous cruise tracks. As we do not have information about timing for the

published cruise data sets, we cannot match their cruises in exact temporal space as in Figures 4.9 and 4.10. We can statistically determine the number of gas transfer limiting incidents at a certain wind speed at the general time of the cruises. The data of the four cruises (SoGasEx, Knorr11, SOAP and this data set) is shown in Figure 4.12. The left panels show the number of instances above or below the Re_{tr} threshold. The right panels show the ratio as described by Equation 4.17. Additionally the k wind speed relationship of the respective cruise is plotted. At the SoGasEx cruise (top right panel Figure 4.12), no rollover was present. This can be backed up by our Re_{tr} reanalysis. The ratio of limiting to non-limiting instances stays below 0.2 (less than 20% of total instances) for most of the time and increases at a wind speed higher than experienced during that cruise. The ratio of the Knorr11 cruise peaks twice (gray shaded area), around 8 ms^{-1} and between 12-18 m s^{-1}. At the same time the gas transfer velocity flattens and at the second incident even decreases. For SOAP, the gas limitation occurs between 10.5-15 m s^{-1}. The ratio peak at 14 m s^{-1} corresponds with a drop in the gas transfer velocity. The SOAP cruise is a special case, because the whole wind speed range was experienced several times during the cruise. Many instances of high winds without gas transfer limitation occurred, which drives down the ratio. For SO234-2/235, the rollover starts at 9.5 m s^{-1}, which is also coincident with an increase in the ratio. It seems that above the ratio of 0.2 limited gas transfer is highly likely.

4.4.6 Bubble mediated gas transfer

In Figure 4.13, k_b calculations using field data of u_{10}, Sc, SST, and salinity are shown together with directly derived k_{total} values. k_{water} DMS [Goddijn-Murphy et al., 2012], modeled using measured k_{total}, is shown in Figure 4.13 (right panel). k_{water} is on average 1.4 cm h^{-1} higher than total measured k_{total}, because of air side resistance. The bubble component is commonly neglected in DMS gas transfer, but our calculations show a non-negligible contribution for stronger wind speed. At the high end of the range (u_{10} ≈16 m s^{-1}), we estimate k_b to be 6, 11, and 17 cm h^{-1} using W-parameterizations MAP, MM and SP respectively.

For k_{water}, the linear regression slope with u_{10} over the whole range was 2.0±0.2. The slope of k_{water} is similar to the one derived by Marandino et al. [2009] and slightly lower than the one derived by Goddijn-Murphy et al. [2012] (Table 4.1). We subtracted from k_{water} the three k_b estimates and derived k_o, which are 1.6 cm h^{-1} (MAP), 1.3 cm h^{-1} (MM) and 1.0 cm h^{-1} (SP) (Equation 4.7). The flatter slopes of k_o account for the non-negligible contribution of bubble mediated gas transfer. However, these regressions do not account the two distinct wind speed regimes over (gas transfer limitation) and under 10 m s^{-1} (Figure 4.7). Following Wanninkhof et al. [2009], we applied a 3rd degree polynomial fit to k_{water} against u_{10} (Equation 4.6). The fit coefficients are shown in Table 4.2. The negative quadratic terms, in the measured data set, were unexpected and illustrated the rollover experienced at higher wind speed.

The same calculations were repeated for CO_2 (Figure 4.13, left panel), but we did not need to correct for air-side resistance (k_{total} ≈k_{water}) as air-sea gas transfer of CO_2 is dominated by waterside resistance. Because CO_2 is less soluble than DMS, the bubble

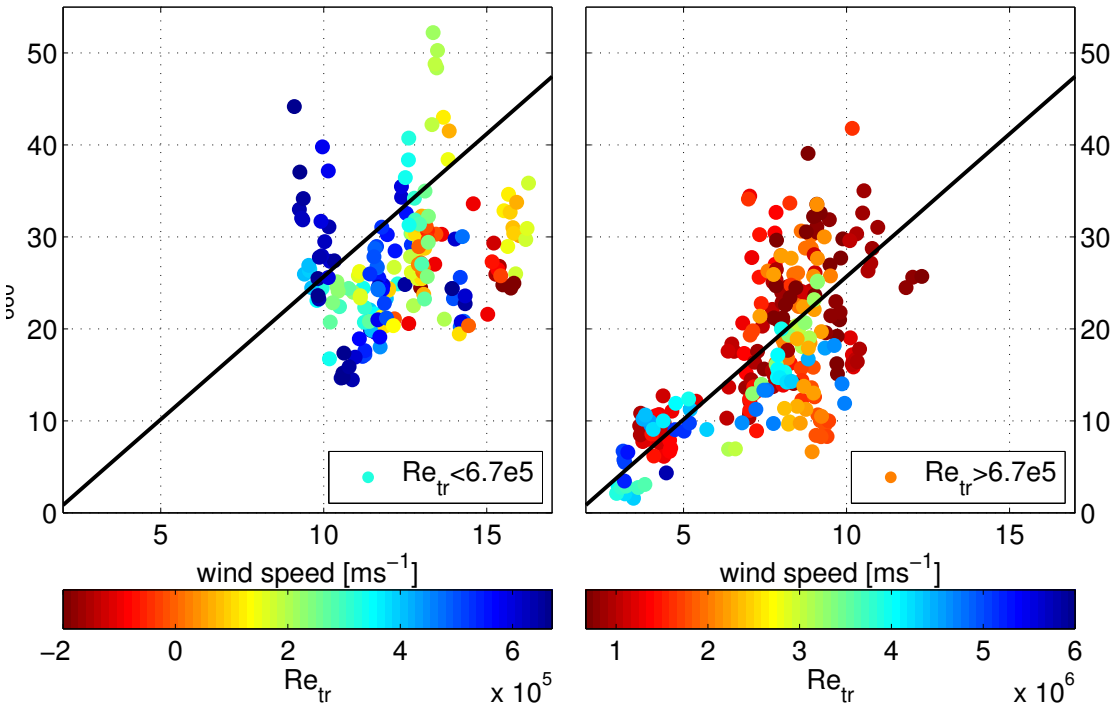

Figure 4.9: Influence of wind-wave interaction on DMS gas transfer. [Left] Limited transfer velocities ($|Re_{tr}| < 6.7 \cdot 10^5$) measured during SO234-2/235. [Right]Non-limited transfer velocities ($|Re_{tr}| > 6.7 \cdot 10^5$). For comparison a linear fit through the non-limited transfer velocities is added to both panels. The color shows the transferred Reynolds number Re_{tr}. The colormap is different for the left and the right panel.

component of gas transfer is expected to be more important (Figure 4.13, left panel). As explained in Section 4.3.3, k_o, scaled to a common Schmidt number, should be the same for DMS and CO_2. So we can use Equation 4.18 to compare measured Δk_{water} to the one published by Bell et al. [2017a].

$$\Delta k_{water} = \Delta k_{total} = (k_{o,CO_2} + k_{b,CO_2}) - (k_{o,DMS} + k_{b,DMS}) = k_{b,CO_2} - k_{b,DMS} \quad (4.18)$$

To verify the hybrid model, by comparing measured Δk_{water} to modeled k_{b,CO_2}, we have to assume that $k_{b,DMS}$ is very small to obtain $\Delta k_{water} \approx k_{b,CO_2}$. We also estimate Δk_{water} using the hybrid model with the three whitecap parameterizations and compare it to Bell et al. [2017a] and our measurements.
Because we did not have enough simultaneous gas transfer measurements for DMS and CO_2, we could not directly regress Δk_{water} against u_{10} as was done by Bell et al. [2017a]. Instead we applied separate fits to DMS and CO_2 data, and subtracted the fit coefficients p_i (Equations 4.19). The error Δd_i was estimated by the hypotenuse of the individual uncertainties of the fit coefficients with 95% confidence bounds (Equation 4.20).

$$p_i = p_{i,CO_2} - p_{i,DMS} \quad (4.19)$$

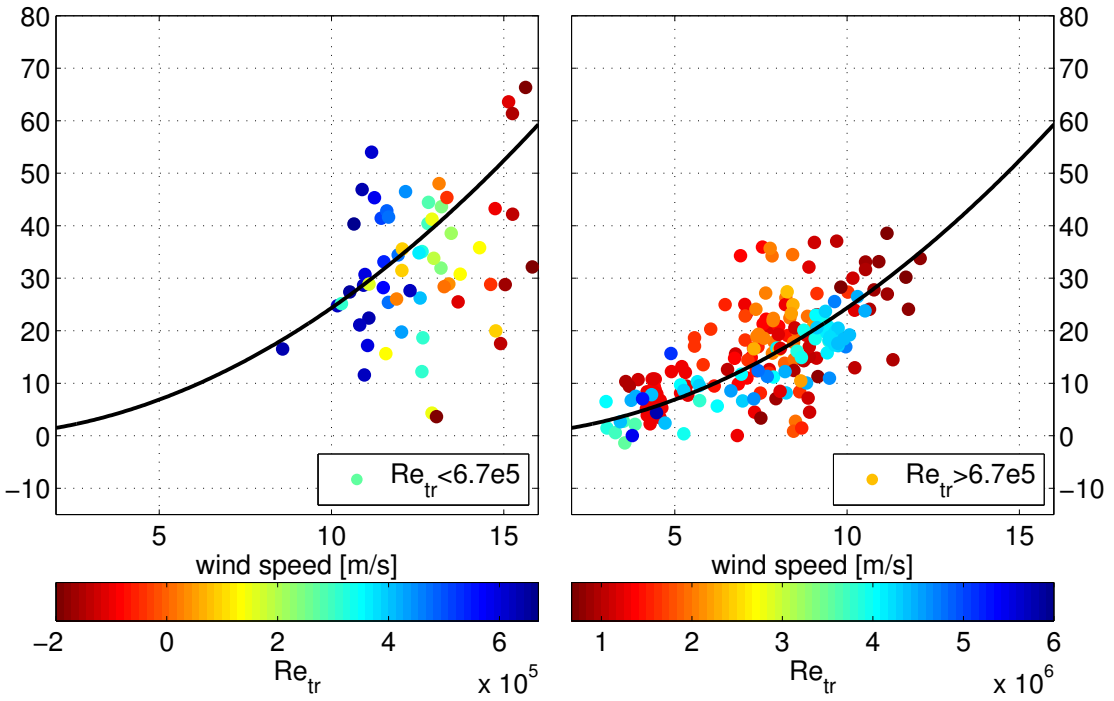

Figure 4.10: Influence of wind-wave interaction on CO_2 gas transfer. [Left] Limited transfer velocities ($|Re_{tr}| < 6.7 \cdot 10^5$) measured during SO234-2/235. [Right] Non-limited transfer velocities ($|Re_{tr}| > 6.7 \cdot 10^5$). For comparison the N00 parameterization is added to both panels. The color shows the transferred Reynolds number Re_{tr}. The colormap is different for the left and the right panel.

$$\Delta d_i = \sqrt{\Delta p^2_{i,CO_2} - \Delta p^2_{i,DMS}} \tag{4.20}$$

In Table 4.2, the fits of measured k_{water} for CO_2 and DMS vs wind speed are shown. We show, in addition, the fits of Δk_{water} from the measurements, those derived by Bell et al. [2017a], and the k_{b,CO_2} vs wind speed fits derived from the hybrid model. The hybrid results from the three different W parameterizations were fit with a 3rd degree polynomial. All coefficients are presented with error estimates (Table 4.2). The fit from Bell et al. [2017a] was taken from the discussion version of their manuscript [Bell et al., 2017b].

Our measured Δk_{water} are in general agreement with those from Bell et al. [2017a]. We observe a constant offset of our functional form and the one from Bell et al. [2017a]. However, the uncertainties, especially in the constant and the linear coefficient, are large. We also recognize, as seen in Figure 4.8, that the CO_2 transfer velocities between 6-10 m s^{-1} are higher than those for DMS. This provides the reason for the negative linear coefficient. Looking at the quadratic coefficient, which is most important at higher wind speed, the coefficients of Bell et al. [2017a] and this study agree. Calculated k_{b,CO_2} from the MAP whitecap model seems to have a similar functional form with regard to our

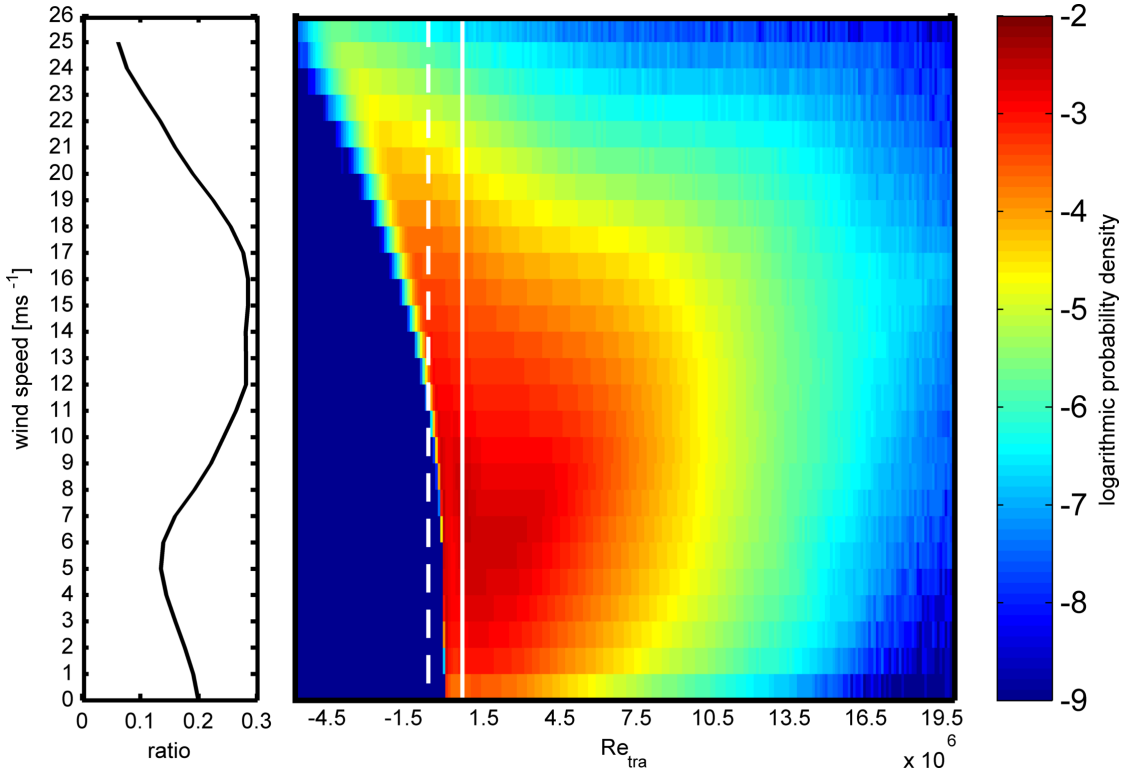

Figure 4.11: We used the global 2014 WWIII data to calculate the transformed Reynolds number. [Right] The global 2014 probability density for the Re_{tr} parameter with respect to wind speed. The limited gas transfer regime is between the dashed and solid white lines. [Left] The ratio of non-limiting (outside the white lines) to limiting (between the white lines) incidents over wind speed.

findings and Bell et al. [2017a] (Figure 4.14). Again an offset is evident. We subtracted modeled $k_{b,DMS}$ from the modeled k_{b,CO_2} to get Δk_{water} (dashed lines in Figure 4.14). This reduces the offset compared to our measurements, but increases the offset to the measurements of Bell et al. [2017a]. Models MM and SP (Figure 4.14) show different trends and overestimate the measured bubble mediated gas transfer at high wind speed. Our DMS gas transfer velocities overlap with those from CO_2 until 11 m s^{-1} (Figure 4.8). In the range from 6-10 m s^{-1} the binned gas transfer velocities for DMS are higher than for CO_2. This overlap is not considered by models describing bubble mediated gas transfer and may cause the discrepancies between our coefficients and those from the models. This is evident in the negative linear coefficient p_1 of the measured Δk_{water} in Table 4.2. The quadratic coefficient p_2 is again positive, as this coefficient is relevant at higher wind speed, when CO_2 is strongly influenced by bubble mediated gas transfer. An overlap of CO_2 and DMS transfer velocities up to 8 m s^{-1} is also reported by Miller et al. [2009], who suggest the influence of solubility on the bubble mediated gas transfer as a reason. The data set of Bell et al. [2017a] shows a clear separation of CO_2 and DMS

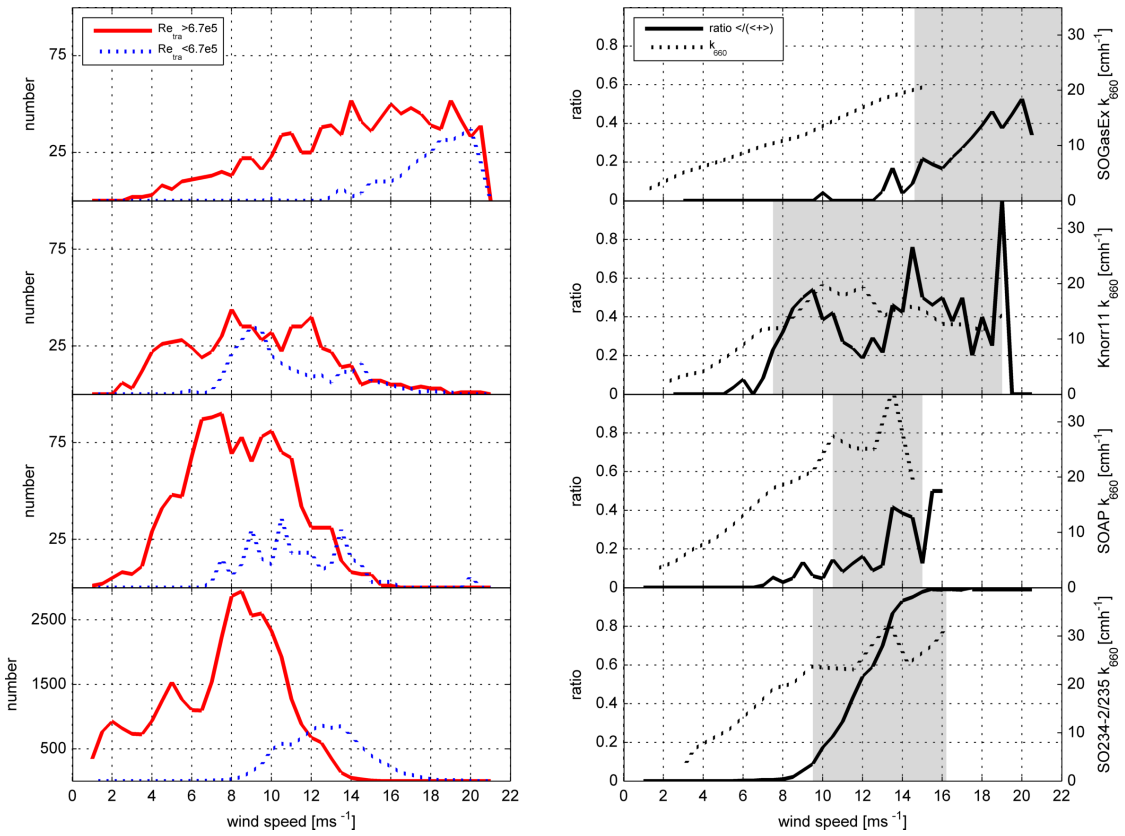

Figure 4.12: A statistical analysis of rollover for three previously published cruises and this dataset on which eddy covariance fluxes and gas transfer velocities were measured. The left panel shows the absolute numbers of limiting (dashed) and non-limiting (solid) occurrences, the right panel shows the ratio (solid) of limiting occurrences to the total occurrences. The gas transfer velocity measured at these cruises is shown in the right panel as a dashed line. The grey areas denote the occurrence of gas transfer limitation. The data sets are SoGasEx [Yang et al., 2011], Knorr11 [Bell et al., 2013], SOAP [Bell et al., 2015] and this data set (SO 234-2/235).

gas transfer velocities at 6 m s^{-1}. To show similarities and differences between the three data sets, we compiled the environmental conditions of these cruises in Table 4.3. Bell et al. [2017a] experienced the lowest temperatures and, therefore, the highest solubility of CO_2 in seawater, but also the difference in flux magnitude stands out. This study and Miller et al. [2009] share the same magnitude of fluxes in and out of the sea surface. The flux magnitudes reported by Bell et al. [2017a] are two times higher larger and only going into the sea surface. From this comparison we suggest an unaccounted for influence of solubility or the flux magnitude on the bubble mediated gas transfer. The effect of solubility is already taken into account in models for k_b, but could be underestimated. The influence of flux magnitude is just a hypothesis and can not be explained by an

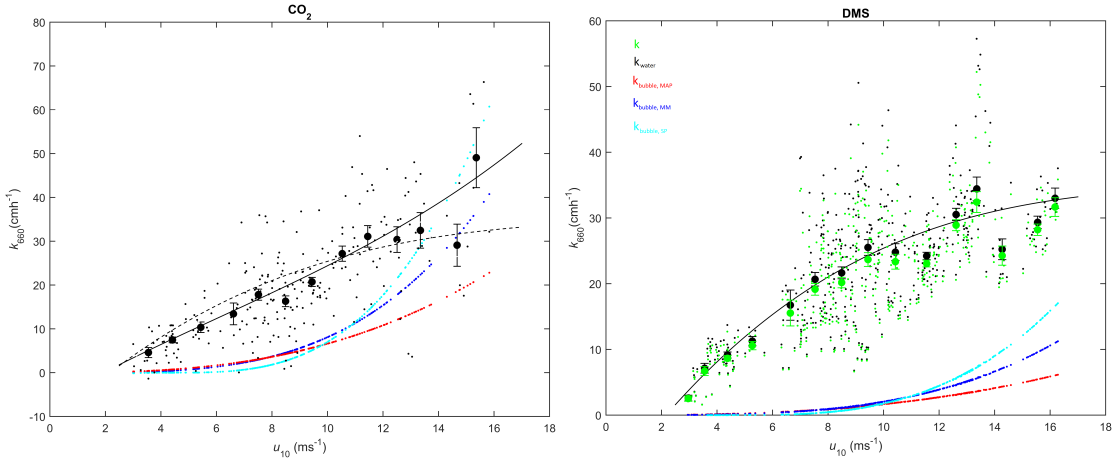

Figure 4.13: Gas transfer velocity scaled to Sc=660 as a function of u_{10} for CO_2 [left] , and DMS [right]. Water side gas transfer (black), total gas transfer for DMS (green), and bubble mediated gas transfer, k_b, derived using the independent bubble model and W parameterizations of MAP, MM and SP, in red, blue and cyan, respectively. Measured water side data are binned in 1 m s^{-1} u_{10} bins. Solid lines are 3rd degree polynomial fits to the measured water side data. The dashed line in the left CO_2 plot is the polynomial fit form the right panel. The fit coefficients can be seen in Table 4.2.

Table 4.2: Fit coefficients [p_0, p_1, p_2, p_3] for $y = p_0 + p_1 \cdot u_{10} + p_2 \cdot u_{10}^2 + p_3 \cdot u_{10}^3$. Measured (meas.) indicates the Monsoon field data (for CO_2 only k_{660} values between -10 and 80 cm h^{-1} were included). Δd_i is the error estimation besed on Equation 4.20. Hybrid model is calculated using 'independent bubble model' [Woolf, 1997] and the MAP, MM and SP W-parameterizations as described in Section 4.3.3. *The polynomial parameterization is taken from the discussion version of the paper[Bell et al., 2017a]. Δk_{water} from Bell et al. [2017a] is referenced to the in situ Sc of CO_2

y	p_0	Δd_0	p_1	Δd_1	p_2	Δd_2	p_3	Δd_3
k_{water} CO_2 meas.	-7	±20	3.6	±7.5	-0.11	±0.88	0.006	±0.03
k_{water} DMS meas.	-12	±12	5.9	±4.3	-0.26	±0.49	0.004	±0.02
Δk_{water} meas.	5	±23	-2.3	±8.6	0.15	±1.0	0.00	±0.04
k_{b,CO_2} MODEL MAP	0.07	±0.04	0.22	±0.02	0.027	±0.002	0.003	±0.0001
k_{b,CO_2} MODEL MM	-1.14	±0.08	0.62	±0.03	-0.123	±0.004	0.0132	±0.0001
k_{b,CO_2} MODEL SP	-2.90	±0.05	1.92	±0.02	-0.422	±0.002	0.0313	±0.0001
$\Delta k_{water,Sc=CO_2}$*	4.280	N/A	-0.535	N/A	0.157	N/A	N/A	N/A

Table 4.3: Comparison of CO_2, during which DMS was simultaneously measured, gas transfer velocity measurement campaigns.'In' and 'out' denote values at conditions of oceanic uptake of CO_2 (in) and oceanic outgassing of CO_2 (out).

poperty	Miller et al. [2009]	Bell et al. [2017a]	this study
SST[^{o}C] min/avg/max	9/13/20	7/10/19	19/25/30
Wind speed[m s^{-1}] avg/max	6.7/11.5	8.9/19.4	8.9/15.8
ΔpCO_2[µatm] avg	-55.2	-60	-30.6 (in)/20 (out)
CO_2 flux [mol m^{-2} y^{-1}] avg	-3.2	-7	-2.3 (in)/1.66 (out)

underlying process.

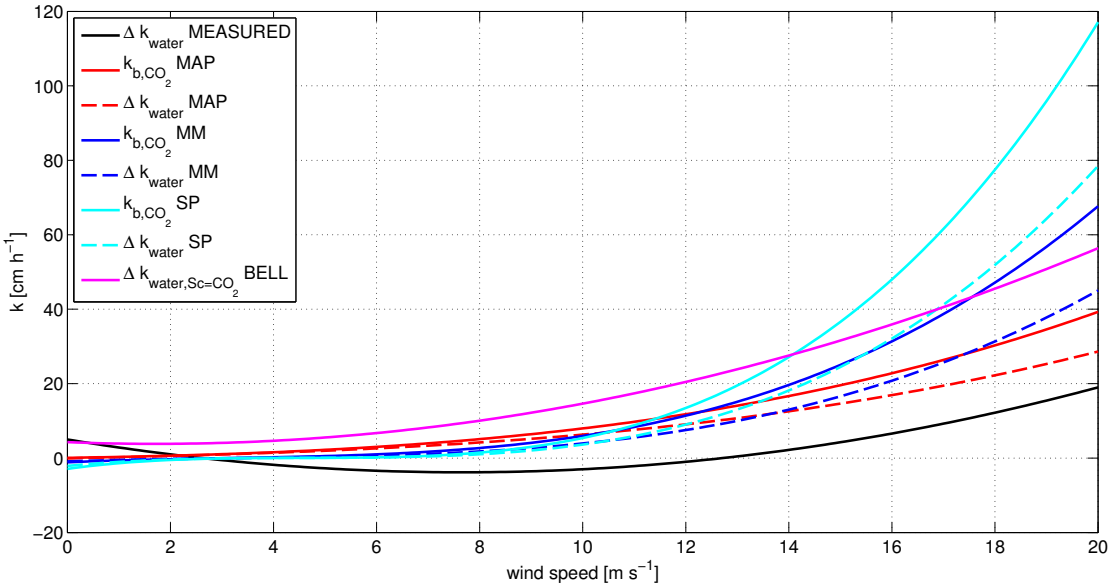

Figure 4.14: Comparison of k_{b,CO_2} and Δk_{water} vs wind speed relationships. MAP, MM and SP are calculated by the hybrid model using the three whitecap fraction models. $\Delta k_{water,Sc=CO_2}$ Bell is derived from direct CO_2 and DMS flux measurements by Bell et al. [2017a]. Δk_{water} MEASURED is derived from the measurements of this study. The dashed lines represent Δk_{water} (Equation 4.18) from the three W models. The difference between the dashed and the equally colored solid line is the modeled $k_{b,DMS}$

4.5 Conclusion

We directly measured DMS and CO_2 fluxes in the Indian Ocean and derived gas transfer velocities for both gases. There have only been two previous directly measured CO_2 and DMS flux and k comparisons before this one ([Miller et al., 2009, Bell et al., 2017a]). The DMS gas transfer relationship k vs u appears to be a linear relationship, whereas the

CO_2 relationship appears to be related to the N00 parameterization, which is a quadratic function. However, both data sets show a limitation of gas transfer at high wind speed, which is referred to as 'rollover'.
We report a gas transfer limitation above 11 m s^{-1} and propose a mechanism parameterized by the transferred Reynolds number Re_{tr}. The mechanism is based on wind-wave interaction and is most importantly dependent on the relative velocities of the wave and the wind. The parameterization is verified using this data set and previously published gas transfer velocities. We suggest a threshold of $|Re_{tr}| = 6.7 \cdot 10^5$ when gas transfer limitation occurs. Re_{tr} can be easily calculated during research cruises as well analyzed for previous cruises to asses the influence of wind-wave interactions. This parameter can also be used to predict gas transfer limitation using weather and wave forecast models.
The k_b wind speed dependance of this study can support the findings of Bell et al. [2017a]. At low to medium wind speed the gas transfer velocity of DMS is higher than CO_2. This results in a negative linear coefficient of the k_b vs wind speed relationship. This is also, but not as prominent, the case for Bell et al. [2017a]. It is interesting that similar functional forms between k_b and wind speed are found for both measured datasets. A reason could be an overestimation of whitecap fraction for our cruise. However, the explanation of the offset between the two relationships needs further study.
Our results in combination with previous studies show that direct gas transfer measurements of two or more gases are necessary to understand and pinpoint processes influencing air-sea gas exchange. These processes have to be taken into account in established gas transfer parameterizations. This is especially important for the quantification of bubble mediated gas transfer. Interfacial gas transfer velocities k_o from gases with a negligible bubble mediated transfer can be used to understand the effect of gas transfer limitation, as limitation seems to affect k_o only. Calculating gas fluxes using the bulk formula (Equation 4.1) and usual gas transfer velocity parameterizations might lead to an overestimation due to unaccounted gas transfer limitation events.

Acknowledgments

The authors thank Kirstin Krüger, the chief scientist of the RV Sonne cruise (SO234-2/235), as well as the captain and crew. E. Atlas helped in measuring the canister samples. Dennis Booge measured the DMS seawater concentration. We thank the Environmental Modeling Center at the NOAA/National Weather Service for providing the WaveWatch III data. This work was carried out under the Helmholtz Young Investigator Group of C. Marandino, TRASE-EC (VH-NG-819), from the Helmholtz Association. L. M. Goddijn-Murphy acknowledges support from the European Space Agency (ESA) Support to Science Element (STSE) projects OceanFlux Greenhouse Gases (contract 4000104762/11/I-AM) and OceanFlux GHG Evolution (4000112091/14/I-LG). The cruise 234-2/235 was financed by the BMBF, 03G0235A. The authors declare no competing financial interests. The data is stored at the data portal of GEOMAR Kiel.

4.6 Supplement

4.6.1 Galilean transformation and the Navier-Stokes Equation

A coordinate transformation is a way of simplifying forces, velocities and boundary conditions. It is important that conservation laws and physical principles are conserved and obeyed, which we achieve using a Galilean transformation. The Galilean transformation is a transformation into a different inertial system. This means that no external forces or pseudo forces have to be considered. Forces, that apply in the original frame of reference, apply the same way in the new frame of reference. Any transformation to a rotating (Coriolis force) or accelerated (inertia) reference system will result in the introduction of pseudo forces.
The Navier-Stoke Equation (NSE), Equation 4.21, is the fundamental equation that describes the flow and turbulence of, in this case, incompressible fluids. u is the velocity vector in three dimensions, x is the coordinate, ν the kinematic viscosity and p the pressure field.

$$\frac{\partial u_i}{\partial t} + u_j \cdot \frac{\partial u_i}{\partial x_j} = -\frac{\partial p}{\partial x_i} + \nu \cdot \nabla^2 u_i \tag{4.21}$$

The NSE is invariant under the Galilean transformation [McComb, 2005] given in Equation 4.22, where c is the constant transformation velocity and $\tilde{x_i}$, $\tilde{u_i}$ are the respective coordinate and velocity vectors in the transformed system.

$$\begin{aligned} x_i &= c \cdot t + \tilde{x_i} \\ u_i &= c + \tilde{u_i} \end{aligned} \tag{4.22}$$

The Reynolds number is deduced from the NSE and, therefore, also valid in any Galilean transformed system. As the Reynolds number is based upon the the characteristic velocity which is also transformed, we think that a transformed Reynolds number is a proper way to describe the wind-wave interaction. The factor $\cos(\theta)$, where θ is the angle between the wind and the wave, is added for describing directional dependencies of the wave height. It is applied in the new reference frame [Högström et al., 2011] and, therefore, does not interfere with the transformation. Figure 4.15 shows the transformation of the wind in the earth's reference system u_{10} (solid arrow) into the wave's reference system u_{tr} (dotted arrow). The wave is traveling from right to left as seen in the wave's phase speed vector c_p (dashed arrow). θ is the angle between u_{tr} and c_p.
Previously used wind-wave interaction parameters such as wave age wa (Equation 4.23) include absolute values of wind speed u_{10} and c_p wave's phase velocity. They do not represent a Galilean transformation and do not provide a vector representation of the interacting velocities and are, therefore, not suitable for describing the wind-wave interactions. Using the directional factor $\cos(\theta)$ in the Equations (Equation 4.23) introduces some directional dependencies, but is not a substitute for a complete vector representation.

$$wa = \frac{c_p}{u_{10}}$$
$$wa = \frac{c_p}{u_{10} \cdot cos\,(\theta)}$$
$$wa = \frac{c_p}{u^*}$$
$$wa = \frac{c_p}{u^* \cdot cos\,(\theta)} \tag{4.23}$$

Paramaterizations based on the the friction velocity u*, such as Toba's Reynolds number Re_{Toba}, are invariant under the Galilean transformation. McComb [2005] states that turbulence and velocity fluctuations are automatically Galilean invariant, as they are differences. However, they lack the wind-wave interaction as they describe only the turbulence of the wind field.

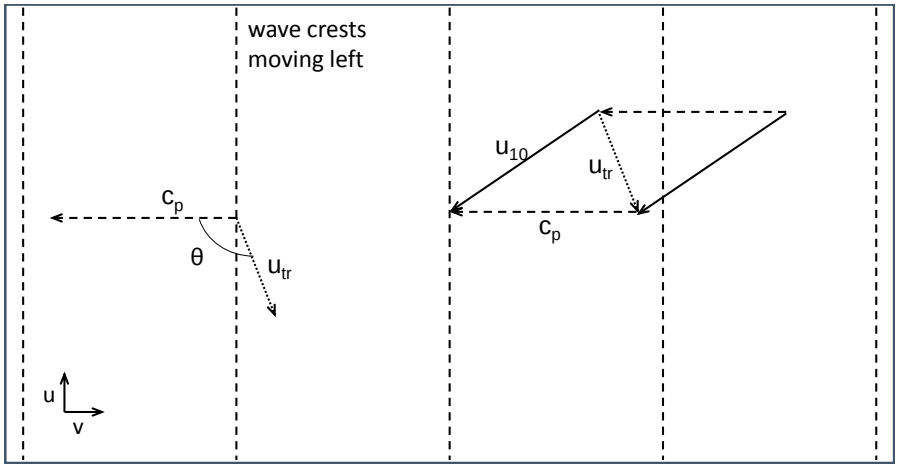

Figure 4.15: Schematic of the transformation of the wind u_{10} (solid arrows) in the Earth's reference system into the wave's reference system u_{tr} (dotted arrows). The wave travels from left to right. The dashed vertical lines denote the wave's crests. θ is the angle between the phase speed c_p (dashed arrows) and u_{tr}.

4.6.2 Motion correction

The correction of the 3-D wind speeds measured by the sonic anemometer was based upon Miller et al. [2010], Edson et al. [1998], Landwehr et al. [2015]. The motion of the ship is measured with an intertial motion unit (IMU) and is subtracted from the measured wind speed. Figure 4.16 shows a power spectrum of the vertical wind. The black line shows the uncorrected raw, as measured, vertical wind power spectrum. Clearly visible is a peak around 0.2 Hz, which originates from the motion of the ship in the wave field.

The red line illustrates the motion corrected vertical wind power spectrum. The dashed line shows the expected $-\frac{2}{3}$ decay of the turbulent power spectrum (TPS) in the inertial subrange [Kolmogorov, 1941] (Equation 4.24). Originally, as porposed by Kolomogorov, the decay is relative to $f^{-\frac{5}{3}}$, but Figure 4.16 shows $f \cdot TPS$ (Equation 4.25) and, as a consequence, the decay is proportional to $-\frac{2}{3}$.

$$TPS \propto f^{-\frac{2}{3}} \tag{4.24}$$

$$TPS \propto f^{-\frac{5}{3}} \cdot f \longrightarrow TPS \propto f^{-\frac{2}{3}} \tag{4.25}$$

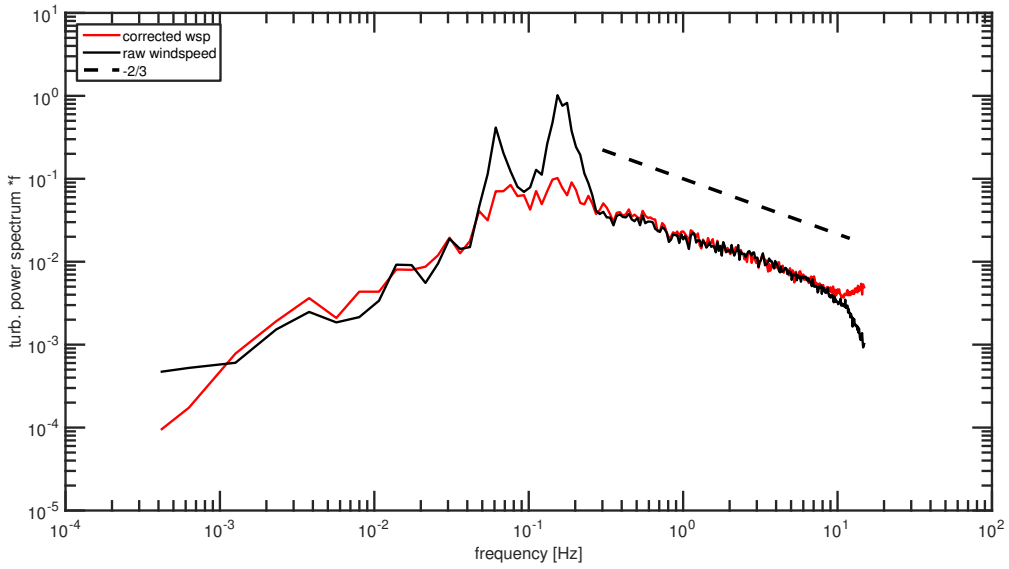

Figure 4.16: A sample vertical wind w' power spectrum before the correction (black) and after the correction (red). The dashed line is a reference to the $-\frac{2}{3}$ decay in the inertial subrange

.

4.6.3 Post processing

Eddy covariance data must be corrected for the delay between gas and wind measurements, as well as high frequency fluctuation losses in the tubing. We use a regular valve switch of an isotopically labeled standard to correct both issues. An ideal valve switch is a rectangular function. The tube's low-pass filter behavior alters the ideal rectangular signal as well as the turbulence in the tube. Therefore, we applied a low-pass filter to an ideal rectangle signal, in order to fit the shape of the measured isotopically labeled gas concentration over time. Figure 4.17 shows an ideal valve switch, the actual measured

valve switch and the output of the low-pass filter applied to the ideal valve switch. The loss in high frequency power, displayed by the low-pass filter, is equal to the loss of high frequency fluctuations in the 1/2"Teflon tube connecting the air-intake to the laboratory container. Using the parameters from the low-pass filter we can put a gain factor on the cospectra. The loss displayed a linear relationship with 10 m neutral wind speed u_{10}. The gain factors for DMS G_{DMS} and CO_2 G_{CO_2} can be seen in equation (4.26).

$$\begin{aligned} G_{DMS} &= 1.032 + 0.0021 \cdot u_{10} \\ G_{CO_2} &= 1.0128 + 0.0021 \cdot u_{10} \end{aligned} \tag{4.26}$$

All data points were then multiplied by the gain factor using their respective u_{10} wind speed.
To get a right time synchronization of the concentration fluctuation c' and the vertical wind fluctuation w', we first set the time delay to the value obtained from the delay tests. Then, to increase the delay precision, we cross correlated the recorded wind w' and the respective air concentration c'. This was done by shifting the two data sets by 0.1 s steps and setting the delay to the maximum correlation (flux out of the ocean) or a minimum correlation (flux into the ocean). The maximum possible offset was set to ± 1 s. Figure 4.18 shows on the x-axis the shifting of the delay time in relation to the delay test time. The y-axis shows the correlation. As the DMS flux is out of the ocean, in this example, we set the delay offset to the value of the maximum correlation. In the example of Figure 4.18 this was -0.3 s.

4.6.4 DMS and CO_2 spectra and cospectra

Figures 4.19 and 4.20 show a power spectrum of measured DMS and CO_2 concentrations. Additionally, a reference line shows the $-\frac{2}{3}$ decay. The original Kolmogorov [Kolmogorov, 1941] decay is $-\frac{5}{3}$, but as $f \cdot power$ is shown $f^{-\frac{5}{3}} \cdot f \longrightarrow f^{-\frac{2}{3}}$. Figures 4.21 and 4.22 show a cospectrum of the covariance c'w' between the fluctuation of the vertical wind speed and the concentration fluctuation for CO_2 and DMS, respectively. We fitted an empirical function, Equation 4.27, proposed by Kaimal et al. [1972] to the measured data as a quality reference. a and b are the fitting parameters.

$$\begin{aligned} C_{cw}(f) &= \frac{a \cdot f}{(1 + b \cdot f)^{2.4}} \quad \text{for } f \geq 0.22 \\ C_{cw}(f) &= \frac{a \cdot f}{(1 + b \cdot f)^{1.75}} \quad \text{for } f \leq 0.22 \end{aligned} \tag{4.27}$$

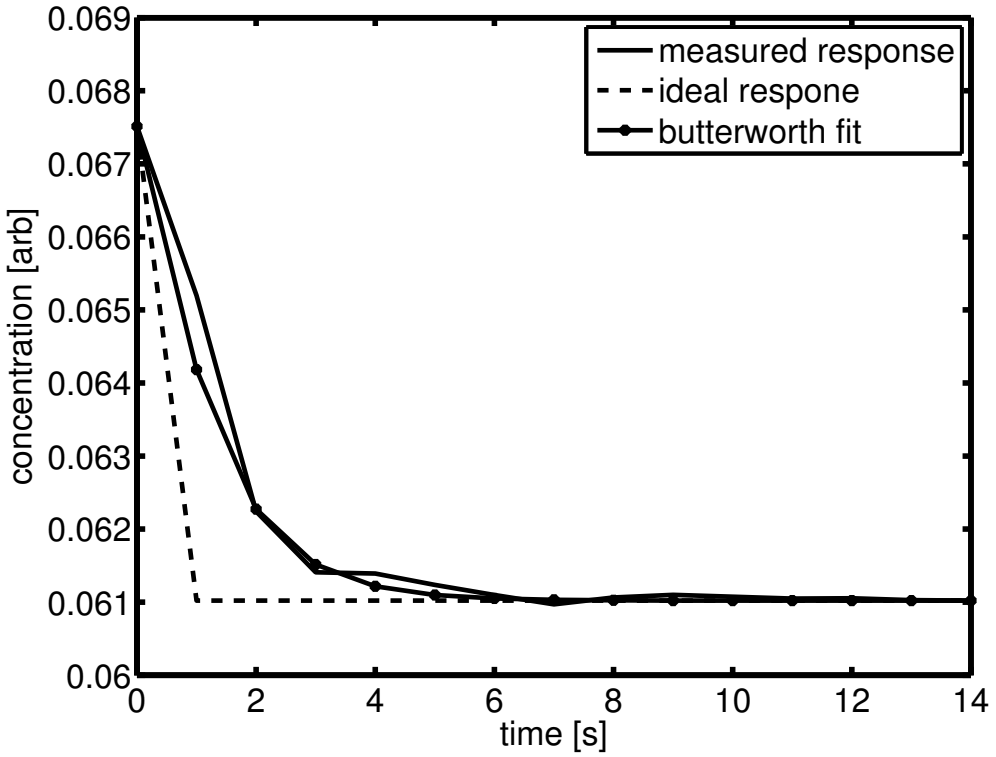

Figure 4.17: The concentration of the isotopically labeled reference gas during a valve switch. We applied and tuned a low-pass filter to an ideal valve switch to match the measured progression. Using the low-pass filter parameters, we accounted for the high frequency loss in the tube.

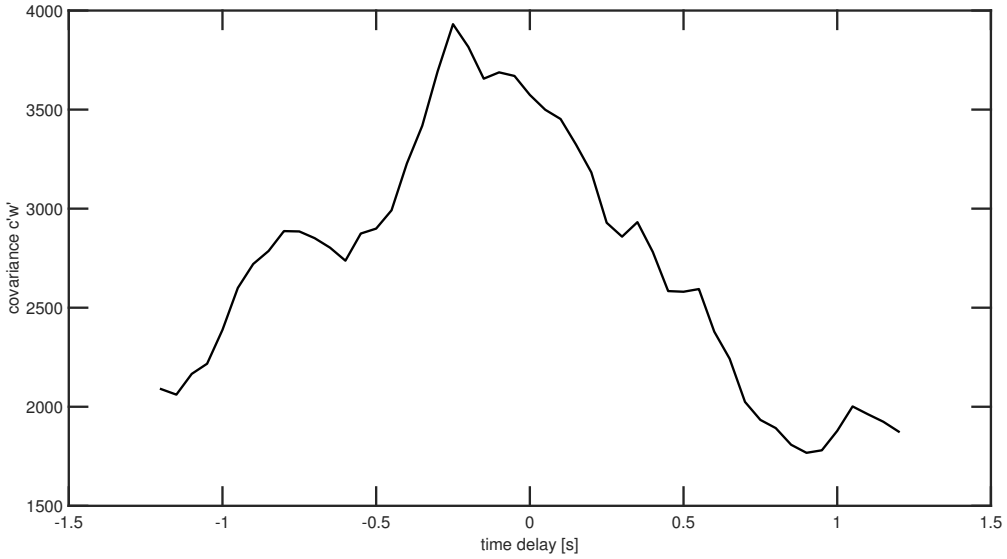

Figure 4.18: The delay offset vs the covariance c'w' between DMS and vertical wind speed. In this example the offset was set to -0.3 seconds. This means after calculating, using the valve switch, the time lag, between wind speed and concentration measurement, was still -0.3 s seconds.

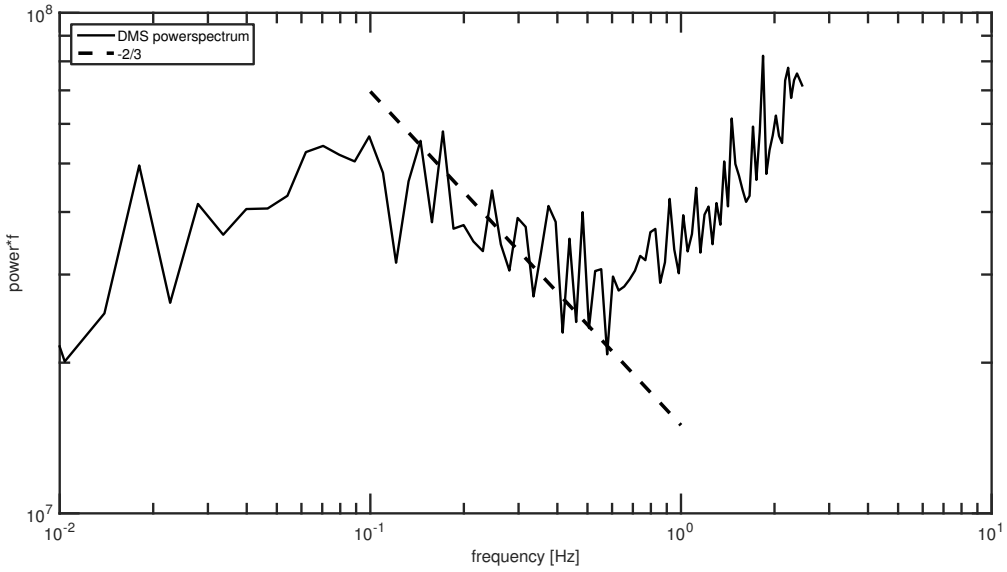

Figure 4.19: A sample power spectrum of the DMS concentration, recorded for 30 minutes. The dashed line is a reference to the $-\frac{2}{3}$ decay in the inertial subrange [Kolmogorov, 1941]. The increase after 1 Hz illustrates noise from the high frequency tubing loss and the instruments measurements.

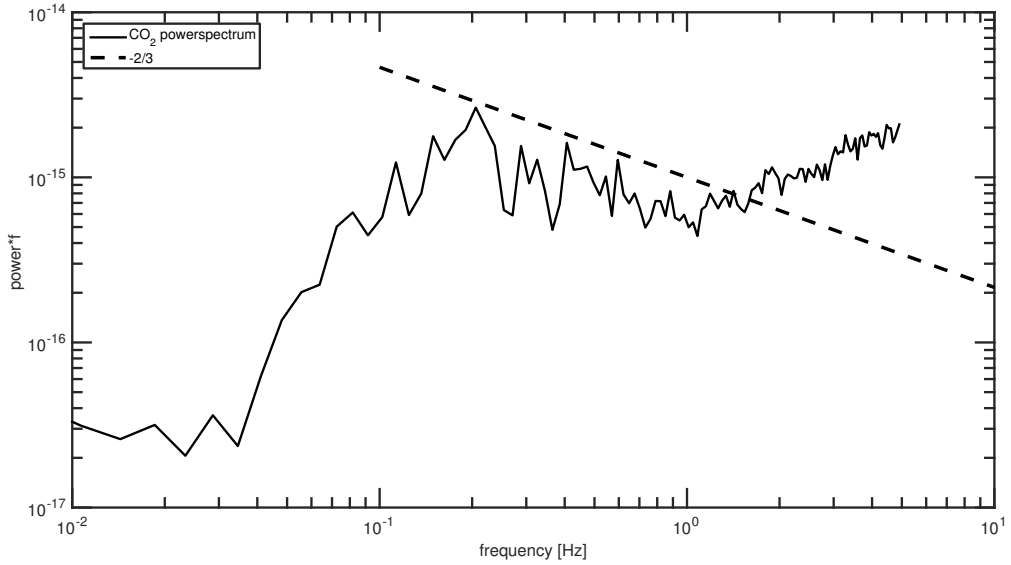

Figure 4.20: A sample power spectrum of the CO_2 concentration, recorded for 30 minutes. The dashed line is a reference to the $-\frac{2}{3}$ decay in the inertial subrange [Kolmogorov, 1941]. The increase after 1 Hz illustrates noise from the high frequency tubing loss and the instruments measurements.

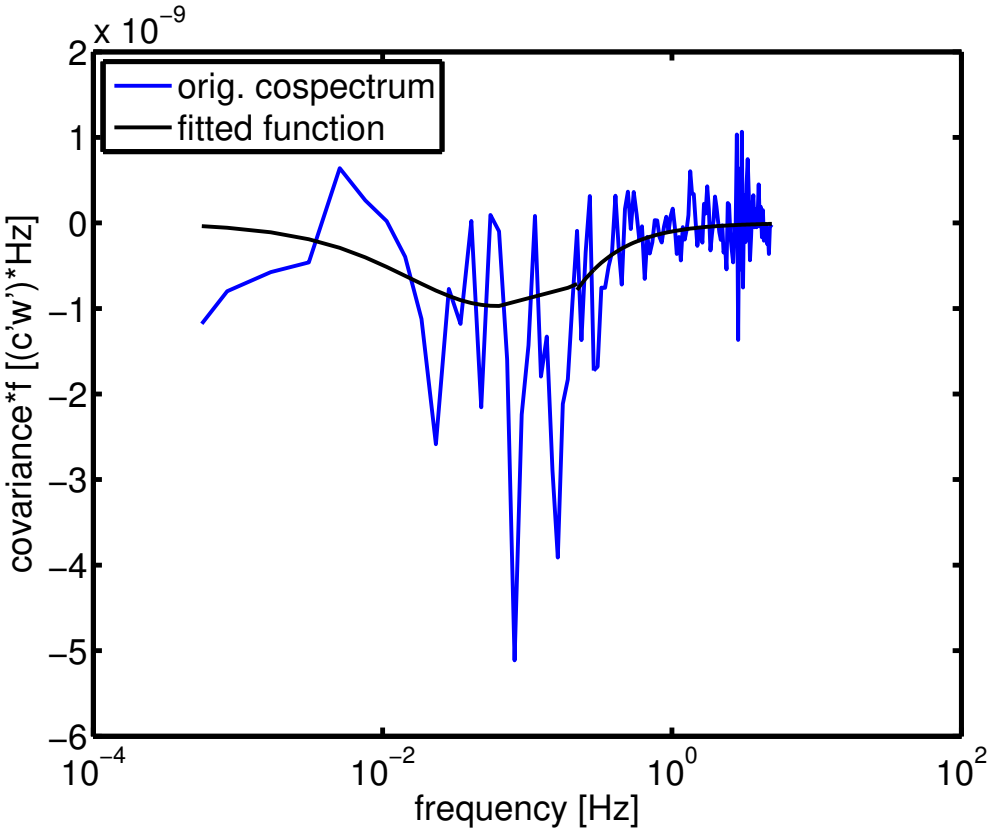

Figure 4.21: A sample CO_2 cospectrum (c'w'). The black line is a fit using an idealized function for scalar cospectra [Kaimal et al., 1972].

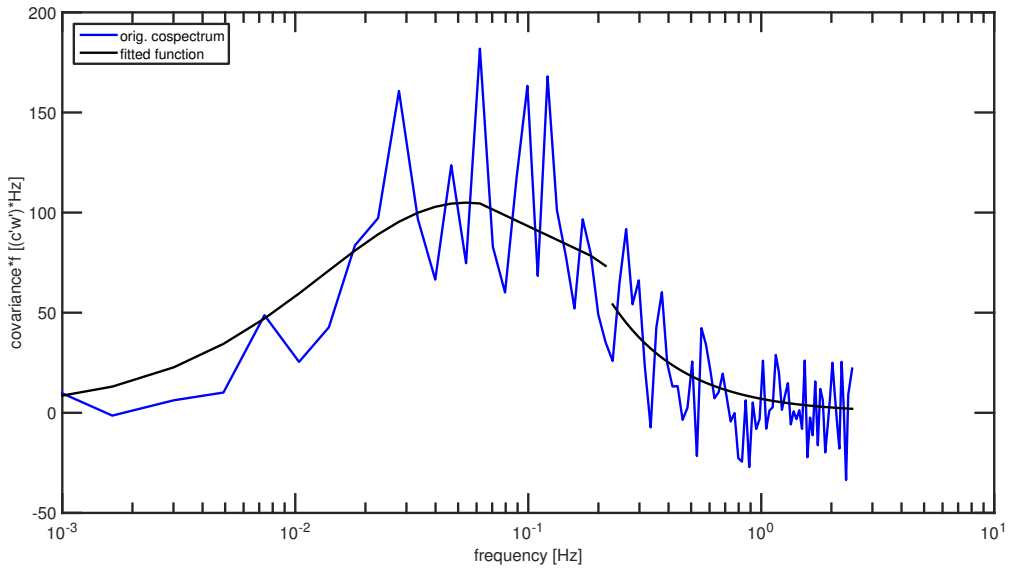

Figure 4.22: A sample DMS cospectrum (c'w'). The black line is a fit using an idealized function for scalar cospectra [Kaimal et al., 1972].

References

D. L. Arevalo-Martinez, M. Beyer, M. Krumbholz, I. Piller, A. Kock, T. Steinhoff, A. Körtzinger, and H. W. Bange. A new method for continuous measurements of oceanic and atmospheric n_2o, co and co_2: performance of off-axis integrated cavity output spectroscopy (oa-icos) coupled to non-dispersive infrared detection (ndir). *Ocean Science*, 9(6):1071–1087, 2013. doi: 10.5194/os-9-1071-2013. URL http://www.ocean-sci.net/9/1071/2013/.

W. E. Asher, L. M. Karle, B. J. Higgins, P. J. Farley, E. C. Monahan, and I. S. Leifer. The influence of bubble plumes on air-seawater gas transfer velocities. *Journal of Geophysical Research: Oceans*, 101(C5):12027–12041, 1996. ISSN 2156-2202. doi: 10.1029/96JC00121. URL http://dx.doi.org/10.1029/96JC00121.

William Asher, James Edson, Wade Mcgillis, Rik Wanninkhof, David T. Ho, and Trina Litchendor. *Fractional Area Whitecap Coverage and Air-Sea Gas Transfer Velocities Measured During GasEx-98*, pages 199–203. American Geophysical Union, 2013. ISBN 9781118668634. doi: 10.1029/GM127p0199. URL http://dx.doi.org/10.1029/GM127p0199.

William E. Asher and Rik Wanninkhof. The effect of bubble-mediated gas transfer on purposeful dual-gaseous tracer experiments. *Journal of Geophysical Research: Oceans*, 103(C5):10555–10560, may 1998. ISSN 2156-2202. doi: 10.1029/98jc00245. URL http://dx.doi.org/10.1029/98JC00245.

Nicholas R. Bates, A. Christine Pequignet, and Christopher L. Sabine. Ocean carbon cycling in the indian ocean: 1. spatiotemporal variability of inorganic carbon and air-sea co2 gas exchange. *Global Biogeochemical Cycles*, 20(3):n/a–n/a, 2006. ISSN 1944-9224. doi: 10.1029/2005GB002491. URL http://dx.doi.org/10.1029/2005GB002491. GB3020.

T. G. Bell, W. De Bruyn, S. D. Miller, B. Ward, K. H. Christensen, and E. S. Saltzman. Air-sea dimethylsulfide (dms) gas transfer in the north atlantic: evidence for limited interfacial gas exchange at high wind speed. *Atmos. Chem. Phys.*, 13(21):11073–11087, nov 2013. ISSN 1680-7324. doi: 10.5194/acp-13-11073-2013. URL http://www.atmos-chem-phys.net/13/11073/2013/.

T. G. Bell, W. De Bruyn, C. A. Marandino, S. D. Miller, C. S. Law, M. J. Smith, and E. S. Saltzman. Dimethylsulfide gas transfer coefficients from algal blooms in the southern ocean. *Atmos. Chem. Phys.*, 15(4):1783–1794, feb 2015. ISSN 1680-7324. doi: 10.5194/acp-15-1783-2015. URL http://www.atmos-chem-phys.net/15/1783/2015/.

T. G. Bell, S. Landwehr, S. D. Miller, W. J. de Bruyn, A. H. Callaghan, B. Scanlon, B. Ward, M. Yang, and E. S. Saltzman. Estimation of bubble-mediated air–sea gas exchange from concurrent dms and co2 transfer velocities at intermediate–high

wind speeds. *Atmospheric Chemistry and Physics*, 17(14):9019–9033, 2017a. doi: 10.5194/acp-17-9019-2017. URL https://www.atmos-chem-phys.net/17/9019/2017/.

T. G. Bell, S. Landwehr, S. D. Miller, W. J. de Bruyn, A. H. Callaghan, B. Scanlon, B. Ward, M. Yang, and E. S. Saltzman. Estimation of bubble-mediated air–sea gas exchange from concurrent dms and co2 transfer velocities at intermediate-high wind speeds; discussion paper. *Atmospheric Chemistry and Physics*, 17(14):9019–9033, 2017b. doi: 10.5194/acp-17-9019-2017. URL https://www.atmos-chem-phys.net/17/9019/2017/acp-17-9019-2017-discussion.html.

D. Booge, C. Schlundt, A. Bracher, S. Endres, B. Zäncker, and C. A. Marandino. Marine isoprene production and consumption in the mixed layer of the surface ocean - a field study over 2 oceanic regions. *Biogeosciences Discussions*, 2017:1–28, 2017. doi: 10.5194/bg-2017-257. URL https://www.biogeosciences-discuss.net/bg-2017-257/.

Sophia E. Brumer, Christopher J. Zappa, Byron W. Blomquist, Christopher W. Fairall, Alejandro Cifuentes-Lorenzen, James B. Edson, Ian M. Brooks, and Barry J. Huebert. Wave-related reynolds number parameterizations of co2 and dms transfer velocities. *Geophysical Research Letters*, 44(19):9865–9875, 2017. ISSN 1944-8007. doi: 10.1002/2017GL074979. URL http://dx.doi.org/10.1002/2017GL074979. 2017GL074979.

Adrian Callaghan, Gerrit de Leeuw, Leo Cohen, and Colin D. O'Dowd. Relationship of oceanic whitecap coverage to wind speed and wind history. *Geophysical Research Letters*, 35(23):n/a–n/a, 2008. ISSN 1944-8007. doi: 10.1029/2008GL036165. URL http://dx.doi.org/10.1029/2008GL036165. L23609.

J. B. Edson, A. A. Hinton, K. E. Prada, J. E. Hare, and C. W. Fairall. Direct covariance flux estimates from mobile platforms at sea. *Journal of Atmospheric and Oceanic Technology*, 15(2):547–562, apr 1998. doi: 10.1175/1520-0426(1998)015<0547:dcfefm>2.0.co;2. URL http://journals.ametsoc.org/doi/abs/10.1175/1520-0426%281998%29015%3C0547%3ADCFEFM%3E2.0.CO%3B2.

James B. Edson, Venkata Jampana, Robert A. Weller, Sebastien P. Bigorre, Albert J. Plueddemann, Christopher W. Fairall, Scott D. Miller, Larry Mahrt, Dean Vickers, and Hans Hersbach. On the exchange of momentum over the open ocean. *Journal of Physical Oceanography*, 43(8):1589–1610, 2013. doi: 10.1175/JPO-D-12-0173.1. URL http://dx.doi.org/10.1175/JPO-D-12-0173.1.

C. W. Fairall, E. F. Bradley, J. S. Godfrey, G. A. Wick, J. B. Edson, and G. S. Young. Cool-skin and warm-layer effects on sea surface temperature. *Journal of Geophysical Research: Oceans*, 101(C1):1295–1308, 1996a. ISSN 2156-2202. doi: 10.1029/95JC03190. URL http://dx.doi.org/10.1029/95JC03190.

C. W. Fairall, E. F. Bradley, D. P. Rogers, J. B. Edson, and G. S. Young. Bulk parameterization of air-sea fluxes for tropical ocean-global atmosphere coupled-ocean atmosphere response experiment. *J. Geophys. Res.*, 101(C2):3747–3764, 1996b. ISSN 2156-2202. URL http://dx.doi.org/10.1029/95JC03205.

A. Fiehn, B. Quack, H. Hepach, S. Fuhlbrügge, S. Tegtmeier, M. Toohey, E. Atlas, and K. Krüger. Delivery of halogenated very short-lived substances from the west indian ocean to the stratosphere during asian summer monsoon. *Atmos. Chem. Phys. Discuss.*, 2017:1–40, jan 2017. ISSN 1680-7375. doi: 10.5194/acp-2017-8. URL http://www.atmos-chem-phys-discuss.net/acp-2017-8/.

Lonneke Goddijn-Murphy, David K. Woolf, and Christa Marandino. Space-based retrievals of air-sea gas transfer velocities using altimeters: Calibration for dimethyl sulfide. *Journal of Geophysical Research: Oceans*, 117(C8):n/a–n/a, 2012. ISSN 2156-2202. doi: 10.1029/2011JC007535. URL http://dx.doi.org/10.1029/2011JC007535. C08028.

Lonneke Goddijn-Murphy, David K. Woolf, Bertrand Chapron, and Pierre Queffeulou. Improvements to estimating the air–sea gas transfer velocity by using dual-frequency, altimeter backscatter. *Remote Sensing of Environment*, 139(Supplement C):1 – 5, 2013. ISSN 0034-4257. doi: https://doi.org/10.1016/j.rse.2013.07.026. URL http://www.sciencedirect.com/science/article/pii/S0034425713002381.

Lonneke Goddijn-Murphy, David K. Woolf, Adrian H. Callaghan, Philip D. Nightingale, and Jamie D. Shutler. A reconciliation of empirical and mechanistic models of the air-sea gas transfer velocity. *Journal of Geophysical Research: Oceans*, 121(1):818–835, jan 2016. ISSN 2169-9291. doi: 10.1002/2015JC011096. URL http://dx.doi.org/10.1002/2015JC011096.

Kirsty E. Hanley, Stephen E. Belcher, and Peter P. Sullivan. A global climatology of wind-wave interaction. *Journal of Physical Oceanography*, 40(6):1263–1282, 2010. doi: 10.1175/2010JPO4377.1. URL http://dx.doi.org/10.1175/2010JPO4377.1.

David T. Ho, Cliff S. Law, Murray J. Smith, Peter Schlosser, Mike Harvey, and Peter Hill. Measurements of air-sea gas exchange at high wind speeds in the southern ocean: Implications for global parameterizations. *Geophysical Research Letters*, 33 (16):n/a–n/a, 2006. ISSN 1944-8007. doi: 10.1029/2006GL026817. URL http://dx.doi.org/10.1029/2006GL026817.

Ulf Högström, Ann-Sofi Smedman, Alvaro Semedo, and Anna Rutgersson. Comments on a global climatology of wind-wave interaction. *JOURNAL OF PHYSICAL OCEANOGRAPHY*, 41(9):1811–1813, SEP 2011. ISSN 0022-3670. doi: 10.1175/jpo-d-10-05015.1.

J. C. Kaimal, J. C. Wyngaard, Y. Izumi, and O. R. Coté. Spectral characteristics of surface-layer turbulence. *Quarterly Journal of the Royal Meteorological Society*, 98 (417):563–589, 1972. ISSN 1477-870X. doi: 10.1002/qj.49709841707. URL http://dx.doi.org/10.1002/qj.49709841707.

Sanshiro Kawai. Structure of air flow separation over wind wave crests. *Boundary-Layer Meteorology*, 23(4):503–521, Aug 1982. ISSN 1573-1472. doi: 10.1007/BF00116275. URL http://dx.doi.org/10.1007/BF00116275.

Andrey Nikolaevich Kolmogorov. The local structure of turbulence in incompressible viscous fluid for very large reynolds numbers. In *Dokl. Akad. Nauk SSSR*, volume 30, pages 299–303, 1941.

Satoru Komori, Wade McGillis, and Ryoichi Kurose. *Gas Transfer at Water Surfaces, 2010*. Kyoto University, 2011. URL http://hdl.handle.net/2433/156156.

Sebastian Landwehr, Niall O'Sullivan, and Brian Ward. Direct flux measurements from mobile platforms at sea: Motion and airflow distortion corrections revisited. *Journal of Atmospheric and Oceanic Technology*, 32(6):1163–1178, jun 2015. doi: 10.1175/jtech-d-14-00137.1. URL http://journals.ametsoc.org/doi/abs/10.1175/JTECH-D-14-00137.1.

C. A. Marandino, W. J. De Bruyn, S. D. Miller, and E. S. Saltzman. Eddy correlation measurements of the air/sea flux of dimethylsulfide over the north pacific ocean. *Journal of Geophysical Research: Atmospheres*, 112(D3):n/a–n/a, feb 2007. ISSN 2156-2202. doi: 10.1029/2006JD007293. URL http://dx.doi.org/10.1029/2006JD007293.

C. A. Marandino, W. J. De Bruyn, S. D. Miller, and E. S. Saltzman. Open ocean dms air/sea fluxes over the eastern south pacific ocean. *Atmos. Chem. Phys.*, 9 (2):345–356, jan 2009. ISSN 1680-7324. doi: 10.5194/acp-9-345-2009. URL http://www.atmos-chem-phys.net/9/345/2009/.

Jean Mathieu. *Introduction to Turbulent Flow*. CAMBRIDGE UNIVERSITY PRESS, 2000. ISBN 0521775388. URL http://www.ebook.de/de/product/3761221/jean_mathieu_introduction_to_turbulent_flow.html.

W. D. McComb. Galilean invariance and vertex renormalization in turbulence theory. *Phys. Rev. E*, 71:037301, Mar 2005. doi: 10.1103/PhysRevE.71.037301. URL https://link.aps.org/doi/10.1103/PhysRevE.71.037301.

Scott Miller, Christa Marandino, Warren de Bruyn, and Eric S. Saltzman. Air-sea gas exchange of co2 and dms in the north atlantic by eddy covariance. *Geophysical Research Letters*, 36(15):n/a–n/a, aug 2009. ISSN 1944-8007. doi: 10.1029/2009GL038907. URL http://dx.doi.org/10.1029/2009GL038907.

Scott D. Miller, Christa Marandino, and Eric S. Saltzman. Ship-based measurement of air-sea co2 exchange by eddy covariance. *Journal of Geophysical Research: Atmospheres*, 115(D2):n/a–n/a, jan 2010. ISSN 2156-2202. doi: 10.1029/2009JD012193. URL http://dx.doi.org/10.1029/2009JD012193.

Edward C. Monahan and IognáidÓ Muircheartaigh. Optimal power-law description of oceanic whitecap coverage dependence on wind speed. *Journal of Physical Oceanography*,

10(12):2094–2099, 1980. doi: 10.1175/1520-0485(1980)010<2094:OPLDOO>2.0.CO;2. URL https://doi.org/10.1175/1520-0485(1980)010<2094:OPLDOO>2.0.CO;2.

Philip D. Nightingale, Gill Malin, Cliff S. Law, Andrew J. Watson, Peter S. Liss, Malcolm I. Liddicoat, Jacqueline Boutin, and Robert C. Upstill-Goddard. In situ evaluation of air-sea gas exchange parameterizations using novel conservative and volatile tracers. *Global Biogeochemical Cycles*, 14(1):373–387, mar 2000. ISSN 1944-9224. doi: 10.1029/1999GB900091. URL http://dx.doi.org/10.1029/1999GB900091.

Denis Pierrot, Craig Neill, Kevin Sullivan, Robert Castle, Rik Wanninkhof, Heike Lüger, Truls Johannessen, Are Olsen, Richard A. Feely, and Catherine E. Cosca. Recommendations for autonomous underway pco2 measuring systems and data-reduction routines. *Deep Sea Research Part II: Topical Studies in Oceanography*, 56(8–10):512 – 522, 2009. ISSN 0967-0645. doi: http://dx.doi.org/10.1016/j.dsr2.2008.12.005. URL http://www.sciencedirect.com/science/article/pii/S0967064508004268. Surface Ocean {CO2} Variability and Vulnerabilities.

N. Reul, H. Branger, and J.-P. Giovanangeli. Air flow separation over unsteady breaking waves. *Physics of Fluids*, 11(7):1959–1961, 1999. doi: 10.1063/1.870058. URL http://dx.doi.org/10.1063/1.870058.

Nicolas Reul, Hubert Branger, and Jean-Paul Giovanangeli. Air flow structure over short-gravity breaking water waves. *Boundary-Layer Meteorology*, 126(3):477–505, Mar 2008. ISSN 1573-1472. doi: 10.1007/s10546-007-9240-3. URL https://doi.org/10.1007/s10546-007-9240-3.

C.L Sabine, R Wanninkhof, R.M Key, C Goyet, and F.J Millero. Seasonal co2 fluxes in the tropical and subtropical indian ocean. *Marine Chemistry*, 72(1):33 – 53, 2000. ISSN 0304-4203. doi: https://doi.org/10.1016/S0304-4203(00)00064-5. URL http://www.sciencedirect.com/science/article/pii/S0304420300000645.

E. S. Saltzman, W. J. De Bruyn, M. J. Lawler, C. A. Marandino, and C. A. McCormick. A chemical ionization mass spectrometer for continuous underway shipboard analysis of dimethylsulfide in near-surface seawater. *Ocean Sci.*, 5(4):537–546, nov 2009. ISSN 1812-0792. doi: 10.5194/os-5-537-2009. URL http://www.ocean-sci.net/5/537/2009/.

A.H. Shapiro. *Shape and Flow*. Heinemann, Garden City, N.Y., 1961.

Malgorzata Stramska and Tomasz Petelski. Observations of oceanic whitecaps in the north polar waters of the atlantic. *Journal of Geophysical Research: Oceans*, 108 (C3):n/a–n/a, 2003. ISSN 2156-2202. doi: 10.1029/2002JC001321. URL http://dx.doi.org/10.1029/2002JC001321. 3086.

Colm Sweeney, Emanuel Gloor, Andrew R. Jacobson, Robert M. Key, Galen McKinley, Jorge L. Sarmiento, and Rik Wanninkhof. Constraining global air-sea gas exchange for

co2 with recent bomb 14c measurements. *Global Biogeochemical Cycles*, 21(2):n/a–n/a, 2007. ISSN 1944-9224. doi: 10.1029/2006GB002784. URL http://dx.doi.org/10.1029/2006GB002784. GB2015.

Taro Takahashi, Stewart C. Sutherland, Rik Wanninkhof, Colm Sweeney, Richard A. Feely, David W. Chipman, Burke Hales, Gernot Friederich, Francisco Chavez, Christopher Sabine, Andrew Watson, Dorothee C.E. Bakker, Ute Schuster, Nicolas Metzl, Hisayuki Yoshikawa-Inoue, Masao Ishii, Takashi Midorikawa, Yukihiro Nojiri, Arne Körtzinger, Tobias Steinhoff, Mario Hoppema, Jon Olafsson, Thorarinn S. Arnarson, Bronte Tilbrook, Truls Johannessen, Are Olsen, Richard Bellerby, C.S. Wong, Bruno Delille, N.R. Bates, and Hein J.W. de Baar. Climatological mean and decadal change in surface ocean pco2, and net sea–air co2 flux over the global oceans. *Deep Sea Research Part II: Topical Studies in Oceanography*, 56(8):554 – 577, 2009. ISSN 0967-0645. doi: http://dx.doi.org/10.1016/j.dsr2.2008.12.009. URL http://www.sciencedirect.com/science/article/pii/S0967064508004311. Surface Ocean CO2 Variability and Vulnerabilities.

Y. Toba, S. Komori, Y. Suzuki, and D. Zhao. Similarity and dissimilarity in air–sea momentum and CO2 transfers: the nondimensional transfer coefficients in light of the windsea reynolds number. In *Atmosphere-Ocean Interactions*, pages 53–82. WIT Press, feb 2006. doi: 10.2495/978-1-85312-929-2/03. URL https://doi.org/10.2495/978-1-85312-929-2/03.

H. L Tolman. User manual and system documentation of wavewatch-iii version 1.15. *NOAA / NWS / NCEP / OMB Technical Note*, 151:97, 1997.

H. L Tolman. User manual and system documentation of wavewatch-iii version 1.18. *NOAA / NWS / NCEP / OMB Technical Note*, 166:110, 1999.

Hendrik L Tolman. User manual and system documentation of wavewatch iii tm version 3.14. *NOAA / NWS / NCEP / MMAB Technical Note*, 276:220, 2009.

Matthias Tomczak and J. Stuart Godfrey. *Regional Oceanography: An Introduction*. Pergamon, 2006. ISBN 978-0-08-041021-0.

F. Veron, G. Saxena, and S. K. Misra. Measurements of the viscous tangential stress in the airflow above wind waves. *Geophysical Research Letters*, 34(19):n/a–n/a, 2007. ISSN 1944-8007. doi: 10.1029/2007GL031242. URL http://dx.doi.org/10.1029/2007GL031242. L19603.

Rik Wanninkhof, William E Asher, David T Ho, Colm Sweeney, and Wade R McGillis. Advances in quantifying air-sea gas exchange and environmental forcing. *Annual Review of Marine Science*, 1(1):213–244, jan 2009. doi: 10.1146/annurev.marine.010908.163742.

F.M. White. *Viscous Fluid Flow*. McGraw-Hill series in mechanical engineering. McGraw-Hill, 1991. ISBN 9780070697126. URL https://books.google.de/books?id=G6IeAQAAIAAJ.

David K. Woolf. Bubbles and their role in gas exchange. In Peter S. Liss and Robert A. Duce, editors, *The Sea Surface and Global Change:*, pages 173–206. Cambridge University Press, Cambridge, 003 1997. doi: 10.1017/CBO9780511525025.007. URL https://www.cambridge.org/core/books/the-sea-surface-and-global-change/bubbles-and-their-role-in-gas-exchange/4DC4463FADA1EE5B852CAF45435C3929.

Di Yang and Lian Shen. Direct numerical simulation of scalar transport in turbulent flows over progressive surface waves. *Journal of Fluid Mechanics*, 819:58–103, 2017. doi: 10.1017/jfm.2017.164.

M Yang, BW Blomquist, CW Fairall, SD Archer, and BJ Huebert. Air-sea exchange of dimethylsulfide in the southern ocean: Measurements from so gasex compared to temperate and tropical regions. *Journal of Geophysical Research: Oceans*, 116(C4), aug 2011. ISSN 2156-2202. doi: 10.1029/2010jc006526.

M Yang, T G Bell, B W Blomquist, C W Fairall, I M Brooks, and P D Nightingale. Air-sea transfer of gas phase controlled compounds. *IOP Conference Series: Earth and Environmental Science*, 35(1):012011, 2016. URL http://stacks.iop.org/1755-1315/35/i=1/a=012011.

Dongliang Zhao and Lian Xie. A practical bi-parameter formula of gas transfer velocity depending on wave states. *Journal of Oceanography*, 66(5):663–671, Oct 2010. ISSN 1573-868X. doi: 10.1007/s10872-010-0054-4. URL https://doi.org/10.1007/s10872-010-0054-4.

CHAPTER 5

The influence of transformed Reynolds number limitation on gas transfer parameterizations and global DMS and CO_2 fluxes

5.1 Abstract

Eddy covariance measurements show gas transfer velocity limitation at medium to high wind speed. A wind-wave interaction described by the transformed Reynolds number is used to characterize environmental conditions favoring this limitation. We take the transformed Reynolds number parameterization to review the two most cited wind speed gas transfer velocity parameterizations, Nightingale 2000 and Wanninkhof 1992/2014. We propose an algorithm to correct for the effect of gas transfer limitation and validate it with two gas transfer limited directly measured DMS gas transfer velocity data sets. A correction of the Nightingale 2000 parameterization leads to an average increase of 22 % of its predicted gas transfer velocity. The increase for Wanninkhof 2014 is 9.85 %. Additionally, the correction is applied to global air-sea flux climatologies of CO_2 and DMS. The global application of gas transfer limitation leads to a decrease of 6-7 % for the uptake CO_2 by the oceans and to decrease of 11 % of oceanic outgassing of DMS. We expect the magnitude of Reynolds limitation on any global air-sea gas exchange to be about 10 %.

5.2 Introduction

Gas transfer F between the ocean and the atmosphere is commonly described as the product of the concentration difference ΔC between the liquid phase (seawater) and the gas phase (atmosphere) and the gas transfer velocity k. ΔC acts as the forcing potential difference and k as the conductance, which includes all processes promoting and limiting gas transfer. c_{air} and c_{water} are the respective air-side and water-side concentrations. H is the dimensionless form of Henry's law constant.

$$F = k \cdot \Delta C = k \cdot \left(c_{air} - \frac{c_{water}}{H} \right) \tag{5.1}$$

ΔC is typically measured with established techniques, although the distance of the measurements from the interface introduce uncertainties in the flux calculation. Parameterizations of k are another source of uncertainty in calculating fluxes. The flux F can be directly measured, for example with the eddy covariance technique, together with ΔC in order to derive k and estimate a k parameterization (Equation (5.2)).

$$k = \frac{F}{\Delta C} = \frac{F}{c_{air} - \frac{c_{water}}{H}} \tag{5.2}$$

It is very common that k is parameterized with wind speed and all wind speed parameterizations have in common that k increases monotonically with increasing wind speed. This assumption is sensible, as higher wind speed increases turbulence both on the air and the water side and hence the flux. Additional processes like bubble generation can additionally enhance gas transfer. The total gas transfer velocity k_{total}, which is measured by eddy covariance or other direct flux methods, is split up into the water side gas transfer velocity k_{water} and the air side gas transfer velocity k_{air} (Equation (5.3)).

$$\frac{1}{k_{total}} = \frac{1}{k_{water}} + \frac{1}{k_{air}} \tag{5.3}$$

We focus, in this work, on k_{water} which is the sum of the interfacial gas transfer k_o and the bubble mediated gas transfer k_b (Equation (5.4)).

$$k_{water} = k_o + k_b \tag{5.4}$$

To make gas transfer velocities of different gases comparable, Schmidt number (Sc) (Equation (5.5)) scaling has been introduced. Sc scaling only applies to k_o and k_{air}. Sc is the ratio of the viscosity ν to the diffusivity D of the respective gas in seawater.

$$Sc = \frac{\nu}{D} \tag{5.5}$$

$$\frac{k_{o,Sc}}{k_{o,660}} = \left(\frac{Sc}{660} \right)^n \tag{5.6}$$

The exponent n is chosen depending on the surface properties. For smooth surfaces $n=-\frac{2}{3}$ and rough wavy surfaces $n=-\frac{1}{2}$ [Komori et al., 2011]. In this study $n=-\frac{1}{2}$ is used.

In contrast to commonly accepted gas transfer velocity parameterizations, parameterizations based on direct flux measurements by eddy covariance systems have shown a decrease or flattening of k with increasing wind speed at medium to high wind speed [Bell et al., 2013, 2015, Yang et al., 2016, Blomquist et al., 2017, Zavarsky et al., 2018]. Here we use the transformed Reynolds number Re_{tr} [Zavarsky et al., 2018] to identify instances of gas transfer limitations.

$$Re_{tr} = \frac{u_{tr} \cdot H_s}{\nu_{air}} \cdot cos(\theta) \tag{5.7}$$

Re_{tr} is the Reynolds number transformed into the reference system of the moving wave. u_{tr} is the wind speed relative to the wave, H_s, the significant wave height, ν_{air} the kinematic viscosity of air and θ the angle between the wave crest and the transformed wind direction. A flux measurement at values of $Re_{tr} \leq 6.7 \cdot 10^5$ is gas transfer limited [Zavarsky et al., 2018]. This parameterization shows that the limitation is primarily dependent on wind speed, wave speed, wave height and a directional component. It is noteworthy that so far only eddy covariance deduced gas transfer velocities have shown a gas transfer limitation. This may be due to the spatial (1 km) and temporal (30 min) resolution of EC measurements, or to the types of gases measured (e.g. CO_2, DMS, OVOCs). The use of rather soluble gases (DMS, acetone, methanol) makes the gas transfer velocity not greatly influenced by bubble mediated gas transfer. Gas transfer limitation only affects k_o [Zavarsky et al., 2018]. Another direct flux measurement technique, the dual tracer method, utilizes sulphur hexafluoride (SF_6) or ^{3}He. The dual tracer measurement usually lasts over few days but could have a similar spatial resolution as eddy covariance. SF_6 and ^{3}He are both very insoluble and heavily influenced by the bubble effect. Hence, if the gas transfer limitation only affects k_o, k_b could be masking the gas transfer limitation. Additionally, the long measurement period could decrease the likelihood of detection of gas transfer limitation as the conditions for limitation might not be persistent over a few days.
Using wind and wave data for the year 2014, we calculate Re_{tr} and perform an analysis of the impact of gas transfer limitation on the yearly global air sea exchange of CO_2 and DMS. So far global estimates of air-sea exchange of these two gases [Lana et al., 2011, Takahashi et al., 2009, Rödenbeck et al., 2015] have been based on k parameterization which have not included a mechanism for gas transfer limitation. We provide an iterative calculation of the effect of gas transfer limitation and apply the correction to existing CO_2 and DMS climatologies.
We investigate the two most commonly used gas parameterizations (both cited more than 1000 times each) for the occurrence of gas transfer limitation. The Nightingale 2000 (N00) [Nightingale et al., 2000] parameterization contains data from the North Sea, Florida Strait and the Georges Bank between 1989-1996. N00 derived the gas transfer velocity from changes in the ratio of SF^6 and ^{3}He (dual trace method). We also compare N00 to the gas transfer parameterization Wanninkhof 2014 (W14) [Wanninkhof, 2014] which is an update to Wanninkhof 1992 [Wanninkhof, 1992]. They use natural and anthropogenically produced carbon isotopes to estimate the air-sea flux over several years. Using a wind speed climatology they can deduce a quadratic k vs wind speed

parameterization. The parameterization W14 must already have gas transfer limitation included as it is solely dependent on seawater measurements of carbon isotopes. The gas transfer limitation is averaged as they use a global, multi-year approach. All studied k vs u relationships (N00,W14) are monotonically increasing with wind speed.

5.3 Methods

5.3.1 Wave Watch Model III

We use wave data from the WWIII model hindcast run by the Marine Modeling and Analysis Branch of the Environmental Modelling Center of the National Center for Environmental Prediction (NCEP) [Tolman, 1997, 1999, 2009]. The data was obtained for the total year 2014 with a temporal resolution of 3 hours and a spatial resolution of 0.5° x 0.5°. It also provides the u (meridional) and v (zonal) wind vectors, assimilated from the Global Forecast System, used in the model. We retrieved wind speed, wind direction, bathymetry, wave direction, wave period and significant wave height. We converted the wave period T_p to phase speed c_p, assuming deep water waves, using Equation (5.8) [Hanley et al., 2010].

$$c_p = \frac{g \cdot T_p}{2\pi} \tag{5.8}$$

5.3.2 Auxiliary variables

Surface air temperature T, air pressure p, sea surface temperature SST and sea ice concentration were retrieved from the ERA-Interim reanalysis of the European Center for Meridional Weather Forecast [Dee et al., 2011]. It provides a six hourly resolution and a global 0.125^o x 0.125^o spatial resolution. Sea surface salinity (SSS) was extracted from the Takahashi climatology [Takahashi et al., 2009].
Air-sea partial pressure difference (ΔpCO_2) was obtained from the Takahashi climatology. ΔpCO_2, in the Takahashi climatology, is calculated for the year 2000 CO_2 air concentrations. Assuming an increase in both the air concentration and the partial pressure in the water side, the partial pressure difference remains constant. The dataset has a monthly temporal resolution, a 4^o latitudinal resolution and a 5^o longitudinal resolution.
DMS water concentrations were taken from the Lana DMS climatology (Lana11) [Lana et al., 2011]. These are provided with a monthly resolution and a 1^o x 1^o spatial resolution. The air mixing ratio of DMS was set to zero $c_{air,DMS} = 0$. Taking air mixing ratios into account, the global air sea flux of DMS reduces by 17 % [Lennartz et al., 2015]. We still think that our approach is reasonable, as we focus on the change of flux due to gas transfer limitation only.
We linearly interpolated all datasets to the grid and times of the WWIII model.

5.3.3 Kinematic viscosity

The kinematic viscosity ν of air is dependent on air's density ρ and the dynamic viscosity μ of air, Equation (5.9).

$$\nu\left(T,p\right)=\frac{\mu\left(T\right)}{\rho\left(T,p\right)} \tag{5.9}$$

The dynamic viscosity is dependent on temperature T and can be calculated using Sutherland's law [White, 1991] (Equation (5.10)).

$$\mu=\mu_0\cdot\left(\frac{T}{T_0}\right)^{\frac{2}{3}} \tag{5.10}$$

$\mu_0 = 1.716 \cdot 10^{-5}$ N s m^{-2} at $T_0 = 273$ K [White, 1991]. Air density is dependent on temperature T and air pressure p and was calculated using the ideal gas law.

5.3.4 Transformed Reynolds number

The Reynolds number describes the balance of inertial forces and viscous forces. It is the ratio of the typical length and velocity scale over the kinematic viscosity. The transformed Reynolds number, in Equation (5.11), uses the wind speed u_{tr}, transformed into the wave's reference system. The significant wave height H_s is used as the typical length scale. The difference between wind direction and wave direction is given by the angle θ. The factor $\cos(\theta)$ is multiplied to H_s to account for directional dependencies. Wind at an angle of $\theta = 90^o$, for example, does not experience a wave crest or trough, but rather an along-wind corrugated surface

$$Re_{tr}=\frac{u_{tr}\cdot H_s}{\nu}\cdot cos\left(\theta\right) \tag{5.11}$$

5.4 Gas transfer limitation model

Below $Re_{tr} \leq 6.7 \cdot 10^5$ a flow separation between the sea surface and the wind flowing above the wave limits gas transfer [Zavarsky et al., 2018]. As a result, common wind speed parameterizations of k are not applicable (Equation (5.1)). To provide a magnitude of this limitation we propose an alternative wind speed u_{alt}, which is lower than u_{10}. This decrease accounts for the effect of gas transfer limitation. u_{alt} can then be used with k parameterizations to calculate the gas flux.
Given a set wave field, if the relative wind speed in the reference system of the wave u_{tr} is big enough that the transformed Reynolds number is greater than the threshold of $6.7 \cdot 10^5$, no limitation occurs. In the no limitation case, k can be estimated by common gas transfer parameterizations. If the wind speed approaches the wave's phase speed, the transformed Reynolds number drops below the threshold, flow separation happens, and limitation occurs. We propose, to estimate the magnitude of the limitation, a stepwise reduction of u_{10}. We recalculated Re_{tr} with a lower $u_{alt} \prec u_{10}$ and decrease u_{alt} as long as Re_{tr} is below the threshold. If the Re_{tr} crosses to the non limiting regime the actual

u_{alt} can be used as an alternative wind speed. The iteration steps are: [1] Calculate Re_{tr} and check if $Re_{tr} \leq 6.7 \cdot 10^5$. [2] If yes, reduce the wind speed u_{10} in the earth reference system to u_{alt} and recalculate Re_{tr} and check if $Re_{tr} \leq 6.7 \cdot 10^5$. [3] If Re_{tr} is greater than the threshold stop. Then the new reduced wind speed u_{alt} can be used in the k parameterization, if otherwise continue with step [1]. The step size in this model was 0.3 m s^{-1}. We think that this is a good balance of computing time and and velocity resolution of the step size. The minimum velocity for u_{alt} is 0 m s^{-1}. Figure 5.1 shows a flowchart of the algorithm. This algorithm is applied to every box at every time step.
A change in the parameters of the wave field is, in our opinion, not feasible as the wave field is externally prescribed. Swell travels long distances and does not necessarily have a direct relation to the wind conditions at the location of the gas transfer and measurement. Therefore, we change the wind speed only.

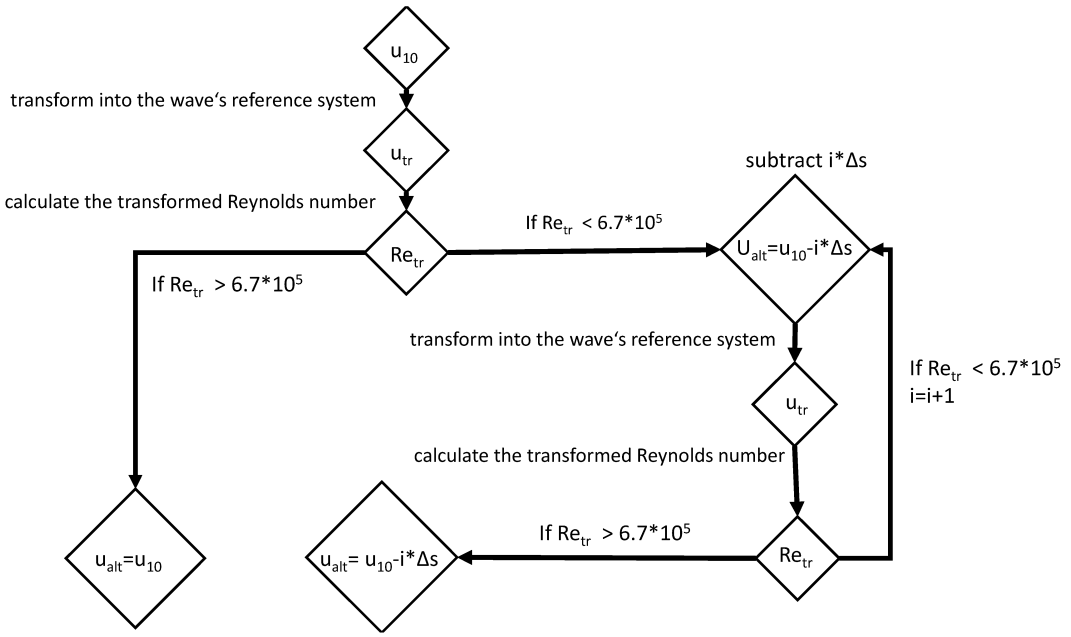

Figure 5.1: Work flow of the gas transfer limitation model. In the case of limited gas transfer, the output is the corrected wind speed u_{alt}, which then can be used in gas transfer parameterizations. The step size Δs can be adapted freely, but considerations of resolution and computing power have to be made. For this manuscript we set $\Delta s = 0.3\ m\ s^{-1}$.

5.4.1 Gas transfer

For the global air-sea exchange of DMS and CO_2 we use the bulk gas transfer formula (Equation (5.1)). We calculate for every grid box and every time step u_{alt} according to the description in Sect. 5.4. If u_{alt} is lower than u_{10} from the global reanalysis then gas transfer limitation occurs and u_{alt} is used in the bulk gas transfer formula (Equation (5.1)). The difference between u_{alt} and u_{10} directly relates to the magnitude of gas transfer limitation.
We assume that the gas transfer limitation only affects k_o. Therefore only the parameterization of k_o should be altered using the new reduced wind speed u_{alt}. This is especially problematic for rather insoluble gases with a high contribution of bubble mediated gas transfer, like CO_2 (at high wind speed), SF_6, ^3He. We use a linear parameterization, ZA18 [Zavarsky et al., 2018], and the quadratic parameterizations, Tak09 [Takahashi et al., 2009], W14 and NI00. The ZA18 parameterization is a linear fit to all data points < 10 m s^{-1} obtained during a cruise in the Indian Ocean (SO234-2/235). This linear fit does not contain data points which are influenced by gas transfer limitation. u_{alt} can be directly inserted into ZA18 as we do not expect a large bubble contribution to k (Equation (5.12)), because of the solubility of DMS. However, all other parameterizations are based on measurements with rather insoluble gases, which have a significant bubble mediated gas transfer contribution. As a consequence we subtract a linear dependency using the ZA18 parametrization, to account for the gas transfer limitation in k_o (Equation (5.13)).

$$F_{lim,ZA18} = (3.1 \cdot u_{alt} - 5.37) \cdot \Delta C \tag{5.12}$$

$$F_{lim,Tak00/W14/NI00} = \left(k_{Tak00/W14/NI00}\left(u_{10}\right) - k_{ZA18}\left(u_{alt}\right)\right) \cdot \Delta C \tag{5.13}$$

For the global DMS transfer we use ZA18 and NI00, which is also used by Lana11 [Lana et al., 2011]. We parameterize the CO_2 flux using Tak09, NI00 and W14.
Sea ice concentration from the ERA-Interim reanalysis was included as a linear factor in the calculation. A sea ice concentration of 90 %, for example, results in a 90 % reduction of the flux. Each time step (3 h) of the WWIII model provided a global grid of air-sea fluxes with and without gas transfer limitation. Theses single time steps were summed up to get a yearly flux result.
For CO_2, ΔC was directly provided by the Takahashi climatology. For DMS the air concentration was neglected and ΔC reduced to c_{water}, which was obtained from Lana11.

5.5 Results

We apply the correction to two data sets (Knorr11 [Bell et al., 2017] and SO234-2/235 [Zavarsky et al., 2018]) of DMS gas transfer velocities. Both data sets experienced gas transfer limitation at high wind speed. Using this proof of concept, we quantify the influence of gas transfer limitation on N00 and W14 and correct for it. Finally, we apply the correction to global flux estimates of CO_2 and DMS.

5.5.1 Correction of the interfacial gas transfer

Figures 5.2 and 5.3 show the corrected DMS gas transfer velocities for the SO234-2/235 and the Knorr11 cruises. The black circles indicate the original data set. The colored circles are k values at the corrected wind speed. If a black circle and a colored circle are concentric the data point was not limited and therefore no correction was applied. For comparison, in both Figure, the linear fit to the data SO234-2/235 below 10 m s^{-1} (ZAV17) is plotted. Both Figures show the significant wave height as color.

Figure 5.2 shows the gas transfer limited data points at 14-16 m s^{-1} moved closer to

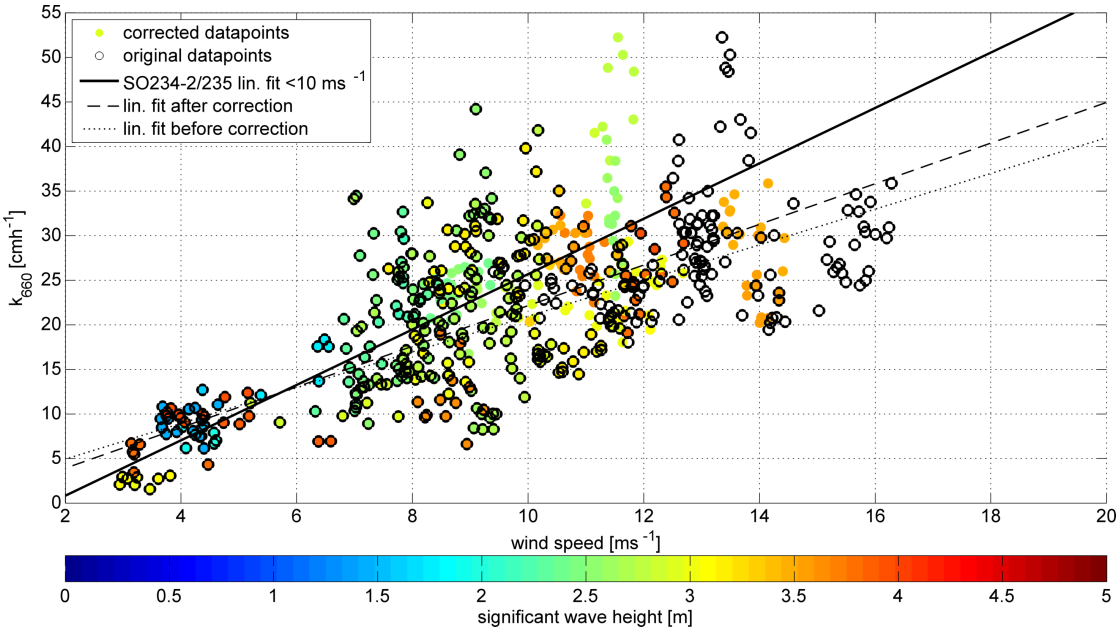

Figure 5.2: Correction of the SO234-2/235 DMS fluxes. The data points with $Re_{tr} < 6.7 \cdot 10^5$ were corrected using the gas transfer limitation model. Black circles denote k values at the original wind speed u_{10}. Colored filled circles denote the k value at wind speed=u_{alt}. The color shows the significant wave height. If a data point has a concentric black and filled circle, it was not corrected as it was not subject to gas transfer limitation. The black solid line is the ZAV17 parameterization. The dotted line is the linear fit to the data points before the correction, the dashed line is the linear fit after the correction.

the linear fit after correction to u_{alt}. The linear fits to the data set before and after the correction are shown with a dotted (before) and dashed (after) line. The large gas transfer velocity values at around 13 m s^{-1} and above 35 cm h^{-1} were moved to 11 m^{-1}. This means a worsening of the the k estimate by the linear fit. These data points have very low ΔC values [Zavarsky et al., 2018], therefore, we expect a large scatter as a result from Equation (5.2).

Figure 5.3 also shows an improvement of the linear fit estimates. The gas transfer limited data points were assigned the new wind speed u_{alt}, resulting in better agreement with the

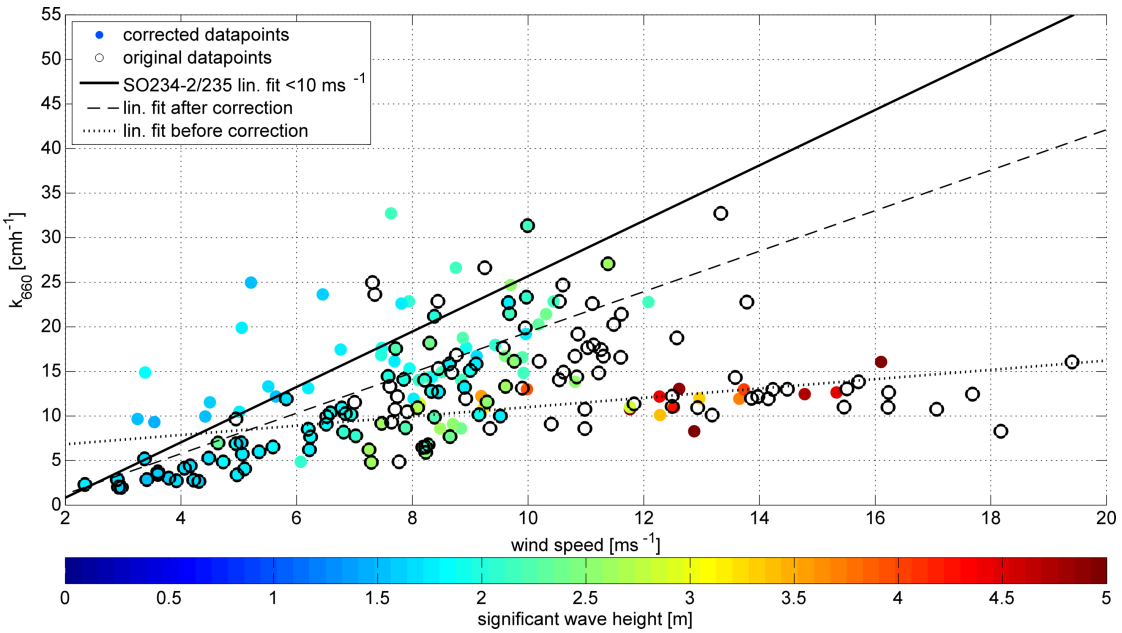

Figure 5.3: Correction of the Knorr11 DMS fluxes. The data points with $Re_{tr} < 6.7 \cdot 10^5$ were corrected using the gas transfer limitation model. Black circles denote k values at the original wind speed u_{10}. Colored filled circles denote the k value at wind speed=u_{alt}. The color shows the significant wave height. If a data point has a concentric black and filled circle, it was not corrected as it was not subject to gas transfer limitation. The black solid line is the ZAV17 parameterization. The dotted line is the linear fit to the data points before the correction, the dashed line is the linear fit after the correction.

linear fit of SO234-2/235. The change of the linear fit to the corrected and uncorrected data set can be seen in the dotted (before) and dashed (after) line. The corrected data points at 12-16 m s^{-1} are still, relative to the linear estimates, heavily gas transfer limited. A reason could be that the significant wave height of these points is larger than 3.5 m and they experienced high wind speed. A shielding of wind by the large wave or an influence of water droplets on the momentum transfer is suggested as reason [Yang et al., 2016, Bell et al., 2013]. In principle, we agree that this process may be occurring, but we hypothesize that it occurs only during exceptional cases of high winds and wave high heights. The Reynolds gas transfer limitation [Zavarsky et al., 2018] occurs over a larger range of wind speeds and wave heights, but obviously does not capture all the flux limitation. Therefore, it appears that several processes may be responsible for gas transfer limitation and they are not all considered in our model. This marks the upper boundary for environmental conditions for our model.
Table 5.1 shows the average offset between every data point and the linear fit ZA18. A reduction of the average offset can be seen for all data combinations. The last two columns of Table 5.1 show the mean absolute error. The absolute error also decreases with the application of our correction. The linear fits to the two data sets, before and

after the corrections, are given in Tab. (5.2).
The slopes for the two corrected data sets show a good agreement. However, we do not correct for the rollover entirely. The corrected slopes are both are in the range of the linear function from SO234-2/235 <10 m s^{-1} $k_{660} = 3.1 \pm 0.37 \cdot u_{10} - 5.37 \pm 2.35$ [Zavarsky et al., 2018], but the slopes barely overlap within the 95 % confidence interval.

reference fit all [cm h^{-1}]	SO234-2/235 mean diff.	Knorr11 mean diff.	SO234-2/235 mean(||)	Knorr11 mean(||)
lin. fit SO234-2/235 to corrected	-1.2	-6.7	5.5	8.1
lin. fit SO234-2/235 to uncorrected	-2.8	-10.3	6.4	10.7

Table 5.1: Mean differences between the fits in column one and the corrected and the uncorrected k data sets. A negative value describes that the fit, on average, overestimates the actual measured data. The mean of the absolute value is presented in the last two columns.

	Knorr11	SO234-2/235
uncorrected	$k_{660} = 0.52 \pm 0.4 \cdot u + 5.79 \pm 4.82$	$k_{660} = 2 \pm 0.42 \cdot u + 0.94 \pm 2.48$
corrected	$k_{660} = 2.27 \pm 0.5 \cdot u - 3.29 \pm 4.08$	$k_{660} = 2.28 \pm 0.45 \cdot u - 0.63 \pm 4.14$

Table 5.2: Linear fits to the corrected and uncorrected data sets of Knorr11 and SO234-2/235. The error estimates correspond to a 95 % confidence interval.

5.5.2 Nightingale parameterization

The N00 [Nightingale et al., 2000] parameterization is a quadratic wind speed dependent parameterization of k. It is widely used, especially for bulk CO_2 gas flux calculations as well as for DMS flux calculations in Lana11 [Lana et al., 2011]. The parameterization is based upon dual tracer measurements in the water performed by in the North Sea [Watson et al., 1991, Nightingale et al., 2000] as well as data from the Florida Strait (FS) [Wanninkhof et al., 1997] and Georges Bank (GB) [Wanninkhof, 1992].
We analyzed each individual measurement that was used in the parameterization to asses the amount of gas transfer limiting instances that are within the N00 parameterization. The single measurements, which are used for fitting the quadratic function of the N00 parametrization, are shown together with N00 in the left panel of Figure 5.4. As the measurement time of the dual tracer technique is on the order of days, we interpolated the wind and wave data to 1 h time steps and calculated the number of gas transfer limiting and gas transfer non-limiting instances. The right panel of Figure 5.4 shows the limitation index which is the ratio of gas limiting instances to the number of data points (x-axis). The value 1 indicates that all of the interpolated one hour steps were gas transfer limited. The y-axis of Figure 5.4 depicts the relation of the individual measurement to the N00 parameterization. A ratio (y-axis) of 1 indicates that the measurement point is exactly the same as the N00 parameterization. A value of 1.1 would indicate that the

value was 10 % higher than predicted by the N00 parameterization.
We expect a negative correlation between the gas transfer limitation index and the relation of the individual measurement vs the N00 parameterization. The higher the limitation index, the higher the gas transfer limitation, the lower the gas transfer velocity k in with respect to the average parametrization. The correlation (Spearman's rank) is -0.43 with a significance level (p-value) of 0.11. This is not significant. However, we have to take a closer look at two specific points: [1] Point 11, GB11 that shows low measurement percentage despite a low limitation index, and [2] point 14, FS14 that shows high measurement percentage despite a high limitation index. GB11 at the Georges Bank showed an average significant wave height of 3.5 m, with a maximum of 6 m and wind speed between 9-13 m s^{-1}. As already discussed in Sect. 5.5.1 using the Knorr11 data set, wave heights above 3.5 m could lead to gas transfer limitation without being captured by Reynolds gas transfer limitation model [Zavarsky et al., 2018]. High waves together with the strong winds could mark an upper limit of the gas transfer limitation model [Zavarsky et al., 2018]. On the other hand the FS14 data point showed an average wave height of 0.6 m and wind speed of 4.7 m s^{-1}. It is questionable if a flow separation and a substantial wind wave interaction can be established at this small wave height. This could mark the lower boundary for the Reynolds gas transfer limitation model [Zavarsky et al., 2018]. Taking out either or both of these measurements (GB11 or FS14) changes the correlation (Spearmans' rank) to -0.62 p=0.0233 (no GB11), -0.59 p=0.033 (no FS14) and -0.79 p=0.0025 (no GB11, no FS14). All three are significant. The black solid line in the right panel of Figure 5.4 is a fit, which is based on the Equation (5.14), to all points but GB11 and FS14.

$$y\left(x\right) = a_1 + a_2 \cdot \frac{1}{x - a_3} \tag{5.14}$$

We chose this functional form, because we follow the finding by Zavarsky et al. [2018] that the effect of gas transfer limitation is not linear but rather has a threshold. This means that the influence of limitation on gas transfer is relatively low with a small limitation ratio, but increases strongly. The fit coefficients are:a_1 =1.52, a_2=0.14 and a_3=1.18 .
Figure 5.5 shows, according to the gas transfer model, corrected data points. A new quadratic fit was applied to the corrected data points ((Equation 5.15), Figure 5.5).

$$k_{660} = 0.359 \cdot u^2 \tag{5.15}$$

On average the new parameterization is 22 % higher than the original N00 parameterization. This increase is caused by the heavy gas transfer limitation of the individual measurements. As we believe that this limitation only affects the interfacial k_o gas exchange, it might not be easily visible (decreasing k vs u relationship) in parameterizations based on dual tracer gas transfer measurements because of the potential of a large bubble influence.

5.5.3 Wanninkhof parameterization

The W14 parameterization estimates the gas transfer velocity using the natural disequilibrium between ocean and atmosphere of ^{14}C and the bomb ^{14}C inventories. The

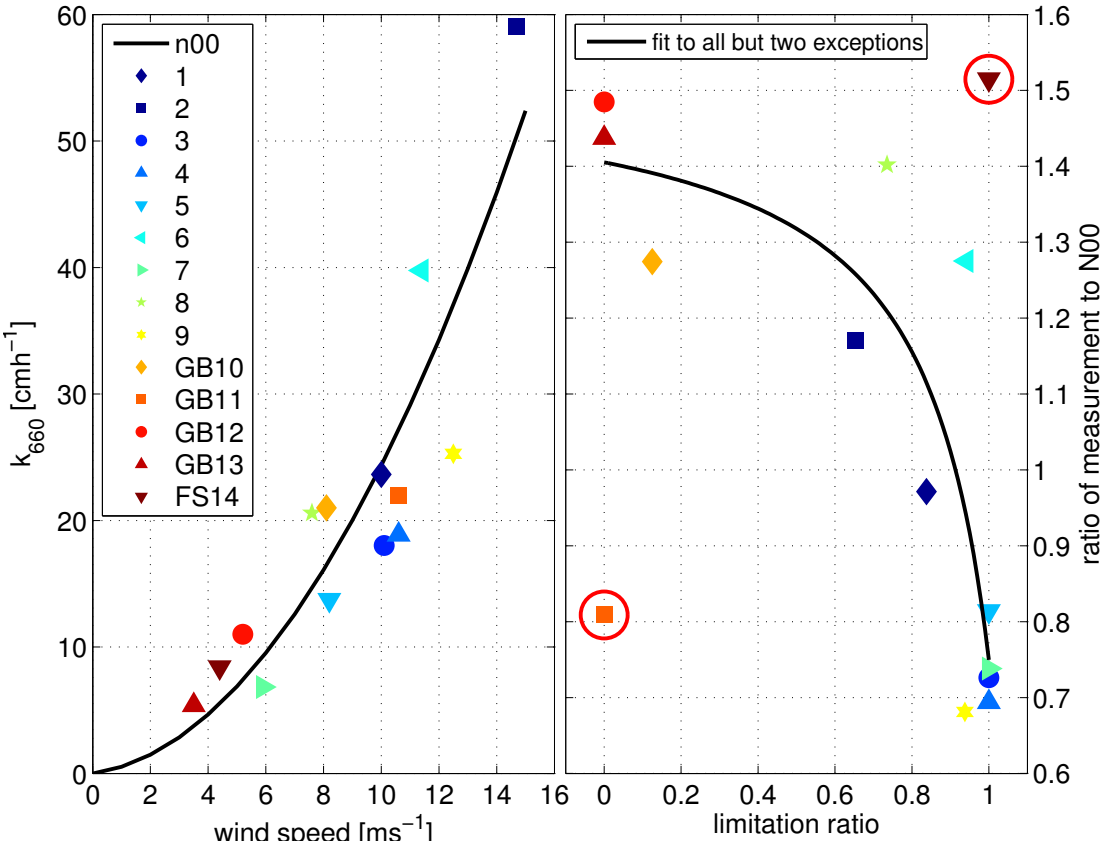

Figure 5.4: Individual dual tracer measurements which contribute to the N00 (solid line) parameterization [left panel]. The relationship of the gas limitation ratio to the measurement/N00 ratio [right panel]. A higher limitation ratio indicates a longer influence of gas transfer limitation on the data point. The solid line in the right panel is a fit to the limitation to measurement/N00 relationship. The two red circles denote the outlier points which are discussed in the text. The black solid line is a fit using the function $y\,(x) = a_1 + a_2 \cdot \frac{1}{x - a_3}$. The fit coefficients are:a_1 =1.52, a_2=0.14 and a_3=1.18 .

total global gas transfer over several years is estimated by the influx of the ^{14}C in the ocean[Naegler, 2009] and the global wind speed distribution over several years. The parameterization from W14 is for winds averaged over several hours. The WWIII model winds, used here, are 3 hourly and therefore in the proposed range [Wanninkhof, 2014]. The W14 parameterization is given in Equation (5.16).

$$k_{660,W14} = 0.251 \cdot (u_{10})^2 \tag{5.16}$$

The interesting point about this parameterization is that it already includes a global average gas transfer limiting factor. The parametrization is independent of local gas transfer limitation events. It utilizes a global, over many years averaged, gas transfer velocity of ^{14}C and relates it to remotely sensed wind speed. This means that the

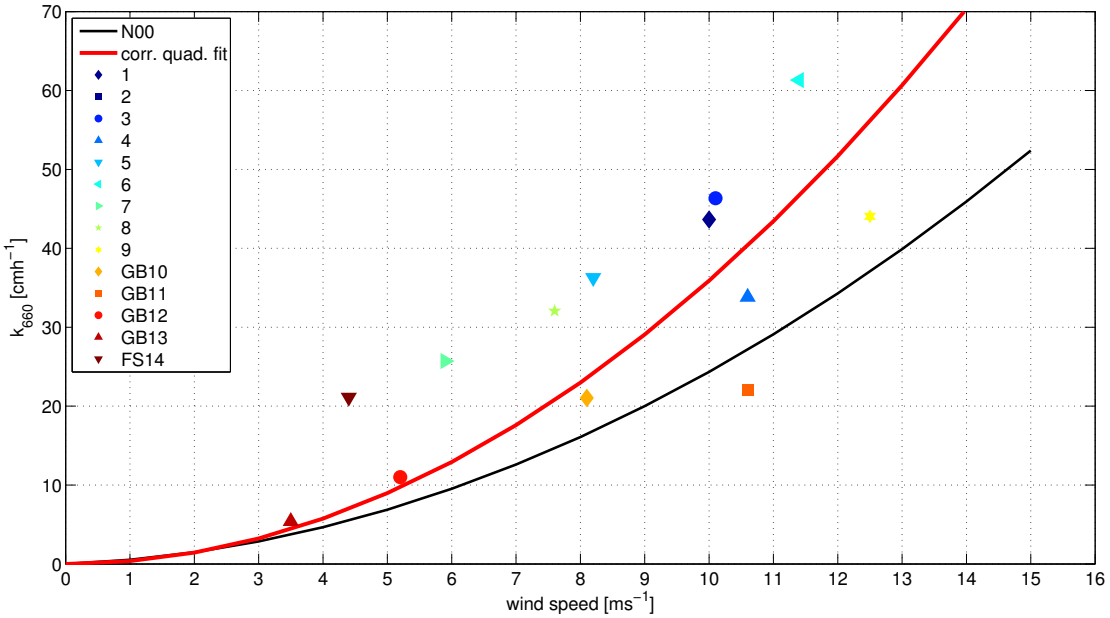

Figure 5.5: Corrected individual measurements, comprising the N00 parameterization, resulting from the algorithm described in Section 5.4. The difference between u_{alt} and the original u_{10} was added to k using the linear parameterization ZAV17. This is correcting the limitation of k_o due to wind-wave interaction. The black solid line is the original N00 parametrization. The red line is a new quadratic fit to the corrected data points k=0.359*u^2.

average gas transfer velocity has experienced the average global occurrence of gas transfer limitation and therefore is incorporated in the k vs u parameterization.
The quadratic coefficient a is calculated by dividing the averaged gas transfer velocity k_{glob} by u^2 and the wind distribution distu of u.

$$a = \frac{k_{glob}}{\sum u^2 \cdot distu} \tag{5.17}$$

The quadratic coefficient then defines the wind speed dependent gas transfer velocity k (Equation (5.18)).

$$k = a \cdot u^2 \tag{5.18}$$

The left panel of Figure 5.6 shows the global wind speed distribution of the year 2014 taken from the WWIII model, which is based on the NCEP reanalysis. Additionally, we added the distribution taking our wind speed correction into account. At the occurrence of gas transfer limitation we calculated, as described in Sect. 5.4, u_{alt} as the representative wind speed for the unlimited transfer. The distribution of u_{alt} shifts higher wind speed (10-17 m s^{-1}) to lower wind speed regimes (0-7 m s^{-1}). This alters the coefficient for the quadratic wind speed parametrization. A global average gas transfer velocity of

k_{glob}=16.5 cm h^{-1} [Naegler, 2009] results in a coefficient a=0.2269, using the uncorrected NCEP wind speed distribution. With the u_{alt} distribution a becomes 0.2439. This is an 9.85 % increase. Our uncorrected value of a=0.2269 differs from the W14 value of a=0.251 because we use a different wind speed distribution. The W14 uses a Rayleigh distribution with $\sigma = 5.83$, our NCEP derived $\sigma = 6.04$ and the corrected NCEP $\sigma = 5.78$. This means that the W14 uses a wind speed distribution with a lower global average speed. However, for correction we use the relative gas transfer reduction between our calculated parameterization and our calculated and corrected parameterization. For the calculation of a, we did not use a fitted Rayleigh function but the corrected wind speed distribution from Figure 5.6.

A comparison of W14, N00 and the corrected parameterizations is shown in the right panel of Figure 5.6. N00 shows the lowest relationship between u and k. W14 shows a parameterization with a global averaged gas transfer limitation influence and is therefore slightly higher than N00. It appears that the gas transfer limitation overcompensates the smaller bubble mediated gas transfer of CO_2 (W14). The corrected N00 is significantly higher than the W14+9.85 %. We hypothesize that this difference is based on the different bubble mediated gas transfer of He, SF_6, and CO_2.

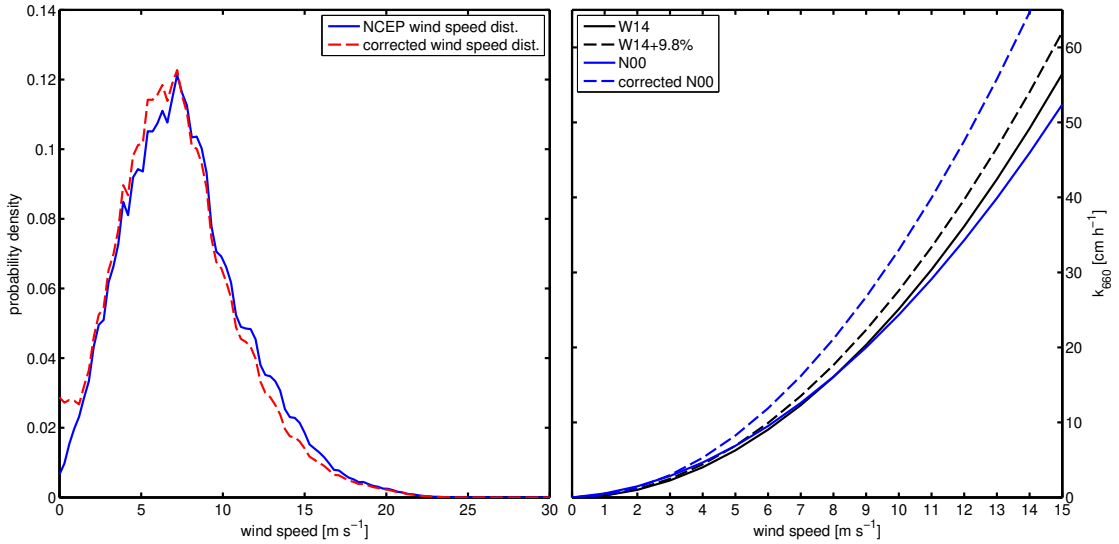

Figure 5.6: Wind speed distributions for the year 2014 [left panel]. The solid line is NCEP derived wind speed distribution, the dashed line the wind speed distribution of the corrected wind speed u_{alt}. Comparison of original and limitation corrected k vs wind speed parameterizations [right panel].

5.5.4 Global Analysis

We used the native global grid (0.5^o x 0.5^o) from the WWIII for the global analysis. The data points from the DMS and CO_2 climatologies as well as all auxiliary variables were

interpolated to this grid.
Figure 5.7 shows the percentage of gas transfer limited data points with respect to the total data points for every month in the year 2014. The average yearly global percentage is 18.6 %. The minimum is 15 % in March and April and the maximum is 22 % JJA. Coastal areas and marginal seas seem to be more influenced than open oceans. The reason could be that gas transfer limitation is likely to occur at fully developed seas when the wind speed is in the same direction and magnitude as the wave's phase speed. At coastal areas and marginal seas, the sea state is less influenced by swell and waves that were generated at a remote location. Landmasses block swell from the open ocean to marginal seas. The intra-annual variability of gas transfer limitation is shown in Figure 5.8. Additionally, we plotted the occurrences split into ocean basins and Northern and Southern Hemisphere. Two trends are visible. There is a higher percentage of gas transfer limitation in the Northern Hemisphere and, on the time axis, the peak is in the respective (boreal and aural) summer season. The Southern Hemisphere has a water-landmass ratio of 81 %, the northern Hemisphere's ratio is 61 %. The area of free open water is therefore greater in the southern part. Fully developed seas without remote swell influence favor gas transfer limitation. In the Southern Hemisphere, the large open ocean areas, where swell can travel longer distances, provide an environment without gas transfer limitation. The peak in summer and minimum in winter can be associated with the respective sea ice extent on the Northern and Southern Hemisphere. Figure 5.7 shows that seas, which are usually ice covered in winter, show a high ratio of gas transfer limitation.

The global reduction of the CO_2 and DMS flux is shown for every month in Figure 5.9 and 5.10. Most areas with a reduced influx of CO_2 into the ocean are in the northern Hemisphere. The only reduced CO_2 influx areas of the Southern Hemisphere are in the south Atlantic and west of Australia and New Zealand. Significantly reduced CO_2 efflux areas are found in the northern tropical Atlantic, especially in the boreal summer months, the northern Indian Ocean and the Southern Ocean.
For the DMS flux (Figure 5.9) the absolute values of reduction, due to gas transfer limitation, coincide with the summer maximum of DMS concentration and therefore large air-sea fluxes [Lana et al., 2011, Simó and Pedrós-Alió, 1999]. In the boreal winter the northern Indian Ocean also shows a high level (10 μmol m^2 d^{-1}) of reduction. The highest water concentrations and fluxes in the Indian Ocean are found in boreal summer [Lana et al., 2011], which does not seem to be greatly influenced by gas transfer limitation.

The total amount of carbon taken up by the ocean is shown in Table 5.3. We calculate a total carbon uptake for the year 2014 of 1.15 Pg C for the N00 parameterization without the effect of gas transfer limitation. This value is reduced by the gas transfer limitation model to 1.06 Pg C, which is a reduction of 8 %. The W14 parameterization yields an uptake of 1.16 Pg C and with the limitation model an uptake of 1.06 Pg C which is a difference of 9 %. For the parameterization used in the Takahashi climatology [Takahashi et al., 2009], we calculated a total uptake of 1.28 Pg C without gas transfer limitation. Adding the effect of gas transfer limitation, we get a value of 1.19 Pgram C which is a reduction of 7 %. The global value from the Takahashi climatology [Takahashi et al., 2009] is 1.42 Pgram C yr^{-1}. Rödenbeck [Rödenbeck et al., 2015] estimate 1.75 Pg C yr^{-1} as

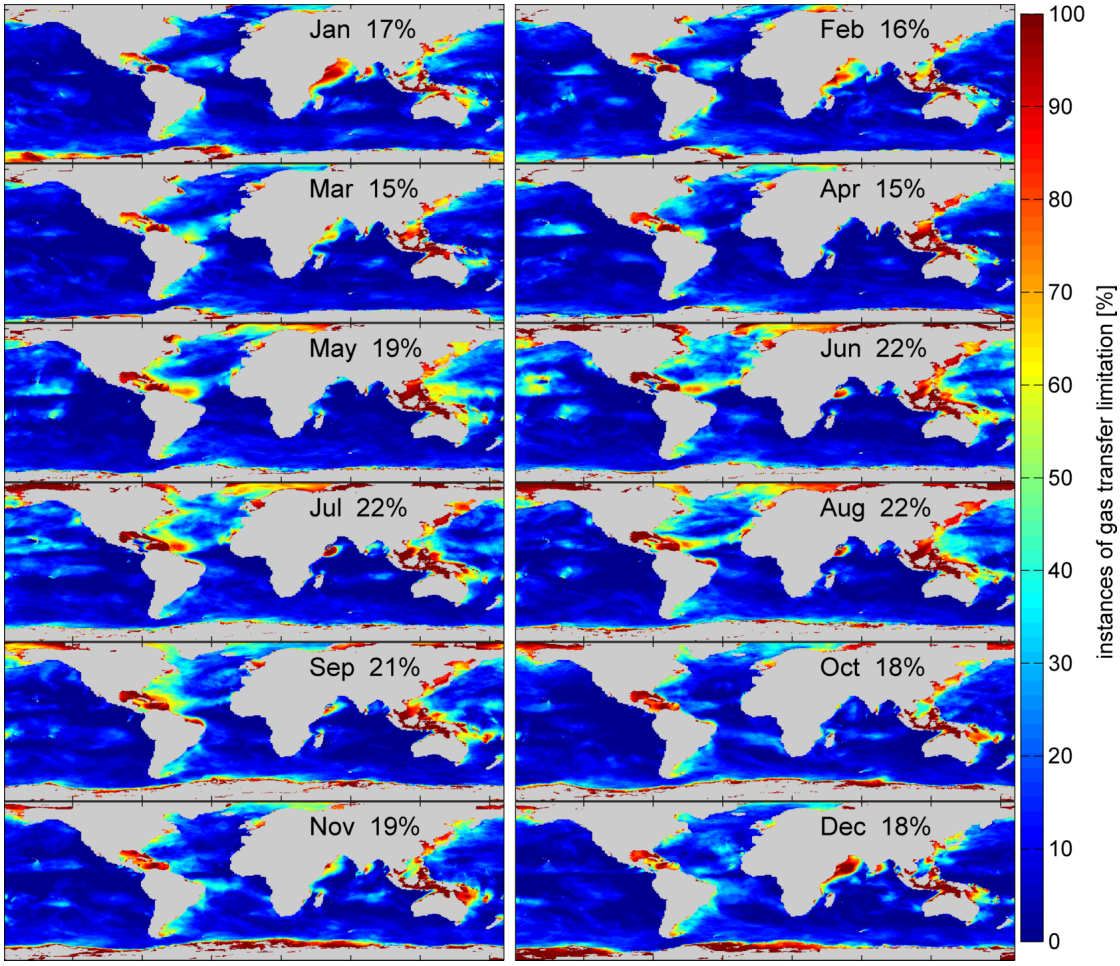

Figure 5.7: The global probability of experiencing gas transfer limitation during the respective month (2014). The percentage is the number of gas transfer limited occurrences with respect to the total data points with a 3 h resolution.

uptake between 1992 and 2009. The difference between our calculation and the estimates from the global climatologies are [1] due to the different reference year, Takahashi 2000 / Rödenbeck 1992-2009 / this study 2014, which leads to different wind speed, ΔpCO_2 and SST data. [2] The data set and influence for sea ice cover is different. However, the estimated reduction of 7-9 %, due to gas transfer limitation, is also valid for the Takahashi and Rödenbeck estimates.

The DMS emissions from the ocean to the atmosphere are shown in Table 5.4. The calculated total emission from the N00 parameterization is 50.72 Tg DMS yr^{-1} for the year 2014. This is reduced, due to our gas transfer limitation calculations, to 45.47 Tg DMS yr^{-1}, which is a reduction of 11 %. The linear parameterization ZA18 estimates an emission of 56.22 Tg DMS yr^{-1}. Using the gas transfer limitation model the linear parameterization is reduced to 51.07 Tg DMS yr^{-1}, which is a reduction

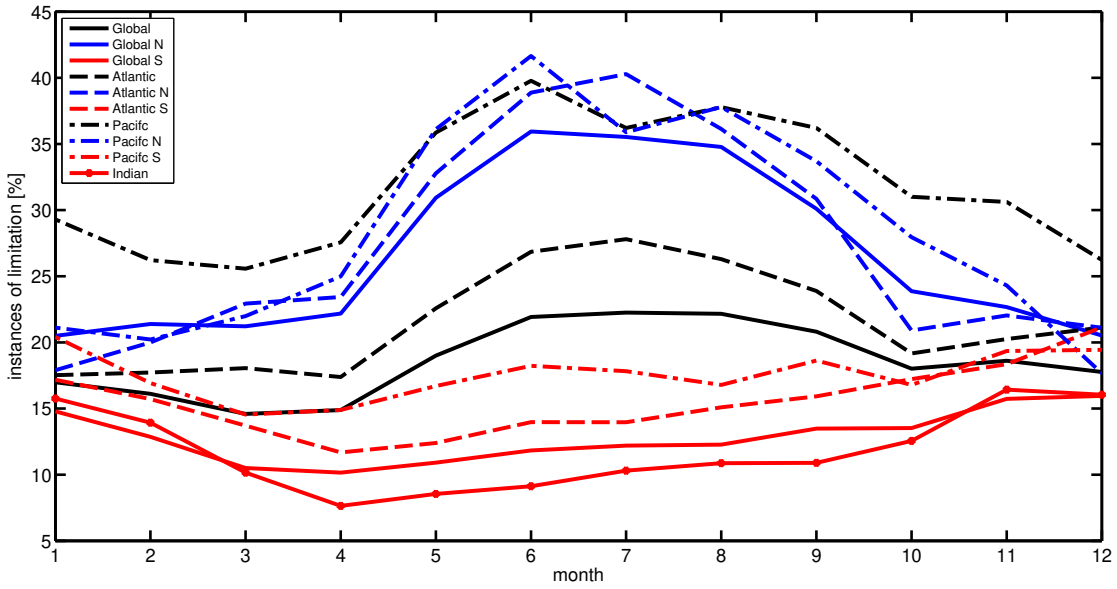

Figure 5.8: The probability of experiencing gas transfer limitation during the respective month (2014) divided into ocean basins and hemisphere. The Southern Ocean was added to the southern part of the respective ocean basin. The percentage is the number of gas transfer limited instances with respect to the total data points with a 3 h resolution.

parameterization	flux [Pg C]
N00	1.15
N00 Re_{tr}	1.06
W14	1.16
W14 Re_{tr}	1.06
Tak09	1.28
Tak09 Re_{tr}	1.19
Takahashi 2009 [Takahashi et al., 2009]	1.42 Pg yr^{-1}
Rödenbeck [Rödenbeck et al., 2015]	1.75 Pg yr^{-1}

Table 5.3: 2014 carbon flux in Pg. Re_{tr} indicates an application of the gas transfer limitation model. The last two lines are estimates from previous published work.

of 11 %. Global estimates are 54.39 Tg DMS yr^{-1}(Lana11 [Lana et al., 2011]) and 45.5 Tg DMS yr^{-1}(Lennartz15 [Lennartz et al., 2015]). Similar to the reasons we mentioned in the paragraph above, a difference in wind speed or sea ice coverage could be the reason for the difference in the global emission estimated between the Lana climatology and our calculations with the N00 parameterization. Lennartz15 [Lennartz et al., 2015] uses the water concentrations from the Lana climatology, but includes air-side DMS concentrations, which reduces the flux by 17 %. We do not include air-side DMS concentrations but gas transfer limitation, which reduces the flux by 11 %. Including

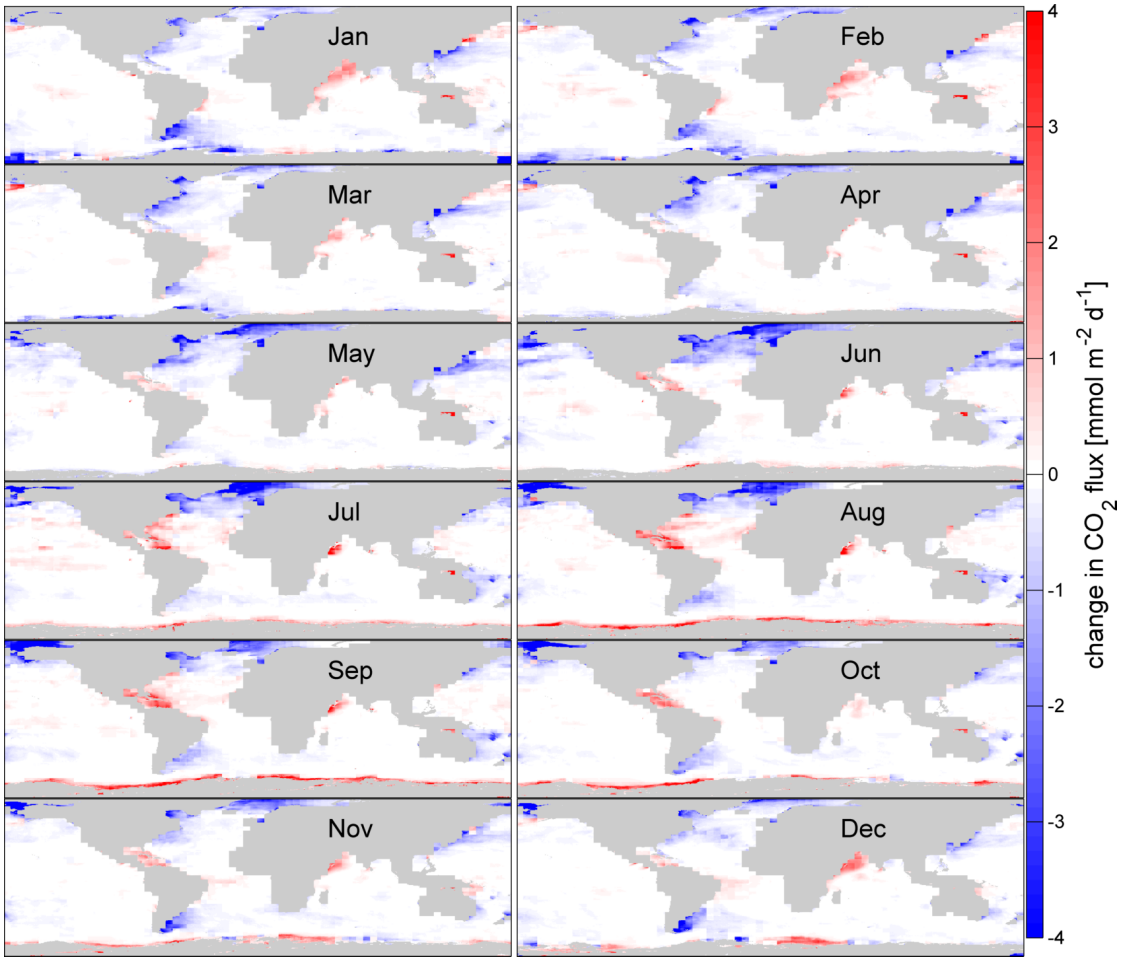

Figure 5.9: The absolute change of CO_2 gas transfer due to limitation for each month of 2014. Negative values (blue) denote areas where a flux into the ocean is reduced by the shown value. Positive values denote areas where flux out of the ocean is reduced by the shown value.

both processes we can expect a reduction of 20-30 %.

The global CO_2 air-sea flux is reduced by 7-9 % due to gas transfer limitation. The impact on the DMS climatology is 11 %. This is in the range of 9.85 % which is the estimated influence of gas transfer limitation on the W14 parametrization through a different wind speed distribution. The different reduction percentages between these two gases are attributed to the larger bubble mediated gas transfer of CO_2, which compensated the loss of flux for CO_2 but not for DMS.

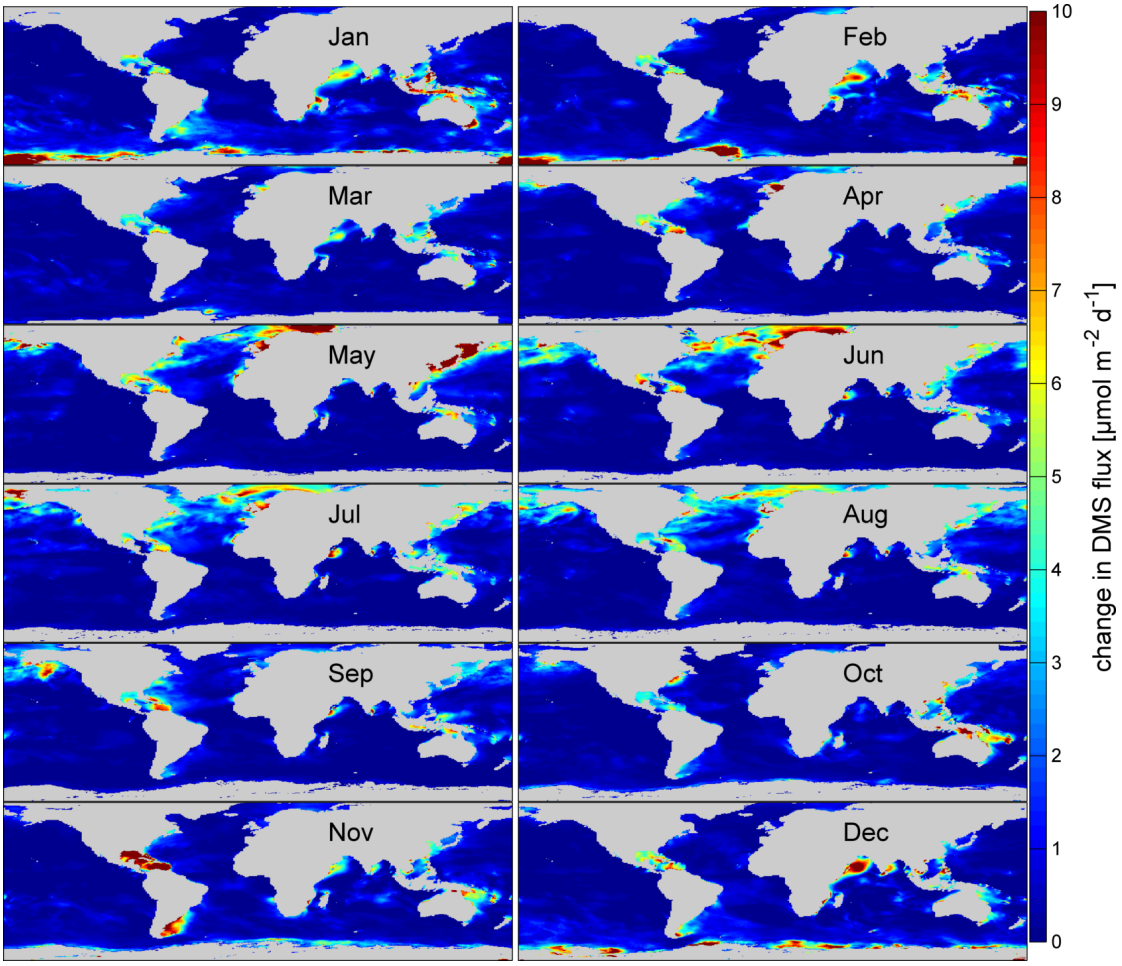

Figure 5.10: The absolute change of DMS gas transfer due to limitation for each month of 2014. The shown magnitudes denote the reduction by gas transfer limitation.

5.6 Conclusion

We provide a model to correct for the gas transfer limitation due to wind-wave interaction [Zavarsky et al., 2018]. Re_{tr} and the resulting alternative wind speed u_{alt} can be calculated from standard meteorological and oceanographic variables. Additionally the condition (period, height, direction) of the ocean waves have to be known or retrieved from wave models. The calculation is iterative and can be easily implemented. The effect of the correction is shown with two data sets from the Knorr11 [Bell et al., 2017] and the SO234-2/235 cruise [Zavarsky et al., 2018]. Both data sets show, after the correction, a better agreement with the linear ZA18 parameterizations (Table 5.1and Table 5.2), which only contains non limited gas transfer velocity measurements from the SO 234-2/235 cruise. Generally, the correction may be only applied to the interfacial gas transfer velocity k_o.

parameterization	flux [Tg DMS yr^{-1}]
N00	50.72
N00 Re_{tr}	45.47
ZA18	56.22
ZA18 Re_{tr}	51.07
Lana11 [Lana et al., 2011]	54.39 Tg DMS yr^{-1}
Lennartz15 [Lennartz et al., 2015]	45.5 Tg DMS yr^{-1}

Table 5.4: 2014 DMS flux in Tg. Re_{tr} indicates an application of the gas transfer limitation model. The last two lines are estimated from global climatologies

We investigated the individual measurements leading to the N00 gas transfer parameterization for the influence of gas transfer limitation. We think that the overall parameterization is heavily influenced by gas transfer limitation but, due to the measurement method (dual tracer measurements), the limitation is masked by bubble mediated gas transfer. We show a significant negative correlation between the occurrence of gas transfer limitation and the ratio of the individual measurement to the N00 parameterization. We applied a gas transfer limitation correction and fitted a new quadratic function to the corrected data set. The new parameterization is on average 22 % higher than the original N00 parameterization. This leads to the conclusion that gas transfer limitation influences gas transfer parameterizations, even if it is not directly visible, via a smaller slope.
For the W14 parameterization we used a global wind speed climatology for the year 2014 and applied the gas transfer limitation model $u_{10} \rightarrow u_{alt}$. Using the distribution function of u_{alt} we calculated a corrected gas transfer parameterization. The coefficient of the corrected parameterization is 9.85 % higher than the original one. W14 already includes the global average of gas transfer limitation. Therefore the increase, due to the correction, is expected to be less than the one for N00. The uncorrected N00 is lower than W14, but after correction N00 is larger than the corrected W14, which is expected due to the larger bubble mediated gas transfer of He and SF_6 over CO_2.
In addition, we calculated the global carbon uptake of CO_2 due to air-sea exchange and the global emission of DMS. The reduction, due to the consideration of gas transfer limitation, is between 7-9 % for CO_2 and 11 % for DMS. This is in the range of the calculated influence of gas transfer limitations on the global parameterization W14.
We think that gas transfer limitation has a global influence on air-sea gas exchange of 7-11 %. These numbers are supported by the correction of the W14 parametrization as well a global DMS and CO_2 gas transfer calculation. Local conditions may lead to much higher influences. Gas transfer velocity parameterizations from regional data sets might be heavily influenced by gas transfer limitations. We have shown this for the N00 parameterization. This should be considered with their use.
For global calculations we recommend the use of the Wanninkhof parameterizations [Wanninkhof, 2014], as it already has an average global gas transfer limitation included. We recommend using a linear parameterization (e.g. ZAV17) for rather soluble gases, such as DMS, in the cases of non-limited gas transfer. The limitation can be determined

using the Re_{tr} parameter. If conditions favor limitation, we recommend our iterative approach to correct u to u_{alt} (Figure 5.1). For gases with a similar solubility as CO_2, we recommend the use of W14. In case of no gas transfer limitation, we recommend the used of the corrected W14+9.85 % parameterization. The corrected N00 (N00+22 %) parameterization is recommended for very insoluble gases with the absence of gas transfer limitation, the original N00 is recommended for the gas transfer limited case.

References

T. G. Bell, W. De Bruyn, S. D. Miller, B. Ward, K. H. Christensen, and E. S. Saltzman. Air-sea dimethylsulfide (dms) gas transfer in the north atlantic: evidence for limited interfacial gas exchange at high wind speed. *Atmos. Chem. Phys.*, 13(21):11073–11087, nov 2013. ISSN 1680-7324. doi: 10.5194/acp-13-11073-2013. URL http://www.atmos-chem-phys.net/13/11073/2013/.

T. G. Bell, W. De Bruyn, C. A. Marandino, S. D. Miller, C. S. Law, M. J. Smith, and E. S. Saltzman. Dimethylsulfide gas transfer coefficients from algal blooms in the southern ocean. *Atmos. Chem. Phys.*, 15(4):1783–1794, feb 2015. ISSN 1680-7324. doi: 10.5194/acp-15-1783-2015. URL http://www.atmos-chem-phys.net/15/1783/2015/.

T. G. Bell, S. Landwehr, S. D. Miller, W. J. de Bruyn, A. H. Callaghan, B. Scanlon, B. Ward, M. Yang, and E. S. Saltzman. Estimation of bubble-mediated air–sea gas exchange from concurrent dms and co2 transfer velocities at intermediate–high wind speeds. *Atmospheric Chemistry and Physics*, 17(14):9019–9033, 2017. doi: 10.5194/acp-17-9019-2017. URL https://www.atmos-chem-phys.net/17/9019/2017/.

B. W. Blomquist, S. E. Brumer, C. W. Fairall, B. J. Huebert, C. J. Zappa, I. M. Brooks, M. Yang, L. Bariteau, J. Prytherch, J. E. Hare, H. Czerski, A. Matei, and R. W. Pascal. Wind speed and sea state dependencies of air-sea gas transfer: Results from the high wind speed gas exchange study (hiwings). *Journal of Geophysical Research: Oceans*, pages n/a–n/a, oct 2017. ISSN 2169-9291. doi: 10.1002/2017JC013181. URL http://dx.doi.org/10.1002/2017JC013181.

D. P. Dee, S. M. Uppala, A. J. Simmons, P. Berrisford, P. Poli, S. Kobayashi, U. Andrae, M. A. Balmaseda, G. Balsamo, P. Bauer, P. Bechtold, A. C. M. Beljaars, L. van de Berg, J. Bidlot, N. Bormann, C. Delsol, R. Dragani, M. Fuentes, A. J. Geer, L. Haimberger, S. B. Healy, H. Hersbach, E. V. Holm, L. Isaksen, P. Kållberg, M. Köhler, M. Matricardi, A. P. McNally, B. M. Monge-Sanz, J. J. Morcrette, B. K. Park, C. Peubey, P. de Rosnay, C. Tavolato, J. N. Thepaut, and F. Vitart. The era-interim reanalysis: configuration and performance of the data assimilation system. *Quarterly Journal of the Royal Meteorological Society*, 137(656):553–597, apr 2011. ISSN 1477-870X. doi: 10.1002/qj.828. URL http://dx.doi.org/10.1002/qj.828.

Kirsty E. Hanley, Stephen E. Belcher, and Peter P. Sullivan. A global climatology of wind-wave interaction. *Journal of Physical Oceanography*, 40(6):1263–1282, 2010. doi: 10.1175/2010JPO4377.1. URL http://dx.doi.org/10.1175/2010JPO4377.1.

Satoru Komori, Wade McGillis, and Ryoichi Kurose. *Gas Transfer at Water Surfaces, 2010*. Kyoto University, 2011. URL http://hdl.handle.net/2433/156156.

A. Lana, T. G. Bell, R. Simo, S. M. Vallina, J. Ballabrera-Poy, A. J. Kettle, J. Dachs, L. Bopp, E. S. Saltzman, J. Stefels, J. E. Johnson, and P. S. Liss. An updated climatology of surface dimethlysulfide concentrations and emission fluxes in the global ocean. *Global Biogeochemical Cycles*, 25(1):n/a–n/a, jan 2011. ISSN 1944-9224. doi: 10.1029/2010GB003850. URL http://dx.doi.org/10.1029/2010GB003850.

S. T. Lennartz, G. Krysztofiak, C. A. Marandino, B.-M. Sinnhuber, S. Tegtmeier, F. Ziska, R. Hossaini, K. Krüger, S. A. Montzka, E. Atlas, D. E. Oram, T. Keber, H. Bönisch, and B. Quack. Modelling marine emissions and atmospheric distributions of halocarbons and dimethyl sulfide: the influence of prescribed water concentration vs. prescribed emissions. *Atmospheric Chemistry and Physics*, 15(20):11753–11772, 2015. doi: 10.5194/acp-15-11753-2015. URL https://www.atmos-chem-phys.net/15/11753/2015/.

Tobias Naegler. Reconciliation of excess 14c-constrained global co2 piston velocity estimates. *Tellus B: Chemical and Physical Meteorology*, 61(2):372–384, 2009. doi: 10.1111/j.1600-0889.2008.00408.x. URL https://doi.org/10.1111/j.1600-0889.2008.00408.x.

Philip D. Nightingale, Gill Malin, Cliff S. Law, Andrew J. Watson, Peter S. Liss, Malcolm I. Liddicoat, Jacqueline Boutin, and Robert C. Upstill-Goddard. In situ evaluation of air-sea gas exchange parameterizations using novel conservative and volatile tracers. *Global Biogeochemical Cycles*, 14(1):373–387, mar 2000. ISSN 1944-9224. doi: 10.1029/1999GB900091. URL http://dx.doi.org/10.1029/1999GB900091.

C. Rödenbeck, D. C. E. Bakker, N. Gruber, Y. Iida, A. R. Jacobson, S. Jones, P. Landschützer, N. Metzl, S. Nakaoka, A. Olsen, G.-H. Park, P. Peylin, K. B. Rodgers, T. P. Sasse, U. Schuster, J. D. Shutler, V. Valsala, R. Wanninkhof, and J. Zeng. Data-based estimates of the ocean carbon sink variability first results of the surface ocean pco2 mapping intercomparison (socom). *Biogeosciences*, 12(23):7251–7278, 2015. doi: 10.5194/bg-12-7251-2015. URL https://www.biogeosciences.net/12/7251/2015/.

Rafel Simó and Carlos Pedrós-Alió. Role of vertical mixing in controlling the oceanic production of dimethyl sulphide. *Nature*, 402(6760):396–399, nov 1999. doi: 10.1038/46516.

Taro Takahashi, Stewart C. Sutherland, Rik Wanninkhof, Colm Sweeney, Richard A. Feely, David W. Chipman, Burke Hales, Gernot Friederich, Francisco Chavez, Christopher

Sabine, Andrew Watson, Dorothee C.E. Bakker, Ute Schuster, Nicolas Metzl, Hisayuki Yoshikawa-Inoue, Masao Ishii, Takashi Midorikawa, Yukihiro Nojiri, Arne Körtzinger, Tobias Steinhoff, Mario Hoppema, Jon Olafsson, Thorarinn S. Arnarson, Bronte Tilbrook, Truls Johannessen, Are Olsen, Richard Bellerby, C.S. Wong, Bruno Delille, N.R. Bates, and Hein J.W. de Baar. Climatological mean and decadal change in surface ocean pco2, and net sea–air co2 flux over the global oceans. *Deep Sea Research Part II: Topical Studies in Oceanography*, 56(8):554 – 577, 2009. ISSN 0967-0645. doi: http://dx.doi.org/10.1016/j.dsr2.2008.12.009. URL http://www.sciencedirect.com/science/article/pii/S0967064508004311. Surface Ocean CO2 Variability and Vulnerabilities.

H. L Tolman. User manual and system documentation of wavewatch-iii version 1.15. *NOAA / NWS / NCEP / OMB Technical Note*, 151:97, 1997.

H. L Tolman. User manual and system documentation of wavewatch-iii version 1.18. *NOAA / NWS / NCEP / OMB Technical Note*, 166:110, 1999.

Hendrik L Tolman. User manual and system documentation of wavewatch iii tm version 3.14. *NOAA / NWS / NCEP / MMAB Technical Note*, 276:220, 2009.

Rik Wanninkhof. Relationship between wind speed and gas exchange over the ocean. *Journal of Geophysical Research: Oceans*, 97(C5):7373–7382, 1992. ISSN 2156-2202. doi: 10.1029/92JC00188. URL http://dx.doi.org/10.1029/92JC00188.

Rik Wanninkhof. Relationship between wind speed and gas exchange over the ocean revisited. *Limnology and Oceanography: Methods*, 12(6):351–362, 2014. ISSN 1541-5856. doi: 10.4319/lom.2014.12.351. URL http://dx.doi.org/10.4319/lom.2014.12.351.

Rik Wanninkhof, Gary Hitchcock, William J. Wiseman, Gabe Vargo, Peter B. Ortner, William Asher, David T. Ho, Peter Schlosser, Mary-Lynn Dickson, Robert Masserini, Kent Fanning, and Jia-Zhong Zhang. Gas exchange, dispersion, and biological productivity on the west florida shelf: Results from a lagrangian tracer study. *Geophysical Research Letters*, 24(14):1767–1770, 1997. ISSN 1944-8007. doi: 10.1029/97GL01757. URL http://dx.doi.org/10.1029/97GL01757.

Andrew J. Watson, Robert C. Upstill-Goddard, and Peter S. Liss. Air-sea gas exchange in rough and stormy seas measured by a dual-tracer technique. *Nature*, 349:145, January 1991. URL http://dx.doi.org/10.1038/349145a0.

F.M. White. *Viscous Fluid Flow*. McGraw-Hill series in mechanical engineering. McGraw-Hill, 1991. ISBN 9780070697126. URL https://books.google.de/books?id=G6IeAQAAIAAJ.

M Yang, T G Bell, B W Blomquist, C W Fairall, I M Brooks, and P D Nightingale. Air-sea transfer of gas phase controlled compounds. *IOP Conference Series: Earth*

and Environmental Science, 35(1):012011, 2016. URL http://stacks.iop.org/1755-1315/35/i=1/a=012011.

A. Zavarsky, L. Goodwijjn-Murphy, T. Steinhoff, and C.A. Marandino. Gas transfer of dms and co2 in the indian ocean. *JGR, Under Review*, 2018.

CHAPTER 6

Conclusion and Outlook

6.1 Future of eddy covariance direct flux measurements

Eddy covariance measurements will be used by a broader scientific community. The need for directly measured, precise and spatially resolved flux measurements is increasing. With decreasing uncertainties of other measurements and their use as model inputs, the bulk formulation (Equation 1.2) together with the choice of the gas transfer parameterization leaves too many open questions about the magnitude of air-sea gas exchange. Eddy covariance, on the other hand, measures the flux directly, including all processes like gas transfer limitation, influence of the SML or bubble enhanced gas transfer.
In the past, both sensors as well as motion correction were an expensive and sophisticated obstacle to a broader usage. Technological advancement has reduced this obstacle. If it is possible to design automated and manageable systems, direct gas flux measurements of at least two different gases could be a standard practice on scientific cruises.

6.1.1 Instrumentation

Motion sensor

With the upcoming use of drones and the improvement of user-electronics, inexpensive and easy-to-use motion sensors are available. The biggest challenge for eddy covariance is the system integration. Sensors have to be synchronized and their data processed. The development work shifts to automation, data processing and book keeping.
Motion sensors can operate at a fast sampling rate (<50 Hz) and can provide much more usable data then necessary to correct for pseudo winds, generated by the ships motion. These data, such as heave or orientation of the ship, can be used for wave analysis or the correction of ocean surface scans.

Gas sensor

The use of a CIMS is expensive, difficult and in connection with radioactive ionization sources a large administrative effort. CIMS have to maintain an ultra-low vacuum, which is an additional difficulty. Generally, mass spectrometers have decreased in size and tend to be more user friendly. However, in my opinion, if they can be replaced with optical measurement methods, the number of users in the scientific community will greatly increase. Optical measurements are fast and easily automatable and electronically controllable by software. They do not use dangerous substances and are able to measure multiple gases simultaneously. Their size is usually much smaller than that of a CIMS, which makes them deployable on small boats or autonomous vehicles. On large ships optical sensors can also be placed directly at the air sample inlet. This has the advantage of a much higher pressure in the measurement cell, which increases the sensitivity. Nevertheless, many compounds may not be measurable with optical methods. Therefore, mass spectrometer need to become smaller, lighter and more user-friendly.
The optical technique shifts from simple absorption measurements (Li-7200, Licor) to cavity ringdown spectroscopy (CRDS, Figure 6.1) and laser dispersion spectroscopy (LDS, Figure 6.2). Both techniques have the advantage to measure more precisely with less cross-correlation with other gas concentrations and to work better in rough environments.

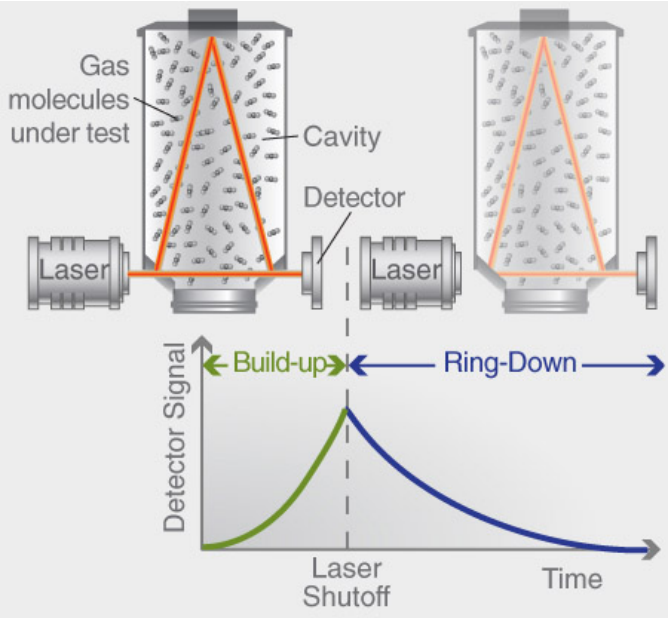

Figure 6.1: Schematic of the CRDS measurement principle. In contrast to simple absorption measurements, CRDS records the decay of the irradiated laser energy. The decay constant is directly related to the gas concentration. Reprinted with the permission of Picarro Inc.

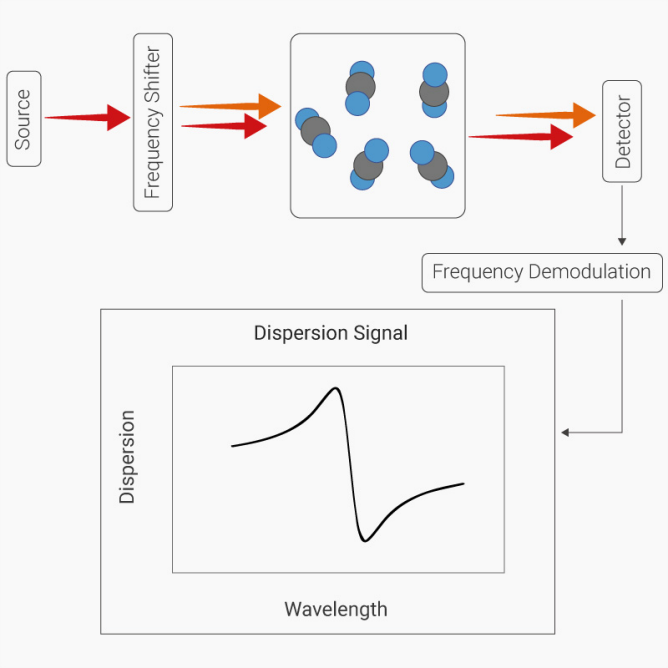

Figure 6.2: Schematic of LDS measurement principle. The molecular dispersion is measured using laser beams with different frequencies. The change of molecular dispersion at a molecular transition is linearly correlated to the mixing ratio of these molecules.

Data acquisition

The technology for recording and synchronizing data is available and inexpensive. With the transition from analog to digital communication and signal processing, the costs will further decrease. The problem is not technology itself but the non-existent best practices for synchronization and data processing. At the moment, each seagoing eddy covariance group is designing its own data acquisition system. There is no common quality goal or quality check for the data acquisition. Publications, also this dissertation, only show the covariance power spectrum c'w' as proof of quality for their data analysis. No one can tell if the c'w' were actually synchronous. Generally, the technology for a sufficient synchronization is available but one has to rely on the programming capabilities of the engineers and researchers that this technology is applied properly.
Data processing also differs significantly between research groups. Figure 2.13 shows the cross correlation (one data set is held constant, the other one is shifted in time) of an eddy covariance measurement. One part of the community is strictly enforcing a time synchronization purely based on estimations and trust in the electronics. They would stick, in this case (Figure 2.13) to an offset of 0 s. The other part of the community would look for a maxima (flux out of the ocean) or minima (flux into the ocean). In this case the offset is set to -0.3 s. The questions is: Who is right? The example in Figure 2.13 shows a flux difference of 10%, depending on this choice.

6.1.2 Calibration

Measurements using a CIMS require constant calibration. First the calibration is done thoroughly in the lab before and after the measurement campaign. Then a calibration gas or secondary standard is also taken to the ship for calibration throughout the campaign. It is not feasible to provide perm tube primary standards on ships. The production, filling, storage and transport is not set to a common standard in the eddy covariance community. Gases like acetone or DMS and their isotopically labeled reference gases might react with the container and over time change their mixing ratio (Table 2.1). Therefore, they are difficult to handle [Allen et al., 2017]. A clear selection of materials and their coatings has to be made to ensure a stable concentration in the reference gas tank. The Swiss Federal Institute of Metrology is and has been involved in several projects (MetNO2, HIGHGAS, KEY-VOCs, [Leuenberger et al., 2017]) to produce high quality and shippable gas standards. A system will be available in cooperation with LNI-Swissgas in the year 2018.
For the CO_2 measurement, certified reference gases which can be taken into the field are readily available.

6.1.3 Standardization

So far, for the sea-going eddy covariance community, no standardization has been done. There has been no workshop, conference or seminar dedicated to best practices or thoughts and improvements about the eddy covariance technique. For the land-based community Aubinet et al. [2012] is a standard reference for eddy covariance. This book is also very useful to the sea-going community, but does not include all necessary steps to calculate fluxes for the sea-going eddy covariance community.
Licor Biosciences maintains the open source project EddyPro[1]. It is a complete flux calculation program which can provide fully corrected fluxes including footprint analysis, random uncertainty estimation and a variety of quality flags. A similar project dedicated to motion correction and flow distortion is strongly needed in the sea-going eddy covariance community.
The sea-going eddy covariance community has the advantage that the land-based community is, in my opinion, in the field of technology, processing and theory 10 years ahead. The sea-going community could just follow their path. This is simple, but it would be wise speed up development and close the 10 years gap. The sea-going community needs a common effort to do this and goals for the development of the technique. Certainly we can learn from the experience of the land-based community.

6.2 Connecting sources and products

Can local DMS emissions be correlated with local satellite aerosol numbers?

[1] https://github.com/LI-COR/eddypro-engine

The positive regional source to product relationship presented in Section 3 appears to agree with the CLAW hypothesis [Charlson et al., 1987]. At the same time, it would weaken the theory that most aerosols are re-entrained from the free troposphere [Quinn and Bates, 2011, Quinn et al., 2017]. I do not call for a revival of the CLAW hypothesis as a whole. In my opinion the strength of the CLAW hypothesis is in the importance of its individual steps, not the feedback overall. The creation of clouds and the aerosol formation in the marine environment are too important just to be investigated in relation to this feedback. The same holds for the other steps. I do call for the idea that air-sea fluxes locally influence aerosol numbers. Using forward trajectories to follow the air parcel, aerosol predecessors were correlated with remotely sensed aerosol numbers. A significant positive correlation was found. For the first time, I connected the advantage of a small spatial and short temporal resolution direct flux measurement with the capabilities of aerosol sensing satellites. It is now possible to connect high and low DMS emission areas with large and small aerosol numbers. This is important for aerosol numbers, local budgets, and models which can draw regional aerosol maps. The radiative aerosol forcing (Figure 6.3) has the greatest uncertainty in its influence on climate change. The future importance is also underlined by 32 already approved aerosol satellite missions (Figure 6.4). It is imperative for the community to take a closer look at the aerosol sources, sinks and pathways.

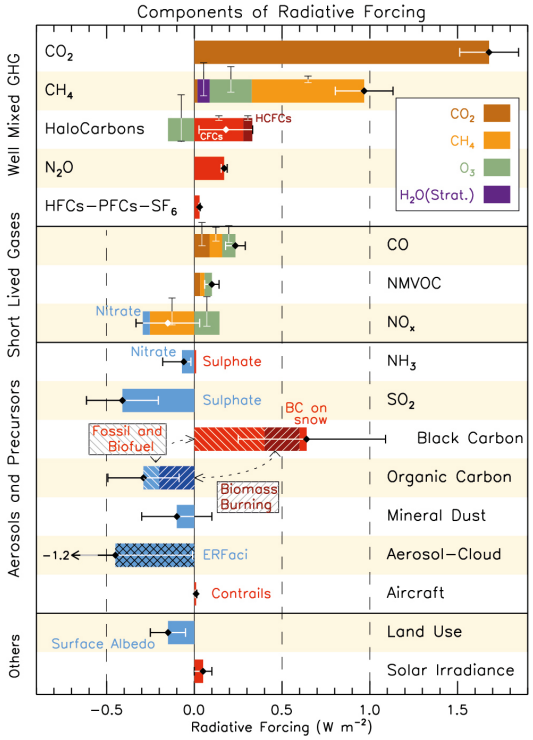

Figure 6.3: Radiative forcing from the AR5 of the IPCC. The error bar of the aerosol-cloud forcing is off the chart.

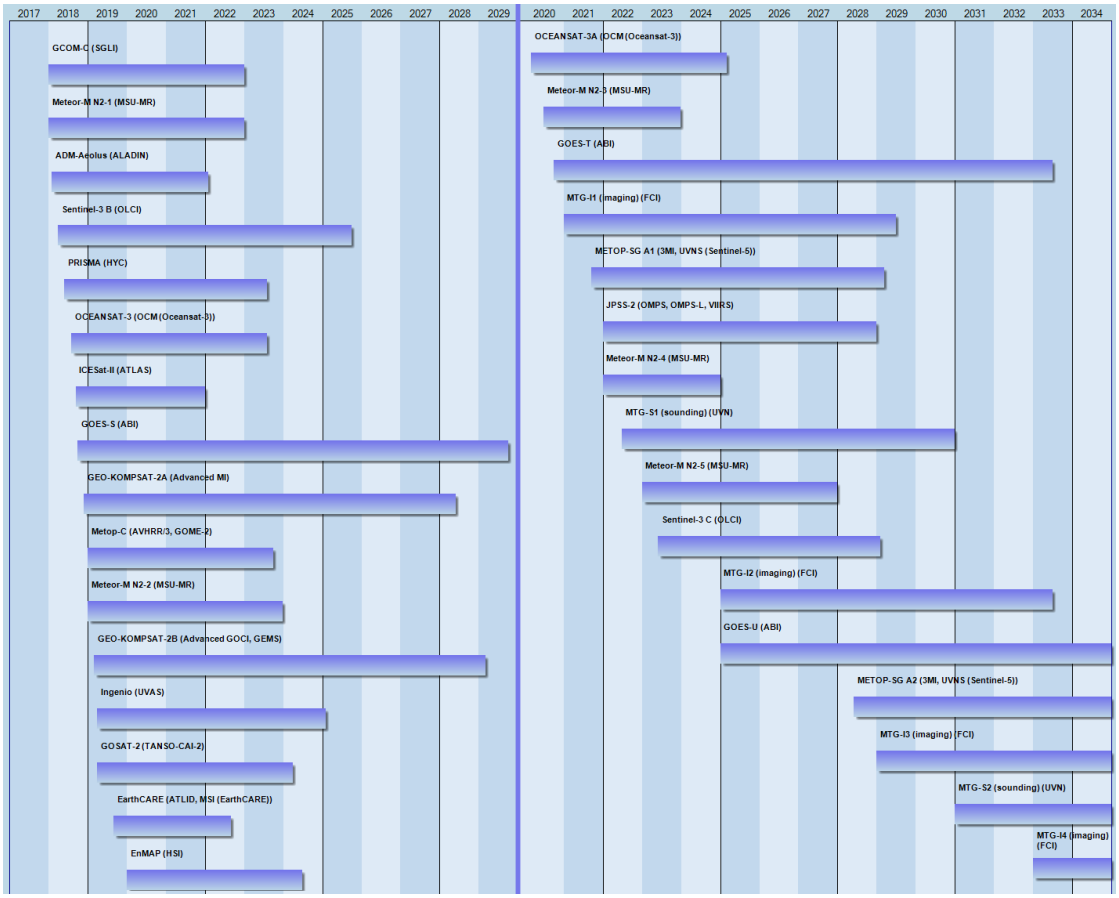

Figure 6.4: Already approved satellite missions with dedicated aerosol measurements [CEOS Database, 2018].

6.2.1 Further investigations

Generally Quinn and Bates [2011] and Quinn et al. [2017] support the idea that aerosol predecessors, along with their conversion processes, are transported into the free troposphere and then are re-entrained into the MBL. My findings in Section 3 do not support this claim. It would be very helpful to redo this work in a different region. The high southern latitudes (40^oS-70^oS) showed a large fraction of sea spray particles contributing to the CCN number [Quinn et al., 2017]. This should be visible in correlations, similar to those presented in Section 5, as the CCN number should not be dominated by the DMS flux. Additionally, Lana et al. [2012] did a correlation of monthly satellite derived CCN numbers with DMS flux and sea spray flux (Figure 6.5). For the southern high latitudes they found a positive correlation with DMS flux, but a negative one for sea spray flux. This contradicts Quinn et al. [2017] and would be interesting to investigate.
The high southern latitudes might also be favorable due to a better satellite coverage

(overlapping satellite passes) and less cloud coverage. In austral summer both satellite passes (ascending and descending orbit) could be used. Remote sensing data would be available twice a day. Lana et al. [2012] also shows negative correlations for DMS flux with CCN around the tropics of Cancer and Capricorn. A measurement campaign there would also be interesting.

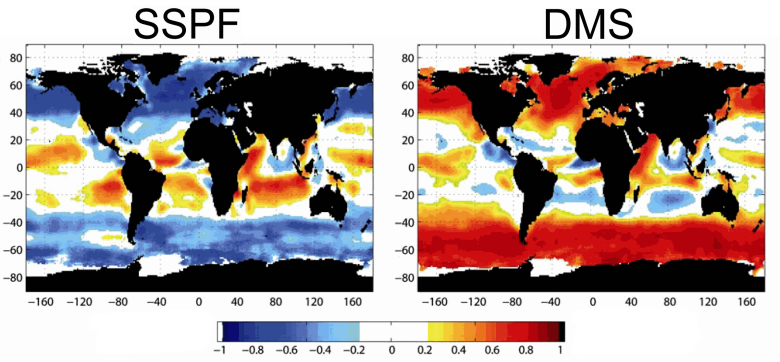

Figure 6.5: Correlation of sea spray flux [left] and monthly DMS flux [right] with satellite derived CCN number. Modified from Lana et al. [2012]

6.3 Gas transfer limitation, parameterization and bubble mediated gas transfer

Can gas transfer limitation be explained at medium to high wind speed? Can a parameterization using the wave and wind field describe the environments at which these gas transfer limitations occur?

Gas transfer limitation is a result of wind-wave interaction. The wind, transformed into the wave's reference system by a simple Galilean transformation, acts like the flow around a cylinder and causes flow separation ([3] in Figure 6.6). This flow separation causes gas transfer limitation. At sufficiently high Reynolds number Re$\approx 10^6$ the flow separation decreases and a turbulent wake is established. Until now, most wave age and wind-wave age parameterizations utilized absolute values of wind speed and wave's phase speed. This description is incomplete and does not include the vectorial characteristics of these two variables. The same mistake was done by Rene Descartes describing elastic collisions. His theory was not valid for all cases. Christiaan Huygens provided a proper mathematical description of elastic collisions with the use of Galilean transformations. He derived the laws of momentum transfer we know. Connecting the wind speed in the wave's reference system with the aerodynamic theory of the flow around a cylinder results in the model for gas transfer limitation, the transformed Reynolds number.
The parameters needed to calculate the transformed Reynolds number are wind speed, wind direction, wave speed, wave direction and wave height. The calculation is easy and

can quickly identify gas transfer limitation environments. It is also possible to predict limitation events with wind and wave forecasts.

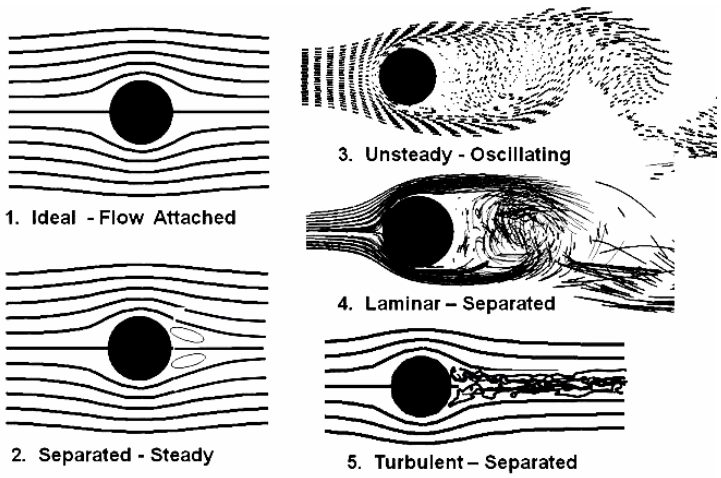

Figure 6.6: Flow around a cylinder at [1] Re=1, [2] Re=10^1, [3] Re=10^2, [4] Re=10^4-10^5, [5]Re>10^6 [Glenn Research Center, 2018].

6.3.1 Further investigations

The process of gas transfer limitation has to be further confined. I estimated the lower and upper boundary of this process in Section 5, but there are clearly other processes that cause flux limitation. It would be helpful to measure direct fluxes of two gases on station, when a storm is passing and the wind-wave field is going through all evolutionary steps: Swell-dominated sea, young-sea, mature-sea, wind-wave-dominated sea, old-sea, swell dominated sea. This investigation should be repeated in the open ocean, in marginal seas (Gulf of Mexico, North Sea) and the marginal ice zone, as the model calculations (Section 5) showed a larger occurrence of gas transfer limitation in the latter two. All investigated areas should have large DMS and CO_2 fluxes to finally rule out measurement errors or noise as the reason for gas transfer limitation.

6.4 Global budgets

How often does gas transfer limitation occur globally? Does it influence the global flux of DMS or CO_2? Are previously published gas transfer parameterizations influenced by gas transfer limitation?

Applying the transformed Reynolds number parameterization to a 2014 global wind and wave data set, reveals that in the year 2014 19% of all time steps are subject to gas transfer limitation (Figure 5.7). Marginal seas and coastal areas are more influenced by gas transfer limitation. Open oceans are less likely to be an environment of gas transfer

limitation. This explains the difference between northern and southern Hemisphere (Figure 5.8). The southern Hemisphere has more open waters without coastal influence, this decreases the likelihood of gas transfer limitation. This variety in occurrence makes it difficult to estimate beforehand if measurements are exposed to gas transfer limitation. Regional measurement campaigns need to calculate their Re_{tr} to check for in situ limitation. Global calculations could use the estimates presented in Section 5 and the recap in the next paragraph.
The global 2014 uptake of CO_2 is reduced by 7-9%, the global 2014 emission of DMS by 11%. For CO_2, the oceanic update is used to constrain the other sources and sinks of the global carbon budget, especially the land carbon sink (Figure 1.10). Together with the reduction through gas transfer limitation for DMS (11%), these two percentages show that, by no means, the global budgets of sulfur or CO_2 are well constrained. This does not mean that global budget estimates are generally flawed or should be disregarded, but a general caution about the errors or possible variances is recommended. It is necessary to include the gas transfer limitation in future global budget calculations.
Furthermore, a reanalysis of previous eddy covariance measurements is necessary. The data processing improved can be reapplied to raw data from previously published campaigns. The updated fluxes can be analyzed with the focus on recently discovered processes. This would be important to make results comparable. This reanalysis should also be done for all gas transfer parameterizations. It is important under which conditions they were recorded and which corrections (for example atmospheric stability) were made. For example, McGillis et al. [2001] and McGillis et al. [2004] show totally different k vs u functional forms of CO_2 gas transfer velocity vs wind speed. The environmental conditions are the key to understanding these differences and are an important step to get closer to a universal parameterization.

6.5 Future of gas transfer parameterizations

Gas transfer parameterizations should fulfill three tasks: [1] Reflect all major processes influencing gas transfer. [2] Provide a parameterization, which can be easily used by others. [3] Be universally applicable.
All three tasks cannot be accomplished at the same time. They even contradict themselves. Any parameterization is a tradeoff between these three properties.

Processes in gas transfer

The turbulence generated by wind is the major driver of gas transfer. But there are obviously, dependent on the environmental conditions, additional processes influencing the exchange. Section 4 adds wind-wave interaction to the game of gas transfer processes. It is not ubiquitous and a general feature of high wind, but is highly likely to be encountered (28%) at a wind speed between 12-16 m s^{-1} (Figure 4.11). At higher wind speed or large wave height, where limitation by the transformed Reynolds number is insignificant, processes such as shielding or spume interaction may take over [Andreas,

2004, Kudryavtsev, 2006, Powell et al., 2003]. This the first attempt to parameterize the influence of this wind-wave interaction on gas transfer. Further investigation is needed. The research community needs simultaneous gas transfer measurements of multiple gases with and without gas transfer limitation during the same measurement campaign. High wind measurements are also needed to determine the upper limit of this parameterization and separating it from high wave (SWH>4 m) and hurricane wind processes.
Bubble mediated gas transfer (Section 4) is not standardized and has not converged to a common understanding in the scientific community. Comparing Section 4 to previously published results [Bell et al., 2017] lead to a general functional form, but the absolute magnitude is still highly uncertain. A possible weakness of bubble mediated gas transfer estimates is the calculation of the whitecap fraction WC. This work used a wind speed based parameterization for this variable. The optical measurement of this variable should be standard practice during direct flux measurements.

Usability of gas transfer parameterizations

For the gas exchange community, gas transfer parameterizations are a means to check the investigated process for universality and to develop air-sea exchange models. Studies that directly measure gas transfer do not need a gas transfer parameterization. However, there are many other scientists who cannot measure it and, therefore, use the bulk formula (Equation 1.2), requiring gas transfer parameterizations.
The gas exchange community has to provide easy algorithms and best-practices recommendations. Parameterizations, in the best case, should consist of parameters (wind speed, temperature, pressure, etc) measured standardly during scientific field work. A parameterization using friction velocity, for example, might be scientifically interesting, but it is not easily measurable. Friction velocity, however, can be parameterized using wind speed, which could be used in the gas transfer parameterization in the first place. The presented Re_{tr} parameterization of gas transfer limitations using Re_{tr} uses standard parameters measured during fieldwork. The wave properties can be easily obtained from global wave models at sufficient temporal and spatial resolution. The influence can also be predicted (weather and wave forecasts) and continuously calculated. Also its magnitude (Section 5) can be calculated easily. It is a simple and easy model that can be imposed on existing wind speed gas transfer parameterizations.

Universal application

A goal in the air-sea interaction community is, while identifying the dominant processes, to provide a unified air-sea gas exchange parameterization. A balance between universality and applicability is crucial.
Wanninkhof et al. [2009] proposes a 3rd degree wind speed dependent polynomial to describe air-sea gas exchange and incorporate all relevant processes. It is questionable that the approach, fitting a functional form to locally measured data, leads to a universal description. This is supported by the lessons learned from the analysis of locally derived gas transfer parameterizations in Section 5.5.2. In my opinion, a compilation of gas

transfer measurements including their environmental conditions should be started.
A first step towards an integration of different processes has been done by the NOAA COARE 3.5 algorithm [Fairall et al., 1996a,b, Edson et al., 2013]. The advantage of COARE is that it provides a complete description of the marine boundary layer (height, stability, friction velocity, etc.). Additionally, it provides outputs of intermediate results. The user can choose to include or exclude processes such as bubble mediated gas transfer, rain influence, etc. in the calculation. If COARE is developed further and new processes, such as gas transfer limitation, are added, it could be a handy tool for gas transfer calculations. In my opinion a modular calculation kit for calculating air-sea gas transfer velocities would be a useful solution to the problem of universality and applicability. The downside of a module is definitely the need of a best practice manual and a 'how to guide. The first step is a review of the most commonly used gas transfer parameterization with a focus on wave breaking, bubble effect and Reynolds gas transfer limitation. The community and the users have to understand under which conditions these parameterizations were measured and therefore which corrections have to applied or under which conditions they can be used. An example is Blomquist et al. [2017]. They published the full data of Yang et al. [2011] (Figure 1.6). We have to make parameterizations comparable. Then by switching on and off further modules (bubble mediated gas transfer, limitations,...) a gas transfer velocity for the specific environmental conditions can be built (Figure 6.7).

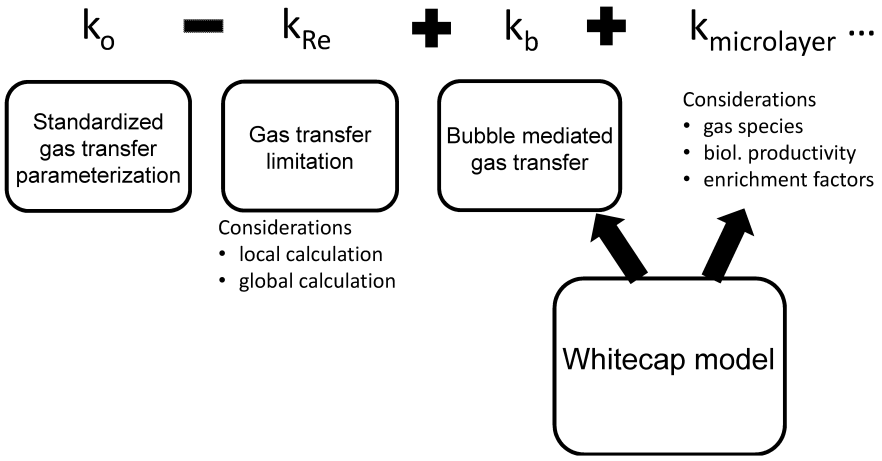

Figure 6.7: Proposed module schematic for the calculation of the gas transfer velocity. Modules with already available models are encased.

References

Nick Allen, Elena Amico di Meane, Paul Brewer, Valerio Ferracci, Marivon Corbel, and David Worton. Long-term stability measurements of low concentration volatile organic compound gas mixtures. In *General Assembly EGU*, 2017.

Edgar L. Andreas. Spray stress revisited. *Journal of Physical Oceanography*, 34(6):1429–1440, 2004. doi: 10.1175/1520-0485(2004)034<1429:SSR>2.0.CO;2. URL https://doi.org/10.1175/1520-0485(2004)034<1429:SSR>2.0.CO;2.

Marc Aubinet, Timo Vesala, and Dario Papale, editors. *Eddy Covariance*. Springer Netherlands, 2012. doi: 10.1007/978-94-007-2351-1.

T. G. Bell, S. Landwehr, S. D. Miller, W. J. de Bruyn, A. H. Callaghan, B. Scanlon, B. Ward, M. Yang, and E. S. Saltzman. Estimation of bubble-mediated air–sea gas exchange from concurrent dms and co2 transfer velocities at intermediate–high wind speeds. *Atmospheric Chemistry and Physics*, 17(14):9019–9033, 2017. doi: 10.5194/acp-17-9019-2017. URL https://www.atmos-chem-phys.net/17/9019/2017/.

B. W. Blomquist, S. E. Brumer, C. W. Fairall, B. J. Huebert, C. J. Zappa, I. M. Brooks, M. Yang, L. Bariteau, J. Prytherch, J. E. Hare, H. Czerski, A. Matei, and R. W. Pascal. Wind speed and sea state dependencies of air-sea gas transfer: Results from the high wind speed gas exchange study (hiwings). *Journal of Geophysical Research: Oceans*, pages n/a–n/a, oct 2017. ISSN 2169-9291. doi: 10.1002/2017JC013181. URL http://dx.doi.org/10.1002/2017JC013181.

ESA CEOS Database. Ceos mission, instruments and measurements database online. *Webpage*, 2018. URL http://database.eohandbook.com.

Robert J. Charlson, James E. Lovelock, Meinrat O. Andreae, and Stephen G. Warren. Oceanic phytoplankton, atmospheric sulphur, cloud albedo and climate. *Nature*, 326 (6114):655–661, apr 1987. doi: 10.1038/326655a0. URL http://dx.doi.org/10.1038/326655a0.

James B. Edson, Venkata Jampana, Robert A. Weller, Sebastien P. Bigorre, Albert J. Plueddemann, Christopher W. Fairall, Scott D. Miller, Larry Mahrt, Dean Vickers, and Hans Hersbach. On the exchange of momentum over the open ocean. *Journal of Physical Oceanography*, 43(8):1589–1610, 2013. doi: 10.1175/JPO-D-12-0173.1. URL http://dx.doi.org/10.1175/JPO-D-12-0173.1.

C. W. Fairall, E. F. Bradley, J. S. Godfrey, G. A. Wick, J. B. Edson, and G. S. Young. Cool-skin and warm-layer effects on sea surface temperature. *Journal of Geophysical Research: Oceans*, 101(C1):1295–1308, 1996a. ISSN 2156-2202. doi: 10.1029/95JC03190. URL http://dx.doi.org/10.1029/95JC03190.

C. W. Fairall, E. F. Bradley, D. P. Rogers, J. B. Edson, and G. S. Young. Bulk parameterization of air-sea fluxes for tropical ocean-global atmosphere coupled-ocean atmosphere response experiment. *J. Geophys. Res.*, 101(C2):3747–3764, 1996b. ISSN 2156-2202. URL http://dx.doi.org/10.1029/95JC03205.

NASA Glenn Research Center. Aerodynamics index. *Webpage*, 2018. doi: https://www.grc.nasa.gov/www/k-12/airplane/short.html.

Vladimir N. Kudryavtsev. On the effect of sea drops on the atmospheric boundary layer. *Journal of Geophysical Research: Oceans*, 111(C7):n/a–n/a, 2006. ISSN 2156-2202. doi: 10.1029/2005JC002970. URL http://dx.doi.org/10.1029/2005JC002970. C07020.

A. Lana, R. Simo, S. M. Vallina, and J. Dachs. Potential for a biogenic influence on cloud microphysics over the ocean: a correlation study with satellite-derived data. *Atmos. Chem. Phys.*, 12(17):7977–7993, sep 2012. ISSN 1680-7324. doi: 10.5194/acp-12-7977-2012. URL http://www.atmos-chem-phys.net/12/7977/2012/.

Daiana Leuenberger, Celine Pascale, Myriam Guillevic, Andreas Ackermann, and Bernhard Niederhauser. State of the art stationary and mobile infrastructure for the dynamic generation and dilution of traceable reference gas mixtures of ammonia at ambient air amount fractions. In *General Assembly EGU*, 2017.

W. R. McGillis, J. B. Edson, J. E. Hare, and C. W. Fairall. Direct covariance air-sea co2 fluxes. *Journal of Geophysical Research: Oceans*, 106(C8):16729–16745, aug 2001. ISSN 2156-2202. doi: 10.1029/2000JC000506. URL http://dx.doi.org/10.1029/2000JC000506.

Wade R. McGillis, James B. Edson, Christopher J. Zappa, Jonathan D. Ware, Sean P. McKenna, Eugene A. Terray, Jeffrey E. Hare, Christopher W. Fairall, William Drennan, Mark Donelan, Michael D. DeGrandpre, Rik Wanninkhof, and Richard A. Feely. Air-sea co2 exchange in the equatorial pacific. *Journal of Geophysical Research: Oceans*, 109(C8):n/a–n/a, aug 2004. ISSN 2156-2202. doi: 10.1029/2003JC002256. URL http://dx.doi.org/10.1029/2003JC002256.

Mark D. Powell, Peter J. Vickery, and Timothy A. Reinhold. Reduced drag coefficient for high wind speeds in tropical cyclones. *Nature*, 422:279, March 2003. URL http://dx.doi.org/10.1038/nature01481.

P. K. Quinn and T. S. Bates. The case against climate regulation via oceanic phytoplankton sulphur emissions. *Nature*, 480(7375):51–56, nov 2011. ISSN 0028-0836. doi: 10.1038/nature10580. URL http://dx.doi.org/10.1038/nature10580.

P. K. Quinn, D. J. Coffman, J. E. Johnson, L. M. Upchurch, and T. S. Bates. Small fraction of marine cloud condensation nuclei made up of sea spray aerosol. *Nature Geosci*, 10(9):674–679, September 2017. ISSN 1752-0894. URL http://dx.doi.org/10.1038/ngeo3003.

Rik Wanninkhof, William E Asher, David T Ho, Colm Sweeney, and Wade R McGillis. Advances in quantifying air-sea gas exchange and environmental forcing. *Annual Review of Marine Science*, 1(1):213–244, jan 2009. doi: 10.1146/annurev.marine.010908.163742.

M Yang, BW Blomquist, CW Fairall, SD Archer, and BJ Huebert. Air-sea exchange of dimethylsulfide in the southern ocean: Measurements from so gasex compared to temperate and tropical regions. *Journal of Geophysical Research: Oceans*, 116(C4), aug 2011. ISSN 2156-2202. doi: 10.1029/2010jc006526.

List of Figures

List of Tables

So sag ich jetzt gegen Ende,
der Zusammenhang spricht Bände.
Ich hab keine Lust auf Garnichts,
was ich will hat bald ein Ende.
Was ich hier genau erkläre
hat nichts mit alldem gemein.
Es geht immer ums Vollenden
und den Superbowl.

Der Nino aus Wien